UNIVERSIDAD DE CÁDIZ
Facultad de Ciencias del Mar y Ambientales
Departamento de Física Aplicada

TESIS DOCTORAL

M. Manuela Reyes Reyes

Modelado de alta resolución para el estudio de la respuesta oceánica al forzamiento del viento en el Estrecho de Gibraltar

Cádiz 2014

UNIVERSIDAD DE CÁDIZ

FACULTAD DE CIENCIAS DEL MAR Y AMBIENTALES

DEPARTAMENTO DE FÍSICA APLICADA

MODELADO DE ALTA RESOLUCIÓN PARA EL ESTUDIO DE LA RESPUESTA OCEÁNICA AL FORZAMIENTO DEL VIENTO EN EL ESTRECHO DE GIBRALTAR

A HIGH-RESOLUTION MODELING STUDY OF THE OCEAN RESPONSE TO WIND FORCING WITHIN THE STRAIT OF GIBRALTAR

TESIS DOCTORAL

M. Manuela Reyes Reyes

Cádiz, 2014

Esta Tesis Doctoral ha sido realizada gracias a la financiación de los proyectos del Plan Nacional de Investigación ESEOO (VEM2003-20577-C14-07) y MONGACLIMAR (CTM2008-06124/MAR), del proyecto TRADE (Trans-regional RADars for Environmental applications) del Programa Operativo de Cooperación Transfronteriza España-Portugal con cofinanciación del Fondo Europeo de Desarrollo Regional (FEDER) y de los proyectos ARCOPOLplus (2011_1/150) y ARCOPOLplatform (2013_1/252) del Programa de Cooperación Transnacional Espacio Atlántico, financiados con fondos FEDER. El trabajo ha sido llevado a cabo en el Departamento de Física Aplicada de la Universidad de Cádiz, en el seno del Grupo de Investigación "Oceanografía Física: Dinámica" (ref. PAI: RNM-205) en el marco del Campus de Excelencia Internacional del Mar (CEI-Mar).

UNIVERSIDAD DE CÁDIZ
Facultad de Ciencias del Mar y Ambientales
Departamento de Física Aplicada

MODELADO DE ALTA RESOLUCIÓN PARA EL ESTUDIO DE LA RESPUESTA OCEÁNICA AL FORZAMIENTO DEL VIENTO EN EL ESTRECHO DE GIBRALTAR

A HIGH-RESOLUTION MODELING STUDY OF THE OCEAN RESPONSE TO WIND FORCING WITHIN THE STRAIT OF GIBRALTAR

Memoria presentada por M. Manuela Reyes Reyes para optar al grado de Doctor por la Universidad de Cádiz

Fdo.: M . Manuela Reyes Reyes

D. ALFREDO IZQUIERDO GONZÁLEZ, Profesor Contratado Doctor del Departamento de Física Aplicada de la Universidad de Cádiz, y D. MIGUEL BRUNO MEJÍAS, Profesor Titular del Departamento de Física Aplicada de la Universidad de Cádiz,

HACEN CONSTAR:

Que esta memoria titulada "MODELADO DE ALTA RESOLUCIÓN PARA EL ESTUDIO DE LA RESPUESTA OCEÁNICA AL FORZAMIENTO DEL VIENTO EN EL ESTRECHO DE GIBRALTAR", presentada por Dña. Mª Manuela Reyes Reyes, ha sido realizada bajo su dirección y autorizan su presentación y defensa para optar al grado de Doctor por la Universidad de Cádiz.

Puerto Real, 7 de Noviembre del 2014

Dr. D. Alfredo Izquierdo González

Dr. D. Miguel Bruno Mejías

Para los autores de mi vida,

de la autora de esta tesis.

Si cada esfuerzo

tiene su recompensa,

esta es la mía,

la vuestra,

la nuestra.

Por ti

AGRADECIMIENTOS

Hay días especiales en los que todos los que te han ofrecido su ayuda o te han sonreído por el camino merecen estar en el recuerdo (de *re-cordis*[1]= volver a pasar por el corazón).

Hoy recuerdo y agradezco profundamente:

A mis Directores, Alfredo Izquierdo y Miguel Bruno, mis griots científicos. Gracias por enseñarme a plantear las preguntas correctas y mostrarme la senda para encontrar las respuestas, por vuestra genialidad y dedicación. El respecto y la admiración que os profeso es únicamente comparable con el cariño que os tengo.

A mis padres y a mi hermano, las piedras angulares de mi vida. Por hacerme feliz, por su amor incondicional y su apoyo inquebrantable. Por alimentar mis alas, aún a sabiendas de mis intenciones de volar, y por avivar mis sueños. A Lore, mi *cuñi* preferida, por alegrar las tierras de secano con sus aires gaditanos.

A mis abuelos, por legarme el valor del esfuerzo y del trabajo, de la constancia y la perseverancia. Especial recuerdo merece mi abuela Manuela, por transmitirme su pasión por las pequeñas cosas que hacen grande la vida.

A mis primos y a mis tíos, por compartir los mejores *veranos azules* de la niñez y buenos ratos de piscina en la madurez. Mención exclusiva merece mi tita Jose por estar siempre, por y para todo, por y para todos, por alimentarme de cariño, de mermeladas y patés caseros.

A todos mis compañeros del Departamento de Física Aplicada por su ayuda, cada uno en la medida de sus competencias, y por sus muestras de ánimo, particularmente en esta última etapa. Agradezco muy especialmente el apoyo de mis colegas de despacho, desde los inicios (mi-Daivi, Carlos) hasta el ahora (Alicia, Alejandro). A Carlitos, porque los marrones unen y a Jeannette, por algo más que su cocido.

A mis guatemaltecas, Estrella, Anabella, Oralia y Lygia por recordarme que hay lugares en el mundo donde ser mujer es sinónimo de valentía y por su cálida hospitalidad durante mi estancia en la Universidad de San Carlos de Guatemala.

[1] De "El Libro de los Abrazos", de Eduardo Galeano.

A Max, Carlos Estuardo, Pana y Chepi, por mostrarme las bellezas del paraíso guatemalteco y advertirme que el Pacífico no hace honor a su nombre.

Herrn Dr. Rainer Reuter und Herrn Dr. Frank Terjung der Carl von der Ossietzky Universität Oldenburg danke ich herzlich dafür mich in die Meeresphysik Gruppe integriert zu haben, wo das Abenteur zuerst begonnen hat. Vielen Dank!

A Breogán Gómez, Vicente Pérez, Silvia Torres y Pedro Montero por acogerme en el seno de MeteoGalicia y ascenderme a niveles de la troposfera, os debo tanto...

A Alberto Álvarez por introducirme en el mundo del *adapting sampling* y maravillarme con sus geniales ideas durante mi participación en el NURC Research Assistantship Programme (Italia).

I am profoundly indebted to Şükrü Beşiktepe for bringing me on board R. V. Alliance during the TSS08 (Turkish-Strait-System) oceanographic survey, which was leading to a better understanding of Marsigli's discovery. Teşekkür ederim!

I gratefully acknowledge the help and support I have received from Chuck Trees and his keeshond Keelee, for their warm hospitality in casa-de-los-árboles. We also really enjoyed the time together at the *terrazza* with the "Why-not" group.

Ich bedanke mich ganz herzlich bei dem MPI für Meteorologie (Hamburg) für die Möglichkeit, einen Forshungsaufenthalt durchzuführen. Ein besonderer Dank gilt Dimitri, Uwe, Fanny, Florian, Alberto, und Vadym, die mir während dieser Zeit immer hilfreich beiseite standen.

A los integrantes de la familia TEMPUS, en especial a la mamita portuguesa Filomena Martins y a Nikolai Plink. Crecí, personal y profesionalmente, a vuestro lado y bajo vuestro inmenso cariño.

A Sergey Vinogradov, por guiarme en mis primeros pasos con linux y bash-scripting y a Elena Plink, por acogerme en la calidez de su hogar en la gélida Rusia.

A los participantes de los proyectos ARCOPOLplus y ARCOPOLPlatform, entre los que hay viejos conocidos, por convertir el trabajo en placer.

A las tripulaciones del BIO Hespérides, Malaspina, Tofiño y Alliance por aguantar estoicamente los interminables transeptos, por su profesionalidad y amabilidad.

A todos aquéllos que mantienen las bases de datos y redes de medida nacionales, regionales e internacionales, por su esfuerzo y dedicación, en beneficio de todos.

A Ffion y Augusto, por transmitirme el entusiasmo de los inicios y hacerme valorar, más aún si cabe, la nada trivial labor de los directores.

A Joaco, porque *todo el ruido del mar huele a ti* y porque tu recuerdo sigue haciéndome reír y me ayuda a olvidar que estás lejos de aquí...Eres el Adiós que jamás sabré ni querré decir.

A mis nenillas: a Erku, por su afecto, su cariño, sus sabios consejos, sus buenas palabras y sus mejores acciones; a Imane, por ser mi remanso de paz y serenidad y por ayudarme a unir lo que una vez Hércules logró separar; a Ire, por su habilidad para desmontarme cualquier argumento y componerme el alma con su sonrisa.

A las viejas glorias de SLN (Cori, Isa, Yvette, Judith) y a los nuevos fichajes, Helena-Duna, Marina, Soraya y Marga. ¡Sois espAciales!,...gracias mil.

A mis amigos del pueblo, por la infancia compartida y la impetuosa juventud disfrutada. Especialmente, agradezco a María Luisa los ratos de desconexión y a Rosana el hecho de entender mis ideas, mejorarlas y plasmarlas en una portada profesional.

A todos los componentes de la *family* gaditana, por hacer inolvidables mis años universitarios y compartir la genial experiencia de crecer juntos. Particular mención merecen Bea, Aran y Seca, por estar siempre, en todo y para todo.

A los multi-disciplinares dispersos por el globo. Mi gratitud a las comunidades chilena, (Manu, Flora y Lucho), ecuatoriana, (Varela, Jenny y paisano), al *guiri* Paco, al *italianini* Dani y al *i-luso* de Nachete. No sabéis cuánto se os echa de menos...

A Pablo y Pablete porque sus locuras y sarcasmos *granaínos*, respectivamente,...me ayudan a mantenerme en guardia.

Al trío de excelencia, Antonio, Gerardo (Joseba) y Abelardo (Iker). Día a día dispuestos a echarme un "cable", con sus "puertos" siempre abiertos y respondiendo a mis CAUs a velocidad "Jumbo".

A Ana porque, no sé cómo pero, sabe que el orden de mi cabeza es proporcional al de mi escritorio e intenta, por todos los medios, mantenerlo despejado.

A Juanma, Sergio y Servando por alimentar mis mañanas con sus bromas y sus sonrisas.

A Luis, Vero, Lolo, Paco y Juan por imponerme el "*mens sana in corpore sano*" o, al menos, intentarlo.

A la Dra. García Valero por trascender los límites del juramento hipocrático y contagiarme su energía y vitalidad, cuando más lo he necesitado.

Si somos lo que admiramos,

espero, algún día, parecerme un poquito a cada uno de vosotros.

PRÓLOGO

Es bien conocida, por todos los habitantes de las costas gaditanas, la influencia del viento de Levante (y de Poniente) en sus hábitos, costumbres y hasta en su semblante.

"Las personas sienten punzadas en las heridas o antiguas llagas, los males crónicos se agravan y los sanos padecen melancolía y laxitud, cuando llega el Levante. El Poniente por el contrario, es el recreo, la primavera sazonada"
(López de Ayala, 1782)[1]

La importancia de estos vientos, intensos y persistentes, ha quedado patente en el saber popular, dando lugar a un refranero plagado de referencias a la meteorología de la zona. Este genial y completo compendio de filosofía ha sido alimentado por siglos de observaciones de hombres de mar y tierra, modificado con los rasgos de la lengua regional, matizado por el temperamento y el carácter de las gentes, y transmitido durante generaciones.

Aforismos tradicionales, o *poesía petrificada,* como decía Borges, que bajo las primeras capas de idiosincrasia, guardan un trasfondo empírico que bien podría convertirlos en la mayor red de observaciones con el más amplio de los registros. A pesar de que *no hay refrán que no sea verdadero*[2], como ya adelantaba Don Quijote a Sancho, la subjetividad del método de observación, alejado de la metodología científica convencional, los relegan al papel de la enseñanza práctica.

"Cádiz,...señorita del mar,
novia del aire o ciudad de la gracia,
la razón y la medida"
(Pemán, 1934)[3]

[1] López de Ayala, I. (Ed.) (1782). Historia de Gibraltar, Madrid.
[2] Cervantes Saavedra, M, 1605. El Ingenioso Hidalgo Don Quijote de la Mancha I, Capítulo XXI.
[3] Pemán, J. M. (1934). Señorita del mar (itinerario lírico de Cádiz).

Forma también parte del conocimiento popular el hecho de que el Levante, seco y cálido, aclara y calienta el agua, mientras que el Poniente, fresco y húmedo, la enfría y la enturbia. Con esta categórica afirmación, definen los gaditanos la transferencia de calor, *momentum* y masa que se realiza a través de la interfaz atmósfera-océano y que constituye el motor de la circulación oceánica y, a su vez, de la circulación atmosférica.

Estos *aires difíciles*, como fueran nombrados en la prosa de Almudena Grandes, protagonistas de los poemas de Rafael Alberti e inspiración de las comparsas carnavalescas, repiten en su papel como actores principales a lo largo de esta Tesis Doctoral. En ella se aborda el estudio de la influencia del viento en la variabilidad espacio-temporal de la circulación del Estrecho de Gibraltar y de las respuestas inducidas que se producen en las fluctuaciones barotrópicas y del intercambio baroclino, a partir de un modelo oceánico forzado por viento.

Esta investigación surge con la finalidad de contribuir a los esfuerzos de comprensión de la dinámica y a los de modelización realizados en el Estrecho de Gibraltar.

Cabe añadir que, para mayor satisfacción de la autora, los modelos implementados y validados en el marco de esta investigación han sido incluidos en un sistema de oceanografía operacional. De esta forma, la predicción a 72 horas de variables océano-meteorológicas para la región andaluza y, a mayor resolución espacial, para el Estrecho de Gibraltar, se pone a disposición de la sociedad, contribuyendo así con la *ciencia* a los grandes valores que aporta el pueblo a través de *la mesma experiencia*[4].

"Cádiz es mujer con dos novios prendaos de su talle,
y están por sus huesos locos el Poniente y el Levante,
ninguno quiere que el otro le ronde sus calles.
Vientos del amor, por las esquinas y azoteas
la requiebran y esa novia pela la pava con los dos,
ay, los enamora, los enamora, los enamora..."
(Pasodoble de los Vientos de Cádiz,
Comparsa "Los Buscavidas" de Antonio Martín, 1997)

[4]Cervantes Saavedra, M., 1605.*El Ingenioso Hidalgo Don Quijote de la Mancha* I, Capítulo XXI.

RESUMEN

El presente trabajo de investigación aborda el estudio de la influencia del viento en la variabilidad espacio-temporal de la circulación del Estrecho de Gibraltar (sur de la Península Ibérica) y de las respuestas inducidas que se producen en las fluctuaciones barotrópicas y del intercambio baroclino, mediante un modelo oceánico forzado por viento.

Para ello, se ha implementado el modelo atmosférico MM5 de área limitada no hidrostático, el cual provee el campo de viento a alta resolución al modelo hidrodinámico, bicapa, bidimensional, no-lineal UCA2.5D, que utiliza coordenadas curvilíneas ajustadas a los contornos y que incluye el forzamiento de marea.

La capacidad del modelo MM5 para reproducir los patrones mesoescalares meteorológicos en la compleja orografía de la región andaluza, así como las brisas de tierra-mar y montaña-valle ha sido evaluada satisfactoriamente. No obstante, existen algunas diferencias entre las simulaciones y las observaciones atribuidas a distintas causas, las cuales han sido discutidas.

Del mismo modo, las salidas del modelo oceánico, forzado por viento, han sido comparadas frente a un amplio conjunto de datos oceanográficos, mostrando una mejora significativa frente al modelo hidrodinámico forzado únicamente por marea.

Los resultados evidencian la importancia del efecto del viento en la dinámica del Estrecho de Gibraltar. Los vientos del este o Levantes (del oeste o Ponientes) originan un hundimiento (surgencia) en la costa española del Estrecho, dando lugar a un incremento (reducción) del espesor de la capa atlántica, profundizando (elevando) la interfaz y elevando (hundiendo) el nivel del mar.

La acumulación de agua en la costa norte (sur) del Estrecho en eventos de viento de Levante (Poniente) intenso y persistente, crea una diferencia de nivel en la sección transversal, dando lugar a una corriente geostrófica hacia el oeste (este). Esta corriente, en el caso de los Levantes, refuerza la contracorriente costera semipermanente de la costa norte, por un lado, y por otro, reduce el flujo medio entrante, llegando incluso a revertirlo. En condiciones de vientos de Poniente, la corriente geostrófica se suma al flujo entrante, llegando éste a alcanzar el doble de intensidad que en eventos de Levante.

Concretamente, los resultados muestran el efecto de los distintos regímenes de viento en las fluctuaciones de la interfaz, modificando la localización de los controles hidráulicos, haciéndolos incluso desaparecer (en el caso de los Levantes) o generando otras regiones supercríticas (en el caso de los Ponientes).

Los cambios en la intensidad del flujo barotrópico y de la posición de la interfaz, debidos al forzamiento de viento, modifican los tiempos de generación del salto hidráulico sobre el Umbral de Camarinal y las velocidades de propagación del bore interno.

Las estimaciones del flujo entrante atlántico y del flujo saliente mediterráneo mejoran al incluir el efecto del estrés del viento, particularmente durante eventos de viento intenso del este (Levante).

Palabras clave:

Estrés del viento, modelo oceánico, MM5, Estrecho de Gibraltar, alta resolución, control hidráulico, bore interno.

ABSTRACT

This research work makes an incremental step in understanding the role of the wind-stress and the associated dynamic ocean response of the barotropic and baroclinic exchange fluctuations by means of a wind-forced ocean model within the Strait of Gibraltar (south of Iberian Peninsula).

The limited-area, non-hydrostatic atmospheric model MM5 was configured to study the mesoscale atmospheric processes in the area of interest and to provide realistic wind-stress forcing to the two-layer, two-dimensional, nonlinear, boundary-fitted coordinate hydrostatic model UCA2.5D at high-resolution, also forced by tidal motions.

A statistical evaluation of the MM5 model performance is undertaken by means of pairwise comparison of observations and model output, showing good skills in reproducing the mesoscale flows over the complex Andalusian orography, sea-land breeze circulation and mountain-valley breezes. However, some discrepancies between observations and predictions have been found and their main causes have been discussed.

Most importantly, comparison of model results with an extensive oceanographic data set collected in situ shows that the wind-forced ocean model provides better agreement with the observations than the ocean-alone model with tidal forcing.

Results show the effect of winds on the dynamics in the Strait of Gibraltar with and without tidal forcing, pointing out the essential sensitivity of the area to different forcings.

The hydrodynamic patterns induced by wind stress are successfully simulated showing that prevailing easterly (westerly) winds originate downwelling (upwelling) phenomena in the Spanish coast of the Strait of Gibraltar, which subsequently will induce an increase (reduction) of the upper layer thickness, deepening (rising up) the interface and rising (dropping) the sea level.

During persistent and intense easterly (westerly) wind episodes, the accumulation of water in the northern (southern) part reduces (reinforces) the downwards south-to-north sea surface slope, which induces a geostrophic current westward (eastward).

Under easterlies, the geostrophic current reinforces the semi-permanent westward countercurrent along the northern coast of the Strait, on the one hand, and reduces the intensity of the inflow, on the other, being able to reverse it.

Westerlies increase the upper layer current intensity, which is almost twice as intense as that of the easterly experiment.

Specifically, it is discussed the fluctuations at the interface due to wind forcing and its consequent impact on the location of the hydraulic controls, being able to activate extra supercritical regions (under westerly episodes) or to inhibit the already existing ones (under easterly episodes).

Changes in the intensity of the barotropic flow and fluctuations of the interface depth, due to wind forcing, induce modifications of the hydraulic jump generation at the lee side of Camarinal Sill and of the internal bore speed.

Estimations of Atlantic inflow and Mediterranean outflow noticeably improved when including wind-stress in the hydrodynamic model, particularly during the intense easterly wind events.

Keywords:

Wind-stress, ocean model, MM5, Strait of Gibraltar, high-resolution hydraulic control, internal bore.

ESTRUCTURA DE LA TESIS

Este trabajo de Tesis Doctoral se estructura de la siguiente forma:

El contexto del trabajo se establece en el **Capítulo 1**, en el que, junto a la revisión de los antecedentes más relevantes y el estado actual de la modelización hidrodinámica en el Estrecho de Gibraltar, se especifica el problema de la investigación, se exponen los objetivos y se describen las hipótesis planteadas. Las limitaciones del estudio se incluyen al final del capítulo.

La revisión de los datos experimentales analizados, la introducción a los modelos atmosférico e hidrodinámico seleccionados y la descripción de la implementación del modelo forzado por viento, se realiza en el **Capítulo 2.** La presentación de los modelos numéricos incluye una detallada descripción de la configuración utilizada y de la validación a la que han sido sometidos en estudios previos o, en su defecto, de la metodología utilizada para su validación en este estudio.

El **Capítulo 3** engloba los resultados más importantes obtenidos de la implementación y evaluación del modelo meteorológico MM5 en el ámbito de la región Andaluza. Los resultados abordan el impacto del aumento de resolución espacial, así como la sensibilidad a las condiciones iniciales y de contorno. Se analiza la habilidad del modelo para simular las brisas de tierra y mar y las de montaña y valle.

Los resultados derivados de la implementación y validación del modelo oceánico forzado por viento a alta resolución, mediante la comparación de las salidas con medidas oceanográficas se presentan en el **Capítulo 4**. En él se analiza el efecto individual y conjunto del estrés del viento y del forzamiento de marea en la circulación del Estrecho de Gibraltar. Las fluctuaciones del flujo de intercambio y la variabilidad espacio-temporal de los controles hidráulicos, debidos al viento, se aborda en este capítulo.

En el **Capítulo 5** se resume el contenido de la Tesis y se exponen las principales conclusiones obtenidas.

Finalmente, se incluye un listado de las referencias bibliográficas que corresponden a las publicaciones citadas en el texto, ordenadas alfabéticamente por el apellido del primer autor.

SECTIONS OF THE THESIS

This Thesis has the following sections:

Chapter 1 presents a detailed review on the subject of research. The problem statement, the main aims and the hypotheses of the study as well as its limitations are also included.

Chapter 2 introduces the meteorological and oceanographic data sets analyzed and the meteorological and ocean models selected for the study, including a description of their configurations. It also provides the procedures for conducting the model performance evaluation of the meteorological model and of the wind-forced ocean model. A summary of the hydrodynamic model performance evaluation carried out previously by other authors is also presented.

Chapter 3 compiles the results of the meteorological model performance evaluation over the Andalusian region, which is being conducted using surface meteorological observations inland and over the ocean. The benefit of increased spatial resolution and the impact of the initial and boundary conditions have also been considered. The model skills to simulate important mesoscale processes occurring in the area such, as the sea-land breezes and mountain-valley breezes, were also analyzed.

Chapter 4 presents the results of the implementation and validation of the wind-forced ocean model at high-resolution by comparing its outputs with oceanographic measurements. The individual and joint role of wind and tidal forcing on the circulation of the Strait of Gibraltar has been analyzed. Fluctuations of the flow exchange and changes in the hydraulic controls due to wind stress forcing are also addressed in this section.

At the end of Chapters 3 and 4 are drawn a series of conclusions, concerning the investigations performed and the results obtained.

Finally, **Chapter 5** includes a summary of the PhD Thesis and brings together the conclusions from this research.

Finally, a reference list, ordered alphabetically by author family name, including all sources cited in the document, is provided.

APLICACIONES

Con el fin de estimar la contribución al conocimiento científico y a la resolución de problemas prácticos, se detallan las aplicaciones derivadas de la tesis:

- Conociendo la importancia del transporte marítimo en el desarrollo económico mundial, debe considerarse también el riesgo que representa para los ambientes marinos y costeros. Teniendo en cuenta, asimismo, que más del 10% del tráfico marítimo internacional atraviesa el Estrecho de Gibraltar, particularmente surcado por petroleros en su ruta al golfo Pérsico, y las numerosas actividades potencialmente peligrosas que convergen en la zona (asentamiento de refinerías, existencia de una monoboya de descarga de crudo, bunkering o suministro a buques), se hace necesario un servicio que mejore la prevención y la respuesta frente a derrames de hidrocarburos. Los modelos implementados y validados en el marco de la Tesis forman parte, entre otros, de este sistema de oceanografía operacional, implementado por el Grupo de Oceanografía Física: Dinámica de la Universidad de Cádiz, el cual proporciona la predicción meteorológica a 72 horas y de corrientes para la región andaluza y, a mayor resolución espacial, para el Estrecho de Gibraltar.

- Las predicciones del sistema de oceanografía operacional han sido utilizadas por los Servicios de Salvamento Marítimo, el Instituto Hidrográfico de la Marina y para la ayuda a la navegación (Vuelta al Mundo de Vela de la Volvo Ocean Race). Este sistema se ha convertido en una herramienta muy útil para: la planificación de campañas oceanográficas en la zona, planes de autoprotección de los espacios naturales protegidos y para estudiar la idoneidad de las distintas regiones de la zona para el emplazamiento de centrales de energía renovables marinas.

- La incorporación de las salidas de los modelos meteorológicos y del modelo oceánico forzado con viento en el sistema de oceanografía operacional permite, por otro lado, proveer la información necesaria a modelos morfodinámicos, aplicados a sistemas de alerta temprana para la predicción del impacto morfológico causado por temporales en las playas. Esta aplicación se llevó a cabo por parte del Grupo de Geología y Geofísica Litoral y Marina de la Universidad de Cádiz, en el marco del proyecto MICORE.

- Habiéndose estudiado la capacidad del modelo oceánico forzado por viento, mediante la comparación de las salidas numéricas con observaciones en la zona, se ha

utilizado para evaluar, de forma cualitativa, junto con boyas de deriva y registros de ADCP, las medidas de corrientes superficiales de radares de alta frecuencia (CODAR's SeaSonde) instalados en el Estrecho de Gibraltar, en el marco del proyecto TRADE (Trans-regional RADars for Environmental applications), desarrollado conjuntamente con Puertos del Estado.

A partir del modelo meteorológico implementado en el marco de la Tesis, se ha iniciado una nueva línea de trabajo relacionada con la previsión de la calidad del aire que ha dado lugar a un proyecto de investigación en colaboración con empresa:

- La Bahía de Algeciras se ha coronado, tristemente, como uno de los lugares con la peor calidad del aire de Europa. La implementación del modelo de pronóstico atmosférico MM5 a alta resolución en el área del Estrecho de Gibraltar, ha abierto la posibilidad de acoplarlo al modelo de diagnóstico meteorológico CALMET a muy alta resolución, el cual, a su vez, provee la información meteorológica al modelo de dispersión de contaminantes atmosféricos CALPUFF. Así se aborda el estudio del impacto en la calidad del aire de las fuentes emisoras localizadas en la Bahía de Algeciras, en el proyecto PreDiCCA (Predicción de la Dispersión y Concentración de Contaminantes Atmosféricos).

En esta nueva línea podrían incluirse aplicaciones futuras al implementar:

- un modelo de transporte de polvo sahariano para alertar acerca de episodios de contaminación atmosférica por partículas en suspensión.
- el modelo CALPUFF para predecir la disminución de visibilidad en las capas bajas de la atmósfera, la cual aumenta el riesgo de accidentes marítimos en la zona.
- la predicción del viento, mediante la implementación del modelo de diagnóstico CALMET a muy alta resolución (100 m), para estudios de evaluación de recursos del potencial eólico terrestre y marino.

ÍNDICE GENERAL

LISTA DE FIGURAS XV
LISTA DE TABLAS XXV
LISTA DE ACRÓNIMOS XXVII

CAPÍTULO 1 1
INTRODUCCIÓN 1
1. Marco geográfico, meteorológico y oceanográfico del Estrecho de Gibraltar. 1
1.1. Marco geográfico 1
1.2. Marco meteorológico 4
1.3. Marco oceanográfico 6
2. Antecedentes de la investigación 8
3. Justificación de la investigación y objetivos 13
4. Hipótesis planteadas 14
5. Limitaciones y alcances de la investigación 16

CAPÍTULO 2 19
SERIES DE DATOS Y MODELOS NUMÉRICOS 19
1. Datos observados 20
1.1. Datos meteorológicos 20
1.1.1. Estaciones Meteorológicas Automáticas 20
1.1.2. Boyas de aguas profundas 22
1.2. Datos oceanográficos 23
1.2.1. Campaña Strait 1994-96 23
1.2.2. Campaña Gibraltar-2008 24
1.2.3. Mareógrafos de Ceuta, Tarifa y Algeciras 25
1.2.4. Boyas de deriva 27
2. Modelos numéricos 28
2.1. Modelo meteorológico de mesoescala MM5 28
2.1.1. Introducción al modelo meteorológico de mesoescala MM5 28
2.1.2. Configuración del modelo meteorológico de mesoescala MM5 30
2.1.3. Validación del modelo de mesoescala MM5 36
2.2. Modelo hidrodinámico UCA2.5D 40
2.2.1. Introducción al modelo hidrodinámico UCA2.5D 40

2.2.2. Configuración del modelo hidrodinámico UCA2.5D 44
2.2.3. Validación del modelo hidrodinámico UCA2.5D 45
2.3. Modelo oceánico forzado por viento 46
2.3.1. Introducción al modelo oceánico forzado por viento 46
2.3.2. Configuración del modelo oceánico forzado por viento 47
2.3.3. Validación del modelo oceánico forzado por viento 51

CAPÍTULO 3 53
IMPLEMENTATION AND PERFORMANCE ASSESSMENT OF THE HIGH-RESOLUTION MM5 MODEL IN THE STRAIT OF GIBRALTAR 53
1. Impact of horizontal resolution 54
2. Influence of initial and boundary conditions 59
2.1. Model versus buoy measurements 60
2.2. Model versus automatic weather station measurements 67
3. Temporal evolution and spatial distribution of model errors 70
3.1. Temporal evolution of errors 70
3.2. Geographical distribution of errors 74
4. Performance assessment of mesoscale phenomena: sea-land-breezes. 78
4.1. Sea-land breezes: qualitative comparison 78
4.1.1. Pure sea-land breezes 79
4.1.2. Non-pure sea-land breezes 83
4.2. Sea-land breezes: quantitative comparison 87
4.2.1. Daily variability of errors 87
4.2.2. Spatial distribution of errors 88
5. Summary and conclusions 91

CAPÍTULO 4 95
A HIGH-RESOLUTION MODEL FOR THE WIND-FORCED CIRCULATION IN THE STRAIT OF GIBRALTAR 95
1. Validation of the wind-forced ocean model 96
1.1. Model versus CTD casts 96
1.2. Model versus current meters 100
1.3. Model versus surface drifters 108
1.4. Model versus tide gauge data 114
2. Dynamic ocean response to wind 118

2.1. NON-TIDE experiments *118*
2.1.1. Sea level and interface depth 118
2.1.2. Upper and lower layer current velocities 120
2.2. TIDE experiments *122*
2.2.1. Sea level and interface depth 122
2.2.2. Upper and lower layer current velocities 124
2.3. Internal waves *125*
3. Hydraulic control variability 131
4. Flow exchange 135
5. Summary and conclusions 142

CAPÍTULO 5 145
SUMMARY AND CONCLUSIONS 145
1. Introduction 145
1.1. Background and previous work *145*
1.2. Statement of the problem *146*
2. General and specific objectives 147
3. Hypothesis 147
4. Data sets and models 148
4.1. Data sets *148*
4.2. Models *149*
4.2.1. Mesoscale meteorological model (MM5) 149
4.2.2. Hydrodynamic model (UCA2.5D) 150
4.2.3. Wind-forced ocean model (MM5UCA2.5D) 151
5. Conclusions 152
REFERENCES 157

LISTA DE FIGURAS

CAPÍTULO 1 1

Figura 1.1.- Mapa bati-topográfico del Estrecho de Gibraltar, golfo de Cádiz y mar de Alborán (fuente de los datos: ETOPO1) 2

Figura 1.2.- Mapa batimétrico del Estrecho de Gibraltar con los accidentes geográficos más importantes citados en el texto (fuente de los datos: IHM)3

Figura 1.3.- Perfil batimétrico a lo largo del eje longitudinal del Estrecho (línea discontinua blanca de la figura 1.2) en el que se destacan los accidentes del relieve submarino más notables citados en el texto (fuente de los datos: IHM) 4

CAPÍTULO 2 19

Figura 2.1.- Mapa topográfico del área de estudio con las localizaciones de las EMAs y las boyas utilizadas en la validación del modelo meteorológico. Los rectángulos en línea discontinua representan los dominios de 10 (D2) y 3.3 km (D3) del MM5. Se indican los nombres de las estaciones y boyas citadas en el texto. 23

Figura 2.2.- Perfiles verticales de salinidad de las estaciones yo-yo de CTD realizadas durante la campaña Gibraltar 2008..... 25

Figura 2.3.- Diagrama de la Referencia Local Revisada (RLR) para Tarifa. 26

Figura 2.4.- Mapa batimétrico del área de estudio con las localizaciones de las medidas oceanográficas realizadas. 28

Figura 2.5.- Representación esquemática de la distribución de los niveles sigma del modelo MM5. 31

Figura 2.6.- Malla Arakawa-B horizontal del modelo MM5. La malla incluida en el dominio interior representa la relación 3:1 entre los dominios anidados... 32

Figura 2.7.- Dominios anidados para la implementación del modelo MM5 a alta resolución en el Estrecho de Gibraltar (los rectángulos negro, rojo y azul representan los límites de los dominios MM5-30 km, MM5-10 km y MM5 3.3 km, respectivamente). 33

Figura 2.8.- Esquema de las ejecuciones en predicción (arriba) y de hindcast (abajo) del modelo MM5. IC y BC son las condiciones iniciales y de contorno,

respectivamente. Los bucles representan la actualización temporal de las condiciones iniciales y de contorno. 35
Figura 2.9.- Malla del modelo UCA2.5D junto con la batimetría utilizada. Se señala el transecto longitudinal al Estrecho (línea continua blanca) y se indican los principales accidentes geográficos mencionados en el texto (CT=Cabo Trafalgar; Pc=Punta Camarinal; T=Tarifa; PE=Punta Europa; CE=Cabo Espartel; PC=Punta Cires; PA=Punta Almina) 42
Figura 2.10.- Profundidad de la interfaz a lo largo del eje longitudinal del Estrecho en la condición inicial (izqda.) y en el estado estacionario resultante (dcha.) del experimento "lock-exchange". 43
Figura 2.11.- Esquema de la ejecución del modelo oceánico forzado únicamente por viento para los experimentos NON-TIDE. El término "cold start" hace referencia al arranque en frío del modelo MM5. Los bucles representan la actualización temporal del forzamiento. 47
Figura 2.12.- Esquema de la ejecución del modelo oceánico forzado por marea y viento para los experimentos TIDE. BC representa el forzamiento de marea en los contornos abiertos. El término "cold start" hace referencia al arranque en frío del modelo MM5. Los bucles representan la actualización temporal del forzamiento. 48
Figura 2.13.- Esquema resumen de los experimentos realizados con el modelo oceánico forzado por viento. 48
Figura 2.14.- Inestabilidades en el nivel del mar por pérdida de ortogonalidad de la malla. 49
Figura 2.15.- Diferencia de la profundidad de la interfaz media (izqda.) y del nivel medio del mar (dcha.) al disminuir un 40% el coeficiente de arrastre para el experimento NON-TIDE-E. 51

CAPÍTULO 3 53
Figure 3.1.- Histogram of RMSE for wind speed (left) and MAE for wind direction (right) from three nested MM5 domains (30,10 and 3.3 km) and HIRLAM (0.2º) at 5 AWS locations. Dashed lines show the model performance benchmarks for simple (blue line) and complex (red line) conditions for each variable and parameter. 56

Figure 3.2.- Biases from the MM5 at 30, 10 and 3.3 km and from HIRLAM *versus* observations from 5 automatic weather stations for wind speed (left) and wind direction (right). Dashed lines show the model performance benchmarks for simple (blue line) and complex (red line) conditions for each variable and parameter. 57

Figure 3.3.- Index of Agreement from the MM5 at 30, 10 and 3.3 km *versus* observations from 5 automatic weather stations for wind speed (left) and wind direction (right). Dashed blue line shows the model performance simple benchmark for wind speed IOA. 57

Figure 3.4.-Index of Agreement for wind speed (left) and for wind direction (right) from MM5-30 km and MM5-10 km at 2 deep buoy locations. Dashed blue line shows the model performance simple benchmark for wind speed IOA. 58

Figure 3.5.- Index of Agreement from the MM5-10 km and HIRLAM *versus* observations from 5 automatic weather stations for wind speed (left) and wind direction (right). Dashed blue line shows the model performance simple benchmark for wind speed IOA. 59

Figure 3.6.- Time-series of observed (blue lines and dots), MM5H (grey lines and dots) and MM5F (black lines and points) hourly sea level pressure (top), wind speed (middle) and wind direction (bottom) at buoy location of cabo de Gata for September and October 2008. Green shaded areas correspond to periods with negative sea level pressure differences between cabo de Gata and golfo de Cádiz. 61

Figure 3.7.-Time-series of observed (blue lines and dots), MM5H (grey lines and dots) and MM5F (black lines and points) hourly sea level pressure (top), wind speed (middle) and wind direction (bottom) at buoy location of golfo de Cádiz for September and October 2008. Green shaded areas correspond to periods with negative sea level pressure differences between cabo de Gata and golfo de Cádiz. Grey shaded bars correspond to sea-land breeze events mentioned in the text. 61

Figure 3.8.- Sea level pressure and wind vectors at 10 m simulated by MM5 (10 km) corresponding to two westward cyclone episodes on October 3 (top) and on October 9, 2008 (bottom) at 1900 UTC (left) and at 2300 UTC (right). Wind speed scale is indicated at the bottom right. 62

Figure 3.9.- Sea level pressure differences between cabo de Gata and golfo de Cádiz buoy locations measured by the buoys (blue line), simulated in the hindcast run (grey line) and in the forecast experiment (black line). Green and yellow shaded areas correspond to periods with negative sea level pressure differences between cabo de Gata and golfo de Cádiz. Yellow shaded bars indicate the periods of the cyclones crossing the Strait westward. 63

Figure 3.10.- Sea level pressure differences between cabo de Gata and golfo de Cádiz locations (top), wind speed (middle) and wind direction (bottom) registered by buoys over the second cyclone episode, between the 7th and 9th of October 2008. 64

Figure 3.11.- Wind roses for the period under study at cabo de Gata location, based on observations (left), on MM5H and MM5F (right) experiments. 65

Figure 3.12.- Wind roses for the period under study at golfo de Cádiz location, based on observations (left), on MM5 (middle) and MM5F (right) experiments. 65

Figure 3.13.- Observed *versus* simulated (from the top) sea level pressure, 10-m wind speed and direction and 2-m temperature at (from the left), Rota, Málaga, Ceuta and Melilla. Black dots are for hindcast experiment while blue dots are for forecast. The line of least squares regression is also shown. 68

Figure 3.14.- Hourly evolution of spatially averaged surface temperature (top), surface wind speed (middle) and direction (bottom) observed (blue line) and simulated by the MM5-10 km (red line). Grey shaded bars correspond to nighttime periods. Yellow and green shaded areas cover the pure and non-pure sea-land breeze periods, respectively. 71

Figure 3.15.- Spatially averaged hourly evolution of errors and biases throughout May 2007 for 2 m-temperature (top), wind speed (middle) and direction (bottom). Grey shaded bars correspond to nighttime periods. Dashed lines show the model performance benchmarks for complex conditions for each variable and parameter. Yellow and green shaded areas cover the pure and non-pure sea-land breeze periods, respectively. 72

Figure 3.16.- Time-averaged bias (top) and MAE (bottom) distributions for 2 m-air temperature over the month of May 2007. 75

Figure 3.17.- Time-averaged bias (top) and MAE (bottom) distributions for wind speed over the month of May 2007. 76

Figure 3.18.- Time-averaged bias (top) and MAE (bottom) distributions for wind direction over the month of May 2007. 77
Figure 3.19.- Surface synoptic chart at 0000 UTC on May 17 (left) and on May 18 (right), 2007. 79
Figure 3.20.-Comparison of observed and simulated wind field at 10 m, on May 17, 2007 at 0500 UTC (top) and 1500 UTC (bottom) under the influence of easterly winds. 81
Figure 3.21.-Comparison of observed and simulated wind field at 10 m, on May 18, 2007 at 0500 UTC (top) and 1500 UTC (bottom) under the influence of easterly winds. 82
Figure 3.22.- Surface synoptic chart at 0000 UTC (left) on May 28 and (right) on May 29, 2007. 83
Figure 3.23.- Comparison of observed and model simulated wind field at 10 m, on May 28, 2007 at 0500 UTC (top) and 1500 UTC (bottom) under the influence of westerly winds. 84
Figure 3.24.- Comparison of observed and model simulated wind field at 10 m, on May 29, 2007 at 0500 UTC (top) and 1500 UTC (bottom) under the influence of westerly winds. 85
Figure 3.25.- Time-averaged BIAS for air temperature at 2 m under pure-breezes (left) and non-pure-breezes episodes (right). 88
Figure 3.26.- Time-averaged MAE for air temperature at 2 m under pure-breezes (left) and non-pure-breezes episodes (right). 89
Figure 3.27.- Time-averaged BIAS for wind direction at 10 m under pure-breezes (left) and non-pure-breezes episodes (right). 89
Figure 3.28.- Time-averaged MAE for wind direction at 10 m under pure-breezes (left) and non-pure-breezes episodes (right). 90
Figure 3.29.- Time-averaged BIAS for wind speed at 10 m under pure-breezes (left) and non-pure-breezes episodes (right). 90
Figure 3.30.- Time-averaged RMSE for wind speed at 10 m under pure-breezes (left) and non-pure-breezes episodes (right). 91

CAPÍTULO 4 95
Figure 4.1.- Salinity profiles (blue points) along with sigmoidal fits (red lines) for different CTD stations (blue squares in the inset). The estimated interface

depth (black square) and simulated (red point) by the TIDE-WIND experiment are also shown. Sea-level prediction at Tarifa is presented (black circle marks the moment when the CTD profile was made). 99

Figure 4.2. - Salinity profile (blue points) along with sigmoidal fit (red line) measured by CTD cast on the mooring place (red diamond). The estimated interface depth, η_2, (black square) and simulated (red point) by the TIDE-WIND experiment are also displayed. Sea-level prediction at Tarifa is presented (black circle marks the moment when CTD profile was made). Locations of the simulated interface (red crosses) within a tidal cycle (black crosses) are shown. 100

Figure 4.3. - Simulated wind speed (black line) and direction (grey dots) over Camarinal Sill (a) and along-strait sea level pressure difference between an eastern point (EP) and CS (b). Subinertial upper layer current velocity anomaly measured by the current meter (c), simulated by the TIDE-WIND (d) and by TIDE (e) experiments. Black arrows indicate the strong easterly wind events mentioned in the text. 101

Figure 4.4.- Sea level at Camarinal Sill (top) from the TIDE run and Hovmöller diagrams of the along-strait current component from the ADCP (flowing eastward -positive values-): hourly records (middle) and low-pass filtered records with a cut-off period at 33 hours (bottom). The depth of maximum vertical shear is also plotted (dashed black line). 103

Figure 4.5.- Vertical distribution of the mean along-strait current (left), horizontal current velocity module (center) and direction (right) measured by the ADCP at Camarinal Sill. 104

Figure 4.6. - Wind speed and direction (grey points) at Camarinal Sill (top). Upper (middle) and lower (bottom) layer along-strait current anomaly from the ADCP (blue line), from the TIDE (black line) and TIDE-WIND (red line) experiments. Black arrows indicate the strong easterly wind events mentioned in the text. Black boxes contain the periods shown in figure 4.8. 105

Figure 4.7. - Atmospheric sea level pressure difference along the Strait between points EP and CS (top). Sea level (middle) and interface depth (bottom) anomalies from the ADCP (blue line), the TIDE (black line) and the TIDE-WIND (red line) experiments. Black arrows indicate the strong easterly

wind events mentioned in the text. Black boxes contain the periods shown in figure 4.8. 106
Figure 4.8. - Wind speed and direction (grey points) at Camarinal Sill (a). Upper (b) and lower (c) layer along-strait current anomaly. Sea level (d) and interface (e) anomaly from the ADCP (blue line), from the TIDE (black line) and TIDE-WIND (red line) experiments. Yellow and grey shaded areas indicate easterly and westerly winds events, respectively. 107
Figure 4.9. - MM5-10 km daily-averaged wind field on October 10, 2011. 108
Figure 4.10. - Tracks of surface drifters (blue lines) and virtual drifters released into the TIDE (yellow lines) and TIDE-WIND (red lines) experiments. Points and triangles denote the start and the end of the tracks, respectively. TIDE-WIND upper layer current field map (arrows) corresponds to the last tracked hour. 109
Figure 4.11.- MODIS / Aqua chlorophyll-a concentration satellite image over the study area (top) and a zoom (bottom) over the area covered by the first drifter track, marked with a black box. 110
Figure 4.12.-Upper layer current map showing the CCC (red arrows) for the TIDE (top) and TIDE-WIND (bottom) experiments at the beginning (left) and at the final stages (right) of the drifter track (blue line). The dot and the triangle denote the start and the end of the track, respectively. 111
Figure 4.13.- Upper layer current map showing the CCC (red arrows) for the TIDE (top) and TIDE-WIND (bottom) experiments under strong easterly wind conditions on October 10, 2008. 112
Figure 4.14.- Upper layer current map showing the CCC (red arrows) for the TIDE-E (top) and TIDE-W (bottom) experiments on October 10, 2008. 113
Figure 4.15. - Upper layer current map showing the cyclonic eddy in the leeward side of Punta Tarifa for the TIDE-WIND experiment. 114
Figure 4.16.-Wind speed (black line) and direction (grey points) at Camarinal Sill (top). Comparison of observed (blue line) and TIDE-WIND simulated (red line) low-pass SLDA between Ceuta-Algeciras (middle) and Ceuta-Tarifa (bottom). Yellow and green shaded areas indicate easterly and westerly winds events, respectively. 115

Figure 4.17.- Sea level (left) and interface depth (right) for the NON-TIDE (top), NON-TIDE-E (middle) and NON-TIDE-W (bottom) experiments. The white areas mark the regions where no lower layer is present. 120

Figure 4.18.- Upper (left) and lower (right) layer current velocity for the *NON-TIDE* (top), NON-TIDE-E (middle) and NON-TIDE-W (bottom) experiments. The white areas mark the regions where no lower layer is present. 121

Figure 4.19.- Time-averaged sea surface (left) and interface depth (right) for the *TIDE* (top), TIDE-E (middle) and TIDE-W (bottom) experiments. The white areas mark the regions where no lower layer is present. 123

Figure 4.20.- Time-averaged upper (left) and lower (right) layer current velocities for the TIDE (top), TIDE-E (middle) and TIDE-W (bottom) experiments. The white areas mark the regions where no lower layer is present. 124

Figure 4.21.-Tidal height at Tarifa showing the analyzed periods at spring tides (red line), mid-tides (black line) and neap tides (blue line). Points correspond to the semi-diurnal tidal cycle analyzed in figure 4.22. White circles correspond to CTD casts at the eastern entrance of the Strait shown in figure 4.23..... 125

Figure 4.22.-Along-strait interface depth anomaly over a semidiurnal tidal cycle for spring tide (left), mid-tide (center) and neap tide (right). Black, red and blue lines correspond to the TIDE, TIDE-E and TIDE-W experiments, respectively. The arrows show the relative intensity and direction of the eastward tidal current component over Camarinal Sill for the upper (black arrows) and lower (grey arrows) layers. Cross-strait sections are also identified (ES=Espartel Sill; CS=Camarinal Sill; T=Tarifa; PC= Punta Cires; G= Gibraltar). Tidal cycle is referred to the high-water (HW) in Tarifa. 127

Figure 4.23.- Salinity profiles (top) at mid-tides on October 19 (left) and during neap tides on October 22 (right). Tidal sea level in Tarifa (middle) with the points indicating the CTD casts (map shows the location of the CTD cast with a blue square). Time series of ADCP-eastward current component at 56 m (mid-tides) and 96 m (neap-tides) are also displayed (bottom)..... 130

Figure 4.24.- Upper layer ($F_1^2 \geq 1$), lower layer ($F_2^2 \geq 1$), and composite ($G^2 \geq 1$) Froude numbers for the different experiments: TIDE (left), TIDE-E

(middle) and TIDE-W (right). Grey contour lines represent the model bathymetry. Value over 1 are shaded. 132

Figure 4.25.- Upper layer thickness (top) and velocity differences (bottom) of the control experiment *versus* TIDE-E (left) and *versus* TIDE-W(right). Grey contour lines represent the model bathymetry. Red (blue) colour implies a shallower (deeper) interface and a decrease (increase) on the velocity, due to wind forcing. 134

Figure 4.26.- Scheme representing the Camarinal Sill cross-section used for the inflow and outflow estimation. For ADCP transport estimates the interface depth in the mooring position at time $\boldsymbol{t}$ is taken as constant (dashed line) for the entire cross-section. 135

Figure 4.27.- Wind speed (black line) and direction (grey points) simulated at Camarinal Sill (a). Sea level at Camarinal Sill from the TIDE run (b). Subinertial upper (c) and lower layer (d) transport anomalies at Camarinal Sill estimated from the ADCP data set (blue line), resulting from the TIDE (black line) and TIDE-WIND (red line) experiments. Black (grey) arrows indicate the strong easterly (westerly) events mentioned in the text..... 137

Figure 4.28.- Subinertial inflow (positive values) and outflow (negative values) transports, for the TIDE experiment, over the different cross-sections showed on the map. 139

Figure 4.29.- Subinertial inflow (positive values) and outflow (negative values) transports for the TIDE-WIND experiment over the different cross-sections showed on the map. Black (grey) arrows indicate the strong easterly (westerly) events mentioned in the text. 140

CAPÍTULO 5 145

LISTA DE TABLAS

CAPÍTULO 1 1

CAPÍTULO 2 19

Tabla 2.1.- Estaciones Meteorológicas Automáticas de AEMET utilizadas en la validación del modelo meteorológico. No se incluyen las estaciones pertenecientes a la red del IFAPA ya que su localización y elevación puede obtenerse en Gavilán *et al.* (2006) y Estévez *et al.* (2011) 21

Tabla 2.2.- Boyas de la red de aguas profundas utilizadas en la validación del modelo meteorológico. 22

Tabla 2.3.- Información del fondeo realizado sobre el Umbral de Camarinal durante el experimento "*Strait 94-96"*. 24

Tabla 2.4.- Información del fondeo realizado al norte de la meseta del Umbral de Camarinal durante la campaña oceanográfica "*Gibraltar-08".* 25

Tabla 2.5.- Información de la localización de los mareógrafos y referencia de las medidas. 27

Tabla 2.6.- Fechas y localizaciones de la liberación de las cuatro boyas de deriva. .. 28

Tabla 2.7.- Parámetros de definición de los dominios de trabajo. 33

Tabla 2.8.- Parametrizaciones físicas incluidas en la configuración del MM5. 34

Tabla 2.9.- Indicadores estadísticos simples (Emery *et al.*, 2001) y complejos (Kemball-Cook *et al.*, 2005) para evaluar el comportamiento del modelo meteorológico. WS=velocidad del viento; WD=dirección del viento; T=temperatura. 40

Tabla 2.10.- Parámetros utilizados en los experimentos de sensibilidad numérica. En negrita se señalan los valores escogidos para el modelo oceánico forzado por viento. 50

CAPÍTULO 3 53

Table 3.1.- Statistical scores comparing MM5-10 km, (hindcast -H- and forecast -F- runs) with each buoy (Cabo de Gata -CG- and Golfo de Cádiz -GC-). The averaged scores are denoted by Av. Those measures that exceed the benchmarks are within shaded cells. Boldface numbers denote the best score for each experiment and statistical measure. Please, note that there is no benchmark for sea level pressure. 66

Table 3.2.- Averaged (Av) MM5-10 km model performance statistics for surface variables, both the hindcast -H- and forecast -F- cases at 7 automatic weather stations (from AEMET). Those measures that exceed the benchmarks are within shaded cells. Boldface numbers denote the best score for each experiment and statistical measure. Please, note that there is not benchmark for sea level pressure. 69

Table 3.3.- Daily variability of average model errors throughout May 2007 at 95 locations. Values within the shaded cells indicate exceedances of the (simple or complex) benchmarks. Boldface numbers denote the best score for each experiment and statistical measure. WS=10 m-Wind Speed; WD=10 m-Wind Direction; T2=2 m-Air Temperature..... 74

Table 3.4.- Summary of the principal characteristics of sea-land breezes patterns in the southwestern Iberian Peninsula. 78

Table 3.5.-Statistical model evaluation for the representative days of pure and non-pure breezes at 0500 UTC and at 1500 UTC. Values within the shaded cells indicate exceedances of the (simple or complex) benchmarks. Boldface numbers denote the best score for each experiment and statistical measure. WS=10 m-Wind Speed; WD=10 m-Wind Direction; T2=2 m-Air Temperature..... 87

CAPÍTULO 4 95

Table 4.1.- Travel times and speed of the bore for the different experiments at spring (the 16th of September) and neap (the 22nd of September) tides between the cross-sections (figure 2.9). 129

Table 4.2.- Correlation coefficients between the low-pass TIDE-WIND and ADCP estimated inflow transports (Q_1) and between inflow time series and wind-stress (τ_{wind}), for easterly and westerly events..... 138

Table 4.3.- Time-averaged transport values obtained from TIDE and TIDE-WIND experiments over different cross-sections under 141

CAPÍTULO 5 145

LISTA DE ACRÓNIMOS

ADCP	Acoustic Doppler Current Profiler
AEMET	Agencia Estatal de Meteorología
AWS	Automatic Weather Station
BFO	Breeze-Forced Oscillations
CANIGO	Canary Islands Azores Gibraltar Observations
CCC	Coastal Counter Current
CE	Cabo Espartel
CG	Cabo de Gata
CODAR	Coastal Ocean Dynamics Applications Radar
COI	Comisión Oceanográfica Intergubernamental
CS	Camarinal Sill
CT	Cabo Trafalgar
CTD	Conductivity-Temperature-Depth
EMA	Estación Meteorológica Automática
ES	Espartel (also known as Spartel) Sill
ETOPO5	5-minute Gridded Global Relief Data
G	Gibraltar-Punta Europa
GC	Golfo de Cádiz
GFS	Global Forecast System
GFS-ANL	Global Forecast System - Analysis Only
GLOSS	Global Sea Level Station Monitoring Facility
GSM	Global System for Mobile communication
HAMSOM	HAMburg Shelf Ocean Model
HIRLAM	HIgh Resolution Limited Area Model
HW	High Water
IEO	Instituto Español de Oceanografía
IFAPA	Instituto de Investigación y Formación Agraria y Pesquera de Andalucía
IHM	Instituto Hidrográfico de la Marina
IOA	Index Of Agreement
LAM	Limited Area Model
MAE	Mean Absolute Error
MITgcm	Massachusetts Institute of Technology general circulation model
MM5	Fifth-Generation Penn State/NCAR Mesoscale Model

MM5F	MM5 Forecast
MM5H	MM5 Hindcast
MPIOM	Max Planck Institute Ocean Model
MRF	NCEP Medium-Range-Forecast
NCAR	National Center of Atmospheric Research
NCEP	National Centers for Environmental Prediction
NWP	Numerical Weather Prediction
OF	Outflow
OMM	Organización Meteorológica Mundial
PA	Punta Almina
PBL	Planetary Boundary Layer
PC	Punta Cires
Pc	Punta Camarinal
PE	Punta Europa
PH	Puertas de Hércules
POM	Princeton Ocean Model
PSMSL	Permanent Service of Mean Sea Level
QuikSCAT	NASA's Quick ScatterometerQuik SCATterometer
REDEXT	Red Exterior
RLR	Revised Local Reference
RMSE	Root Mean Square Error
ROMS	Regional Ocean Modeling System
SECEG	Sociedad Española para la Comunicación Fija a través del Estrecho de Gibraltar SA
SLDA	Sea Level Difference Anomaly
SRTM30	30 arc-second Shuttle Radar Topography Mission
SST	Sea Surface Temperature
SWS	SeaWindS
T	Tarifa
TB	Tangier Basin
TGBM	Tide Gauge Bench Mark
TGZ	Tide Gauge Zero
TN	Tarifa Narrows
USGS	US Geological Survey
WAG	Western Alboran Gyre
WRF-ARW	Weather Research and Forecasting - Advanced Research WRF

Capítulo 1

Introducción

Capítulo 1

INTRODUCCIÓN

1. Marco geográfico, meteorológico y oceanográfico del Estrecho de Gibraltar.

Son innumerables las características, de diversa índole, que hacen del Estrecho de Gibraltar un sistema hidrodinámico tan complejo. A lo largo de esta primera parte de la introducción, nos centraremos en la descripción de las particularidades geográficas y meteorológicas que influyen en la singular dinámica de este Estrecho localizado al sur de España, donde el Atlántico y el Mediterráneo se encuentran y, en cuyas aguas, se reflejan Europa y África.

1.1. Marco geográfico

Su situación geográfica, lo convierte en el único nexo de unión entre dos cuencas de características diferentes, la del océano Atlántico Norte y la del mar Mediterráneo. Esta localización, estratégica, según los historiadores, invasores y defensores, lo han convertido unas veces en aliado y otras en enemigo.

Geológicamente, el Estrecho de Gibraltar representa el límite de las placas Euroasiática y Africana, por su posición sobre la falla de Azores-Gibraltar, transformándolo en testigo excepcional del terremoto de Lisboa (Ayala *et al.*, 1988), y el posterior tsunami, el más destructivo que ha azotado a la Península Ibérica hasta la fecha.

Visto también desde el punto de vista geológico cabe añadir que el Estrecho conforma el Arco de Gibraltar (Faccenna *et al.*, 2004) junto con la cordillera Penibética (Esteras, 1984), que lo delimita por el norte y se extiende paralela a la costa creciendo por encima de los 3000 m y, al sur, por el abrupto relieve de violentos acantilados de las montañas del Alto Rif. La disposición de las cordilleras Bética y Rifeña (ver en la figura 1.1), flanqueando el Estrecho, dan a éste forma de embudo que, junto a la existencia de un dipolo de presión de origen orográfico, constituyen una primera explicación de las particularidades del viento en la zona.

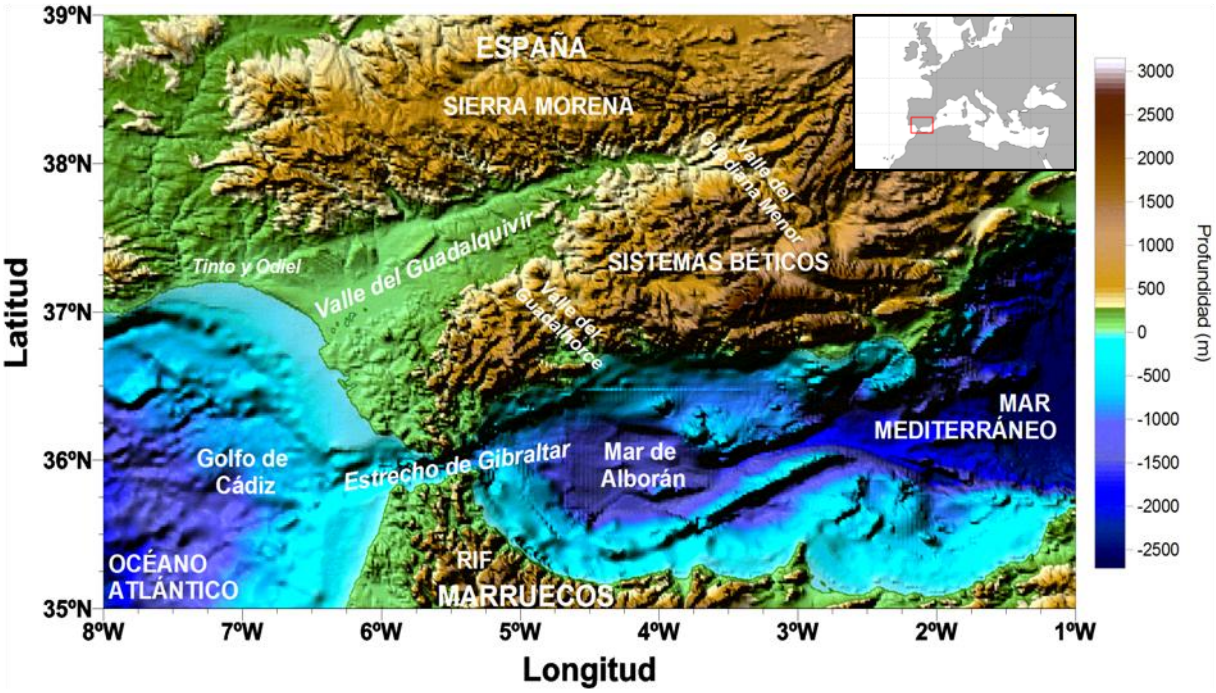

Figura 1.1.- Mapa bati-topográfico del Estrecho de Gibraltar, golfo de Cádiz y mar de Alborán (fuente de los datos: ETOPO1)

Si en su parte más meridional y septentrional el Estrecho queda protegido por cadenas montañosas, en su límite occidental se abre paso a las aguas del golfo de Cádiz entre la línea imaginaria que dibujan los cabos Trafalgar y Espartel (figura 1.2), separados 45 km. En el límite oriental, se asoma al mar de Alborán a través de la franja ficticia que conforman punta Europa y punta Almina, y que separan ambos continentes a lo largo de 23 km. Su eje longitudinal, girado 15° respecto a la dirección este-oeste a una latitud media de 35º 58' N, se extiende a lo largo de unos 60 km.

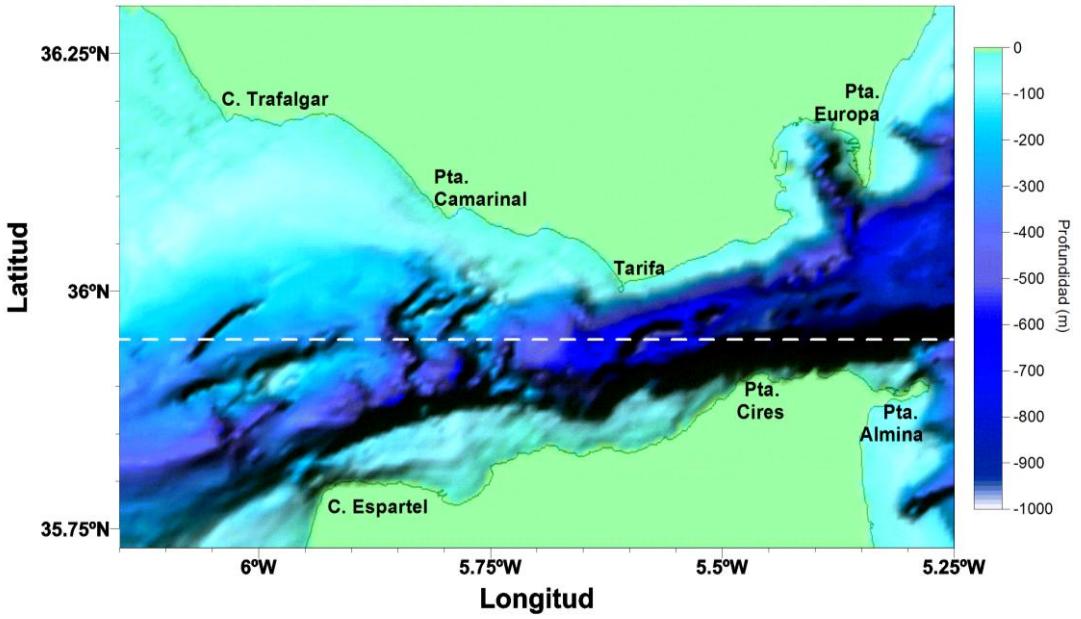

Figura 1.2.- Mapa batimétrico del Estrecho de Gibraltar con los accidentes geográficos más importantes citados en el texto (fuente de los datos: IHM)

Bajo el agua, la batimetría presenta una brusca pendiente hacia el Mediterráneo, caracterizada por la alternancia de zonas profundas que superan los 1500 m en la cuenca Occidental del mar de Alborán, y elevaciones submarinas en el lado Atlántico, como el denominado Umbral Principal o de Camarinal (CS[1]) que recorre el Estrecho de norte a sur con una profundidad máxima en torno a los 284 m. Esta sección de poca profundidad, queda flanqueada por dos depresiones, las Hoyas de Poniente o Cuenca de Tánger (Tangier Basin, TB) al oeste (620 m bajo el nivel del mar) y las Hoyas de Levante al este (500 m de profundidad) (Sanz *et al.*, 1991). Éstas, junto con el Umbral de Espartel (ES[2]) o Bajo Majuán (56 m de profundidad mínima), localizado frente al cabo Trafalgar, el Monte de Hércules (447 m) en la sección más angosta de 14 km (Tarifa Narrows, TN), y las Puertas de Hércules (PH), con unos 900 m de profundidad, y coincidente con el límite oriental, constituyen los accidentes de relieve más notables (ver en la figura 1.3) de esta irregular morfología submarina.

[1] De la notación inglesa, Camarinal Sill.
[2] De la notación inglesa, Espartel Sill.

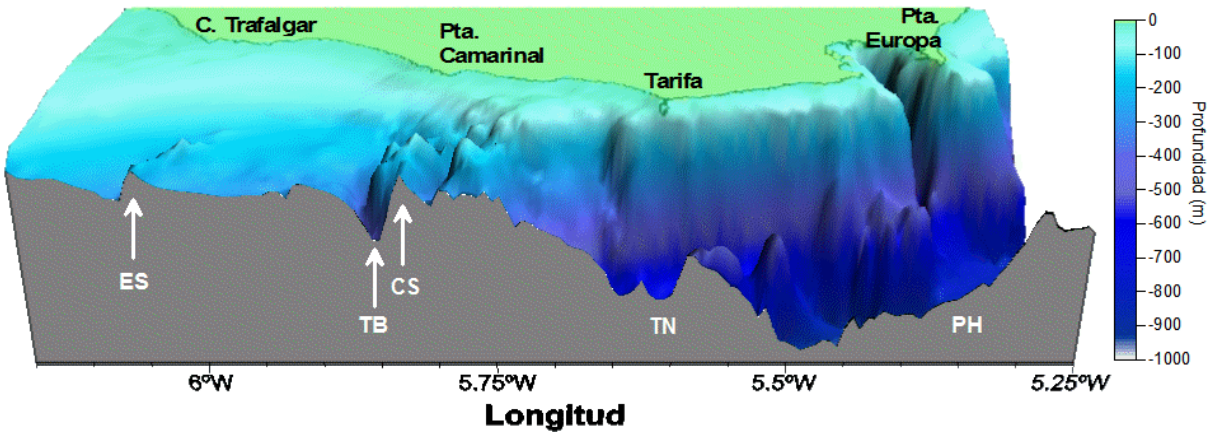

Figura 1.3.- Perfil batimétrico a lo largo del eje longitudinal del Estrecho (línea discontinua blanca de la figura 1.2) en el que se destacan los accidentes del relieve submarino más notables citados en el texto (fuente de los datos: IHM)

1.2. Marco meteorológico

En el Estrecho de Gibraltar, el viento constituye un meteoro muy importante, tanto en la parte terrestre como en la parte marítima. Las particularidades del viento en el Estrecho se explican a partir de tres factores que determinan su dirección e intensidad:

- la presencia del océano, que da lugar a circulaciones térmicas, conocidas con el nombre de brisas de tierra-mar.
- el estrechamiento, el cual induce la existencia de un dipolo de presión de origen orográfico (Bendall, 1982). Este gradiente de presión a ambos lados del Estrecho se manifiesta por una zona de altas presiones en el lado de barlovento, debido a la acumulación de aire, y un mínimo de presión a sotavento, por el efecto de abrigo. La principal consecuencia de esta estructura mesoescalar de presión es una redistribución de los vientos que puede dar lugar a fuertes temporales locales de viento o alterar las áreas de convergencia y divergencia en niveles bajos, lo que puede llegar a activar, inhibir o dificultar la convección.
- la peculiaridad de la topografía de la región caracterizada por franjas paralelas a la costa que canalizan los vientos, modificando progresivamente su dirección, haciéndolos completamente zonales, favoreciendo las direcciones del Este (Levantes) y del Oeste (Ponientes) e intensificándolos a su paso (Sánchez Ayllo *et al.*, 1983; Dorman *et al.*, 1995).

Los Levantes (vientos del sureste y este), procedentes del Mediterráneo y Norte de África, son cálidos y más secos, en el lado occidental del Estrecho, pudiendo llegar a producir precipitaciones y nieblas en el lado oriental. Su presencia suele coincidir con el

desarrollo de una depresión térmica superficial sobre el NW de Marruecos, la aparición de un área depresiva en superficie sobre el golfo de Cádiz, o por condiciones anticiclónicas sobre el Mediterráneo occidental. En el Estrecho de Gibraltar, los Levantes se clasifican en vientos localizados o generalizados, dependiendo de la posición de los centros ciclónicos y anticiclónicos. En los primeros, el viento fuerte suele restringirse a la zona de Tarifa y aledaños. Los Levantes fuertes generalizados se prolongan por la costa hasta afectar la Bahía de Cádiz, acompañados por una ligera bajada del barómetro y una subida del termómetro en el golfo de Cádiz.

Los vientos de Poniente (del oeste y suroeste), más frescos y húmedos, corresponden a la influencia atlántica, es decir, al régimen atmosférico general de Europa occidental y son más frecuentes entre los meses de noviembre a marzo. Llevan asociado, por norma general, tiempo tormentoso y temperaturas más bajas.

No obstante, es importante señalar que, en contra de lo que sería esperable a primera vista, los vientos más fuertes no ocurren en la zona más angosta del Estrecho (Tarifa Narrows) sino a la salida del mismo.

Esto se debe a que, además del efecto de la canalización debido a la topografía, existen otros mecanismos que modulan la velocidad del viento a su paso por el Estrecho de Gibraltar:

- la ausencia de capa rígida en la naturaleza: por lo que la altura del aire que se aproxima al estrechamiento suele aumentar debido a efectos de bloqueo del flujo, lo que incrementa la presión en el centro del canal, disminuyendo la velocidad del flujo desde la entrada hasta la parte central. La rápida apertura del canal en la salida hace que la altura de la columna de aire disminuya por conservación de masa, induciendo un gradiente de presión que acelera el viento. Esto constituye una primera explicación, junto a las condiciones verticales de estabilidad, al hecho de que los Levantes sean más intensos, ya que la sección transversal aumenta en el lado occidental del Estrecho.
- la existencia de un gradiente de presión sinóptico o mesoescalar a ambos lados del Estrecho que resulta en una aceleración del viento ageostrófico desde las altas a las bajas presiones alcanzando la máxima velocidad en la salida (zona de menor presión). A mayor gradiente de presión, más intenso es el viento.

1.3. Marco oceanográfico

El papel principal del Estrecho de Gibraltar como nexo de unión entre dos cuencas con aguas de propiedades distintas, es el que determina el intercambio baroclino, conducido por pérdidas de masa por la evaporación neta que tiene lugar en el mar Mediterráneo. Dichas pérdidas están compensadas por el intercambio del flujo de agua entre el océano Atlántico y el mar Mediterráneo, que viene dado por la entrada en superficie de aguas menos salinas del Atlántico que retornan en profundidad como aguas intermedias y profundas mediterráneas, más densas y más salinas (Stommel & Farmer, 1953; Lacombe & Richez, 1982; Farmer & Armi, 1986). El flujo saliente del Mediterráneo está controlado hidráulicamente en el Umbral de Espartel y en la sección de menor profundidad (Umbral de Camarinal), mientras que la sección más angosta (Tarifa Narrows) controla el flujo entrante atlántico, según la teoría del control hidráulico en un sistema bicapa (Armi & Farmer, 1985; Farmer & Denton, 1985; Farmer & Armi, 1986; Armi & Farmer, 1987). En el marco de esta teoría, ambas capas están separadas por una superficie infinitesimal, denominada interfaz atlántico-mediterránea, que no permite la mezcla entre las propiedades de ambas masas de agua y que ha sido definida por diferentes autores en función de diversos criterios (Lacombe & Richez, 1982; Armi & Farmer, 1988; Farmer & Armi, 1988; Pettigrew & Needell, 1989; Watson & Robinson, 1990; Bray *et al.*, 1995; Send & Baschek, 2001; Bruno *et al.*, 2002).

Siendo el intercambio baroclino el motor principal de la dinámica en el Estrecho de Gibraltar, el flujo medio resultante es modificado por distintos procesos de escalas espaciales y temporales diferentes (Lacombe & Richez, 1982). Entre las principales causas de estas variabilidades cabe destacar el efecto de las mareas, que genera intensas corrientes a través del Estrecho, el forzamiento por viento y las diferencias de presión atmosférica entre las cuencas atlántica y mediterránea a escala subinercial (Candela *et al.*, 1989; García-Lafuente *et al.*, 2002b; Vázquez *et al.*, 2008) y las fluctuaciones de más baja frecuencia, de escala estacional e interanual (Garrett *et al.*, 1990b; García-Lafuente *et al.*, 2002b; Vargas *et al.*, 2006).

La banda de marea es la que posee mayor energía (Lacombe & Richez, 1982; Candela *et al.*, 1990). Los estudios experimentales, teóricos y numéricos realizados indican que el carácter de la marea en el Estrecho de Gibraltar es principalmente semidiurno (Candela *et al.*, 1990), alcanzando la velocidad de la corriente de marea las

máximas amplitudes en el Umbral de Camarinal, donde existe una estructura esencialmente barotrópica (Candela *et al.*, 1990; Candela *et al.*, 1991). En la parte más oriental, la banda diurna cobra importancia en la capa de agua atlántica, presentando una estructura marcadamente baroclina (García-Lafuente *et al.*, 2000; Sánchez-Román *et al.*, 2009). Las corrientes de marea son tan intensas en la zona que llegan a invertir el flujo entrante superficial con periodicidad diurna en toda la sección del Estrecho sobre el Umbral de Camarinal (Candela *et al.*, 1990; Bryden *et al.*, 1994).

Por otro lado, la interacción de estas corrientes de marea con los obstáculos batimétricos, particularmente con el Umbral de Camarinal, induce fluctuaciones de gran amplitud de la interfaz entre las aguas atlánticas y mediterráneas (Armi & Farmer, 1988; Farmer & Armi, 1988). Al debilitarse la corriente saliente de marea (hacia el Atlántico), estas perturbaciones se propagan hacia el este evolucionando como un frente de ondas internas, cuyas "huellas dactilares", en forma de zonas de hervideros visibles en la superficie del mar, son recogidas por las imágenes de satélites, radares de apertura sintética e incluso en fotografías de vuelos comerciales o las tomadas desde la Estación Espacial.

Además de estos procesos que inducen las fluctuaciones barotrópicas y conducen al intercambio baroclino, existen fluctuaciones del flujo medio relacionadas con el forzamiento atmosférico que ocurren con períodos mayores a los de marea y menores a un mes. Los efectos más relevantes, a escala subinercial, son el de la tensión tangencial del viento y el de las variaciones de presión atmosférica sobre el mar de Alborán.

En concreto, las oscilaciones de presión atmosférica sobre la cuenca mediterránea han sido relacionadas con la respuesta isostática de las variaciones del nivel del mar (Crepon, 1965; Garrett *et al.*, 1989) y las corrientes barotrópicas asociadas (Candela *et al.*, 1989; Mañanes *et al.*, 1998). Otros estudios las han vinculado con la activación/inhibición de las ondas internas generadas en el Umbral de Camarinal (Vázquez *et al.*, 2008), los cambios en la intensidad del flujo atlántico entrante (Macías *et al.*, 2008) que, a su vez, afecta a la extensión del Giro Occidental de Alborán (WAG, *Western Alboran Gyre*) y a su dinámica. Incluso, un rápido incremento de la presión atmosférica en el Mediterráneo se ha relacionado con la interrupción del flujo atlántico entrante en el Estrecho durante varios días seguidos, en meses de invierno (García-Lafuente *et al.*, 2002b).

El efecto de la tensión tangencial del viento se ha asociado con movimientos verticales de la interfaz, en relación con episodios de viento intensos de Poniente o Levante. Garrett (1983), Fukumori (2007) y Menemenlis *et al.* (2007) señalan a los vientos del Estrecho como la quinta causa responsable de la diferencia de nivel del mar entre el Atlántico y el Mediterráneo. Por otro lado, Stanichny *et al.* (2005) encontraron una alta correlación entre la componente zonal de los vientos y la diferencia transversal de nivel del mar entre Tarifa y Ceuta.

2. Antecedentes de la investigación

Siendo el Estrecho de Gibraltar un objeto de estudio de gran relevancia en numerosas disciplinas (geología, historia, meteorología, geografía, etc.), ha sido y sigue siendo considerado como uno de los mayores desafíos por los oceanógrafos y una fuente inagotable de procesos a diferentes escalas temporales y espaciales con distintos orígenes y con complejas interacciones entre la atmósfera y el océano.

Desde que Carpenter & Jeffreys (1870), a bordo del *"Porcupine"*, confirmaron la sospecha de Marsigli (1681) acerca de la existencia de una corriente saliente por el Estrecho de Gibraltar como la observada anteriormente por este último en el Bósforo, han sido numerosas las investigaciones y diversos los intentos de estimar los flujos y su variabilidad en esta singular zona de forma experimental, teórica y numérica .

Los esfuerzos por estudiar el intercambio gravitacional de dos fluidos de densidades diferentes entre dos cuencas conectadas por un canal o estrecho se iniciaron en la década de los 60 a manos de Stommel & Farmer (1953), quienes también definieron por primera vez el concepto de "overmixing[3]". El primer modelo analítico unidimensional para un flujo bicapa lo formularon Assaf & Hecht (1974). Examinaron el intercambio estacionario a través de cuatro estrechos (Gibraltar, Bósforo, Dardanelos y Bab-el-Mandeb) con una sección transversal trapezoidal constante (sin variaciones de profundidad ni anchura). Incluyeron también la fricción interfacial y la fricción por fondo. A partir de la solución teórica obtenida, pronosticaron la existencia de una pendiente de la profundidad de la interfaz con una inclinación ascendente hacia la cuenca con agua más salina.

[3] El concepto de overmixing define la situación de intercambio máximo, que se corresponde con la profundidad más somera de la interfaz sobre el Umbral de Camarinal y la mínima diferencia de salinidad entre las cuencas (la salinidad de las aguas mediterráneas es menor). Una vez alcanzado este límite, se mantiene la estratificación de dos capas y se alcanza el estado estacionario.

En el caso del Estrecho de Gibraltar, los precursores de la aplicación de la clásica teoría del control hidráulico fueron Stommel & Farmer (1953). El trabajo de Armi & Farmer (1985), basado en los datos presentados por Lacombe & Richez (1982), está enfocado a la localización y determinación del número de controles hidráulicos en la zona y en cómo éstos influyen a las corrientes, a la profundidad de la interfaz y a la magnitud del intercambio.

Posteriormente, los análisis de Armi & Farmer (1986) y Farmer & Armi (1986) se basaron en un modelo unidimensional, con secciones transversales rectangulares que variaban en profundidad y en anchura y que ignoraba los efectos de la fricción y de las fluctuaciones barotrópicas. Concluyeron que el intercambio máximo sólo era posible cuando existían dos zonas hidráulicamente controladas: la zona de mínima profundidad (Umbral de Camarinal) y la de mínima anchura (Tarifa Narrows, TN). Por otro lado, mientras el flujo fuese crítico únicamente sobre el Umbral de Camarinal, el intercambio sería submáximo. Ambos regímenes presentan diferentes implicaciones en las propiedades de los flujos y otras características de la circulación acoplada entre el Estrecho y el Mediterráneo. En el caso del régimen máximo, los flujos de masa, calor y sal son mayores y responden más lentamente a cambios en la estratificación y al forzamiento termohalino que tiene lugar en el mar Mediterráneo y en el océano Atlántico. El flujo se hace supercrítico al este de TN, la interfaz se hace más somera y la corriente en la capa superior más intensa, aislando los procesos hidráulicos en el Estrecho de las variaciones de la interfaz que ocurren en el Mediterráneo. El régimen submáximo implica que los flujos intercambiados son los menores posibles compatibles con las diferencias de salinidad entre ambas cuencas y que la profundidad de la interfaz en el Estrecho y, en general, el intercambio, esté determinado por los procesos que ocurren en la región del Mediterráneo exclusivamente.

Bormans & Garrett (1989a) evolucionaron el modelo desarrollado por los anteriores considerando unas secciones transversales más realistas que, en comparación con la solución obtenida usando secciones rectangulares (Farmer & Armi, 1986), reducían el intercambio, ascendían la profundidad de la interfaz a lo largo del Estrecho y hacían que ésta permaneciese en el rango de las observaciones en la sección oriental entre Gibraltar-Ceuta, para la solución de intercambio submáximo. En este modelo también se incluyeron los efectos de fricción interfacial y por fondo que influencian el intercambio y afectan a la profundidad de la interfaz. Como aconsejaban Farmer & Armi (1986), en este último modelo también se tuvieron en cuenta las fluctuaciones

barotrópicas en el flujo a través del Estrecho usando una aproximación quasi-estacionaria.

Los efectos de la rotación terrestre en el flujo también fueron introducidos por Bormans & Garrett (1989b), ya que, según Lacombe & Richez (1982) ésta produce una inclinación de la interfaz transversal al Estrecho, más profunda en la zona sur y más somera en el norte.

Bajo la hipótesis de que la aproximación bicapa subestimaba los controles hidráulicos en el Estrecho, Wang (1989) desarrolló un modelo numérico tridimensional que incluía el efecto de la marea. Éste reproducía las características más significativas de la dinámica del Estrecho pero no la existencia del control hidráulico en el Umbral de Camarinal, debido a su baja resolución espacial horizontal (~4 km).

Durante el experimento *"Gibraltar 1985-86*" (Kinder & Bryden, 1987), se progresó en el desarrollo de modelos de control hidráulico para un flujo bicapa a través de un estrecho. Bryden & Kinder (1991) usaron una topografía más realista, e hicieron hincapié en cómo la solución de intercambio máximo determinaba la tasa de intercambio y la diferencia de salinidad entre las cuencas atlántica y mediterránea para una determinada evaporación neta en esta última.

La estructura del intercambio de masas de agua a través del Estrecho siempre se había considerado un sistema bicapa hasta que Bray *et al.* (1995), extendiendo el modelo de Knudsen (1899), introducen una tercera capa, denominada capa interfacial, definida como una región con un alto gradiente de salinidad o de velocidad longitudinal nula, a la que considera un participante activo en el proceso de intercambio.

Tal y como se ha comentado anteriormente, las mareas ejercen una gran influencia en el flujo del Estrecho. Por ello, el problema de la dinámica de mareas ha sido tratado tanto desde el punto de vista experimental (Lacombe & Richez, 1982; Candela *et al.*, 1990; García-Lafuente *et al.*, 2000), como de forma numérica (Sánchez & Pascual, 1988; Wang, 1989; Sein *et al.*, 1998; Tejedor *et al.*, 1999). Sin embargo, nos detendremos más en la descripción del modelo numérico bicapa de Izquierdo *et al.* (2001), de alta resolución (1 km nominal y 125 m en el centro del Estrecho), bidimensional, no-lineal, que utiliza coordenadas curvilíneas ajustadas a los contornos y está basado en la hipótesis hidrostática. El modelo incluye la fricción por fondo e interfacial y el forzamiento de marea, mediante la prescripción de la oscilación del nivel del mar a través de las amplitudes y las fases de las cuatro constituyentes de marea principales, diurnas (K_1, O_1) y semidiurnas (M_2, S_2) en los contornos abiertos. Éste

reproduce la generación del bore interno y su propagación con bastante precisión. De igual modo, predice la presencia de los controles hidráulicos en el Umbral de Camarinal y Espartel y en la constricción de Tarifa y que, en el caso de estos dos últimos, el control no se extiende a lo ancho del Estrecho (Sein *et al.*, 1998; Izquierdo *et al.*, 2001; Brandt *et al.*, 2004). Este modelo y su formulación se tratará con más detalle en el Capítulo 2, ya que supone el punto de partida para la implementación del modelo forzado atmósfera-océano.

Partiendo de los datos de correntímetros obtenidos en la parte este del Estrecho y complementando con las medidas oceanográficas del proyecto CANIGO (*Canary Islands Azores Gibraltar Observations*), Bascheck *et al.* (2001) desarrollaron un modelo inverso de marea bidimensional para la sección oriental del Estrecho. A partir de funciones analíticas simples, obtienen las corrientes utilizando las frecuencias de las siete constituyentes armónicas más importantes (O_1, K_1, N_2, M_2, S_2, K_2, M_4) como funciones temporales, determinando la profundidad de la interfaz a partir de las constituyentes M_2 y S_2. Con este modelo, se calcularon las corrientes medias y el volumen de los transportes en ambas capas, logrando mejores resultados en las corrientes de la capa inferior que en la superior y transportes ligeramente sobreestimados respecto a los obtenidos por Bryden *et al.* (1994) y Tsimplis & Bryden (2000) en el Umbral de Camarinal. Los resultados de este modelo fueron comparados con los del modelo de Izquierdo *et al.* (2001), por Brandt *et al.* (2004), utilizando un dominio extendido para estudiar la sensibilidad de la dinámica del Estrecho frente a cambios en la diferencia de densidades entre las aguas atlánticas y mediterráneas.

Conociendo las dificultades del modelo 3D de Wang (1989) para reproducir el control hidráulico en Camarinal y mediante el uso del modelo tridimensional POM (Princeton Ocean Model) (Blumberg & Mellor, 1987) a alta resolución, Sannino *et al.* (2002) añadieron complejidad a la simulación del régimen hidráulico del flujo medio a través del Estrecho encontrando, finalmente, la presencia de controles hidráulicos en toda la sección transversal del Umbral de Camarinal y en la parte norte del estrechamiento de Tarifa.

Otro de los procesos ampliamente estudiado ha sido la generación y evolución del bore baroclino generado por interacción de la marea barotrópica con la topografía del Umbral de Camarinal, que termina desintegrándose y propagándose como un tren de ondas internas hacia el mar de Alborán (Armi & Farmer, 1988; Farmer & Armi, 1988; Brandt *et al.*, 1996; Bruno *et al.*, 2000; Izquierdo *et al.*, 2001; Sannino *et al.*, 2002;

Vázquez *et al.*, 2006). Su propagación a lo largo del Estrecho revela un comportamiento tridimensional que ha sido modelizado numéricamente por Vlasenko *et al.* (2009) mediante el modelo MITgcm (Massachusetts Institute of Technology general circulation model) (Marshall *et al.*, 1997a; Marshall *et al.*, 1997b). Sánchez-Garrido *et al.* (2011) también han hecho uso del modelo anterior para estudiar la importancia de los efectos tridimensionales, debidos a la irregularidad de la batimetría, a la estratificación variable y a la estructura compleja de las mareas barotrópicas, en el proceso de generación de las ondas internas sobre el Umbral de Camarinal.

Una vez descritos los aspectos más relevantes de la circulación media y del forzamiento de marea en el Estrecho de Gibraltar, es necesario estudiar el papel del forzamiento atmosférico, relacionado con la respuesta del nivel del mar, del flujo neto y del intercambio baroclino debidas a las fluctuaciones de los gradientes horizontales de presión atmosférica y de la tensión tangencial del viento.

El flujo neto subinercial a través del Estrecho ha sido estimado por García-Lafuente *et al.* (2002a) con el modelo de circulación HAMSOM (HAMburg Shelf Ocean Model) (Backhaus, 1983; Backhaus & Hainbucher, 1987), forzado por viento y por presión atmosférica, por separado y de forma conjunta para estimar su contribución relativa al flujo subinercial. Los resultados obtenidos permitieron concluir que la fuerza del gradiente de presión es más importante en el Mediterráneo, mientras que la contribución de la tensión tangencial del viento es más apreciable en el lado atlántico del Estrecho. Sin embargo, cabe señalar que, en este caso, el modelo HAMSOM se utilizó en su versión verticalmente integrada, lo que imposibilitó obtener detalles sobre el intercambio baroclino.

Otro ejemplo de interacción atmósfera-océano, lo conforma la simulación de la generación de un filamento de agua más fría en la costa sur del Estrecho que, eventualmente se dirige hacia el Atlántico y ha sido asociado con la ocurrencia de vientos de Levante (Peliz *et al.*, 2009). Las simulaciones se llevaron a cabo con el modelo ROMS (Shchepetkin & McWilliams, 2005), forzado por el campo de viento superficial obtenido de las salidas del modelo atmosférico WRF-ARW (Skamarock *et al.*, 2005), pero ignoran el forzamiento de marea.

Según los resultados obtenidos en los trabajos revisados, los principales puntos a tener en cuenta a la hora de desarrollar un modelo hidrodinámico de alta resolución con forzamiento atmosférico serían:

- La utilización de una batimetría realista a lo largo y ancho del Estrecho.

- La consideración de los distintos regímenes de intercambio baroclino: el intercambio máximo que ocurre cuando el flujo está controlado en el Umbral de Camarinal y en el estrechamiento de Tarifa. Durante este régimen, el intercambio de flujos entre el Atlántico y el Mediterráneo es máximo, y viene determinado por los procesos que ocurren en la región subcrítica comprendida entre ambos controles hidráulicos. El intercambio submáximo caracteriza a los flujos controlados únicamente en el Umbral de Camarinal.
- La necesidad de trabajar a muy altas resoluciones espaciales para localizar los controles hidráulicos.
- La introducción de la capa de la interfaz en el modelo, considerándola como una superficie activa, capaz de oscilar con las fluctuaciones barotrópicas.
- La importancia del forzamiento de marea en la zona del Estrecho, teniendo en cuenta las constituyentes más significativas del régimen semidiurno.
- La relevancia del viento, como forzamiento atmosférico, obtenido de la salida de un modelo atmosférico, también a alta resolución.

3. Justificación de la investigación y objetivos

La trascendencia de la meteorología en la dinámica del Estrecho de Gibraltar, ha quedado clara en la revisión de los trabajos, de naturaleza experimental, teórica o numérica que analizan la influencia del viento (García-Lafuente *et al.*, 2002a; Peliz *et al.*, 2009) y de las fluctuaciones del gradiente horizontal de presión entre las cuencas atlántica y mediterránea (Crepon, 1965; Candela *et al.*, 1989; García-Lafuente *et al.*, 2002a; Vázquez *et al.*, 2008). Particularmente, su importancia ha sido evidente a la hora de entender las oscilaciones de la interfaz, la activación o inhibición de la generación de las ondas internas en el Umbral de Camarinal, el aumento de intensidad del flujo atlántico entrante y la variabilidad en la dinámica del WAG.

Por otra parte, es conveniente señalar la necesidad de datos meteorológicos de alta resolución en la zona del Estrecho de Gibraltar, lo que conduce al uso de datos meteorológicos de baja resolución espacio-temporal para abordar procesos de carácter regional o, incluso, local que llegan a presentar variaciones diurnas (p. ej. brisas de mar y de tierra). Esto pone de manifiesto la necesidad de combinar modelos hidrodinámicos y meteorológicos de alta resolución para hacer frente al estudio de los patrones de circulación marina inducidos por la meteorología en el Estrecho.

Los primeros esfuerzos para incluir el forzamiento atmosférico en la modelización de la circulación del Estrecho (Crepon, 1965; Candela *et al.*, 1989) marcaron las pautas iniciales pero no afrontaron el estudio de la respuesta conjunta al forzamiento de marea y el atmosférico, ni resolvían las escalas a nivel regional de los vientos en el Estrecho de Gibraltar, ya que trabajaban con bajas resoluciones, ni consideraban la respuesta del intercambio baroclino a las fluctuaciones barotrópicas inducidas por la meteorología.

Conociendo estas carencias y contribuyendo así a los esfuerzos de comprensión de la dinámica y a los de modelización realizados en el Estrecho, el **principal objetivo** de este trabajo es el de:

- cuantificar la relevancia de la influencia del viento en la variabilidad espacio-temporal de la circulación marina del Estrecho de Gibraltar, y estudiar las respuestas inducidas que se producen en las fluctuaciones barotrópicas y del intercambio baroclino, a partir de la implementación de un modelo oceánico forzado por viento a alta resolución.

Para facilitar la consecución del objetivo principal se proponen y se abordan los siguientes **objetivos específicos**:

- Estudiar la variabilidad espacio-temporal de los fenómenos atmosféricos en el ámbito del Estrecho de Gibraltar, utilizando un modelo atmosférico de mesoescala, y observaciones meteorológicas.
- Estudiar la variabilidad espacio-temporal de la circulación del Estrecho de Gibraltar, basándonos en las salidas de un modelo hidrodinámico de alta resolución, considerando conjuntamente el forzamiento de marea y del arrastre del viento.
- Analizar la influencia del viento en la variabilidad espacio-temporal de la circulación del Estrecho de Gibraltar, cuantificando las respuestas inducidas en la dinámica a diferentes escalas temporales e identificando la variabilidad de la circulación a escala subinercial.

4. Hipótesis planteadas

Tras la revisión de los antecedentes y planteamientos del estado actual del problema, surgen diferentes incógnitas acerca del efecto del viento en solitario y de su efecto conjunto con la marea en la variabilidad espacio-temporal de los patrones hidrodinámicos, las cuales constituyen las hipótesis de este trabajo:

- La transferencia de *momentum* de la atmósfera al océano tiene lugar a través de la capa límite y, por lo tanto, el viento produce un efecto de arrastre directo sobre el agua afectando a la corriente superficial, pero ¿cómo se comportan las corrientes bajo los distintos regímenes de viento?
- Se ha analizado la influencia de los distintos procesos de fricción por fondo y la fricción interfacial en las oscilaciones de la interfaz, pero ¿y el viento?, ¿induce fluctuaciones de la interfaz?, ¿de qué forma?
- La inclusión de la interfaz, como una superficie activa en un modelo hidrodinámico de alta resolución, resuelve la localización de los controles hidráulicos en el Umbral de Camarinal y en el estrechamiento de Tarifa en distintos regímenes de intercambio baroclino. Si el viento es capaz de producir variaciones en la interfaz, ¿podría también modificar la localización de los controles hidráulicos?, ¿aparecerán otros puntos de control? o, por el contrario, ¿desaparecerán?
- Se ha estudiado el efecto de las variaciones de presión sobre el Mediterráneo en la activación/inhibición de las ondas internas en el Umbral de Camarinal y se ha comparado la correlación directa entre la existencia de gradientes de presión a ambos lados del Estrecho y el viento. A tenor de lo anterior nos plantemos si un cambio en la intensidad de los flujos baroclinos y en la posición de la interfaz, debidos al forzamiento de viento, podrían inducir modificaciones de las características de las ondas internas (amplitud, velocidad de propagación) y de los tiempos de generación del salto hidráulico sobre el Umbral de Camarinal, así como de los tiempos de arresto y liberación del bore interno.
- Al verse modificadas las secciones de entrada de las aguas atlánticas y de salida de las aguas mediterráneas por las supuestas oscilaciones de la interfaz, ¿podría el viento afectar a la corriente saliente en profundidad?
- El flujo atlántico entrante se ve modificado también por las variaciones de presión atmosférica sobre el Mediterráneo Occidental, llegando incluso a interrumpirse durante varios días, particularmente en invierno. Conociendo la relación directa entre un rápido incremento de la presión atmosférica en el Mediterráneo y un evento intenso de levante, nos planteamos: ¿cómo responde el flujo atlántico entrante ante episodios de vientos de Levante?, ¿puede un Levante intenso llegar a revertir el flujo atlántico?
- Las variaciones del nivel del mar, debidas al viento, ¿modificarán el gradiente de nivel transversal en el Estrecho de Gibraltar, perturbando los flujos de intercambio?

5. Limitaciones y alcances de la investigación

Es de obligada mención la principal limitación de este estudio, al no incluir las variaciones de presión atmosférica sobre la cuenca Mediterránea por las restricciones impuestas por la elección del propio modelo hidrodinámico (Izquierdo *et al.*, 2001). Éste ha sido seleccionado por su capacidad para reproducir tanto las corrientes de marea, como la generación y propagación del bore interno con gran exactitud y la localización y evolución temporal de los controles hidráulicos en el área del Estrecho de Gibraltar. Además, su eficiencia computacional (bajo coste en tiempo y reducidas necesidades de memoria), justifican su utilización y viabilidad para llevar a cabo simulaciones anuales en tiempos razonables, lo que sería inabarcable en el caso de los modelos tridimensionales. Por otra parte, su mayor simplicidad, respecto a los modelos tridimensionales, lo hace más conveniente para analizar cierto tipo de procesos. Sin embargo, su malla generada en coordenadas curvilíneas, diseñada para disminuir los errores en los contornos, dificulta, al mismo tiempo, la ampliación del dominio y la extensión del contorno oriental a todo el Mediterráneo, impidiendo resolver la naturaleza remota del gradiente de presión atmosférica a la escala requerida (Candela *et al.*, 1989; García-Lafuente *et al.*, 2002a).

No bastaría tampoco con imponer la presión atmosférica sobre el dominio modelado, pues daría lugar a una respuesta barométrica del nivel del mar en las dimensiones del mismo, ignorando que parte de este ajuste tiene lugar internamente en la propia cuenca mediterránea (Candela & Lozano, 1994).

Una solución futura a este problema podría implicar el anidamiento del modelo hidrodinámico con un modelo de circulación global, como el MPIOM (Max Planck Institute Ocean Model) (Marsland *et al.*, 2003), que incluya el forzamiento por presión atmosférica. El nivel del mar, obtenido en la ejecución del modelo global, se interpolaría en los nodos computacionales que conforman los contornos abiertos del modelo regional.

Una segunda opción supondría incluir en los contornos abiertos del modelo regional los flujos subinerciales predichos por un modelo barotrópico, como el HAMSOM o el UCA2D (Álvarez *et al.*, 1999), forzado por presión atmosférica, y cuyo dominio cubra la cuenca Mediterránea en su totalidad. De este modo, la prescripción de la elevación de la superficie a partir de las fases y amplitudes de las principales

constituyentes de marea y de las obtenidas para la banda subinercial, permitirían una interacción no lineal entre las diferentes escalas temporales.

Otra limitación de este estudio lo supone la carencia de información meteorológica disponible en la costa sur del Estrecho (territorio perteneciente a Marruecos) y el número insuficiente de boyas oceanográficas en la región para poder llevar a cabo una validación cuantitativa significante del modelo meteorológico en mar abierto. En un principio se pensó en utilizar los datos procedentes de la medición del sensor SeaWindS (SWS), instalado a bordo del satélite QuikSCAT (Quick Scatterometer). Finalmente esta idea se rechazó debido a su baja resolución espacio-temporal (~25 km y 12 horas, respectivamente), ya que la zona más angosta del Estrecho tiene una anchura de 14 km, y a la existencia de numerosas zonas de sombra de la cobertura del satélite por la cercanía de la costa. Por otro lado, cabe añadir que el dispersómetro[4] de viento estima el viento superficial a partir de la rugosidad de la superficie oceánica y que, por lo tanto, las intensas corrientes del Estrecho de Gibraltar pueden introducir errores en la medida, especialmente bajo condiciones de viento suave (Kelly *et al.*, 2001). Así, la intensidad del viento suele ser menor que la observada por los anemómetros cuando la corriente se desplaza en el mismo sentido que el viento y mayor, cuando los sentidos de la corriente y del viento son opuestos.

A pesar de estas restricciones cabe esperar que, si la validación del modelo meteorológico resulta satisfactoria sobre un terreno de orografía compleja, como se verá en el Capítulo 3, su comportamiento sea aún mejor sobre la superficie del océano, como también demuestra la comparación de las salidas numéricas frente a los registros de las boyas de aguas profundas.

Aunque los recursos computacionales son cada vez mejores y más asequibles, en los inicios supusieron, como en cualquier otro estudio numérico, una limitación a la hora de simular períodos superiores al año.

[4] El dispersómetro de viento es un radar de microondas que debe su nombre al principio en que se basa, es decir, a la forma en que la superficie oceánica, libre de hielo, refleja y dispersa la luz.

Capítulo 2

Series de datos
y
modelos numéricos

Capítulo 2

SERIES DE DATOS Y MODELOS NUMÉRICOS

En este capítulo se realiza un inventario y clasificación de las principales medidas analizadas, así como también una descripción de los modelos numéricos utilizados. Una particularidad de este trabajo es que no se han llevado a cabo campañas de medida exclusivas para su desarrollo, sino que se han compilado datos históricos oceanográficos de campañas anteriores y datos meteorológicos pertenecientes a redes de medidas existentes, promovidas por las comunidades autónomas y organismos públicos. Esto ha supuesto un ahorro de costes en cuanto a planificación de campañas a favor de la inversión en servidores y recursos computacionales, contribuyendo, por otro lado, a la explotación y aprovechamiento de los datos existentes.

Las medidas meteorológicas han sido clasificadas según si el registro ha sido realizado en tierra firme, o por el contrario, en mar abierto. Las observaciones meteorológicas registradas en tierra han sido catalogadas según la red de medida a la que pertenecen.

Las medidas oceanográficas han sido clasificadas cronológicamente, según la campaña en la que fueron registradas.

En una segunda sección de este capítulo se detallan los modelos numéricos utilizados: el modelo meteorológico mesoescalar MM5 (Dudhia, 1993; Grell *et al.*, 1994) y el modelo hidrodinámico UCA2.5D (Izquierdo *et al.*, 2001). El primero es de

distribución libre y, tanto éste como el hidrodinámico, están en código Fortran 90, lo que ha permitido utilizar compiladores de uso no comercial. El modelo oceánico forzado por viento, bautizado como MM5-UCA2.5D, se describe al final del capítulo.

1. Datos observados

1.1. Datos meteorológicos

1.1.1. Estaciones Meteorológicas Automáticas

Se ha utilizado la información de 107 Estaciones Meteorológicas Automáticas (EMAs) para validar los resultados del modelo meteorológico: 95 de las cuales pertenecen a la Red de Información Agroclimática de Andalucía (Pérez de los Cobos *et al.*, 2003) del Instituto de Investigación y Formación Agraria y Pesquera de Andalucía (IFAPA) y 12 a la Agencia Estatal de Meteorología (AEMET). Las estaciones de la red del IFAPA están distribuidas ampliamente sobre el territorio andaluz, con mayor concentración sobre áreas de regadío, ofreciendo una alta representatividad de la variabilidad atmosférica regional (Gavilán *et al.*, 2006; Estévez *et al.*, 2011). Las estaciones de AEMET están localizadas en zonas cercanas a la costa a ambos lados del Estrecho de Gibraltar. Todas ellas están incluidas dentro de la zona de cobertura del dominio intermedio de 10 km del modelo MM5 y algunas dentro del dominio de mayor resolución (figura 2.1).

Según el Manual del Sistema Mundial de Observación (OMM-Nº 544) de la Vigilancia Meteorológica Mundial publicado por la Organización Meteorológica Mundial (OMM), las estaciones automáticas son aquellas en las que "los instrumentos efectúan y transmiten o registran automáticamente las observaciones, realizando, en caso necesario, directamente la conversión a la clave correspondiente o bien realizándose esa conversión en una estación transcriptora". Estas estaciones surgieron de la necesidad de obtener información en tiempo real, y de forma operacional.

Cada una de las estaciones registra: temperatura del aire, a través de un sensor de temperatura Pt1000; la humedad relativa mediante el sensor Humicap 180; la velocidad y dirección del viento con la anemoveleta Young 05103; el pluviómetro ARG 100 registra la precipitación y la radiación solar viene dada por el piranómetro Skye SP1110. La velocidad del viento se mide a 2 m sobre la superficie del suelo, siendo necesario un ajuste de las medidas hasta la altura estándar de 10 m. Las EMAs de la red del IFAPA no miden presión atmosférica.

La medida de la velocidad del viento tiene una precisión de ±0.3 $m \cdot s^{-1}$; la dirección de ±3º y la temperatura de ±0.2 ºC, según (Estévez *et al.*, 2011).

El intervalo de registro es horario, en la mayoría de los casos, excepto en 7 estaciones de AEMET, en las que sólo se ha podido acceder a los registros diarios (tabla 2.1).

Tabla 2.1.- Estaciones Meteorológicas Automáticas de AEMET utilizadas en la validación del modelo meteorológico. No se incluyen las estaciones pertenecientes a la red del IFAPA ya que su localización y elevación puede obtenerse en Gavilán *et al.* (2006) y Estévez *et al.* (2011) .

Estación	Provincia	Intervalo	Localización
Almería / Aeropuerto	Almería	diario	2.3560°W / 36.8460°N
Cádiz	Cádiz	diario	6.2567°W / 36.5011°N
Ceuta (Monte Hacho)	Ceuta	diario	5.2894°W / 35.8922°N
Jerez de la Frontera / Aerop.	Cádiz	diario	6.0558°W / 36.7506°N
Málaga / Aeropuerto	Málaga	diario	4.4881°W / 36.6667°N
Melilla	Melilla	diario	2.9553°W / 35.2778°N
Rota	Cádiz	diario	6.3317°W / 36.6389°N
Cádiz Cortadura	Cádiz	horario	6.2578°W / 36.4997°N
Ceuta	Ceuta	horario	5.3469°W / 35.8886°N
San Fernando	Cádiz	horario	6.2056°W / 36.4656°N
Tarifa	Cádiz	horario	5.5989°W / 36.0139°N
Vejer de la Frontera	Cádiz	horario	5.9650°W / 36.2456°N

Teniendo en cuenta que la finalidad de la implementación del modelo meteorológico es la de proveer el forzamiento de viento al modelo oceánico, los períodos seleccionados para la validación del MM5 han sido escogidos considerando la existencia de:

- transiciones bruscas entre vientos de Poniente (del oeste) y vientos de Levante (del este), como en el evento estudiado del 20-23 de agosto, 2004.
- brisas de tierra-mar con una probabilidad mayor al 30%, como en el mes de mayo del 2007 (Hernández-Ceballos *et al.*, 2013).
- fuertes perturbaciones meteorológicas, como los ciclones acontecidos entre el 15 de septiembre y el 12 de octubre del 2008. Además, este período abarca todas las fases de la campaña oceanográfica "*Gibraltar'08*".

1.1.2. Boyas de aguas profundas

Sobre el mar se han utilizado dos boyas de la red de boyas de aguas profundas (Red Exterior, REDEXT) de Puertos del Estado (ver tabla 2.2). Estas son del tipo SeaWatch y alojan sensores meteorológicos y también oceanográficos.

La velocidad y la dirección del viento se miden por los sensores YOUNG/AANDERA 2740 y 3590, respectivamente. La temperatura del aire viene dada por el registro del sensor OMEGA-OCEANOR/AANDERAA 3455 y la presión atmosférica por el VAISALA PTB200A(D).

Las boyas, localizadas en el golfo de Cádiz y en el cabo de Gata, presentan datos históricos desde agosto del 1996 y Marzo del 1998, respectivamente. La velocidad del viento se obtiene promediando las medidas de los primeros 10 minutos de cada hora, proporcionando datos a intervalo horario, mientras que las medidas de temperatura del aire y presión a nivel del mar son instantáneas. Ambas registran los parámetros meteorológicos a una altura de 3 m sobre la superficie del mar.

El control de calidad básico, llevado a cabo por Puertos del Estado, se ha establecido para todos los parámetros y consiste en rechazar aquellos que superen un valor máximo y aquellos que presenten diferencias con los datos adyacentes mayores que un determinado umbral.

Debe considerarse también que la altura del registro del viento es de 3 m (altura del mástil de la boya sobre el agua), por lo que deben ajustarse las medidas desde la altura de registro hasta la altura estándar de 10 m.

Tabla 2.2.- Boyas de la red de aguas profundas utilizadas en la validación del modelo meteorológico.

Boya	Profundidad de fondeo	Entorno	Red de medida	Localización
Cabo de Gata[1]	536 m	Mar Mediterráneo	REDEXT	2.3200°W / 36.5700°N
Golfo de Cádiz	450 m	Océano Atlántico	REDEXT	6.9600°W / 36.4800°N

En la figura 2.1 se muestran las localizaciones de las estaciones meteorológicas automáticas pertenecientes a las diferentes redes de medida y las boyas de aguas profundas utilizadas para la validación del modelo meteorológico.

[1] De aquí en adelante, se nombrarán al cabo de Gata y golfo de Cádiz, siempre en castellano, para hacer referencia a las estaciones de las boyas, distinguiéndolas de los nombres de los accidentes geográficos donde se ubican.

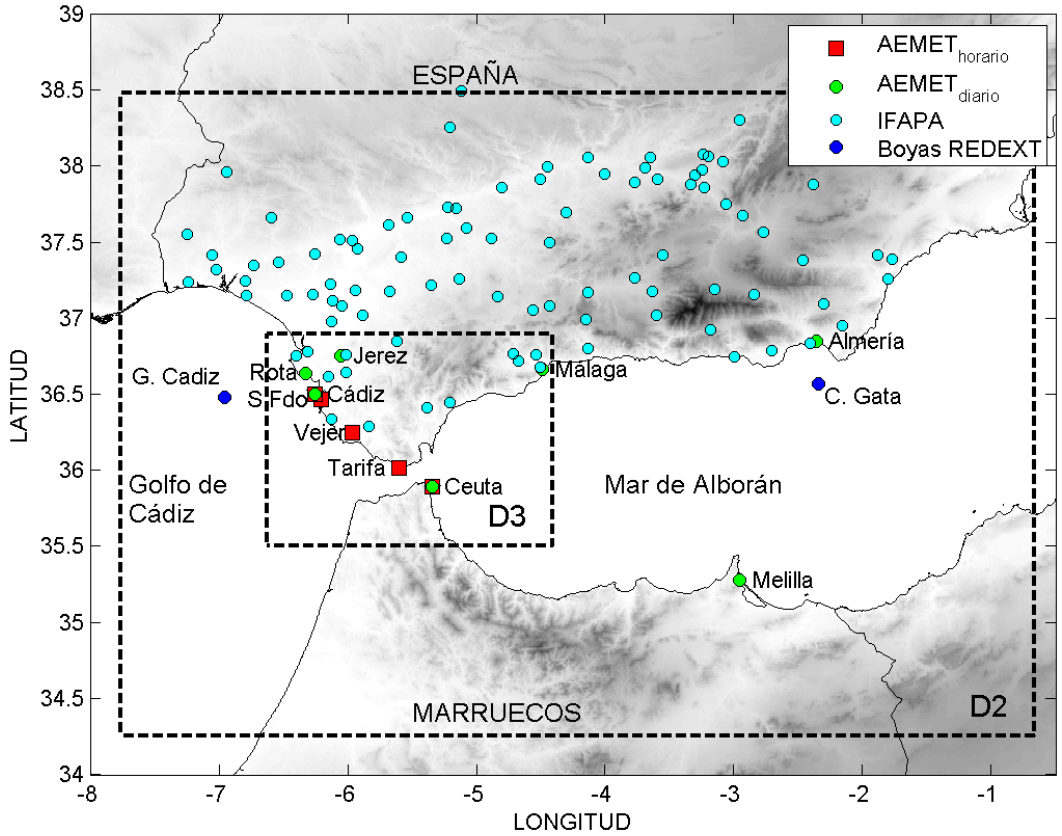

Figura 2.1.- Mapa topográfico del área de estudio con las localizaciones de las EMAs y las boyas utilizadas en la validación del modelo meteorológico. Los rectángulos en línea discontinua representan los dominios de 10 (D2) y 3.3 km (D3) del MM5. Se indican los nombres de las estaciones y boyas citadas en el texto.

1.2. Datos oceanográficos

1.2.1. Campaña Strait 1994-96

El experimento internacional "*Strait 94-96*" (Candela, 2001) fue una campaña muy intensa de adquisición de datos dividida a lo largo de 5 fases con una duración aproximada de seis meses cada una. En cada una de las fases, se registró la velocidad de la corriente en toda la columna de agua mediante el fondeo de un perfilador de corriente ADCP (150 KHz). Estos registros han dado lugar a una de las series más largas de corriente existentes en el Umbral de Camarinal, ya que abarca dos años (desde octubre de 1994 hasta octubre de 1996) de medidas casi continuas.

La información acerca de los períodos de muestreo considerados y las profundidades de fondeo durante las fases 2, 3 y 4, utilizadas en este estudio, se encuentran en la tabla 2.3. Para homogeneizar las medidas registradas durante las diferentes fases, se ha considerado el perfil vertical de la velocidad de corriente cada 10 m, desde los 45 hasta los 265 metros de profundidad, con un intervalo de muestreo de 15 minutos.

Tabla 2.3.- Información del fondeo realizado sobre el Umbral de Camarinal durante el experimento "*Strait 94-96"*.

Fondeo	Localización	Fase	Prof. (m)	Resolución vertical (m)	Num. celdas	Δt (min)	Períodos analizados
ADCP (150 KHz)	5.7494°W 35.9184°N	2	274	10	25	15	01-01-95 00:00
							04-04-95 08:00
		3	280	10	28	15	06-04-95 18:00
							13-10-95 12:00
		4	275	10	23	15	16-10-95 14:00
							26-12-95 11:00

La longitud de estas series ha permitido calcular los flujos entrante, saliente y neto, teniendo en cuenta la variabilidad estacional.

1.2.2. Campaña Gibraltar-2008

Esta campaña representa una de las más ambiciosas realizadas en aguas del Estrecho y áreas adyacentes desde el experimento "*Strait 94-96"*, no por la longitud de los registros, sino por el despliegue de instrumentación y la cobertura espacial de las medidas.

La campaña se desarrolló a bordo del B/O Sarmiento de Gamboa y del B/O Mytilus, con el principal objetivo de realizar una descripción del sistema de corrientes y la distribución de variables biológicas para perfeccionar los modelos implementados en la zona del Estrecho de Gibraltar y la parte occidental del mar de Alborán. Abarcó el período comprendido entre el 15 de septiembre y el 12 de octubre del 2008, estando dividida en 16 fases, varias de ellas repetidas en condiciones de mareas vivas y mareas muertas.

Los registros que hemos utilizado en este trabajo comprenden las series de velocidad de la corriente de la línea de correntímetros fondeada en el norte de la meseta del Umbral de Camarinal y los perfiles verticales de temperatura y salinidad registrados en las estaciones de CTD realizadas en la totalidad de las fases de la campaña.

Las velocidades de la corriente fueron registradas por un correntímetro AANDERAA RCM-7 9827, localizado a 120 m. La serie registrada a 70 m se descartó debido a la existencia de un alto porcentaje de datos anómalos. Las medidas fueron adquiridas con un intervalo de 10 minutos para el período comprendido entre el 15 de septiembre y el 15 de octubre del 2008 (tabla 2.4). Estos registros han sido filtrados para obtener la serie subinercial, siendo ésta utilizada como serie control para su comparación con las series subinerciales del modelo forzado atmósfera-océano.

Tabla 2.4.- Información del fondeo realizado al norte de la meseta del Umbral de Camarinal durante la campaña oceanográfica "*Gibraltar-08*".

Fondeo	Localización	Prof. (m)	Δt (min)	Período de registro
AANDERAA RCM-7	5.7385°W / 35.9809°N	120	10	15-09-08 19:01 16-10-08 23:51

A lo largo de cada una de las fases, y de forma más intensa durante la llamada Fase Descriptiva, se realizaron perfiles de CTD en una malla de estaciones distribuidas de forma equidistante en estaciones con diferentes profundidades (ver figura 2.2), según la batimetría de la zona. Los perfiles de salinidad registrados han sido una información muy útil a la hora de estudiar la variación de la profundidad de la interfaz en el área cubierta por las estaciones.

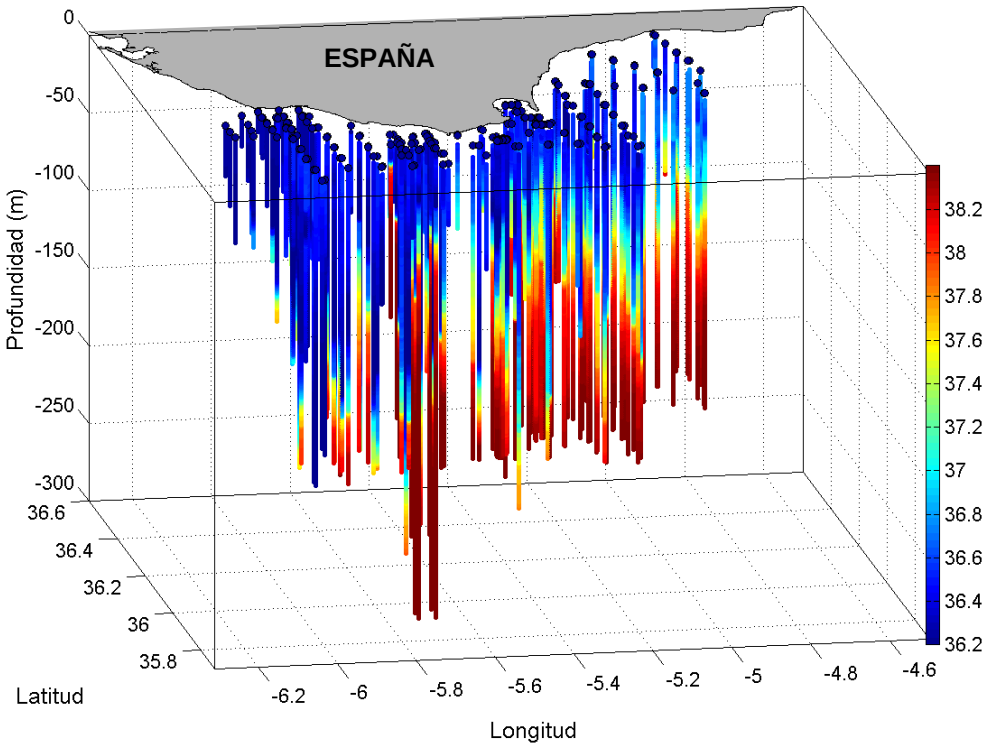

Figura 2.2.- Perfiles verticales de salinidad de las estaciones yo-yo de CTD realizadas durante la campaña Gibraltar 2008.

1.2.3. Mareógrafos de Ceuta, Tarifa y Algeciras

Los datos de nivel del mar utilizados pertenecen a las series históricas de la red mareográfica del Instituto Español de Oceanografía (IEO), que se encuentran almacenadas en el Servicio Permanente del Nivel Medio del Mar (PSMSL). Por su localización, a ambos lados del Estrecho, se han elegido las estaciones de Ceuta, Tarifa y Algeciras.

Los instrumentos son mareógrafos mecánicos de flotador con salidas digitales, basados en el movimiento ascendente y descendente del mismo. Registran alturas horarias de nivel del mar, las cuales están referenciadas al cero del mareógrafo o TGZ[2] (tabla 2.5). Para normalizar las medidas de las tres estaciones, además de trabajar con las anomalías del nivel del mar, se han ajustado a una Referencia Local Revisada (Revised Local Reference, RLR), utilizada por convenio en las principales bases de datos de nivel del mar: GLOSS (Global Sea Level Observing System) y PSMSL (Permanent Service for Mean Sea Level). El datum RLR se define como el punto situado por debajo de una señal geodésica, para que el nivel medio del mar de un año determinado sea lo más cercano posible a 7 m (figura 2.3). Con este valor, se pretende evitar los valores negativos en las medias anuales y mensuales.

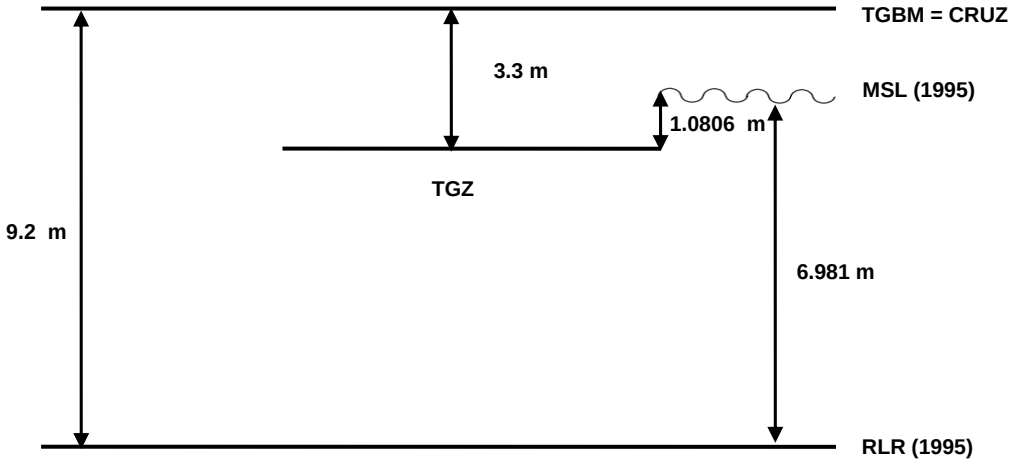

Figura 2.3.- Diagrama de la Referencia Local Revisada (RLR) para Tarifa.

El mareógrafo de Ceuta es, además, una estación GLOSS (Global Sea Level Observing System)[3], la cual se actualiza diariamente en el sitio web de Sea-Level Station Monitoring Facility.

Las series históricas de alturas de nivel, correspondientes al año 1995, han sido obtenidas para cada uno de los mareógrafos con el propósito de estudiar la respuesta de la diferencia del nivel del mar, a través del Estrecho, frente a distintos episodios de viento.

[2] Las medidas están referenciadas al denominado cero del mareógrafo, en notación inglesa Tide Gauge Zero (TGZ).

[3] El Sistema Mundial de Observación del Nivel del Mar (GLOSS) fue establecido en 1985 por la Comisión Oceanográfica Intergubernamental (COI) de la Organización de las Naciones Unidas para la Educación, la Ciencia y la Cultura (UNESCO) a fin de que supervisara y coordinara las redes mundiales y regionales de medición del nivel del mar para respaldar a las investigaciones científicas.

Tabla 2.5.- Información de la localización de los mareógrafos y referencia de las medidas.

Mareógrafo	ID[4]	Localización	Clavo de referencia (TGBM[5])	Cero del mareógrafo (TGZ)	RLR (1995)
Algeciras	490	5.4333°W / 36.1167°N	NGR-15	2.3 m debajo del TGBM	8.4994 m debajo del TGBM
Tarifa	488	5.6000°W / 36.0000°N	Cruz	3.3 m debajo del TGBM	9.2 m debajo del TGBM
Ceuta (estación GLOSS)	498	5.3167°W / 35.9000°N	NGR-101	4.195 m debajo del TGBM	10.3053 m debajo del TGBM

1.2.4. Boyas de deriva

Para aportar información adicional sobre las corrientes superficiales se han utilizado las boyas lagrangianas SouthTEK.

Las boyas utilizadas están diseñadas para experimentos a corto plazo en aguas costeras bajo cobertura GSM[6]. Presentan de 2 a 7 días de autonomía dependiendo de la cobertura y de la configuración de muestreo y transmisión de datos utilizada. Las medidas estándar son la posición y el estatus del GPS (1 o 0 si la posición se ha calculado correctamente o no, respectivamente), la fecha y hora de registro.

En octubre del 2011, se soltaron 4 boyas en las proximidades de Punta Carnero (Bahía de Algeciras), en la entrada este del Estrecho. La tabla 2.6 resume la información de la fecha y la localización de la suelta de cada boya, así como el número total de horas de registro. La frecuencia de muestreo y de transmisión se configuraron en 10 min para todas las boyas excepto para la primera, cuyo intervalo fue de 1 hora.

Las trayectorias de las boyas de deriva y las virtuales, simuladas por los diferentes experimentos numéricos (TIDE y TIDE-WIND), han sido comparadas. La trayectoria de la primera boya ha sido dividida en dos tramos, de los cuales, sólo el segundo ha sido considerado en la validación. El primer trayecto ha sido utilizado para probar la existencia de una contracorriente costera entre Tarifa y Punta Paloma (Capítulo 4).

[4] El código de cada estación se muestra conforme a la información disponible en el Servicio Permanente del Nivel del Mar (http://www.psmsl.org/data/obtaining/)

[5] La calibración del mareógrafo se realiza con respecto a la señal principal del mareógrafo o clavo de referencia del mareógrafo, en notación inglesa Tide Gauge Bench Mark (TGBM).

[6] GSM es el Sistema Global para Comunicaciones Móviles, en notación inglesa Global System for Mobile communications.

Tabla 2.6.- Fechas y localizaciones de la liberación de las cuatro boyas de deriva.

Boya	Fecha y hora	Localización	Período de registro (horas)
1a	10/10/2011-21 UTC	5.4033°W / 36.0656°N	22
1b	11/10/2011-19 UTC	5.4708°W / 36.0185°N	43
2	10/10/2011-19 UTC	5.3222°W / 35.9313°N	20
3	10/10/2011-20 UTC	5.3316°W / 36.0082°N	8
4	10/10/2011-21 UTC	5.3344°W / 36.0198°N	9

A modo de resumen, de igual forma que se ha realizado en el caso de las observaciones meteorológicas, se incluyen en la figura 2.4 todas las medidas oceanográficas consideradas y descritas a lo largo de este apartado.

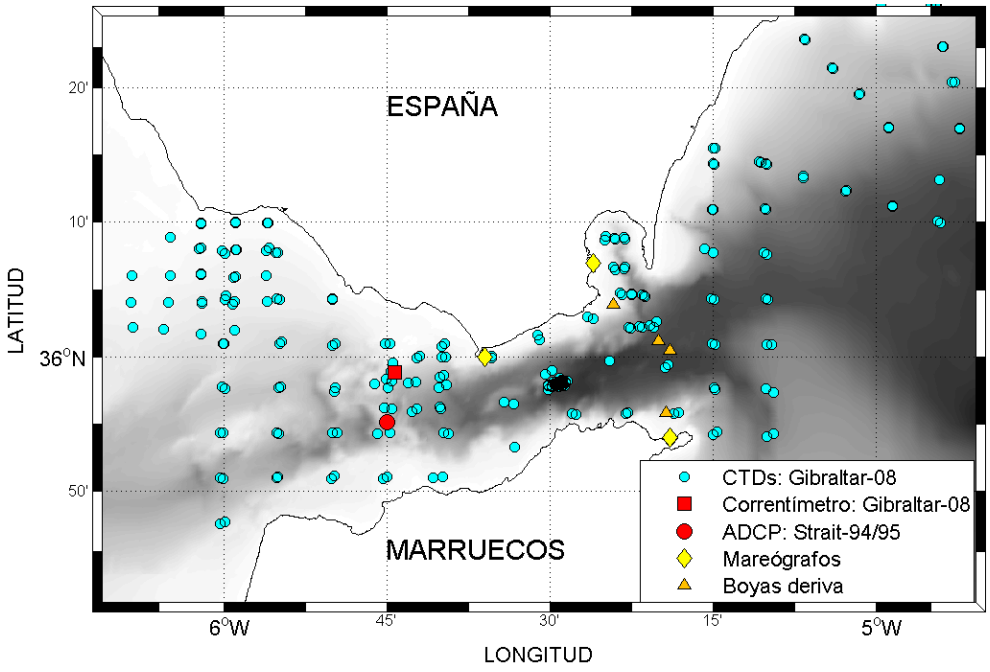

Figura 2.4.- Mapa batimétrico del área de estudio con las localizaciones de las medidas oceanográficas realizadas.

2. Modelos numéricos

2.1. Modelo meteorológico de mesoescala MM5

2.1.1. Introducción al modelo meteorológico de mesoescala MM5

El campo de la modelización numérica de la atmósfera se inició a principios de los años 20, aunque no se obtuvieron resultados realistas hasta l950. Aún así, la predicción meteorológica jugó un papel crucial durante la Segunda Guerra Mundial, jugando a favor de los aliados cuando el meteorólogo jefe de la Operación Overlord, el capitán de la Real Fuerza Aérea británica, James Stagg, persuadió a los mandos para

posponer un día el desembarco de Normandía. Nadie niega que en muchas de las batallas, el vencedor a menudo tuvo el viento y el tiempo a su favor.

Actualmente, el avance en la modelización atmosférica, en paralelo al desarrollo de los ordenadores, permite estudiar fenómenos meteorológicos que ocurren en un rango muy amplio de escalas espacio-temporales. Se puede, por ejemplo, predecir las brisas de mar y de tierra en cualquier zona costera remota (a una escala espacial de 1 km y temporal de 1 día), o analizar el aumento paulatino de la temperatura media del planeta en los últimos 100 años empleando modelos globales de circulación general. Los modelos de mesoescala reducen estas predicciones para su aplicación a las variaciones locales del tiempo, especialmente las que están influenciadas por la topografía.

En la mesoescala, la aproximación cuasi-geostrófica (Charney, 1948) deja de ser válida ya que la aceleración de Coriolis deja de ser dominante respecto a la advección de *momentum* de los procesos mesoescalares. Por otro lado, la validez de la hipótesis hidrostática, admitida en procesos con una escala horizontal mucho mayor que la escala vertical, es muy discutible en la mesoescala debido a la existencia de aceleraciones verticales importantes.

En términos de cifras, la mesoescala estaría comprendida entre los 2 km y los 200 km, presentando los fenómenos asociados a ella una escala temporal comprendida entre los 30 min y 1 día (Stull, 1988). Pielke (1984) coincide con las dimensiones de la escala espacial pero sitúa la escala temporal de los procesos de mesoescala entre 1 h y 1 día. Por otro lado, no existe una división clara entre los modelos regionales y mesoescalares ya que ambos describen óptimamente fenómenos comprendidos entre la macroescala y la microescala. Sin embargo, puede considerase que los modelos regionales trabajan con resoluciones espaciales de entre 50 -150 km y los mesoescalares con menos de 50 km.

Teniendo en cuenta que nuestro objeto de estudio es la influencia del viento en la dinámica marina del Estrecho de Gibraltar y que éste, en su constricción, presenta no más de 14 km de anchura, se hace necesario el uso de un modelo mesoescalar.

Por otro lado, considerando la complejidad de la orografía en la zona de estudio, que da lugar al desarrollo de convecciones fuertes e importantes aceleraciones verticales, imponiendo la obligatoriedad de trabajar con elevadas resoluciones verticales y horizontales, debe utilizarse un modelo que pueda configurarse en modo no-hidrostático.

Por estas razones, entre otras que se mencionarán a continuación, se ha utilizado el modelo meteorológico de quinta generación MM5-Mesoscale Model 5th Generation (Dudhia, 1993; Grell *et al.*, 1994), versión 3.7. (formulado en modo no-hidrostático), de la Penn State University y desarrollado en colaboración con NCAR (National Center of Atmospheric Research). El modelo MM5 está ampliamente extendido entre la comunidad científica internacional (sólo en la Península Ibérica es utilizado por más de 50 grupos de investigación) y está avalado por más de 400 publicaciones. Además, presenta una amplia gama de manuales de instalación según el compilador utilizado (el código fuente está escrito en lenguaje de programación Fortran 90/77), y es de libre distribución.

El sistema de modelado del MM5 consiste en una serie de módulos, los cuales se resumen a continuación. En el módulo TERRAIN se configuran los dominios y se especifica la altura del terreno y los usos de suelo. La información meteorológica en niveles de presión, de análisis o de otros modelos, se prepara en el módulo REGRID, para utilizarla como condición de frontera e inicial del dominio mayor. El módulo INTERPF interpola en la vertical los niveles de presión a un sistema de coordenadas sigma (σ), generando los tres ficheros de condiciones iniciales y de contorno que requiere el módulo MM5, en el que se realiza la ejecución del modelo para predicción meteorológica. El anidamiento se realiza a través del módulo NESTDOWN, el cual interpola horizontalmente los datos en coordenadas sigma al dominio anidado, creando las condiciones iniciales y de frontera para éste.

Como complemento a los módulos anteriores, el módulo INTERPB permite reconvertir los niveles sigma en niveles isobáricos y el MM5toGrADs transformar las salidas del modelo al formato de entrada del software gráfico GrADs.

2.1.2. Configuración del modelo meteorológico de mesoescala MM5

El dominio de trabajo, consta de la superficie topográfica de interés y la capa de la atmósfera a estudiar situada encima de ésta. De esta forma, se genera una malla 3D de la zona de estudio, donde el límite inferior es, en cada caso, la topografía discretizada, y el límite superior viene impuesto por el nivel del presión de 100 hPa, siendo abiertos los límites laterales, pero quedando bien establecidos al tratarse de un modelo de área limitada (Limited Area Model, LAM).

En el caso del MM5, se utiliza una coordenada vertical que sigue el terreno, conocida como coordenada sigma (σ), cuyo valor adimensional varía desde 1, en la

superficie, hasta 0, en el límite superior del modelo. Todas las variables, excepto la componente vertical de la velocidad del viento, se definen en la mitad de cada capa vertical, es decir, en medio de dos niveles sigma consecutivos, representados con una línea discontinua en la figura 2.5.

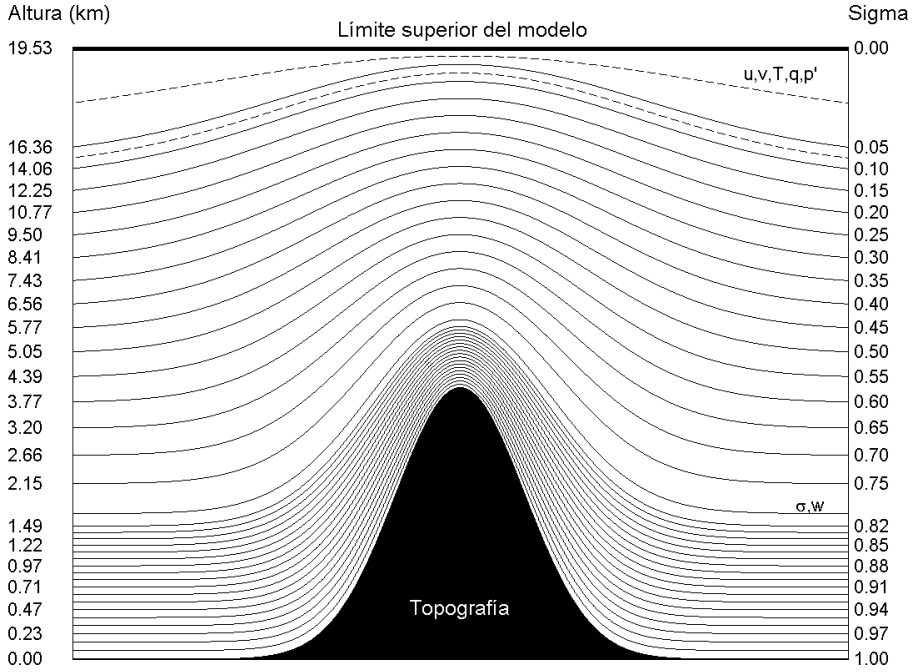

Figura 2.5.- Representación esquemática de la distribución de los niveles sigma del modelo MM5.

La influencia del terreno en la estructura de los niveles sigma disminuye con la altura, por lo que las superficies sigma cerca del límite superior del modelo son casi paralelas y tienden a aproximarse a las superficies isobáricas, presentando más detalle en las capas cercanas a la superficie.

Para discretizar horizontalmente el dominio, se crea una malla regular Arakawa-B (Arakawa & Lamb, 1977), donde las variables escalares y la componente vertical de la velocidad del viento están definidas en el centro de cada celda y las componentes horizontales del viento en los vértices de la misma (ver figura 2.6).

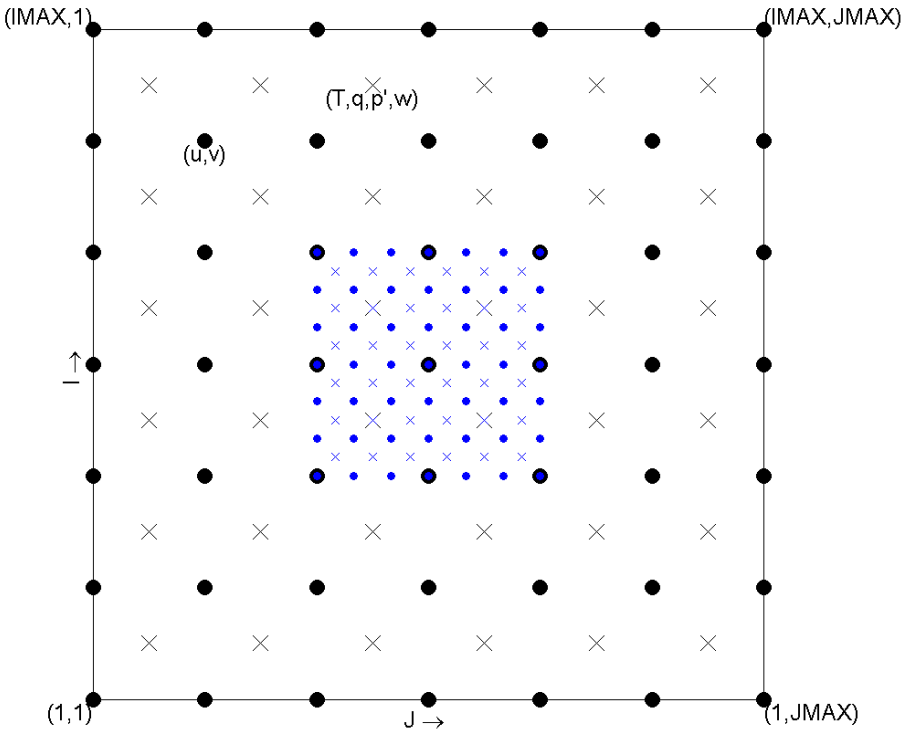

Figura 2.6.- Malla Arakawa-B horizontal del modelo MM5. La malla incluida en el dominio interior representa la relación 3:1 entre los dominios anidados.

Al resolver las ecuaciones dinámicas de la atmósfera mediante métodos numéricos, no sólo se discretiza el espacio sino también el tiempo. El esquema de integración en el tiempo es el de "leap-frog step" de segundo orden, que utiliza diferencias centradas.

El modelo MM5 posee capacidad de anidamiento múltiple, consistente en resolver la dinámica de una región con una baja resolución, para describir los fenómenos que suceden en una escala sinóptica y, a continuación, se focaliza la atención en un subdominio interior, con mayor resolución espacial, para estudiar fenómenos de menor escala. De esta manera, se han definido tres dominios, utilizando la proyección de Lambert, recomendada para latitudes medias.

El dominio "madre", de menor resolución horizontal (30 km), centrado en 11°W, 43.15°N, abarca el norte de Marruecos, la Península Ibérica, Francia y el sur de las islas Británicas. El dominio de resolución intermedia (10 km) está englobado en el dominio exterior, y cubre la región andaluza en su totalidad y la costa sur del Estrecho de Gibraltar. Con una resolución de 3.3 km, el tercer dominio, contenido en los dos anteriores, se centra en el área del Estrecho de Gibraltar (ver figura 2.7).

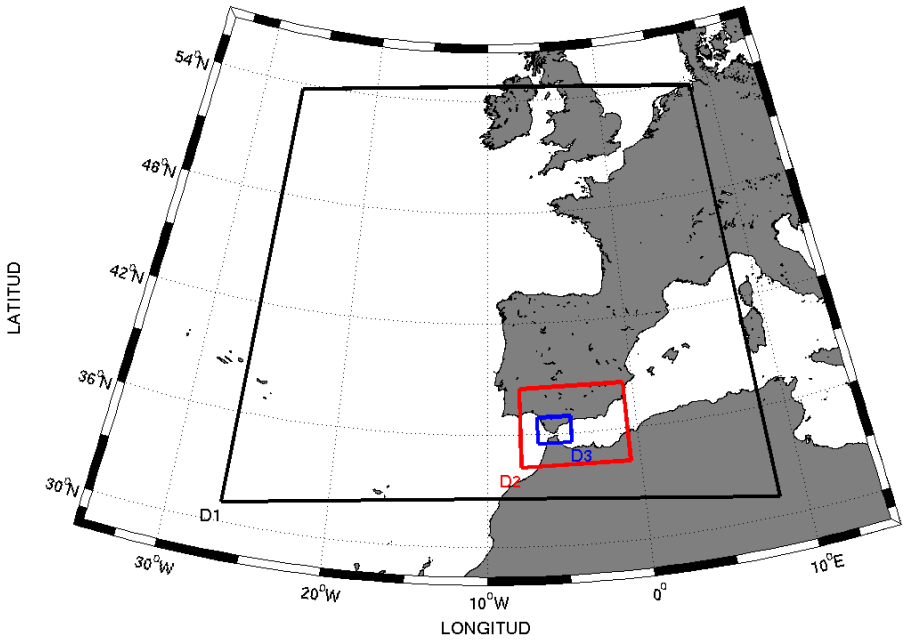

Figura 2.7.- Dominios anidados para la implementación del modelo MM5 a alta resolución en el Estrecho de Gibraltar (los rectángulos negro, rojo y azul representan los límites de los dominios MM5-30 km, MM5-10 km y MM5 3.3 km, respectivamente).

Para su implementación en el área del Estrecho de Gibraltar, el MM5 se ha configurado con anidamiento unidireccional "one-way", (ver detalles de la configuración en la tabla 2.7). La técnica de anidamiento bidireccional es muy sensible a la definición de los dominios de trabajo, sobre todo, a la localización de los límites a barlovento de importantes obstáculos orográficos, resultando la primera mucho más robusta (Lozej & Bornstein, 1999; Stenger, 2000) y presentando unos costes computacionales inferiores. Además, mientras que para la técnica bidireccional el MM5 está obligado a mantener una relación de resoluciones entre los dominios de 3:1, esta imposición se relaja en la técnica unidireccional.

Tabla 2.7.- Parámetros de definición de los dominios de trabajo.

Parámetros	Dominio 1	Dominio2	Dominio 3
Resolución horizontal (km)	30	10	3.3
Número de puntos de malla	100 × 80	61 × 43	58 × 43
Resolución de la topografía y uso de suelo (km)	3.7	0.925	0.925
Fuente de datos de elevación del terreno y usos de suelo	USGS[7]-2 minutes (global)	USGS-30 seconds (global)	
Anidamiento	One-way		
Niveles sigma medios	35	35	35
Intervalo de integración (s)	90	30	10

[7] US Geological Survey (USGS)

Los fenómenos que suceden en escalas inferiores a las del tamaño de la celda (como la evaporación, los procesos convectivos, etc), fundamentados en mecanismos de escala de sub-malla, se representan mediante el uso de parametrizaciones físicas.

El modelo MM5 incorpora modernos y realistas esquemas de parametrización de los procesos físicos de la atmósfera. Su configuración se ha ido perfeccionando mediante la revisión continua de otras ya existentes del propio modelo (Dudhia *et al.*, 1999; Stenger, 2000; Chen & Dudhia, 2001; Hervella *et al.*, 2002; Soriano *et al.*, 2002; Soler *et al.*, 2003) y de otros modelos de mesoescala, teniendo en cuenta las características orográficas y la elevada resolución de los dominios implementados. El MM5 incluye la parametrización del esquema de Cumulus, los procesos turbulentos dentro de la capa límite PBL (Planetary Boundary Layer), la microfísica de nubes, la radiación atmosférica y la interacción entre las capas del suelo (ver resumen de la configuración en la tabla 2.8).

Tabla 2.8.- Parametrizaciones físicas incluidas en la configuración del MM5.

Parametrizaciones	Descripción	Esquema utilizado
Cúmulos: ICUPA	Parametriza los procesos verticales asociados con columnas convectivas y el desarrollo de cumulus	8.- Kain-Fritsch 2 (Kain & Fritsch, 1993)
Capa Límite Planetaria (PBL): IBLTYP	Parametriza la turbulencia asociada al transporte de calor y la mezcla en la PBL	5.- NCEP[8] Medium-Range-Forecast (MRF) (Hong & Pan, 1998)
Humedad explícita: IMPHYS	Parametriza los procesos relacionados con las fases del agua y sus cambios (líquido, hielo y fase de mezcla)	7.- Reisner graupel (Reisner 2)
Radiación atmosférica: IFRAD	Parametriza la radiación de onda larga y corta con interacción de nubes	2.- Cloud-radiation scheme[9] (Dudhia, 1989)
Procesos en superficie: ISOIL	Parametriza el intercambio de calor y humedad entre la superficie y la atmósfera y entre las diferentes capas del suelo	1.- Five-Layer Soil Temperature model[10] (Dudhia, 1996)

El MM5, como cualquier modelo regional, necesita condiciones iniciales y de contorno lateral de modelos globales o mesoescalares de mayor extensión, en las cuales se represente adecuadamente el estado y la evolución de la atmósfera a gran escala. Los datos, para inicializar el modelo, pueden proceder de diversas fuentes dependiendo las condiciones de contorno laterales, en último término, de un modelo global.

[8] NCEP (National Centers for Environmental Prediction)

[9] El esquema de radiación utilizado incluye los efectos de las nubes en los flujos de radiación de onda larga y onda corta.

[10] El modelo de superficie multicapa predice la temperatura del suelo en 5 capas con espesores de 1, 2, 4, 8, y 16 cm (de arriba hacia abajo). La humedad del suelo está prescrita de acuerdo a las características del suelo y a la estación.

Los experimentos de "hindcast" o retrosimulación (en lo sucesivo, MM5H) fueron realizados utilizando las condiciones iniciales y de contorno de GFS-ANL (Global Forecast System - Analysis Only) (Kalnay *et al.*, 1996). Las series de datos están accesibles a través de los servidores NCDC-NOMADS (http://nomads.ncdc.noaa.gov/) y presentan una resolución espacial de 1º×1º, una resolución temporal de 6 horas e incluyen variables atmosféricas en 26 niveles (desde los 1000 a los 10 mb).

En el marco operacional, las simulaciones de predicción (en adelante, MM5F) han consistido en ejecutar diariamente el modelo MM5 con un horizonte de predicción de 72 horas, utilizando la salida de la ejecución operacional de las 0000 UTC del MM5 a 30 km que proveía MeteoGalicia (actualmente, desde Marzo del 2013, se utilizan las salidas del WRF-ARW a 36 km). A su vez, el dominio de 30 km de MeteoGalicia utiliza las condiciones de contorno e iniciales del modelo GFS de predicción operativa de NCEP, con una resolución horizontal de 1º, actualizadas cada 3 horas (Penabad *et al.*, 2008). Para crear series continuas de predicción (figura 2.8), se han concatenado las simulaciones individuales utilizando las primeras 24 horas de cada una (Lenderink *et al.*, 2009; Hu *et al.*, 2010), ya que el objetivo del presente estudio no incluye analizar la dependencia del error de la longitud de la predicción.

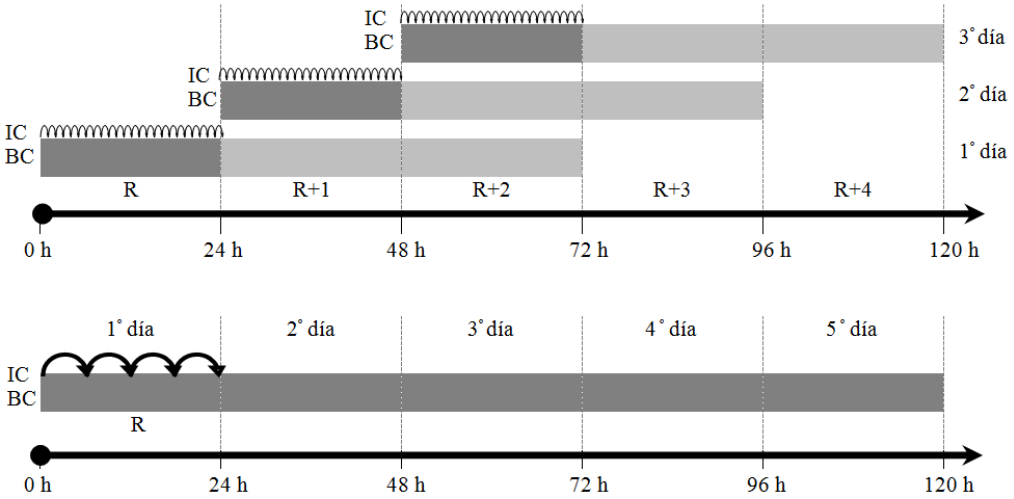

Figura 2.8.- Esquema de las ejecuciones en predicción (arriba) y de hindcast (abajo) del modelo MM5. IC y BC son las condiciones iniciales y de contorno, respectivamente. Los bucles representan la actualización temporal de las condiciones iniciales y de contorno.

Como herramienta aplicada de la implementación del MM5 en el área de estudio, el Grupo de Oceanografía Física: Dinámica de la Universidad de Cádiz ha puesto en marcha la ejecución diaria en modo pre-operacional del modelo

meteorológico, ofreciendo salidas con un horizonte de predicción de 72 horas para el dominio de la región andaluza (MM5-10 km) y para el dominio del Estrecho de Gibraltar (MM5-3.3 km), las cuales se encuentran disponibles en internet (http://oceand.uca.es/prediccion). De este modo, el usuario final puede acceder a los resultados de la predicción meteorológica de un modo rápido y sencillo a través de una interfaz gráfica.

2.1.3. Validación del modelo de mesoescala MM5

La validación ha sido llevada a cabo mediante comparación cualitativa y cuantitativa de las salidas numéricas con las observaciones. Se ha utilizado la aproximación grid-to-point (Pielke, 1984) ya que las observaciones presentan menor resolución que las salidas del modelo y, particularmente, en las zonas montañosas donde los gradientes son mayores, se encuentran más dispersas. De este modo, los campos simulados han sido interpolados a la localización de las observaciones utilizando el esquema de Cressman (1959). Es decir, los resultados del modelo en los cuatro puntos más próximos a la observación son ponderados dependiendo del cuadrado de la distancia de cada punto de la malla a dicha localización.

En este trabajo, adicionalmente a la comparación subjetiva de series temporales de variables simuladas frente a las observadas, como las realizadas por Michelson & Bao (2006) y Zhong *et al.* (2007) para mostrar cualitativamente la bondad del modelo meteorológico, se han usado métodos estadísticos objetivos utilizados por otros autores (Willmott, 1982; Pielke, 1984; Willmott, 1984; Willmott *et al.*, 1985; Stauffer & Seaman, 1990; Stenger, 2000; Emery *et al.*, 2001; Tesche *et al.*, 2002).

Estos estadísticos permiten medir el promedio del grado de correspondencia entre pares individuales de valores pronosticados y valores observados o detectar las principales fuentes de error de diversa procedencia: (i) errores en la formulación del modelo; (ii) errores de resolución temporal y espacial de la configuración implementada en una zona determinada; (iii) errores de las observaciones utilizadas para la comparación.

Los errores han sido descritos en términos de errores estadísticos dimensionales[11] y negativamente-orientados[12], como el error medio absoluto (MAE), el error cuadrático medio (RMSE) y el sesgo o BIAS y en términos del índice de acuerdo

[11] Expresan el error medio en las unidades de la variable de interés.
[12] Cuanto menor sea el valor, mejor es la validación del modelo.

(IOA). Los mencionados estadísticos fueron calculados para la temperatura a 2 m, la presión a nivel del mar y el viento a 10 m de la superficie.

- MAE es la medida más habitual para estimar la magnitud del error medio (Stauffer & Seaman, 1990; Willmott & Matsuura, 2005) para pares de predicciones - observaciones en una región determinada y para un período dado, estando definido por:

$$MAE = \frac{1}{IJ}\sum_{i=1}^{I}\sum_{\mathrm{j}=1}^{\mathrm{J}}\left|P_j^i - O_j^i\right|; \quad \textbf{(2.1)}$$

donde P_j^i y O_j^i son los pares de variables predicha y observada en el punto i y en el instante j, respectivamente. El sumatorio se calcula para todos los puntos (I) y para todo el período (J).

- La típica magnitud para estimar las diferencias, en promedio, entre los valores simulados y los observados, viene dada por el RMSE, el cual es sensible a valores extremos debido a las diferencias cuadradas.

$$RMSE = \left[\frac{1}{IJ}\sum_{i=1}^{I}\sum_{\mathrm{j}=1}^{\mathrm{J}}\left(P_j^i - O_j^i\right)^2\right]^{1/2} \quad \textbf{(2.2)}$$

- El error sistemático o BIAS (Pielke, 1984) mide la tendencia del modelo a sobreestimar o subestimar un valor y se define como:

$$BIAS = \frac{1}{IJ}\sum_{i=1}^{I}\sum_{\mathrm{j}=1}^{\mathrm{J}}\left(P_j^i - O_j^i\right) \quad \textbf{(2.3)}$$

Es importante resaltar que el BIAS no da información sobre la magnitud de errores individuales y, por lo tanto, no se trata de una medida de exactitud del modelo a la hora de reproducir los fenómenos atmosféricos mesoescalares.

Los errores sistemáticos del modelo son debidos a una irreal representación de la topografía y del uso de suelo; a las parametrizaciones físicas o a factores numéricos (disipación) (Zhong & Fast, 2003).

Para la dirección del viento, al ser una variable angular y, para evitar problemas asociados con el solapamiento de 0° y 360°, se han utilizado el MAE (2.1), el RMSE (2.2) y el BIAS (2.3) con ligeras modificaciones.

- Primero se define una variable circular (Jiménez & Dudhia, 2013), D_i, acotada entre [-180,180], a partir de las direcciones observadas (d_i^o) y $predi$chas (d_i^p):

$$D_i^j = \begin{cases} d_{ij}^p - d_{ij}^o & if \quad \left|d_{ij}^p - d_{ij}^o\right| < 180 \\ d_{ij}^p - d_{ij}^o - 360 & if \quad d_{ij}^p - d_{ij}^o > 180 \\ d_{ij}^p - d_{ij}^o + 360 & if \quad d_{ij}^p - d_{ij}^o < -180 \end{cases} \quad \textbf{(2.4)}$$

Al trabajar con el valor mínimo de la diferencia entre la dirección simulada y observada, los resultados del promedio de los estadísticos, no incluirán una desviación por método de cálculo que no represente la diferencia real entre las medidas (p. ej. la diferencia entre un viento simulado de 350°, con un viento observado de 1°, es de 349°, pero realmente el modelo únicamente se diferencia en 11°).

- A partir de la definición de la variable circular, el BIAS para la dirección del viento se calcula como sigue:

$$BIAS_{dir} = \frac{1}{IJ}\sum_{i=1}^{I}\sum_{\mathrm{j}=1}^{\mathrm{J}} D_i^j \quad \textbf{(2.5)}$$

Valores de $BIAS_{dir}$ positivo indican la tendencia del modelo a rotar anticiclónicamente (sentido horario) los vectores de viento respecto a las observaciones, mientras que los valores negativos de $BIAS_{dir}$ reflejan una rotación ciclónica (anti-horario).

- El $RMSE_{dir}$ se calcula de la siguiente forma:

$$RMSE_{dir} = \left[\frac{1}{IJ}\sum_{i=1}^{I}\sum_{\mathrm{j}=1}^{\mathrm{J}} {D_i^j}^2\right]^{1/2} \quad \textbf{(2.6)}$$

- y el MAE_{dir} así:

$$MAE_{dir} = \frac{1}{IJ}\sum_{i=1}^{I}\sum_{\mathrm{j}=1}^{\mathrm{J}} \left|D_i^j\right| \quad \textbf{(2.7)}$$

- El error cuadrático medio del vector horizontal de viento (RMSVE) se calcula considerando las dos componentes horizontales del viento y viene definido por:

$$RMSVE = \left[\frac{1}{IJ}\sum_{i=1}^{I}\sum_{\mathrm{j}=1}^{\mathrm{J}} \left(\left(u_{ij}^p - u_{ij}^o\right)^2 + \left(v_{ij}^p - v_{ij}^o\right)^2\right)\right]^{1/2} ; \quad \textbf{(2.8)}$$

donde u y v son las componentes zonal y meridional del viento, respectivamente, predichas (p) y observadas (o).

- El índice de acuerdo (Willmott, 1981) es una medida estandarizada del grado del error de la predicción del modelo y está acotado entre 0 y 1 y, por lo tanto, es fácilmente interpretable:

$$IOA = 1 - \left[\frac{\mathrm{IJ} \cdot \mathrm{RMSE}^2}{\sum_{i=1}^{I}\sum_{\mathrm{j}=1}^{\mathrm{J}}\left(\left|P_j^i - \bar{O}\right| + \left|O_j^i - \bar{O}\right|\right)^2}\right] \qquad \textbf{(2.9)}$$

$$= 1 - \left[\frac{\sum_{i=1}^{I}\sum_{\mathrm{j}=1}^{\mathrm{J}}\left(P_j^i - O_j^i\right)^2}{\sum_{i=1}^{I}\sum_{\mathrm{j}=1}^{\mathrm{J}}\left(\left|P_j^i - \bar{O}\right| + \left|O_j^i - \bar{O}\right|\right)^2}\right]$$

A pesar de las ventajas que presentan las versiones posteriores de este índice (Willmott *et al.*, 1985; Willmott *et al.*, 2012), en relación a la versión utilizada, ya que son menos sensibles a los errores grandes[13] (Willmott *et al.*, 2012), los indicadores estadísticos o valores de referencia relacionados con el IOA fueron calculados siguiendo la aproximación de (Willmott, 1981).

Valores nulos de RMSE y MAE indican un ajuste perfecto, mientras que para el IOA es el valor 1 el que indica una coincidencia perfecta entre las medidas y los valores predichos (Willmott, 1981).

Además de los estadísticos descritos anteriormente, se han calculado las desviaciones estándar de las observaciones y de las estimaciones del modelo, así como el coeficiente de determinación (r^2) y de correlación (r).

Valores similares de las desviaciones estándar del modelo y de las medidas indican que las simulaciones capturan las variaciones espacio-temporales observadas.

El coeficiente de determinación mide la bondad del ajuste de la regresión lineal entre los valores observados y simulados. Cuando $r^2=1$, todos los puntos se concentran en la línea de mejor ajuste, indicando un menor error de varianza. Valores mayores de 0.5 se consideran aceptables (Santhi *et al.*, 2001; Van *et al.*, 2003).

Adicionalmente, los valores de los errores estadísticos se compararon frente a los indicadores (resumidos en la tabla 2.9), propuestos por Emery *et al.* (2001) y Kemball-Cook *et al.* (2005), para condiciones simples (terrenos llanos y condiciones meteorológicas simples) y complejas (terrenos abruptos y condiciones meteorológicas complejas), respectivamente. Estos valores de referencia están basados en resultados históricos de validación de simulaciones del MM5 en terrenos llanos del este y en zonas montañosas del oeste de Estados Unidos y Alaska, para el caso de los indicadores

[13] Están basados en la suma de los valores absolutos de los errores y no en la suma de sus cuadrados.

simples y complejos, respectivamente. El principal objetivo de las validaciones de Emery *et al.* (2001) y Kemball-Cook *et al.* (2005) era comprobar la calidad de las simulaciones meteorológicas del MM5 utilizadas para alimentar modelos de calidad del aire, por ello la presión a nivel del mar no presenta indicador.

Tabla 2.9.- Indicadores estadísticos simples (Emery *et al.*, 2001) y complejos (Kemball-Cook *et al.*, 2005) para evaluar el comportamiento del modelo meteorológico. WS=velocidad del viento; WD=dirección del viento; T=temperatura.

Estadísticos	Indicadores Simples	Indicadores Complejos
WS BIAS	$\leq \pm 0.5$ m·s^{-1}	$\leq \pm 1.5$ m·s^{-1}
WS RMSE	≤ 2 m·s^{-1}	≤ 2.5 m·s^{-1}
WS IOA[14]	≥ 0.6	No se contempla
WD BIAS	$\leq \pm 10$ º	No se contempla
WD MAE	≤ 30 º	≤ 55 º
T BIAS	$\leq \pm 0.5$ °C	$\leq \pm 2$ °C
T MAE	≤ 2 °C	$\leq \pm 3.5$ °C
T IOA	≥ 0.8	No se contempla

Los resultados obtenidos de la aplicación de los estadísticos descritos y de la comparación de las series observadas y simuladas se analizan el Capítulo 3.

2.2. Modelo hidrodinámico UCA2.5D

2.2.1. Introducción al modelo hidrodinámico UCA2.5D

Como punto de partida para el modelo forzado atmósfera-océano, se ha considerado el modelo UCA2.5D (Izquierdo *et al.*, 2001) para simular la hidrodinámica del Estrecho de Gibraltar. El modelo representa, en dos dimensiones, el flujo de intercambio mediante dos capas superpuestas de fluidos inmiscibles de densidad constante y diferente para cada una de las capas y resuelve las ecuaciones no lineales de aguas someras. Una descripción más completa, incluyendo las ecuaciones está disponible en Izquierdo *et al.* (2001)

Las ecuaciones de *momentum* y continuidad, para la capa superior, en términos de transporte y en coordenadas cartesianas son:

$$\frac{\partial(h_1\boldsymbol{u_1})}{\partial \mathrm{t}} + \nabla \cdot h_1\boldsymbol{u_1}\boldsymbol{u_1} + f\mathbf{k} \times h_1\boldsymbol{u_1} + gh_1\nabla\zeta_1 = -\frac{\boldsymbol{\tau_1}}{\rho_1} \qquad \textbf{(2.10)}$$

$$\frac{\partial(h_1)}{\partial \mathrm{t}} + \nabla \cdot h_1\boldsymbol{u_1} = 0 \qquad \textbf{(2.11)}$$

[14] El IOA de Emery and Tai (2001) ha sido calculado siguiendo la aproximación de Willmot (1981).

, y para la capa inferior:

$$\frac{\partial(h_2\boldsymbol{u_2})}{\partial \mathrm{t}} + \nabla \cdot h_2\boldsymbol{u_2}\boldsymbol{u_2} + f\mathbf{k} \times h_2\boldsymbol{u_2} + g\frac{\rho_1}{\rho_2}h_2\nabla\zeta_1 + g'h_2\nabla\zeta_2 = (\boldsymbol{\tau_1} - \boldsymbol{\tau_2}/\rho_2) \quad \textbf{(2.12)}$$

$$\frac{\partial(h_2)}{\partial \mathrm{t}} + \nabla \cdot h_2\boldsymbol{u_2} = 0 \quad \textbf{(2.13)}$$

Donde ∇ es el operador horizontal de Hamilton, $\cdot$ el producto escalar y $\times$ el producto vectorial, f es el parámetro de Coriolis, h_1 *y* h_2, $\boldsymbol{u_1}$ y $\boldsymbol{u_2}$, son los espesores y los vectores de velocidad horizontal promediados en la vertical de la capa superior e inferior, respectivamente; $\zeta_1 = h_1 + h_2 - H$ es la elevación de la superficie libre y $\zeta_2 = h_2 - H$ es la profundidad de la interfaz; ρ_1 *y* ρ_2 son las densidades de las aguas atlántica y mediterránea, respectivamente; $g' = g(\rho_2 - \rho_1)/\rho_2$ es la gravedad reducida, siendo g la aceleración de la gravedad; τ_1 *y* τ_2 son la tensión de fricción interfacial y la tensión de fricción por fondo, respectivamente.

Las ecuaciones de movimiento (2.10) y (2.12) expresan la conservación del impulso, y las ecuaciones de continuidad (2.11) y (2.13), la conservación de la masa.

Debido a la compleja geometría del Estrecho, las ecuaciones, en un plano-f[15], discretizadas en una malla tipo C de Arakawa (Mesinger & Arakawa, 1976; Arakawa & Lamb, 1977), se resuelven empleando el esquema semi-implícito de Crank-Nicolson en coordenadas curvilíneas ajustadas al contorno del dominio de integración. El uso de estas coordenadas hace posible modelizar zonas de geometrías complejas y permite aumentar la resolución espacial allí donde las características morfométricas y/o dinámicas más lo requieren (como en el caso de la constricción de Tarifa o zonas con un abrupto cambio en la profundidad).

La generación de la malla se realiza a partir de datos batimétricos y la línea de costa obtenidos de la base de datos de ETOPO5, y complementados con datos de las cartas batimétricas del Instituto Nacional de Geología y SECEG (1988), creando un canal equivalente a la geometría del Estrecho de Gibraltar.

La resolución promedio es de 1 km, alcanzando los 125 m en la parte central del Estrecho (ver figura 2.9), debido a que existen fenómenos, como las ondas internas, que requieren una alta resolución espacial para poder ser resueltos adecuadamente.

[15] En el plano-f se ignora la variación del parámetro de Coriolis con el seno de la latitud, asignando un valor constante de f, para una latitud determinada, en todo el dominio.

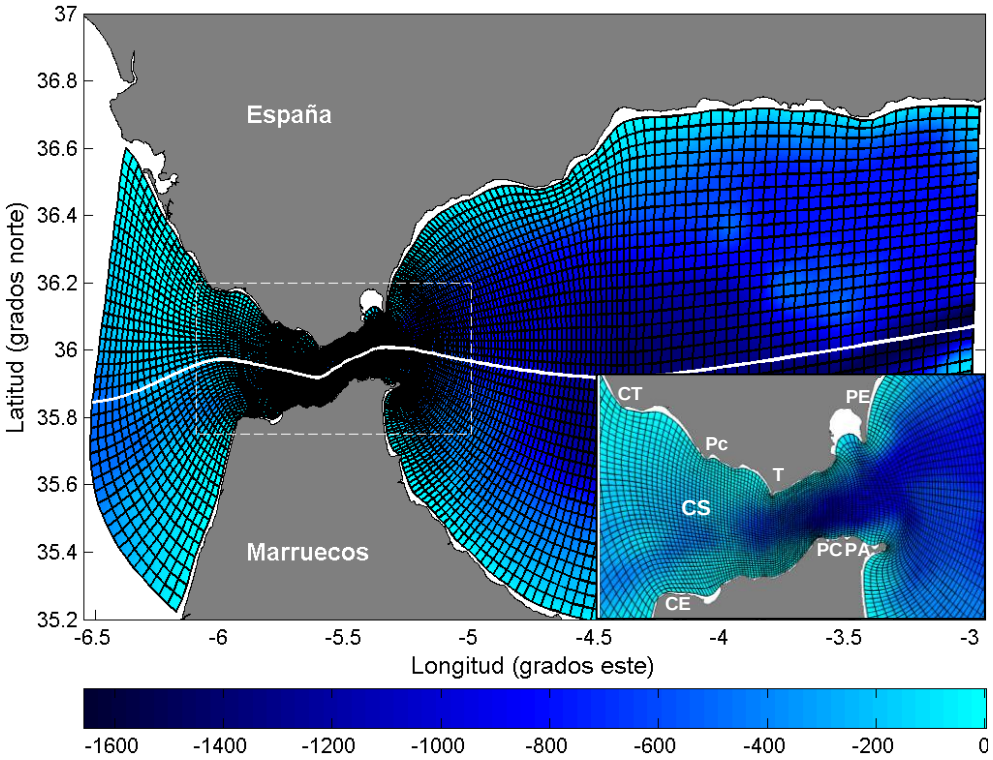

Figura 2.9.- Malla del modelo UCA2.5D junto con la batimetría utilizada. Se señala el transecto longitudinal al Estrecho (línea continua blanca) y se indican los principales accidentes geográficos mencionados en el texto (CT=Cabo Trafalgar; Pc=Punta Camarinal; T=Tarifa; PE=Punta Europa; CE=Cabo Espartel; PC=Punta Cires; PA=Punta Almina) .

En este canal de geometría realista se obtiene, en primer lugar, una primera aproximación de la profundidad de la interfaz y de la elevación de la superficie a partir de una solución estacionaria resultante de un experimento "lock-exchange" (Sein *et al.*, 1998). Es decir, partiendo de una condición inicial en la que las aguas atlánticas (ρ_1 = 1027 kg·m^{-3}) y mediterráneas (ρ_2 = 1029 kg·m^{-3}) están separadas artificialmente por una barrera localizada en la zona de mínima anchura y permanecen en equilibrio hidrostático (figura 2.10, izquierda). Una vez que se abre la esclusa, el agua atlántica, más ligera, fluye en superficie hacia el Mediterráneo y las aguas mediterráneas, más densas, salen en profundidad hacia el Atlántico (figura 2.10, derecha). Las soluciones de intercambio se obtienen de la integración del modelo a partir de condiciones iniciales de tipo "lock-exchange"

El estado estacionario implica que la derivada parcial de cualquier propiedad del sistema respecto al tiempo tiende a ser nula, es decir, el comportamiento del flujo simulado permanece constante.

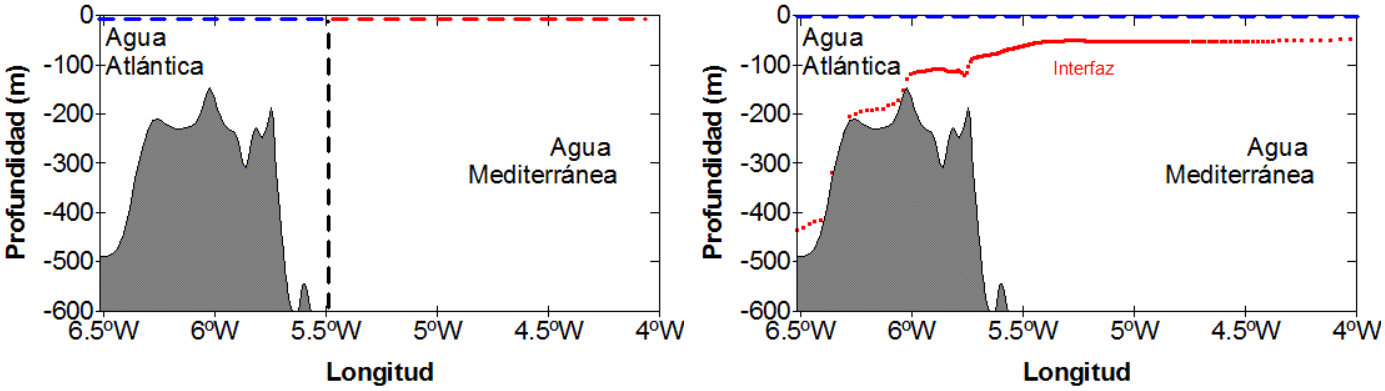

Figura 2.10.- Profundidad de la interfaz a lo largo del eje longitudinal del Estrecho en la condición inicial (izqda.) y en el estado estacionario resultante (dcha.) del experimento "lock-exchange".

A continuación, considerando esta solución estacionaria como condición inicial, se simulan los efectos de la marea mediante la prescripción, en los nodos de malla de los contornos abiertos, de la elevación de la superficie a partir de las fases y amplitudes de las principales constituyentes de marea (M_2, S_2, K_1 y O_1), derivados por interpolación de la solución del modelo global de mareas FES95.2 de 0.5º (Le Provost *et al.*, 1998) y estaciones mareográficas costeras, sobreimpuesta a la sobreelevación obtenida en la solución estacionaria.

Para evitar la reflexión en los contornos abiertos de las ondas generadas en el interior del dominio, se emplean condiciones de radiación para los transportes de las capas superior e inferior, prescribiendo como niveles de referencia para los desplazamientos de la superficie y para la profundidad de la interfaz la solución del modelo estacionario (Sein *et al.*, 1998).

Las condiciones de contornos abiertos vienen dadas por la siguiente expresión para el modo barotrópico:

$$(h_1\boldsymbol{u_1} + h_2\boldsymbol{u_2} - H\boldsymbol{u}) \cdot \boldsymbol{n} = \pm(gH)^{\frac{1}{2}}\left(\zeta_1 - \sum_{i=1}^{N} A_i \cos(\sigma_i t - \varphi_i)\right); \quad \textbf{(2.14)}$$

donde $\boldsymbol{u}$ es el vector velocidad promediado verticalmente en profundidad, ζ_1 es la sobreelevación obtenida en la solución estacionaria, A_i y φ_i son las amplitudes de la elevación de la superficie y la fase del i constituyente de marea; σ_i es su frecuencia; N

es el número de constituyentes armónicos utilizados para incluir el forzamiento de marea (cuatro, en este caso).

Para el modo baroclino:

$$(\boldsymbol{u_1} - \boldsymbol{u_2}) \cdot \boldsymbol{n} = \pm (g'H')^{\frac{1}{2}} (\zeta_2 - h_1 - (h_2/H)\zeta_1) \quad \textbf{(2.15)}$$

, donde $H' = (h_1 h_2)/H$ es un equivalente a la profundidad de la interfaz; g' es la gravedad reducida; $\boldsymbol{n}$ es el vector unitario perpendicular al contorno abierto.

El modelo hidrodinámico forzado con marea necesita un tiempo mínimo de ejecución de 30 ciclos semidiurnos de marea (360 horas) para alcanzar una solución periódica estable.

En los contornos cerrados o sólidos ($\partial\Omega_1$), se impone la condición de impenetrabilidad en la forma de libre deslizamiento ("free-slip"). Estas condiciones implican que la velocidad normal a la frontera sea nula y la derivada normal de la velocidad tangencial también se anule.

$$\boldsymbol{u} \cdot \boldsymbol{n}|_{\partial\Omega_1} = 0 \quad \textbf{(2.16)}$$

En el fondo oceánico, la tensión por la fricción de la capa inferior con el fondo se trata como una aproximación cuadrática, proporcional a la velocidad, en la que el coeficiente de fricción c_2, parametriza la tasa de conversión de energía cinética en calorífica:

$$\boldsymbol{\tau_2} = \rho_2 \cdot C_2 \cdot \boldsymbol{u_2} \cdot |\boldsymbol{u_2}| \quad \textbf{(2.17)}$$

Del mismo modo, la capa de agua inferior es afectada por el movimiento de la capa superior, dando lugar a la tensión por la fricción interfacial, cuya formulación también sigue la ley cuadrática:

$$\boldsymbol{\tau_1} = \rho_1 \cdot C_1 \cdot (\boldsymbol{u_1} - \boldsymbol{u_2}) \cdot |\boldsymbol{u_1} - \boldsymbol{u_2}| \quad \textbf{(2.18)}$$

La viscosidad horizontal, incluida en el modelo hidrodinámico mediante un valor constante de $1.5 \cdot 10^{-4}$ $m^2 \cdot s^{-1}$, aporta estabilidad al modelo evitando, al mismo tiempo, una excesiva alteración de la dinámica de los procesos estudiados.

2.2.2. Configuración del modelo hidrodinámico UCA2.5D

La configuración utilizada, como modelo de predicción de marea, utiliza valores de densidad para las capas superior (agua atlántica) e inferior (agua mediterránea de salida) que fueron especificados en 1027 y 1029 $kg \cdot m^{-3}$, respectivamente. Los valores prescritos durante experimentos de forzamiento de marea, para los parámetros de fricción interfacial, fricción por fondo y de viscosidad horizontal, fueron $1.5 \cdot 10^{-3}$, $1 \cdot 10^{-2}$

y $1.5 \cdot 10^{-4}$ $cm^2 \cdot s^{-1}$, respectivamente. El tiempo de integración estaba establecido en 3 s para el forzamiento de marea. Esta serie de parámetros han sido modificados, como resultado de los experimentos de sensibilidad llevados a cabo para la calibración del modelo forzado atmósfera-océano y que se exponen al final de este punto.

2.2.3. Validación del modelo hidrodinámico UCA2.5D

Este modelo ha sido validado previamente para diferentes aplicaciones (Sein *et al.*, 1998; Izquierdo *et al.*, 2001; Brandt *et al.*, 2004), permitiendo reproducir fielmente las principales características de la circulación del Estrecho de Gibraltar, con un coste computacional netamente inferior al de un modelo tridimensional basado en ecuaciones primitivas.

Los resultados del modelo hidrodinámico predicen la variabilidad temporal de los controles hidráulicos y su localización sobre los Umbrales de Espartel y Camarinal y en la constricción de Tarifa Narrows (Izquierdo *et al.*, 2001; Brandt *et al.*, 2004). Aún más allá, también predice que los controles, denominados "aparentes", que se establecen sobre Espartel y en Tarifa no se extienden a lo ancho del Estrecho y que, por lo tanto, no proveen un bloqueo eficiente y no pueden determinar la tasa de intercambio (Izquierdo *et al.*, 2001).

El modelo también reproduce la activación/inhibición de los controles hidráulicos a lo largo de un ciclo semidiurno de marea y la concurrencia o la pérdida conjunta de los controles sobre el Umbral de Camarinal y en la parte central de Tarifa Narrows (TN). Estos resultados muestran los distintos regímenes de intercambio baroclino existentes en la zona, de acuerdo con Armi & Farmer (1986), Farmer & Armi (1986) y Garrett *et al.* (1990a): máximo, cuando existen ambos controles, y submáximo, cuando el flujo queda controlado únicamente en el Umbral de Camarinal.

Por otro lado, el modelo simula la generación de los bores internos debido a la interacción de la marea semidiurna barotrópica con la batimetría, concretamente en el Umbral de Camarinal. La propagación del bore hacia el este, como ondas internas de gran amplitud, ha sido validado frente a imágenes SAR ERS-1 por Izquierdo *et al.* (2001) y Sein *et al.* (1998).

La señal semidiurna de la onda de marea, su desigualdad diurna y la variabilidad quincenal también es predicha con precisión por el modelo. La velocidad longitudinal en el Estrecho ha sido validada frente a medidas de una línea de correntímetros localizados en mitad del canal en la entrada oriental del Estrecho fondeados durante el

proyecto CANIGO (Candela *et al.*, 1990; García-Lafuente *et al.*, 2000). La comparación de las series temporales de corriente de la capa superior muestra que, en general, el modelo subestima las amplitudes observadas, aunque la variabilidad es muy similar. La concordancia entre resultados del modelo y observaciones es mayor en la capa inferior (Brandt *et al.*, 2004).

Del mismo modo, el régimen de corrientes simuladas ha sido comparado con los resultados del modelo inverso de marea de Bascheck *et al.* (2001) por Brandt *et al.* (2004). En este caso, las series temporales resultantes del modelo UCA2.5D muestran, en ambas capas, una sobreestimación de las amplitudes simuladas por el modelo inverso.

La profundidad de la interfaz simulada por el modelo UCA2.5D es significativamente más somera que la observada (Brandt *et al.*, 2004) al no estar considerados los procesos de mezcla.

Debido a los excelentes resultados que reflejan las validaciones previas realizadas y, muy especialmente, a su bajo coste computacional, el modelo UCA2.5D ha sido seleccionado para constituir el módulo oceánico del modelo forzado por viento.

2.3. Modelo oceánico forzado por viento

2.3.1. Introducción al modelo oceánico forzado por viento

El campo de viento, simulado por el modelo meteorológico de mesoescala MM5, representa el forzamiento atmosférico del modelo hidrodinámico. Las componentes horizontales del viento simulado a 10 m de altura, traducidas en forma de tensión tangencial, se interpolan linealmente en el tiempo y bilinealmente en el espacio, desde la malla del dominio MM5-10 km a la malla curvilínea del modelo hidrodinámico.

La tensión tangencial impuesta por el viento en la superficie ($\boldsymbol{\tau_s}$) actúa como término de fricción sobre el flujo en las ecuaciones de *momentum*, estando relacionado con la velocidad del viento por la ley cuadrática con un coeficiente de transferencia (C_d):

$$\boldsymbol{\tau_s} = \rho_0 \cdot C_d \cdot (\mathbf{W} - \boldsymbol{u_1}) \cdot |\mathbf{W} - \boldsymbol{u_1}|; \qquad \textbf{(2.19)}$$

donde ρ_0 es la densidad del aire, y C_d es el coeficiente adimensional de arrastre debido a la velocidad del viento $\boldsymbol{W}$.

Al añadir la tensión tangencial del viento, en el segundo término de la ecuación de *momentum* para la capa superior (2.10), en términos de transporte, quedaría como sigue:

$$\frac{\partial(h_1\boldsymbol{u_1})}{\partial \mathrm{t}} + \nabla \cdot h_1\boldsymbol{u}_1\boldsymbol{u}_1 + f\mathbf{k} \times h_1\boldsymbol{u}_1 + gh_1\nabla\zeta_1 = \frac{\boldsymbol{\tau_s} - \boldsymbol{\tau_1}}{\rho_1} \quad \textbf{(2.20)}$$

2.3.2. Configuración del modelo oceánico forzado por viento

Se han llevado a cabo diversas simulaciones con distintos tipos de forzamiento. Con el objetivo de determinar la respuesta de los patrones de circulación debida únicamente a la tensión tangencial del viento y, partiendo de la solución estacionaria del experimento "lock-exchange" (primera aproximación), el modelo se ejecutó forzado con un campo constante y espacialmente homogéneo de viento (figura 2.11). Considerando las direcciones predominantes del viento en el Estrecho, las simulaciones se llevaron a cabo con campos de vientos de levante (identificados con el prefijo "E", de *easterly*) y de poniente (con el prefijo "W", de *westerly*), con una velocidad constante de 10 $m \cdot s^{-1}$. En lo sucesivo, este conjunto de experimentos serán referidos como NON-TIDE.

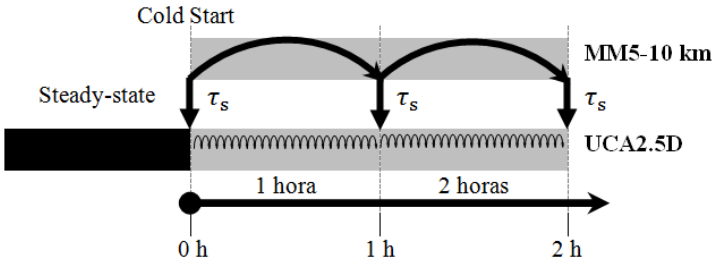

Figura 2.11.- Esquema de la ejecución del modelo oceánico forzado únicamente por viento para los experimentos NON-TIDE. El término "cold start"[16] hace referencia al arranque en frío del modelo MM5. Los bucles representan la actualización temporal del forzamiento.

El segundo conjunto de simulaciones (experimentos TIDE), parten de la solución periódica estable de marea (denominado experimento *control*, en adelante), alcanzada después del tiempo de spin-up del modelo hidrodinámico. De esta forma, el modelo se inicializa únicamente con el forzamiento en los contornos abiertos mediante la prescripción de las amplitudes y fases de la elevación de los cuatro armónicos principales de marea y, transcurridas 360 horas (30 ciclos semidiurnos de marea), se introduce el forzamiento de viento (figura 2.12).

[16] Para el arranque en frío se utiliza el análisis del modelo global, para poner en marcha el modelo de mesoescala y se deja que éste desarrolle gradualmente las circulaciones divergentes, los movimientos verticales y la precipitación.

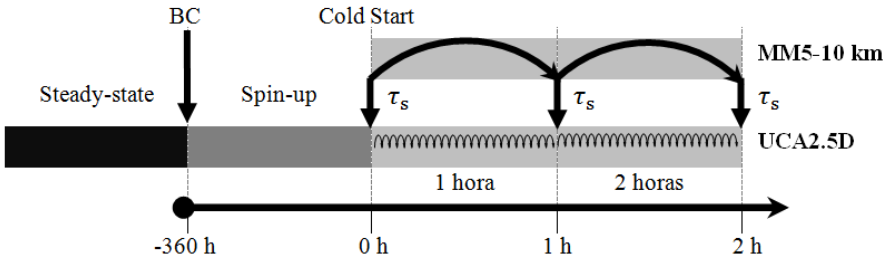

Figura 2.12.- Esquema de la ejecución del modelo oceánico forzado por marea y viento para los experimentos TIDE. BC representa el forzamiento de marea en los contornos abiertos. El término "cold start" hace referencia al arranque en frío del modelo MM5. Los bucles representan la actualización temporal del forzamiento.

En este caso, para evaluar el efecto conjunto del forzamiento de marea con el de viento, el modelo se fuerza con los campos constantes y espacialmente homogéneos de viento de levante y de poniente, como en los experimentos anteriores.

La simulación más realista consiste en forzar el modelo hidrodinámico con el campo de viento variable obtenido de la ejecución del modelo meteorológico MM5-10 km, en el denominado experimento TIDE-WIND.

Los experimentos anteriormente mencionados se resumen en la figura 2.13.

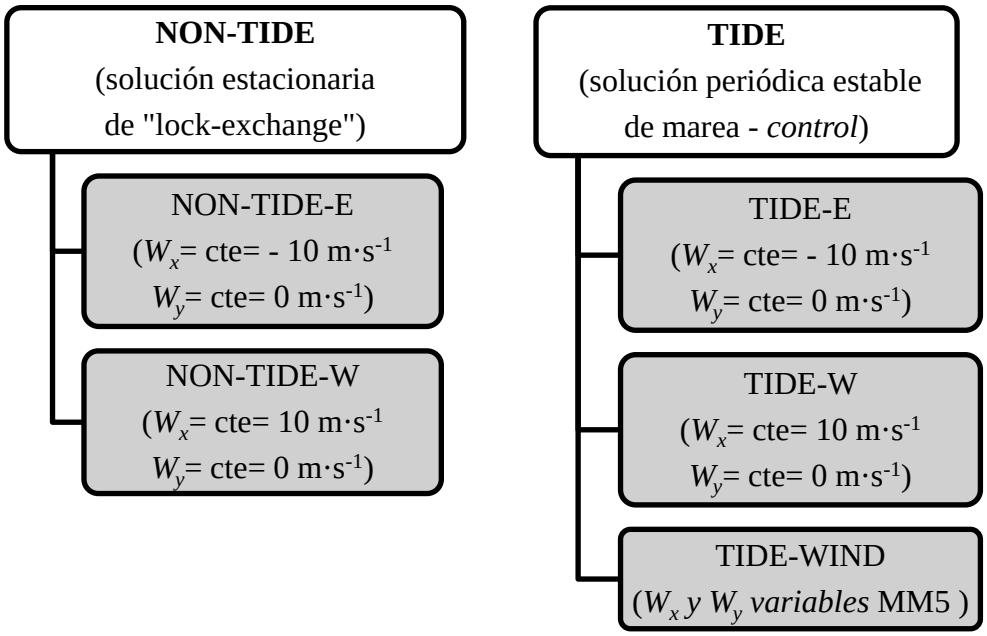

Figura 2.13.- Esquema resumen de los experimentos realizados con el modelo oceánico forzado por viento.

La introducción del forzamiento atmosférico al modelo hidrodinámico originó inestabilidades numéricas derivadas de la configuración de la malla en determinadas zonas, de las especificaciones de las condiciones de contorno, y del tiempo de integración.

En la figura 2.14 se muestra un ejemplo de las inestabilidades surgidas en el nivel del mar cerca de la península de Ceuta, donde la curvatura de la malla es mayor, es decir, donde la suavidad de la malla curvilínea es menor y la pérdida de ortogonalidad es mayor. Estas inestabilidades del nivel del mar causaron, consecuentemente, inestabilidades en el flujo de la capa superior.

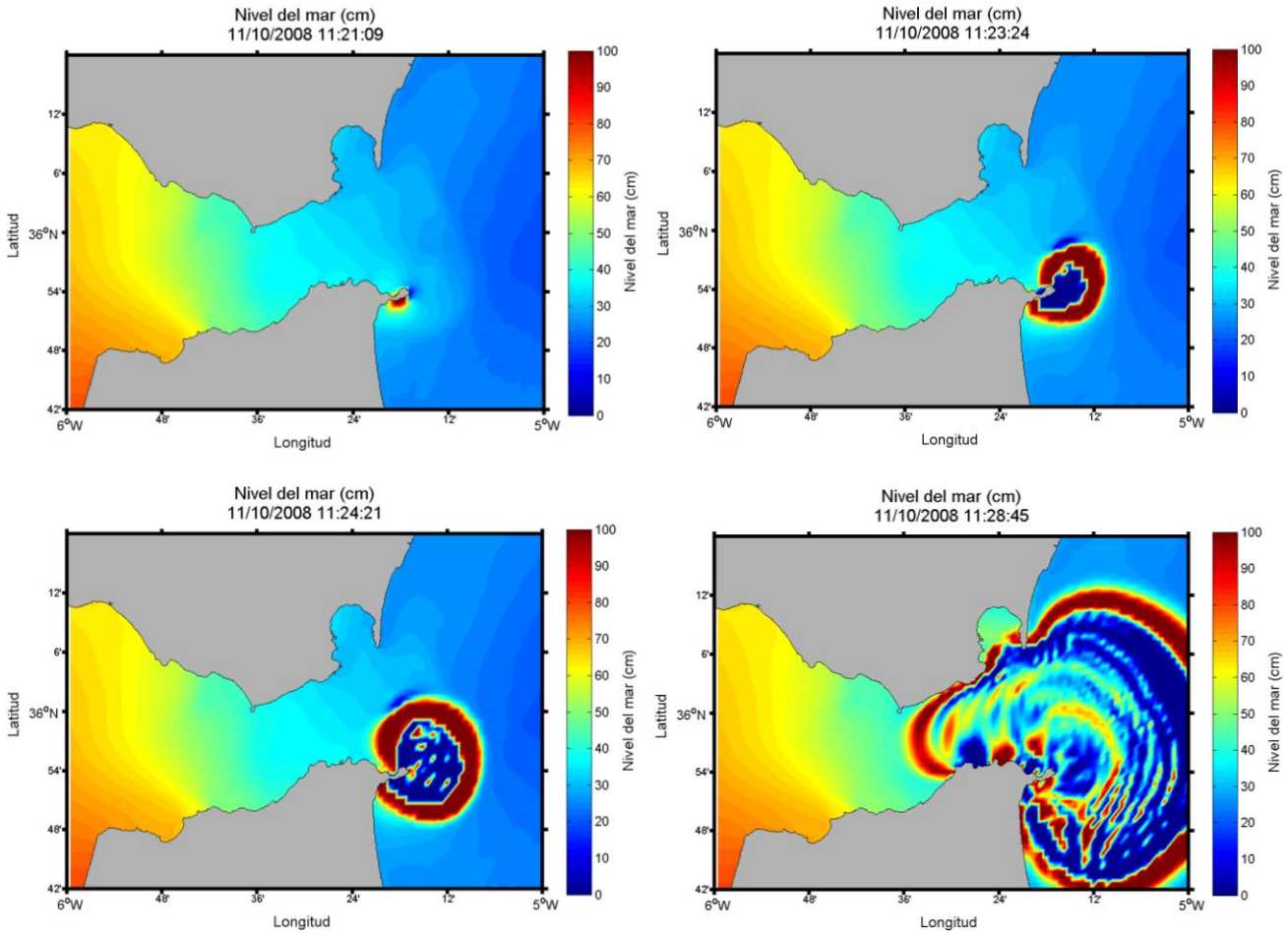

Figura 2.14.- Inestabilidades en el nivel del mar por pérdida de ortogonalidad de la malla.

Primero para garantizar la estabilidad numérica del modelo forzado atmósfera-océano y, segundo, para ajustar los resultados a las observaciones y, de paso, investigar la sensibilidad de la dinámica simulada en el Estrecho frente a cambios en los parámetros del modelo, se realizaron varios experimentos de sensibilidad numérica con diversos valores de los coeficientes de fricción de fondo, fricción interfacial y distintos pasos de tiempo de integración. En la tabla 2.10 se presentan los parámetros modificados y el rango de valores utilizados durante los experimentos de sensibilidad numérica.

Tabla 2.10.- Parámetros utilizados en los experimentos de sensibilidad numérica. En negrita se señalan los valores escogidos para el modelo oceánico forzado por viento.

Parámetros	Rango de valor de los parámetros
Tiempo de integración (s)	0.5, 1.0, 2.0, **3.0**
Coeficiente de fricción por fondo, C_2	$1.5 \cdot 10^{-2}$, $\mathbf{1 \cdot 10^{-2}}$
Coeficiente de fricción interfacial, C_1	$\mathbf{1 \cdot 10^{-3}}$, $1.5 \cdot 10^{-3}$, $2 \cdot 10^{-3}$, $3 \cdot 10^{-3}$, $4 \cdot 10^{-3}$
Coeficiente de arrastre por viento, C_d	$1.2 \cdot 10^{-3}$, $1.8 \cdot 10^{-3}$, $\mathbf{2 \cdot 10^{-3}}$
Viscosidad horizontal ($cm^2 \cdot s^{-1}$)	$1.5 \cdot 10^{-4}$

Los resultados de los experimentos demuestran la sensibilidad del intercambio frente a variaciones de parámetros de fricción cuadráticos. Los parámetros de fricción por fondo e interfacial se modificaron considerando el primero siempre un orden de magnitud mayor que el segundo.

Lógicamente, un aumento de la fricción interfacial conlleva un aumento del intercambio de *momentum* entre las capas y, consecuentemente, el flujo de la capa superior disminuye significativamente. Las variaciones del parámetro de fricción por fondo no inducen una respuesta significativa en el flujo, en el rango de valores usado.

Una disminución del 40% del coeficiente de transferencia del viento (de $2.0 \cdot 10^{-3}$ a $1.2 \cdot 10^{-3}$) muestra la sensibilidad del flujo ante variaciones de este parámetro. Para analizar la respuesta ante la variación del coeficiente de arrastre, se ha utilizado el experimento NON-TIDE-E y se ha calculado la profundidad media de la interfaz y del nivel del mar a lo largo del período de la simulación.

Por un lado, al disminuir el coeficiente de arrastre un 40%, la interfaz permanece más somera en la parte oriental del dominio hasta el Umbral de Camarinal (figura 2.15, izquierda) y, en mayor medida, en la costa norte del Estrecho donde, por otro lado, el nivel del mar desciende (figura 2.15, derecha). Esto quiere decir que un menor coeficiente de arrastre, debilita la tensión tangencial ejercida por el viento en la superficie del océano haciendo disminuir el espesor de la capa superior. Por contra, un mayor coeficiente de arrastre hace aumentar el espesor de la capa superior (el nivel del mar se eleva y la interfaz se profundiza) respondiendo a una disminución de la velocidad de la corriente superficial dirigida hacia el Mediterráneo y al efecto de apilamiento, en la zona costera española, debido al transporte de Ekman generado por el viento de Levante.

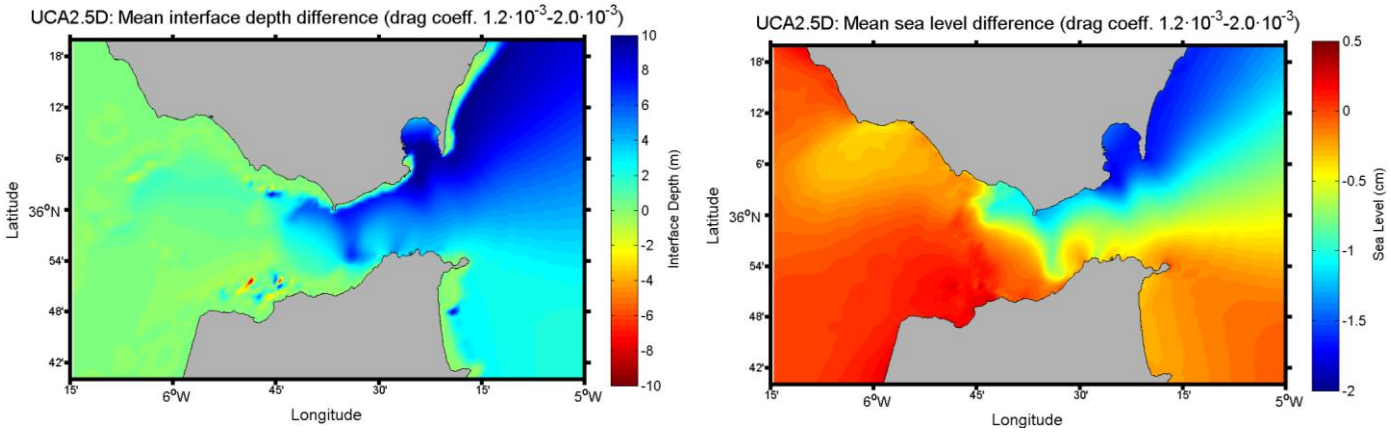

Figura 2.15.- Diferencia de la profundidad de la interfaz media (izqda.) y del nivel medio del mar (dcha.) al disminuir un 40% el coeficiente de arrastre para el experimento NON-TIDE-E.

2.3.3. Validación del modelo oceánico forzado por viento

Ante la ausencia de la formulación de protocolos normalizados de validación, conociendo que, idealmente, cada nuevo forzamiento o parametrización introducido en un modelo debe validarse frente a observaciones apropiadas, se ha llevado a cabo una comparación cualitativa de los resultados del modelo oceánico forzado por viento frente a las variables observadas.

Cada una de las variables obtenidas de los resultados del modelo ha sido validada de forma independiente.

Las salidas del experimento TIDE-WIND han sido comparadas con un mes de datos de velocidad de corriente registrados por el correntímetro mono-punto fondeado al Norte de la Meseta del Umbral de Camarinal, durante la campaña *"Gibraltar'08"*, y con un año de medidas (1995) de corriente registradas por el ADCP fondeado sobre el Umbral de Camarinal durante el experimento "*Strait 94-96"*.

Por otro lado, considerando la definición de la interfaz como la superficie de máximo gradiente del perfil vertical de la componente zonal de la velocidad (Tsimplis & Bryden, 2000), se ha calculado su profundidad a partir de los perfiles de corriente medidos por el ADCP y se ha comparado con la obtenida en el experimento TIDE-WIND.

Las profundidades de la interfaz, estimadas por el ajuste sigmoidal de los perfiles de salinidad obtenidos de las estaciones de CTD, se han comparado también con la profundidad de la interfaz simulada por el experimento TIDE-WIND en cada punto e instante.

Los patrones superficiales de circulación, obtenidos de las posiciones de las boyas de deriva, han sido comparados también con las trayectorias de boyas virtuales simuladas por el experimento TIDE-WIND.

Los datos de nivel del mar registrados por los correntímetros de Tarifa, Algeciras y Ceuta se han utilizado para obtener las diferencias de nivel del mar transversales al Estrecho y estudiar su respuesta frente a los vientos predominantes. Estas diferencias también han sido calculadas a partir de las salidas del experimento TIDE-WIND y han sido validadas frente a las observadas.

Capítulo 3

Implementation and performance assessment of the high-resolution MM5 model in the Strait of Gibraltar

Capítulo 3

IMPLEMENTATION AND PERFORMANCE ASSESSMENT OF THE HIGH-RESOLUTION MM5 MODEL IN THE STRAIT OF GIBRALTAR

The complex orography of the Gibraltar Arc, described in the first chapter, contributes to the intense local acceleration of winds within the Strait. Also, the presence of a sea-land interface and the unequal heating of air over land and water, results in land-sea breezes near the coast, mostly during the warm seasons. Inland areas are also affected by convective processes, like the mountain and valley breezes.

Several studies (McQueen *et al.*, 1995; Doyle, 1997; Ballentine *et al.*, 1998; Colle & Mass, 1998; Martin, 1998; Davis *et al.*, 1999; Rao *et al.*, 1999; Colle & Mass, 2000b, a; Leung & Qian, 2003) concluded that in such regions, where orographic flows or diurnal circulations are important and where there are sharp gradients in land surface conditions, frontal zones and other mesoscale features are better defined as grid spacing decreased below 15 km, but it does not significantly improve the synoptic evolution of fronts and cyclones. Furthermore, in such cases, model runs need to be non-hydrostatic, since the hydrostatic assumption limits the resolution to around 10 km except in weak flow and no convective situations (Dudhia, 1993) and additionally, vertical velocities can approach or even exceed horizontal velocities (over short distances).

Therefore, the implementation of a high-spatial resolution non-hydrostatic atmospheric model is critical to success in capturing the mesoscale atmospheric circulation, having horizontal scales ranging from a few to several hundred kilometres (Orlanski, 1975; American Meteorological Society., 2013), and the topographically generated weather phenomena in the Strait.

An accurate modeling of the wind circulation is a fundamental requirement for reliable computations of marine currents in the region, since surface winds are a major forcing mechanism of circulation in the coastal ocean, the main aim of this Ph-D thesis. Furthermore, surface wind field is the best parameter for evaluating the skill of a mesoscale model since wind direction is greatly modulated by the terrain and diurnal circulation.

Since the dominant response from orographically driven circulations is in the near-surface layer, a statistical evaluation of the model performance is undertaken using in-situ surface measurements from more than 100 automatic weather stations and 2 deep ocean buoys.

The chapter is divided into four main sections. Firstly, considering the validation methodology described in the Chapter 2, we make a pairwise comparison of model outputs and observations. Validation results are focused into the impact of horizontal resolution of the model, by examining the relationship between model resolution and predictive skill and the improvement on the previous model existent in the area, which has been addressed by comparing MM5 outputs with the hydrostatic grid-point HIRLAM (HIgh Resolution Limited Area Model) (Undén *et al.*, 2002). Secondly, the impact of different initial conditions has been analyzed by means of short-term operational forecast and hindcast errors study. Model performance has been characterized in terms of the temporal evolution and the spatial distribution of the errors in the third section. Finally, the model ability to correctly simulate mesoscale winds associated with sea-land breezes or mountain-valley breezes, is evaluated.

1. Impact of horizontal resolution

The important question addressed in this section is whether it is worth increasing the spatial resolution to successfully reproduce the mesoscale phenomena in the area.

In order to answer this question, we evaluated the performance of the MM5 model, run in non-hydrostatic mode, with three domains of different horizontal resolutions, against hourly observations from 5 AWS (Cádiz, Ceuta, San Fernando,

Tarifa and Vejer), shown with red squares in figure 2.1. According to the same procedure, we also assessed the accuracy of HIRLAM, a hydrostatic grid-point model developed by several European institutes (Källén, 1996; Undén *et al.*, 2002). The AEMET (Spanish Agency of Meteorology) is in charge of running HIRLAM operationally in Spain at four different set-ups. Details on the model physics can be found in (Undén *et al.*, 2002). The configuration used in this study ran operationally in 2002 over Europe and the North Atlantic Ocean with a horizontal resolution of 0.2º and 31 hybrid vertical layers and a six hour output. Assimilation of different meteorological variables available at the Global Telecommunication System (GTS) is performed. Meteorological stations of Ceuta and Cádiz are available in GTS.

To present a more comprehensive view, histograms of the MAE, RMSE, BIAS and IOA summarize the mean errors and model skills for wind speed and direction at all three resolutions for the MM5 and for HIRLAM at 5 locations for the period ranging from 20-23 August, 2004. This episode corresponds to a sudden transition from westerlies to easterlies, a very common situation within the Strait of Gibraltar, being also one "worst-case" or exigent scenario related to weather events.

Figure 3.1 shows the RMSE of the model by simulating wind speed (left) and MAE[1] for wind direction (right) at the AWS locations. On average, the MM5-10 km wind speed errors are always slightly less than those of the 30-km domain, except at Cádiz and Vejer, where values are very close. The 3.3-km domain performs better only at Ceuta and very similar to that of 10 km at Tarifa, where the wind funnels and accelerates through the nearby narrow Strait of Gibraltar.

Despite the fact that wind direction errors are nearly unchanged by increased resolution, MM5-30 km exhibits better performance at all locations, closely followed by MM5-10 km, with the 3.3-km grid generally being the least skillful.

HIRLAM 0.2° have larger errors than MM5 at all resolutions for both variables. Nevertheless, it performs better than all MM5 domains at simulating wind speed at Ceuta, where it also presents MAE values of wind direction close to that of MM5 domains. Wind speed RMSE value at Cádiz location is very similar to that of MM5-3.3 km, while the wind direction error is the largest of HIRLAM.

[1] For wind direction the MAE was chosen over RMSE because of the greater sensitivity to large difference between the model and observations (Wilks, 1995), which often occurs with wind direction, especially during light wind conditions (i.e. if the difference between the modeled and observed wind direction are 1, 10 and 100 degrees, the RMSE would be 58 degrees while the MAE is 37 degrees).

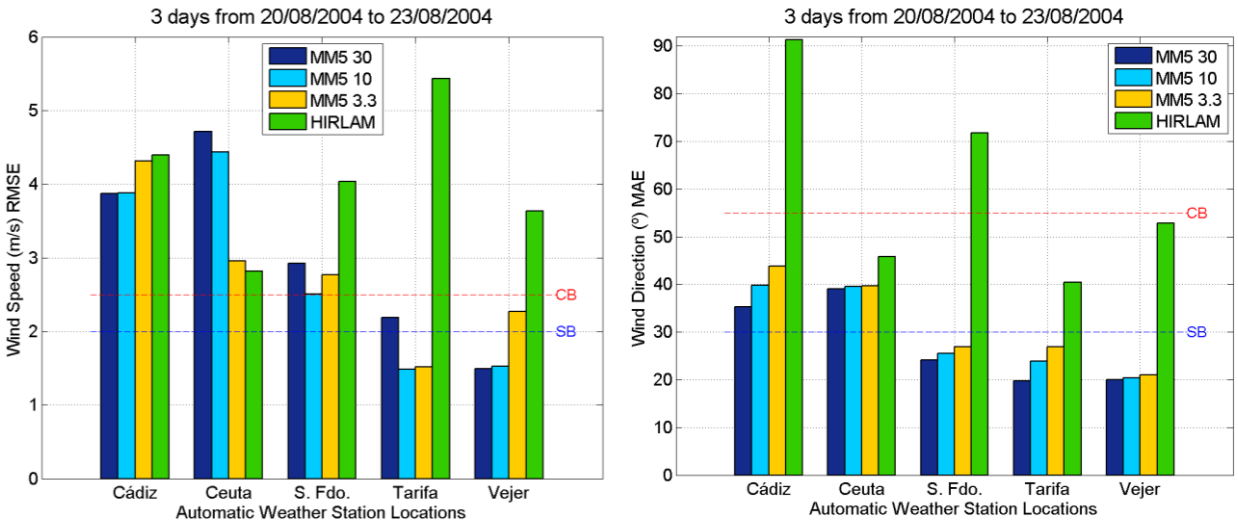

Figure 3.1.- Histogram of RMSE for wind speed (left) and MAE for wind direction (right) from three nested MM5 domains (30,10 and 3.3 km) and HIRLAM (0.2º) at 5 AWS locations. Dashed lines show the model performance benchmarks for simple (blue line) and complex (red line) conditions for each variable and parameter.

All domains of MM5 have a positive wind direction BIAS (figure 3.2, right) at all stations, except Cádiz. That means that, in general, the model wind vector is rotated anticyclonically compared to the observed. The shift to larger angles may be interpreted as underestimation of surface roughness by the model due to topography smoothing and/or inappropriate land-sea mask and land uses (Mass & Ovens, 2011). Colle *et al.* (2003) have also related the positive bias in wind direction to an excessive mixing of geostrophic momentum from aloft in the vertical. It is a characteristic for several of the MM5 boundary layer parameterizations, including the Medium-Range Forecast (MRF)[2] scheme used (Braun & Tao, 2000; Vilà-Guerau de Arellano *et al.*, 2001; Steeneveld *et al.*, 2008). The positive wind speed BIAS, at almost all stations, (figure 3.2) is also consistent with too much mixing.

Although all resolutions have reasonable biases, results of wind speed show a major improvement at 10-km grid spacing for nearly all stations, while the 30-km domain is the most skillful for wind direction. Only at that location with the highest wind intensity (Tarifa), the BIAS of the 3.3-km domain by simulating wind speed is almost inexistent. HIRLAM tends to rotates the wind vector cyclonically (negative BIAS) from the observed, except at Tarifa and Ceuta, where it shows the lowest positive BIAS for wind direction and also for wind speed at the later.

[2] The MRF PBL scheme is a first-order, nonlocal scheme in which the eddy diffusivity is parameterized using mean variables and boundary layer depths determined from wind shear and stability.

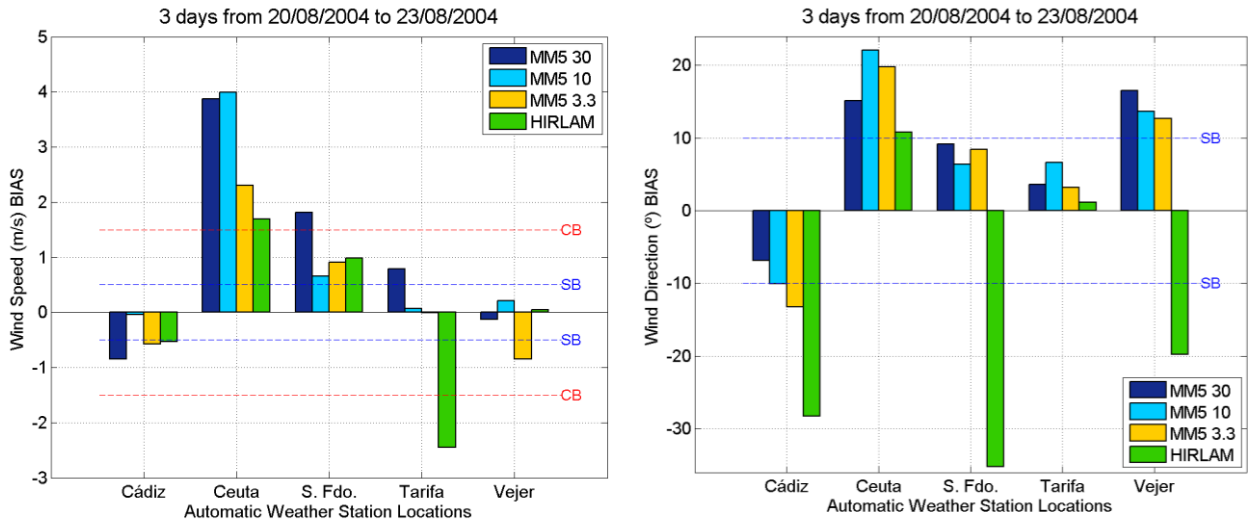

Figure 3.2.- Biases from the MM5 at 30, 10 and 3.3 km and from HIRLAM *versus* observations from 5 automatic weather stations for wind speed (left) and wind direction (right). Dashed lines show the model performance benchmarks for simple (blue line) and complex (red line) conditions for each variable and parameter.

Overall, we found a slight improvement in wind speed prediction skill, by means of the Index of Agreement[3] analysis, (figure 3.3, left) from 30 to 10 km resolution, except at Cádiz and S. Fdo. In contrast, going from 10-km to 3.3-km grid spacing does not improve the model performance, neither wind speed nor wind direction (figure 3.3, right), according to IOA.

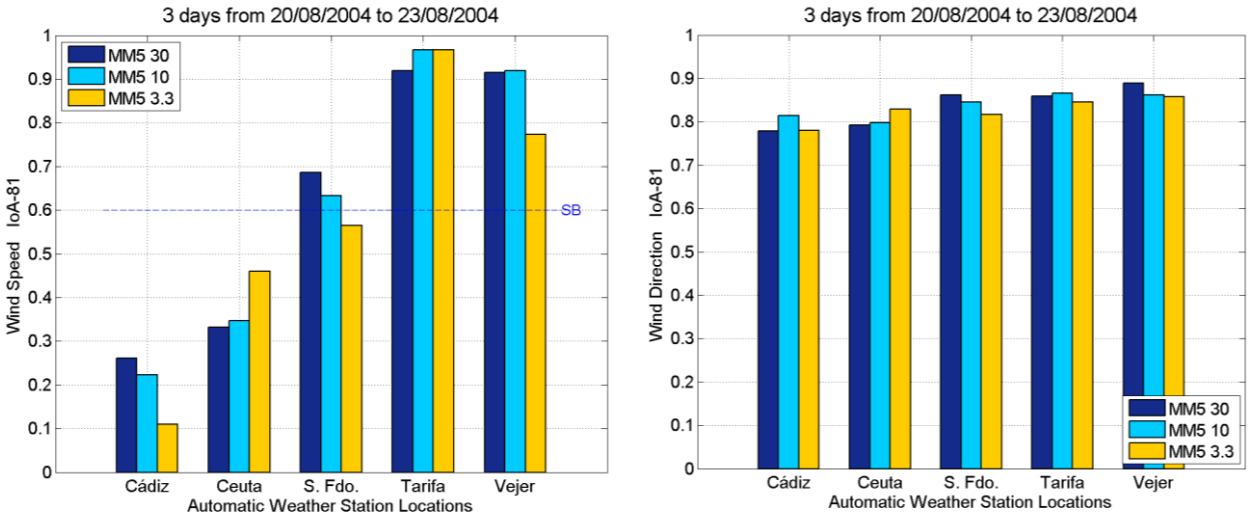

Figure 3.3.- Index of Agreement from the MM5 at 30, 10 and 3.3 km *versus* observations from 5 automatic weather stations for wind speed (left) and wind direction (right). Dashed blue line shows the model performance simple benchmark for wind speed IOA.

[3] It is recalled that the Index of Agreement is a positively-oriented metric (the highest value, the best) and that a computed value of 1.0 indicates perfect agreement between the observed and predicted observations.

Bearing in mind that the main objective of the atmospheric model implementation is to provide the wind forcing to the ocean model, the performance of the MM5 model domains (MM5-30 km and MM5-10 km), covering the deep buoy locations (shown with dark blue circles in figure 2.1), has also been assessed over the water. Wind field simulated by MM5-30 km and MM5-10 km and measured from the deep buoys has been compared, over the whole available period of observations (from the 15th of September to the 12th of October, 2008), characterized by strong atmospheric perturbations due to the passage of consecutive cyclones, which induced sudden and strong changes in wind speed and direction.

At both buoy locations, increasing the model resolution from 30 km to 10 km does improved the wind speed prediction, by means of the Index of Agreement (figure 3.4, left). The MM5-10 km better solved the wind direction measured by the buoy at cabo de Gata, while the coarse domain (MM5-30 km) performs slightly better at golfo de Cádiz buoy location.

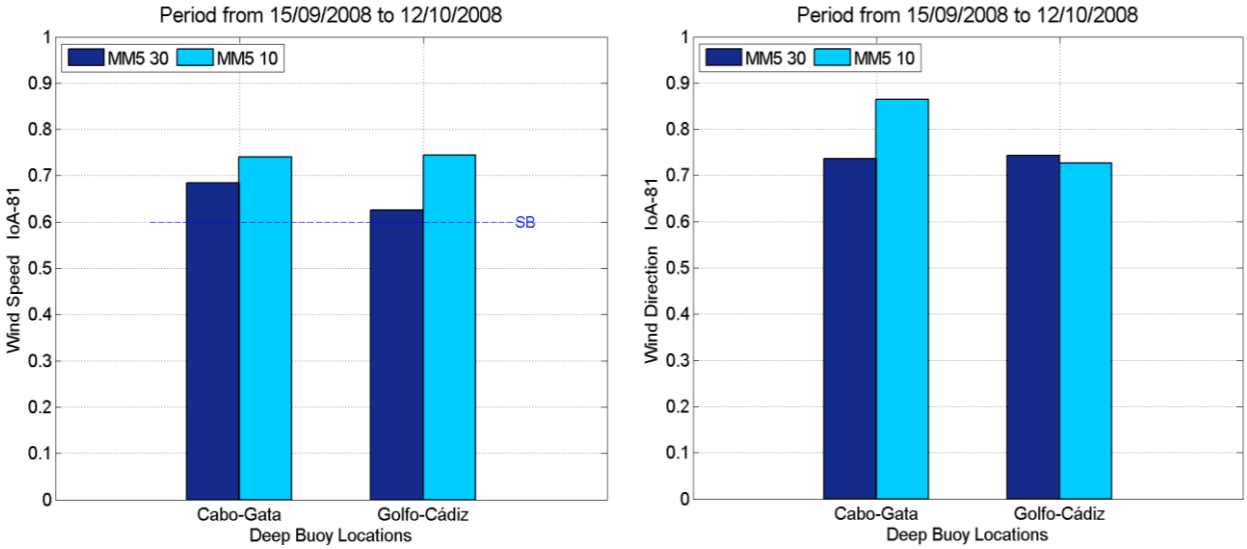

Figure 3.4.-Index of Agreement for wind speed (left) and for wind direction (right) from MM5-30 km and MM5-10 km at 2 deep buoy locations. Dashed blue line shows the model performance simple benchmark for wind speed IOA.

Considering the overall statistics, we can conclude that the MM5-10 km shows slightly better scores for wind field than the MM5-30 km, but there is no improvement from 10 to 3.3 km. This is likely due to the fact that MM5 produces more stochastic variations at finer resolution, which, on another hand, it requires a higher level of exigency on surface information (land uses, topography accuracy, etc), which unfortunately is not available and that result in more disagreement with observations. Actually, one has to expect that an optimal implementation of the MM5 model (using

the optimum combination of physical parameterizations and a more detailed physiographic properties), which is beyond the scope of this work, would improve MM5 predictions due to higher model resolution, especially in mountainous areas where features depending on topography are better described and at coastal stations, due to the improved of ground surface parameterization parameters (land fraction, soil type or roughness length).

Regarding the improvement of the MM5 on the previous model existent in the area, HIRLAM, results of figure 3.5 show a poor performance of the later as compared to MM5-10 km. The main differences between MM5 and HIRLAM, beside physics parameterizations, could be due to the fact that MM5 is a non-hydrostatic model and HIRLAM a hydrostatic one. The higher skill of HIRLAM in reproducing wind speed in Cádiz and, particularly, at Ceuta is due to the assimilation of meteorological variables from these stations, available at the GTS.

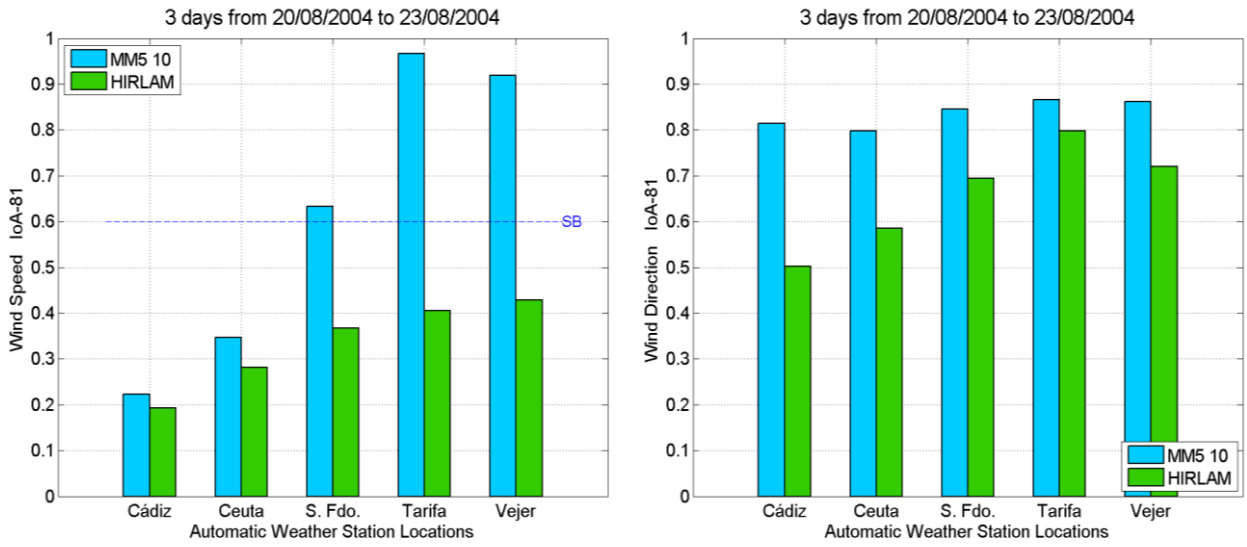

Figure 3.5.- Index of Agreement from the MM5-10 km and HIRLAM *versus* observations from 5 automatic weather stations for wind speed (left) and wind direction (right). Dashed blue line shows the model performance simple benchmark for wind speed IOA.

2. Influence of initial and boundary conditions

Based on previous results, considering that the MM5-10 km has better wind field skill than the other resolutions and with the aim to reduce interpolation errors, which worsen as the grid coarsens, between the atmospheric and ocean model grids, the MM5-10 km will be used to provide the meteorological forcing to the ocean model (~ 1 km nominal spatial resolution).

Furthermore, the MM5-10 km model is being used for operational short-range regional weather forecasting, so then, we found it necessary to evaluate the performance for both hindcast and forecast (hereinafter referred as MM5H and MM5F, respectively) in sea level pressure, surface wind speed and direction and surface temperature.

Simulations were done for one month from September 15-October 12, 2008, a period when the "*Gibraltar'08*" extensive oceanographic survey cruise over the Strait of Gibraltar took place. MM5-10 km wind field output for this period, was used to force the ocean model (results are available in the Chapter 4).

Model performance was assessed using hourly data from two deep buoys and daily observations at seven coastal meteorological stations (from AEMET) were used (dark blue and green circles of figure 2.1, respectively).

2.1. Model versus buoy measurements

Figure 3.6 and figure 3.7 show comparison of time series of observations and simulations for both, hindcast (MM5H) and forecast (MM5F).

The model reproduces the sea level pressure variations at both locations (figure 3.6 and figure 3.7, top), as well as its semidiurnal variability, related to gravitational and thermal tides in the atmosphere (Lindzen, 1967; Hamilton, 1981).

Simulated wind speed and direction closely follow the observations. Nevertheless, the maximum wind speeds are overestimated by the model along the analyzed period, particularly for the forecast experiment at cabo de Gata location (figure 3.6, middle). However, hindcast run shows unrealistic spikes in wind speed the 9th of October, attributable to lateral boundary interpolation problem, which is related to an inconsistency between the domains due to the impacts of strong frontal system (large baric gradient induced by the cyclone passage) moving from the coarse-resolution model into a finer-resolution model domain. The presence of these outliers leads to substantial distortions of statistic estimates.

The variability of wind direction is well reproduced by the model, with better fit in cabo de Gata buoy location, where winds are more channelled. Special attention must be paid to the transition periods between the two predominant wind directions and the development of sea-land breezes at golfo de Cádiz buoy location (figure 3.7, bottom, grey shaded areas: 15-19,23, 26-28 September, 1, 5-7 October), when the synoptic winds are very weak, which are also properly reproduced by both runs.

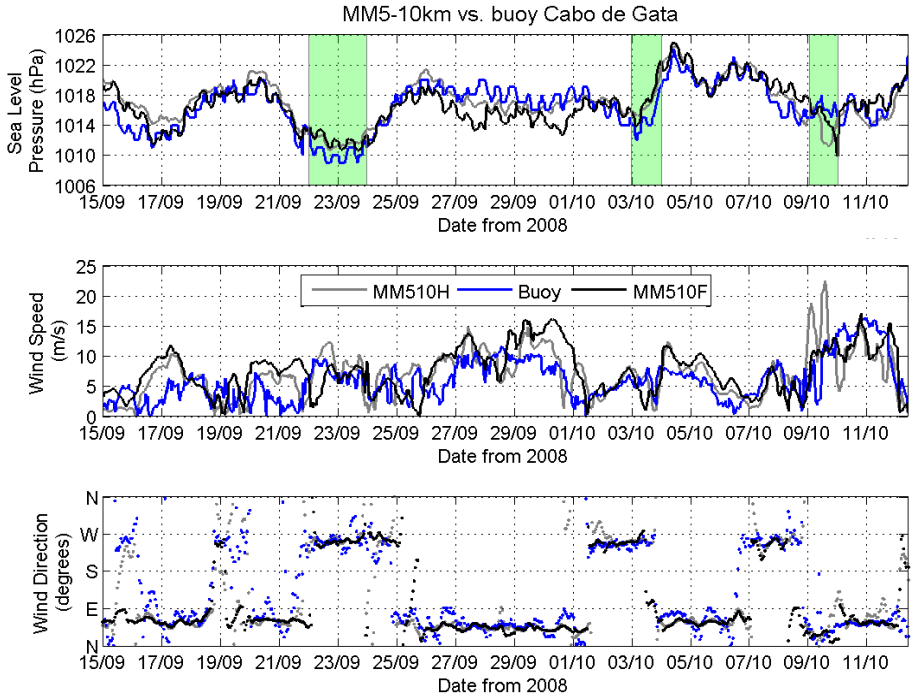

Figure 3.6.- Time-series of observed (blue lines and dots), MM5H (grey lines and dots) and MM5F (black lines and points) hourly sea level pressure (top), wind speed (middle) and wind direction (bottom) at buoy location of cabo de Gata for September and October 2008. Green shaded areas correspond to periods with negative sea level pressure differences between cabo de Gata and golfo de Cádiz.

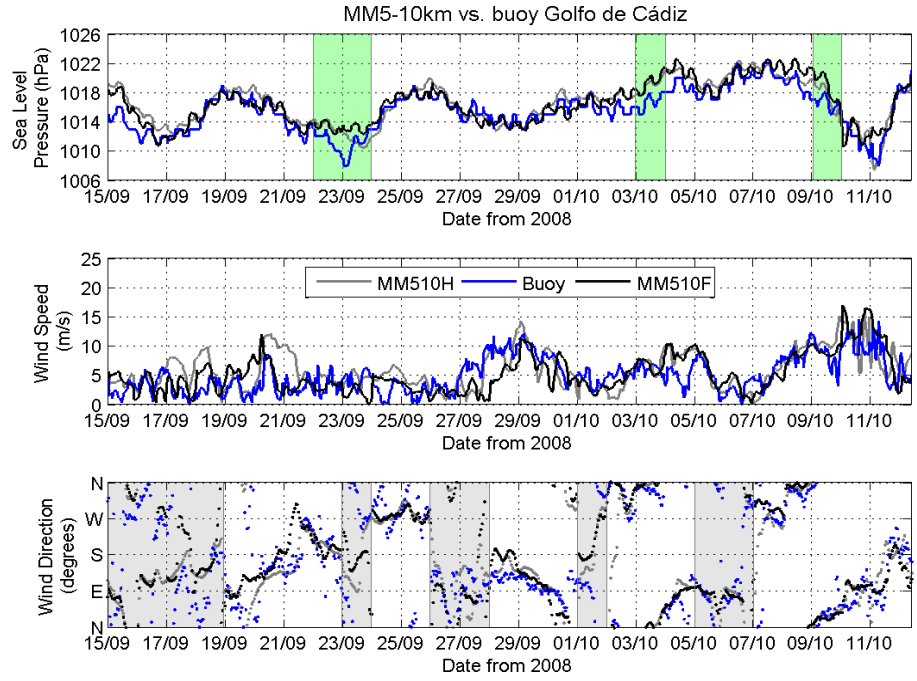

Figure 3.7.-Time-series of observed (blue lines and dots), MM5H (grey lines and dots) and MM5F (black lines and points) hourly sea level pressure (top), wind speed (middle) and wind direction (bottom) at buoy location of golfo de Cádiz for September and October 2008. Green shaded areas correspond to periods with negative sea level pressure differences between cabo de Gata and golfo de Cádiz. Grey shaded bars correspond to sea-land breeze events mentioned in the text.

Sea level pressure changes in phase at both locations with higher values at cabo de Gata, with the exceptions of 3 events (from 22 to 24 September, on 3 and on 9 October, shown as green shaded bars in figure 3.6 and figure 3.7). Particularly remarkable are these two last episodes in October, which correspond to two consecutive cyclones crossing the Strait westward, inducing intense winds within the Strait (figure 3.8).

The first cyclone (the 3rd of October) was affecting the western Alboran Sea and it weakened over the Strait, without reaching however the golfo de Cádiz buoy location.

The second cyclone (the 9th of October) took more than 72 hours to cross from Cape of Gata to the Gulf of Cádiz, resulting in a 5 mb sea level pressure difference down the strait and the consequent surface flow acceleration.

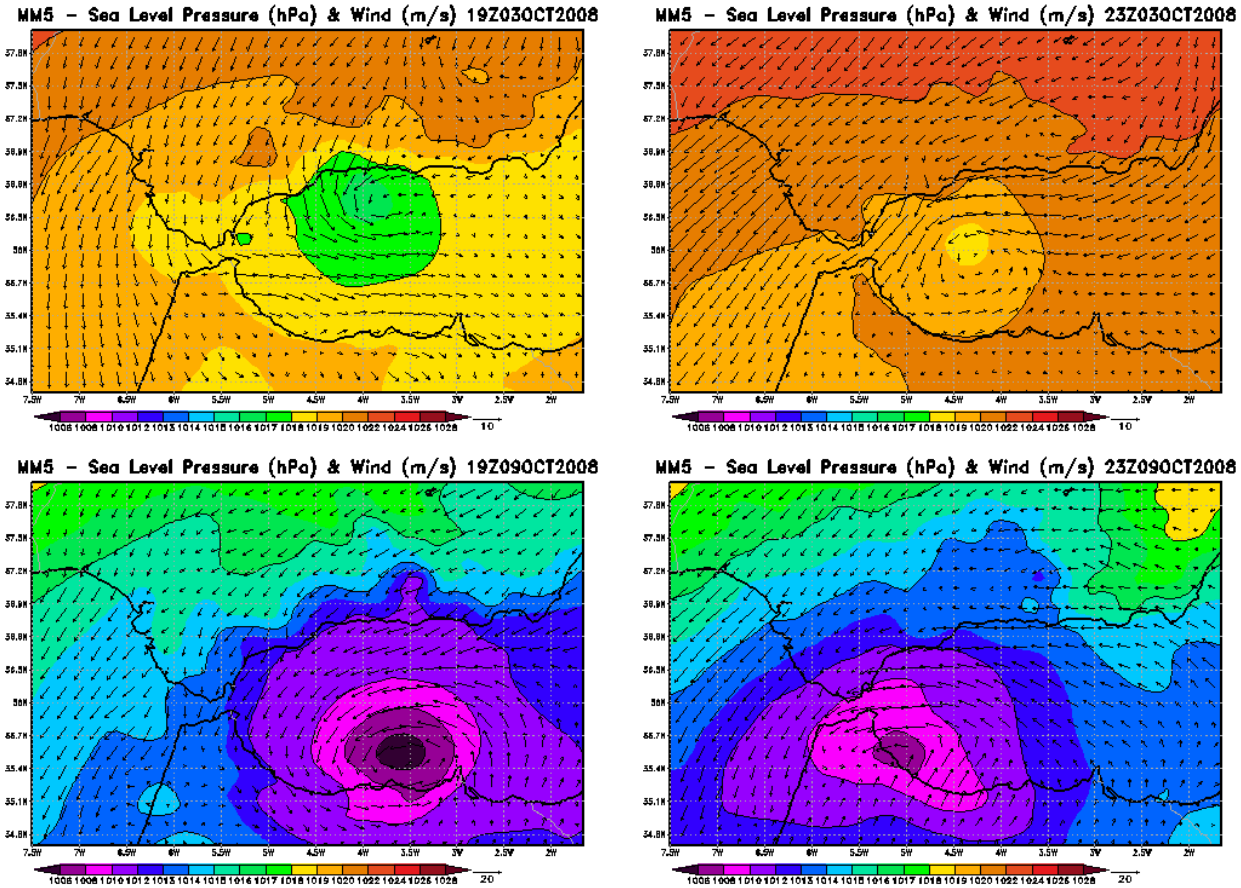

Figure 3.8.- Sea level pressure and wind vectors at 10 m simulated by MM5 (10 km) corresponding to two westward cyclone episodes on October 3 (top) and on October 9, 2008 (bottom) at 1900 UTC (left) and at 2300 UTC (right). Wind speed scale is indicated at the bottom right.

The fluctuations in the pressure difference (figure 3.9), associated to strong events, are well predicted by the model with respect to both timing and pressure magnitude, for the hindcast and forecast runs. Despite the fact that both simulations

underestimate the highest sea level pressure differences down the Strait (BIAS values of -0.4 mb and -0.79 mb for MM5H and MM5F, respectively), results from hindcast run are slightly better (RMSE vales of 1.49 mb and 1.68 mb for MM5H and MM5F, respectively).

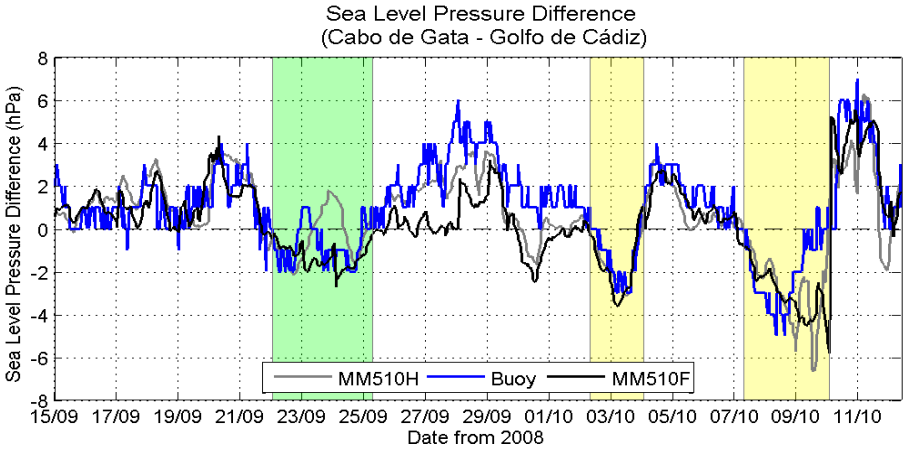

Figure 3.9.- Sea level pressure differences between cabo de Gata and golfo de Cádiz buoy locations measured by the buoys (blue line), simulated in the hindcast run (grey line) and in the forecast experiment (black line). Green and yellow shaded areas correspond to periods with negative sea level pressure differences between cabo de Gata and golfo de Cádiz. Yellow shaded bars indicate the periods of the cyclones crossing the Strait westward.

Sea level pressure differences were in phase with changes in wind speed (figure 3.10). The rapid decrease in the along-strait pressure difference, over 5 mb from 0600 UTC on October 7 to 0600 UTC on October 8 corresponded well with a further intensification of the westerlies up to 12 $m \cdot s^{-1}$ in the golfo de Cádiz (at the end of the day on October 8). Just one day after the cyclone, the sea level pressure difference raised to 6 mb and the induced easterly wind blew over 16 $m \cdot s^{-1}$ in the cabo de Gata (at 0600 UTC on October 10). In the next chapter, the ocean response due to the passage of the cyclone, which triggers strong easterly winds within the Strait of Gibraltar, is reviewed and simulated using a wind-forced ocean model.

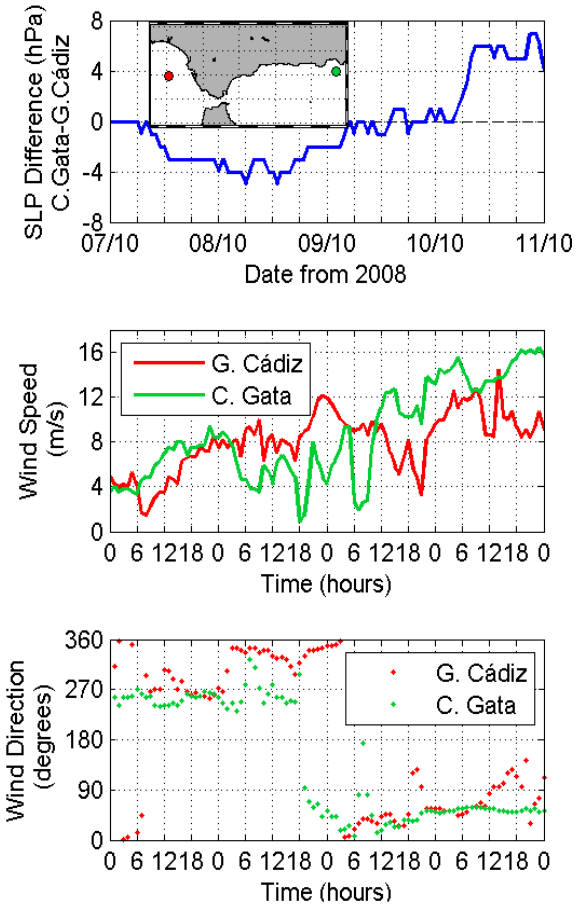

Figure 3.10.- Sea level pressure differences between cabo de Gata and golfo de Cádiz locations (top), wind speed (middle) and wind direction (bottom) registered by buoys over the second cyclone episode, between the 7th and 9th of October 2008.

For a better visualization of the prevailing wind patterns for these locations, wind roses of observed and simulated winds, for hindcast and forecast cases, are shown in figure 3.11 and figure 3.12.

At cabo de Gata buoy, results show a model overestimation of the occurrence of the prevailing northeasterly winds (figure 3.11), which is also indicated by the positive BIAS of wind speed (table 3.1), probably due to an incorrect wind funnelling by oversmoothed model orography. At the same time, results illustrate the tendency for the direction of the MM5 winds to be cyclonically rotated from the observed, it is said, the model tends to be more North-Northeasterly and more South-Southwesterly (as shown by the negative BIAS of wind direction in table 3.1). Hindcast experiment shows better results.

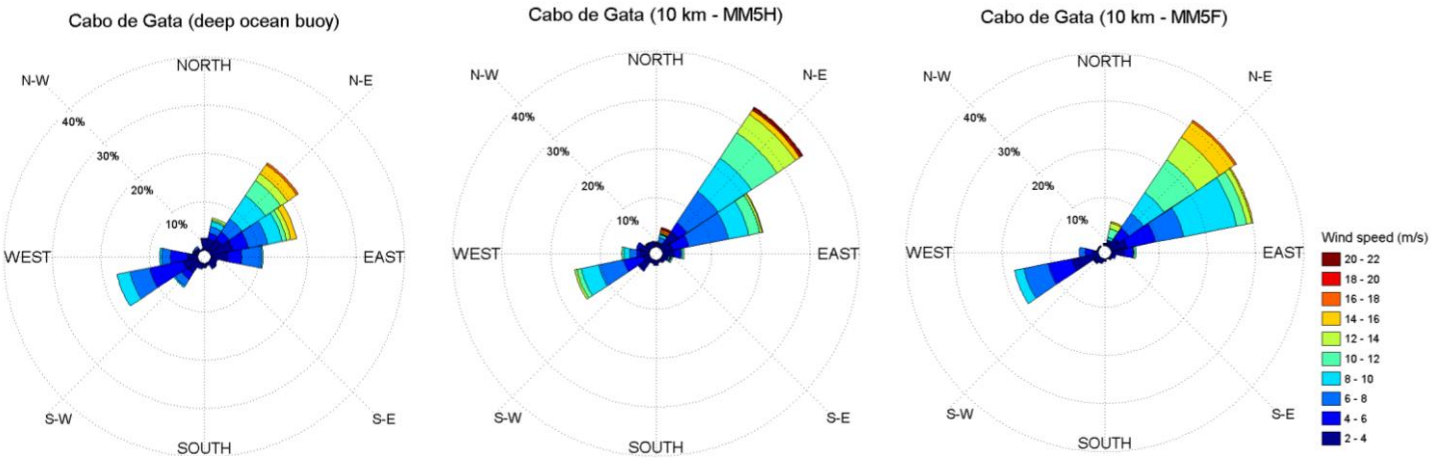

Figure 3.11.- Wind roses for the period under study at cabo de Gata location, based on observations (left), on MM5H and MM5F (right) experiments.

Although the model is able to capture the high variability of the wind flow at the golfo de Cádiz location (figure 3.12), it overestimates the occurrence and the intensity of easterly and southeasterly winds while it underestimates prevailing winds from north-northwest. This difference is even higher in the case of hindcast experiment.

Northeasterly winds, channelled along the Guadalquivir valley axis, are also measured by the buoy and simulated by the model.

In the forecast experiment, winds from the north and from the south appear also as prevailing winds. This could actually be due to small uncertainties in the larger spatial scales, introduced throughout the boundary conditions (Paegle *et al.*, 1997), which have a significant impact on isolated events (see time series of figure 3.7, bottom).

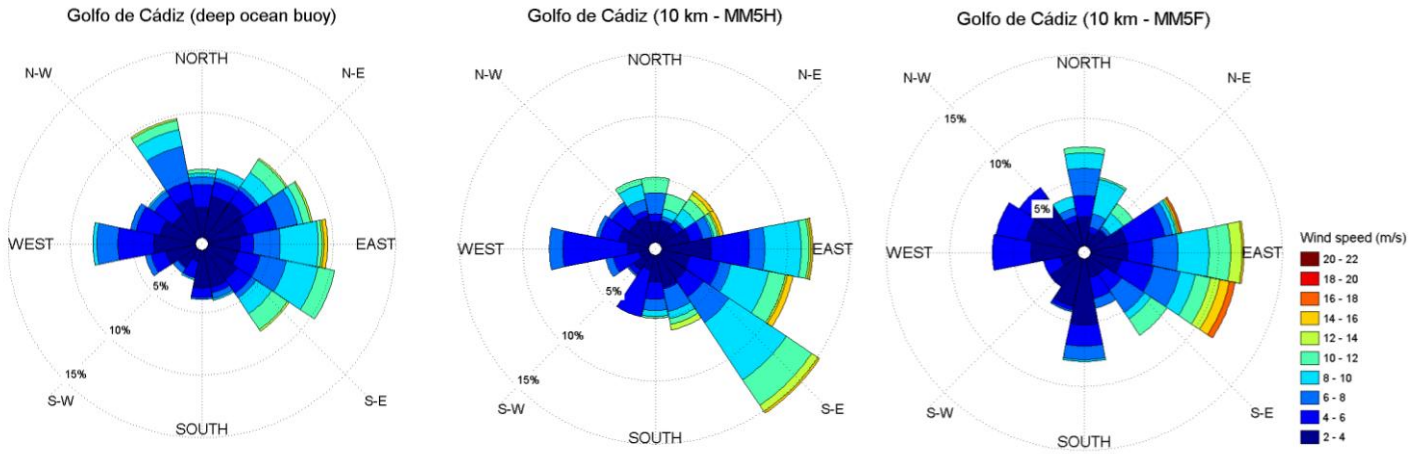

Figure 3.12.- Wind roses for the period under study at golfo de Cádiz location, based on observations (left), on MM5 (middle) and MM5F (right) experiments.

Reliability of the model by reproducing sea level pressure, surface temperature and wind field at buoy locations has also been quantified by means of standard statistics (given in table 3.1). Scores were calculated for 658 hourly data.

Table 3.1.- Statistical scores comparing MM5-10 km, (hindcast -H- and forecast -F- runs) with each buoy (Cabo de Gata -CG- and Golfo de Cádiz -GC-). The averaged scores are denoted by Av. Those measures that exceed the benchmarks are within shaded cells. Boldface numbers denote the best score for each experiment and statistical measure. Please, note that there is no benchmark for sea level pressure.

	Sea Level Pressure									
	MAE (hPa)		**RMSE (hPa)**		**BIAS (hPa)**		**IOA**		**r**	
	H	*F*	*H*	*F*	*H*	*F*	*H*	*F*	*H*	*F*
Av.	**1.37**	1.39	**1.69**	1.79	0.81	**0.52**	**0.91**	0.90	**0.87**	0.83
CG	**1.43**	1.53	**1.75**	1.95	0.61	**0.13**	**0.91**	0.88	**0.84**	0.78
GC	1.32	**1.25**	1.64	**1.63**	1.01	**0.91**	0.92	0.92	**0.90**	0.89
	Wind speed at 10 m									
	MAE (ms^{-1})		**RMSE (ms^{-1})**		**BIAS (ms^{-1})**		**IOA**		**r**	
	H	*F*	*H*	*F*	*H*	*F*	*H*	*F*	*H*	*F*
Av.	**2.51**	2.66	**3.25**	3.35	0.94	**0.84**	**0.74**	0.73	**0.57**	0.54
CG	**2.71**	3.14	**3.47**	3.87	**0.94**	1.47	**0.74**	0.70	**0.58**	0.52
GC	2.31	**2.20**	3.03	**2.84**	0.94	**0.22**	0.74	**0.76**	0.57	**0.59**
	Wind direction at 10 m									
	MAE (º)		**RMSVE (º)**		**BIAS (º)**		**IOA**		**r**	
	H	*F*	*H*	*F*	*H*	*F*	*H*	*F*	*H*	*F*
Av.	**40.53**	46.37	**4.83**	8.23	**4.05**	5.68	**0.79**	0.75	**0.61**	0.53
CG	**33.57**	40.50	**4.60**	11.59	-2.88	**-2.61**	**0.86**	0.81	**0.74**	0.65
GC	**47.49**	52.25	5.07	**4.87**	**10.98**	13.97	**0.73**	0.69	**0.49**	0.41
	2 m Air Temperature									
	MAE (Cº)		**RMSE (Cº)**		**BIAS (Cº)**		**IOA**		**r**	
	H	*F*	*H*	*F*	*H*	*F*	*H*	*F*	*H*	*F*
Av.	0.98	**0.96**	1.26	**1.25**	**0.18**	0.56	0.63	**0.69**	0.33	**0.52**
CG	0.97	**0.91**	1.25	**1.18**	**-0.42**	0.51	0.64	**0.78**	0.46	**0.66**
GC	**0.99**	1.02	**1.27**	1.33	0.79	**0.62**	**0.63**	0.61	**0.48**	0.39

A quick glance of the table 3.1 results reveals that the model skilfully simulates surface flows and variables over the sea, in hindcast or forecast run. As expected, the reliability of the model by reproducing sea level pressure and surface wind velocity at buoy locations is slightly better for the hindcast run.

Results of both experiments exhibit a strong correlation between the simulated and observed sea level pressure and wind direction, with average correlation coefficients generally above 0.8 and around 0.6, respectively.

The model performance achieves the benchmark values (summarized in table 2.9) in both runs, except for the wind speed RMSE (> 2.5 $m \cdot s^{-1}$) and air temperature

IOA (< 0.8), at both locations, and for the wind direction BIAS (> 10 º), at the golfo de Cádiz.

Overall, the simulated wind speed and the sea level pressure are higher than the observed and the temperature shows systematic warm bias at both stations. The model shows a tendency to rotate the wind vectors anticyclonally (positive bias) from the observed at the golfo de Cádiz and cyclonically (negative bias) at the cabo de Gata.

In spite of different model reliability by comparing the hindcast and the forecast runs, variation in model initial and lateral boundary conditions did not drastically affect the model performance.

2.2. Model versus automatic weather station measurements

The behaviour of the model (for both hindcast and forecast cases) at the coast is assessed by comparison with the daily data of seven automatic weather stations, belonging to AEMET. Spatio-temporal averaged statistics are summarized in table 3.2 and scatter plots of four of them (Rota, Málaga, Ceuta and Melilla) are shown in figure 3.13.

It can be seen (figure 3.13) that the simulated values generally matched well with the observed values of sea level pressure ($r^2 > 0.6$) in the case of hindcast run. Further agreement between observed and forecasted wind speed and temperature at Malaga are shown by $r^2 > 0.5$ values (Santhi *et al.*, 2001; Van *et al.*, 2003).

At all other locations, the r^2 values are lower than the considered acceptable (they seem to be unduly influenced by a small number of outliers).

On average, r-squared values are higher when comparing pair-wise of predicted (forecast run) and observed surface temperature, while the strength of relationship between observed wind speed and sea level pressure is better with the hindcast results.

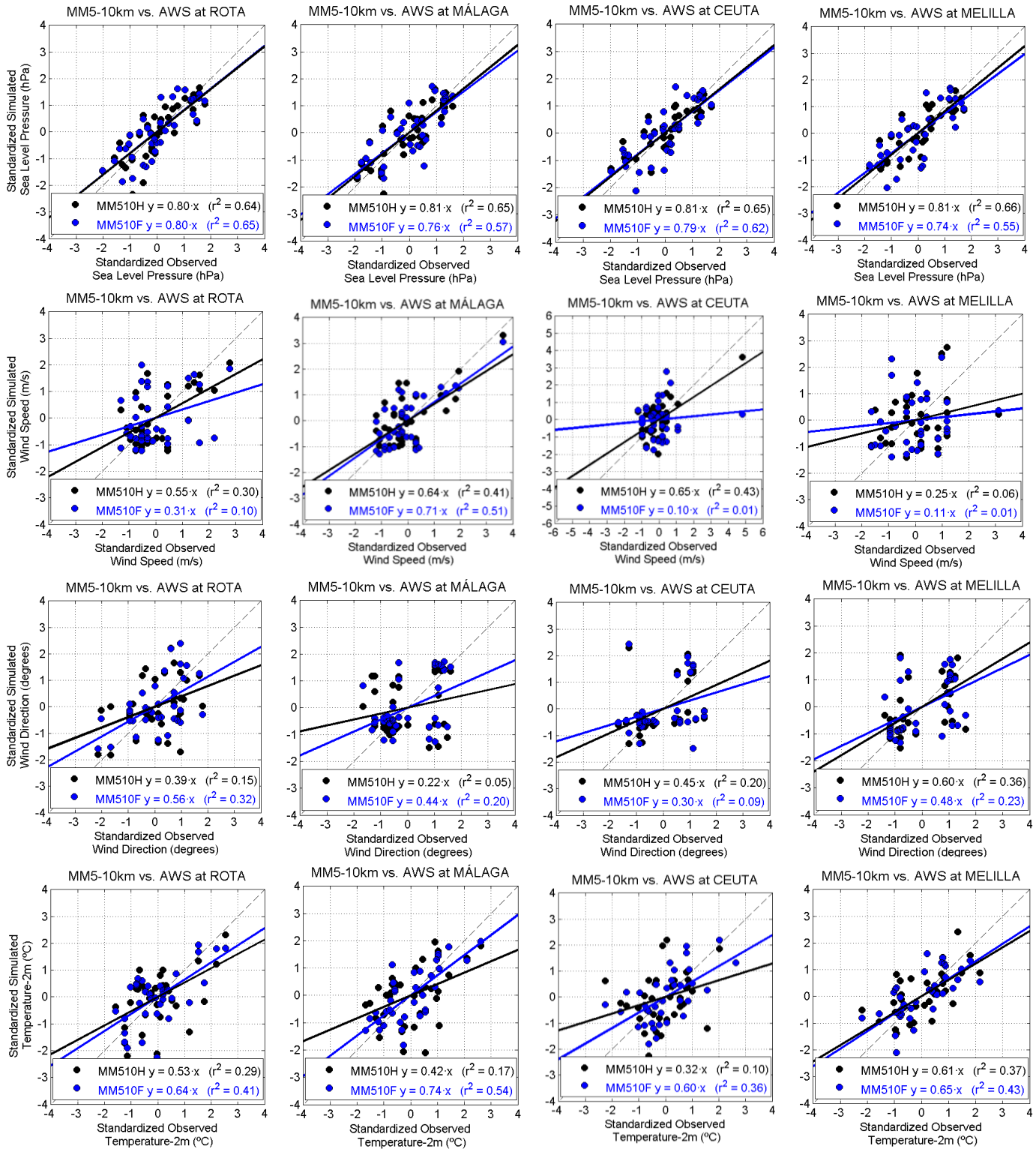

Figure 3.13.- Observed *versus* simulated (from the top) sea level pressure, 10-m wind speed and direction and 2-m temperature at (from the left), Rota, Málaga, Ceuta and Melilla. Black dots are for hindcast experiment while blue dots are for forecast. The line of least squares regression is also shown.

It is known that, even although the coefficient of determination is a useful measure of the strength of the linear relationship between two variables, it becomes weaker as the data points become more scattered. This means that r-squared is highly

affected by outliers. Therefore, it might not be the best accuracy measure between simulated and observed values, making it convenient the use of other statistics (table 3.2) and the comparison of their values against different benchmarks (Emery *et al.*, 2001; Kemball-Cook *et al.*, 2005).

Table 3.2.- Averaged (Av) MM5-10 km model performance statistics for surface variables, both the hindcast -H- and forecast -F- cases at 7 automatic weather stations (from AEMET). Those measures that exceed the benchmarks are within shaded cells. Boldface numbers denote the best score for each experiment and statistical measure. Please, note that there is not benchmark for sea level pressure.

	Sea Level Pressure (hPa)									
	MAE (hPa)		**RMSE (hPa)**		**BIAS (hPa)**		**IOA**		**r**	
	H	*F*	*H*	*F*	*H*	*F*	*H*	*F*	*H*	*F*
Av.	4.48	**4.08**	4.85	**4.55**	4.23	**3.83**	0.64	**0.66**	**0.77**	0.76
	Wind speed at 10 m (ms^{-1})									
	MAE (ms^{-1})		**RMSE (ms^{-1})**		**BIAS (ms^{-1})**		**IOA**		**r**	
	H	*F*	*H*	*F*	*H*	*F*	*H*	*F*	*H*	*F*
Av.	2.76	**2.38**	3.31	**2.93**	1.56	**0.92**	0.55	0.55	**0.48**	0.39
	Wind direction at 10 m (degrees)									
	MAE (º)		**RMSVE (º)**		**BIAS (º)**		**IOA**		**r**	
	H	*F*	*H*	*F*	*H*	*F*	*H*	*F*	*H*	*F*
Av.	58.41	**58.09**	6.55	**5.91**	-6.45	**1.45**	0.63	**0.65**	0.35	**0.40**
	Air Temperature at 2 m (ºC)									
	MAE (ºC)		**RMSE (ºC)**		**BIAS (ºC)**		**IOA**		**r**	
	H	*F*	*H*	*F*	*H*	*F*	*H*	*F*	*H*	*F*
Av.	1.59	**1.53**	2.03	**1.90**	**-0.87**	-0.89	0.57	**0.70**	0.45	**0.65**

Statistical scores show that both runs, forecast and hindcast, are able to simulate surface-layer meteorology with a satisfactory level of skill. Nevertheless, forecast run scores much better for surface temperature (Index of Agreement > 0.7) and slightly better for sea level pressure, wind direction (Index of Agreement ≥ 0.65) and wind speed (see MAE, RMSE and BIAS boldfaced values).

On average, surface temperature presents a cold bias, while the model tends to overestimate the sea level pressure and wind speed, even more for the hindcast run, for which RMSE and MAE are also larger. Wind direction BIAS reflects the tendency of the simulated winds to be cyclonically rotated from observed (negative) in the case of hindcast runs and anticyclonically (positive) for the forecast experiments. The simulation of too geostrophic or overestimated winds (positive bias) has been explained as an excessive mixing in the vertical, a characteristic from the MRF PBL scheme. This seems to be also an inherent problem with all PBL scheme available with WRF according to (Mass & Ovens, 2011)

Overall, we can see that the average values of hindcast and forecast simulations fall inside of the complex benchmarks, with the exception of all wind speed parameters, even though bias and the IOA are seen to be on the threshold ($\leq$ 1.5 $m \cdot s^{-1}$ and 0.6, respectively), MAE of wind direction, also closer to the complex benchmark ($\leq$ 55 degrees), and the IOA of temperature. Being outside one or more of these ranges does not mean the meteorological data fields for a particular parameter are unacceptable. However, such a result indicates that caution should be exercised in the use of such variables. Additionally, Emery *et al.* (2001) admit that the proposed benchmarks for wind direction error appear to be especially lenient and stringent.

The unexpected result that the short-term forecast is in better accordance with the coastal observed meteorological fields than hindcast suggest that site-specific effects are more important than initial and boundary conditions. Strong local forcing mechanisms resulting from the complex terrain may have limited the effect of lateral boundary conditions errors, being the wind velocity more sensitive to the topographic and land-use characteristics of each observing site. Nevertheless, errors are expected to grow with the length of the forecast horizon. However, the model performs better over the sea than inland, as expected.

3. Temporal evolution and spatial distribution of model errors

In the previous section it has been analyzed and confirmed the model reliability to reproduce surface fields over the sea and hinterland. Nevertheless, results have been expressed in terms of the average, while the considerable regionwide temporal and spatial variation in MM5 errors and biases has also been highlighted.

Throughout this section, the evolution of daily MAE and RMSE errors and bias for the surface temperature and wind velocity will be addressed for the hindcast run. The geographical patterns in model errors and biases will be also examined.

3.1. Temporal evolution of errors

Wind velocity at 10 m and temperature at 2 m measured at 95 IFAPA stations, were used to compute statistical scores of the MM5-10 km model run throughout May 2007. This period was selected because, firstly, the frequency of breeze days in the area is greater than 30% between May and September (Hernández-Ceballos *et al.*, 2013) and, secondly, because the percentage of stations with reliable measurements was high.

The hourly evolution of spatially averaged observed meteorological variables (blue lines in figure 3.14) shows that the averaged surface winds blow mainly from the third quadrant (figure 3.14, bottom), influenced by the axis direction of the valley, although winds from the second quadrant were also detected. May 2007 was specially warmer than the climate mean, and was also very sunny, with higher number of hours of bright sunshine than average throughout the national territory, as stated in the AEMET monthly climate report (AEMET, 2007). Observed averaged surface temperature (figure 3.14, top) remains over 10 ºC throughout the period, with some strong warm events (from May 8 until May 11 and from May 17 until May 20), which are, on another hand, associated to weak winds (figure 3.14). All variables present a high diurnal variation.

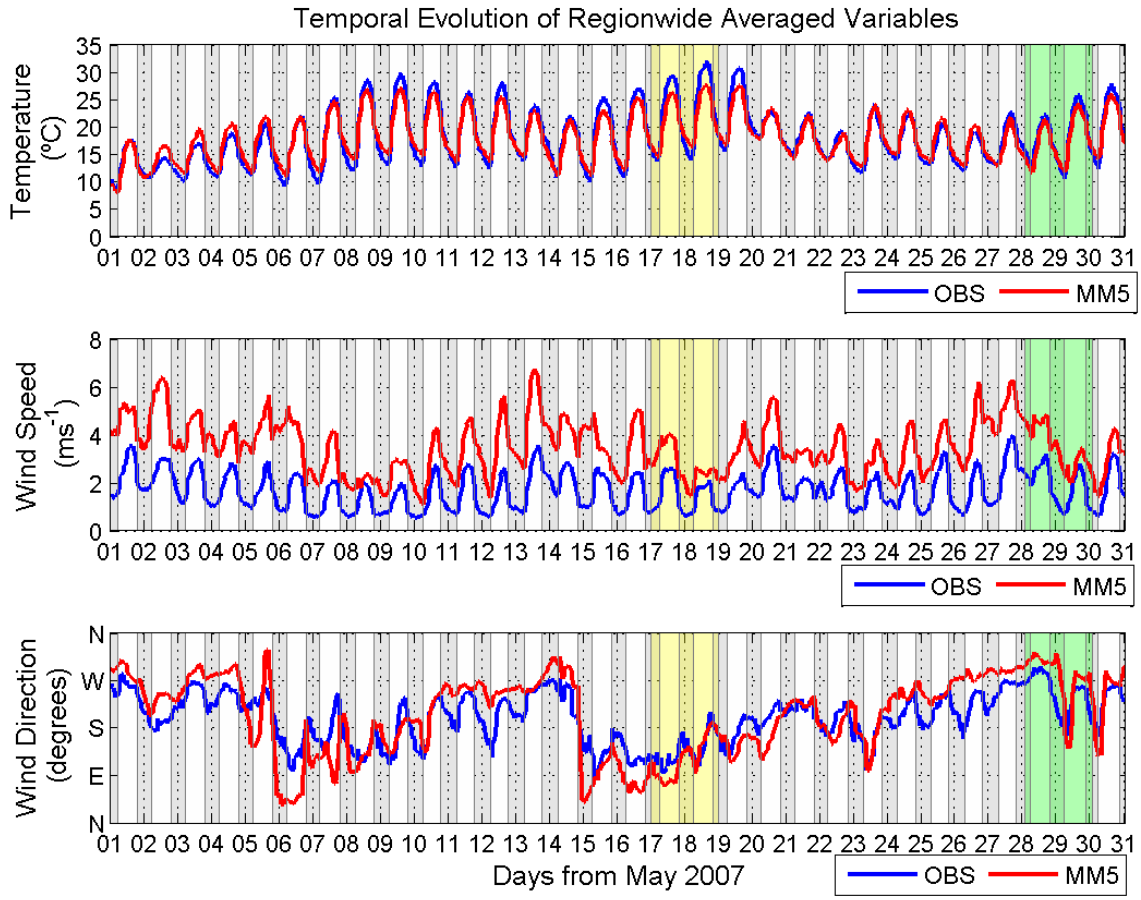

Figure 3.14.- Hourly evolution of spatially averaged surface temperature (top), surface wind speed (middle) and direction (bottom) observed (blue line) and simulated by the MM5-10 km (red line). Grey shaded bars correspond to nighttime periods. Yellow and green shaded areas cover the pure and non-pure sea-land breeze periods, respectively.

The temporal evolution of model bias and errors in surface wind speed (RMSE), wind direction (MAE) and 2 m-temperature (MAE) is plotted (figure 3.15) to show the diurnal variation of model performance.

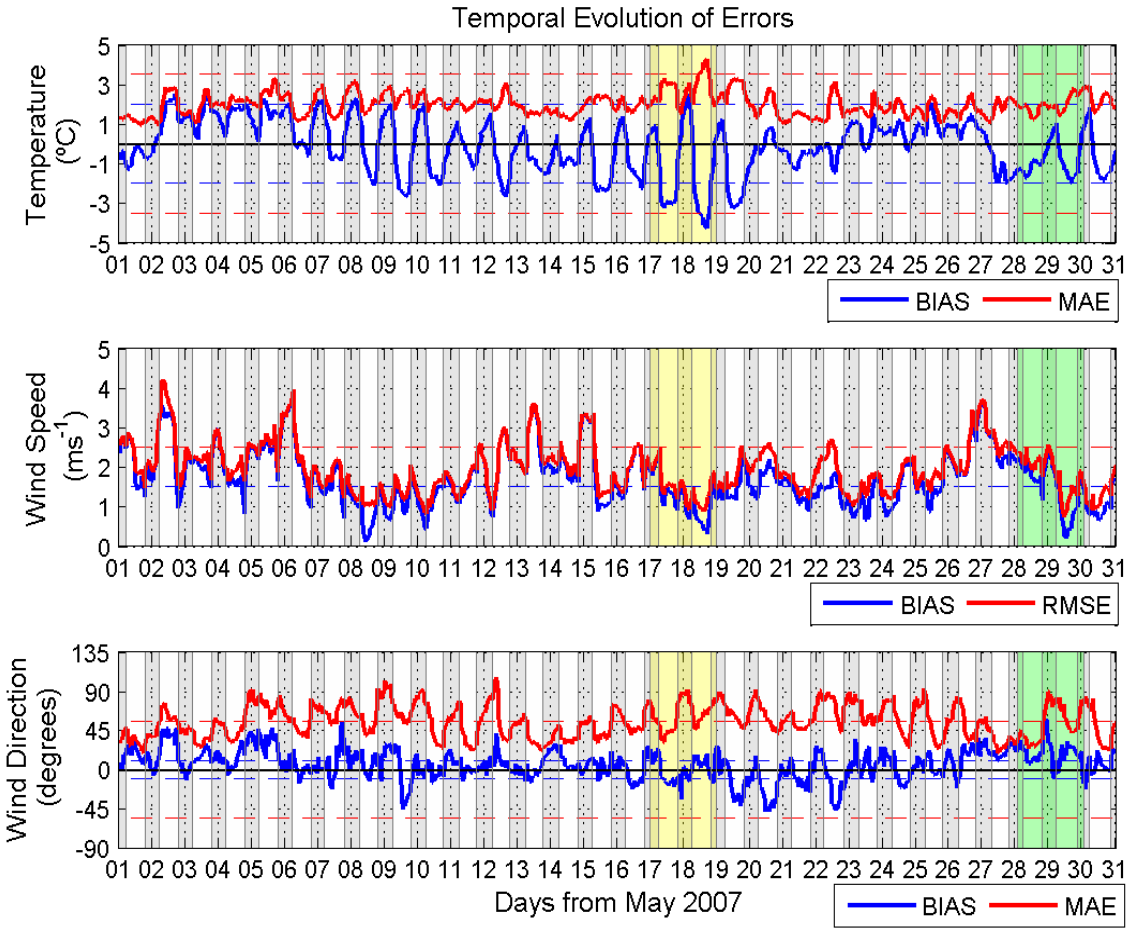

Figure 3.15.- Spatially averaged hourly evolution of errors and biases throughout May 2007 for 2 m-temperature (top), wind speed (middle) and direction (bottom). Grey shaded bars correspond to nighttime periods. Dashed lines show the model performance benchmarks for complex conditions for each variable and parameter. Yellow and green shaded areas cover the pure and non-pure sea-land breeze periods, respectively.

The model tends to underestimate surface temperature (figure 3.15, top) during daytime, being the averaged simulated temperatures consistently colder than the observations. At night, it produces a warm bias, being the diurnal temperature cycle amplitude underestimated by the model, particularly during the warmest periods mentioned above (from May 8 until May 11 and from May 17 until May 20). This fact is in agreement with previous studies for other areas (Oncley & Dudhia, 1995; Manning & Davis, 1997; White *et al.*, 1999; Colle *et al.*, 2003). These cold and warm biases were the major contributors to the large daytime and nighttime MAE values, indicating a systematic nature of errors.

This behaviour might be associated to the radiation scheme used, the cloud-radiation scheme[4] (Dudhia, 1989), which, on the one hand, it underpredicts the amount of incident shortwave downwelling flux on the surface of the earth, at least partially due, to uncertainties or discrepancies in the cloud fraction used for the radiation scheme (Armstrong, 2000), displaying a cold temperature bias during the daytime. And, on the other hand, it predicts too much downward longwave radiation, resulting in a warm bias, which together with low level wind speeds, leads to a weaker nocturnal inversion, particularly in the last hours of the night (Zhong *et al.*, 2007) and especially under moist clear sky conditions (Guichard *et al.*, 2003) and overestimated surface layer winds (Zhang & Zheng, 2004).

It can also be observed that MM5 simulated temperature achieves the complex benchmarks (BIAS and MAE) with just some periods (from May 8 until May 11 and from May 17 until May 20) falling just outside of the value due to too warm temperatures (see yellow shaded area of figure 3.15). Crawford *et al.* (2001) also showed that the MM5 tends to be too cool during extremely hot days.

Wind direction errors (MAE) are smaller during the daytime and largest during the night (figure 3.15, bottom), when the wind speed and the vertical mixing are lower, pointing out the difficulties of the model to simulate weak nocturnal winds and surface temperatures.

A slight positive BIAS predominance of wind direction (wind shifts to larger angles) could be interpreted as underestimation of surface roughness by the model due to topography smoothing and/or inappropriate land-sea mask and land uses (Mass & Ovens, 2011). In fact, these authors were able to reduce wind speed and wind direction biases by using surface roughness length proportional to the magnitude of sub-grid scale terrain variance. In this sense, Jiménez & Dudhia (2012) improved intra-diurnal wind speed variability by adding a new surface sink term in the WRF momentum equation to take into account the effects of the unresolved terrain.

The surface wind speed (figure 3.15, middle) exhibits strong positive biases throughout the month (> 1.5 $m \cdot s^{-1}$), especially during the nighttime hours, suggesting that the magnitude of MAE includes a systematic component. These results could suggest a possible excessive mixing of the surface layer under stable conditions, particularly at night, related to the PBL scheme (MRF), which is also consistent with

[4] Dudhia's radiation scheme included cloud effects on shortwave and longwave radiative fluxes (Armstrong, 2000).

the warm bias for surface temperature and with the positive bias of wind direction (Wyszogrodzki *et al.*, 2013). Steeneveld *et al.* (2008) also suggested that the excessive mixing may be in turn due to unresolved small-scale terrain drag. At daytime, when the wind speeds increase as the convective boundary layer grows and entrains higher momentum air from aloft, the errors are smaller.

A summary of the quantitative model evaluation reproducing daily variability of surface variables is shown in table 3.3. Metrics have been computed throughout the month of May 2007, considering the 95 locations and their results reflect the findings of the above time-series: The underestimation of the 2-m daytime temperature, in contrast to the nighttime warm biases; the model overestimation of surface wind speed, particularly at night; the systematic flow shift to larger angles and the error dependency of the time of day.

Values of wind speed BIAS throughout the day and wind direction MAE at night, although closer, fall outside the complex benchmarks (WS BIAS $\leq \pm$ 1.5 $m \cdot s^{-1}$ and WD MAE $\leq$ 55 º).

Table 3.3.- Daily variability of average model errors throughout May 2007 at 95 locations. Values within the shaded cells indicate exceedances of the (simple or complex) benchmarks. Boldface numbers denote the best score for each experiment and statistical measure. WS=10 m-Wind Speed; WD=10 m-Wind Direction; T2=2 m-Air Temperature.

Scores	**BIAS**						**RMSE**		**MAE**			
Variables	*WS (ms^{-1})*		*WD (º)*		*T2 (℃)*		*WS (ms^{-1})*		*WD (º)*		*T2 (℃)*	
Period	*Night*	*Day*	*Night*	*Day*	*Night*	*Day*	*Night*	*Day*	*Night*	*Day*	*Night*	*Day*
May.2007	1.80	**1.68**	9.07	**4.21**	**0.49**	-0.55	1.97	**1.94**	64.98	**49.11**	**1.93**	1.99

3.2. Geographical distribution of errors

Together with the analysis of the spatially averaged temporal variation of errors, it is important to know which locations have large errors and biases in order to identify model failures related to complex topography.

Spatial distribution of monthly averages of BIAS and MAE for 2 m temperature is shown in figure 3.15. Statistical parameters are presented at the station locations over the topography derived from SRTM30 (~1 km) digital elevation data (on grey contours) for a better visualization and identification of those regions with larger errors.

The spatial distribution of the surface temperature bias (figure 3.16, top) shows two opposite patterns: the Guadalquivir Valley and plains (see figure 1.1 showing topographic features), where the model clearly overestimate the surface temperature and

over the Baetic mountain range, characterized by a cold bias (Mass & Ovens, 2011; Jiménez & Dudhia, 2013).

Geographical distribution of surface temperature MAE (figure 3.16, bottom) is also related to the heterogeneity in terrain structure closely following the pattern of the biases, indicating a systematic nature of errors. The model performs better in the interior and along the Atlantic coast with surface temperature predicted within 2.5 degrees of observations, while the locations along the Penibaetic system are affected by strong temperature gradients and so thus, they present larger errors.

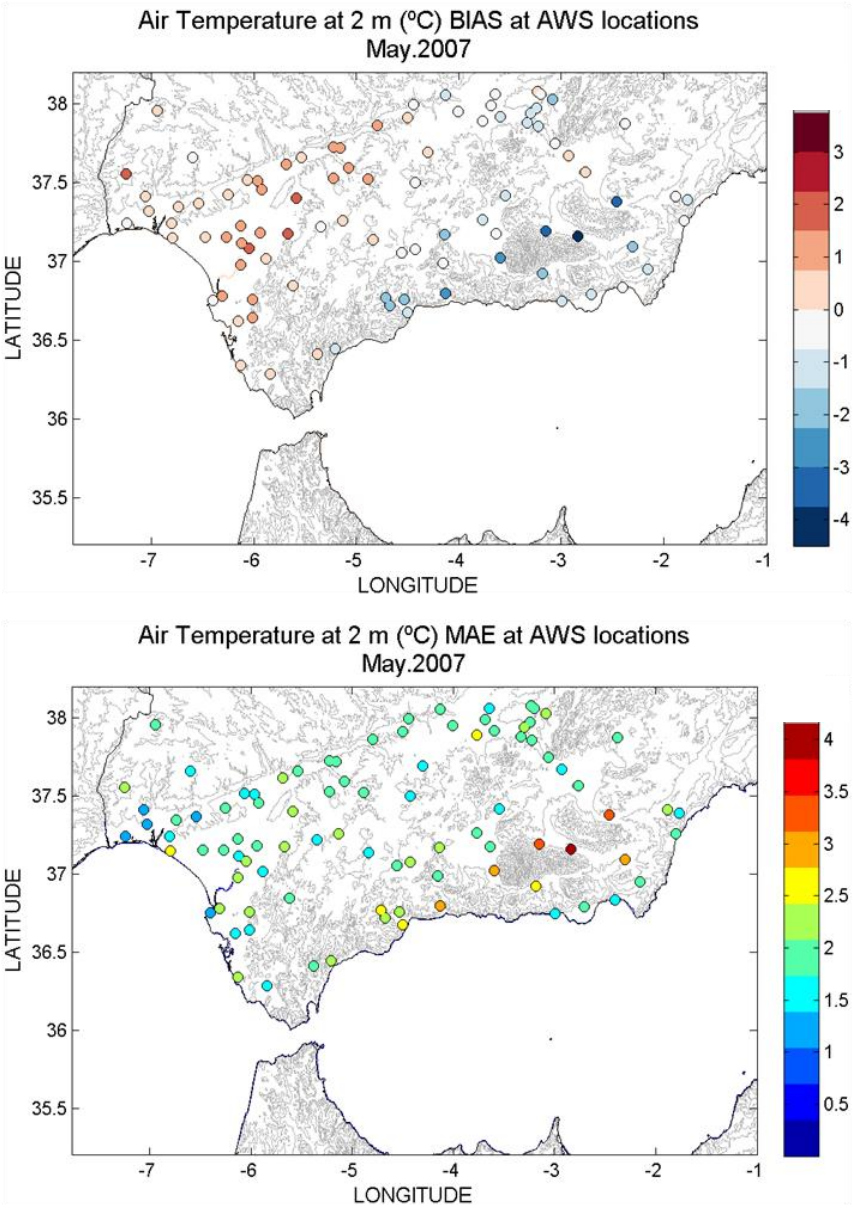

Figure 3.16.- Time-averaged bias (top) and MAE (bottom) distributions for 2 m-air temperature over the month of May 2007.

The general behaviour of the model shows a tendency to overestimate surface wind speed over the region (figure 3.17, top), to a lesser extent over plains and valleys, suggesting the unresolved roughness or friction of subgrid terrain as the main cause (Mass & Ovens, 2011).

In this regard, the largest wind speed errors (figure 3.17, bottom) are associated with strong overestimation biases, being found in some coastal locations, affected by the different diurnal land-water heating and subjected to the difficulties in simulating the onset of sea-land breezes, especially at those closer to the narrowest point of the Gibraltar Strait, where the simulated wind funnels and accelerates, and along depressions (Guadiana Menor and Guadalhorce valleys) surrounded by the high terrain.

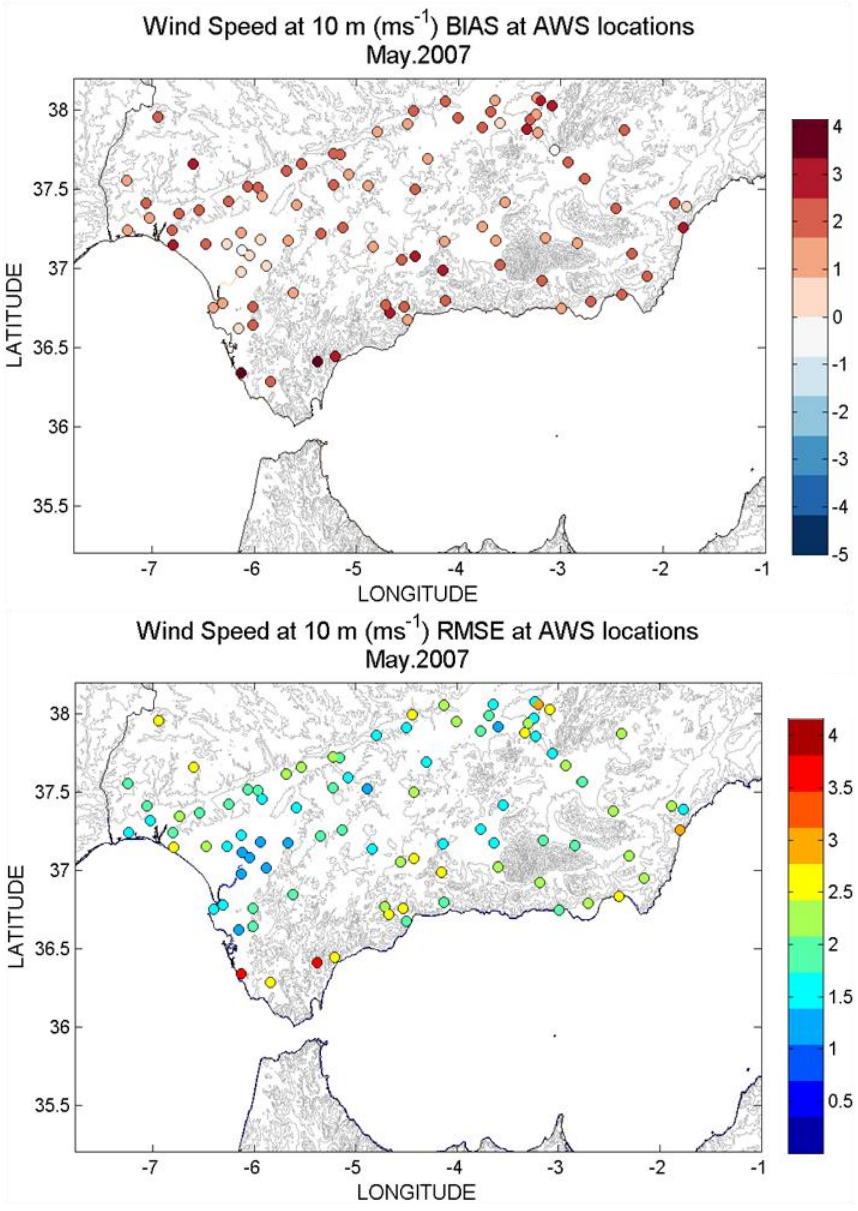

Figure 3.17.- Time-averaged bias (top) and MAE (bottom) distributions for wind speed over the month of May 2007.

Winds are anticyclonically rotated from the observed along the Guadalquivir Valley, as it is indicated by the positive direction biases (figure 3.18, top) and it could be due to the improper representation of the Guadalquivir valley (smoother model topography), causing systematic flow shifts.

At the coastal areas, mostly from the eastern part of the region, and along the Guadiana Menor Valley, simulated winds are rotated cyclonically (negative biases).

Wind direction geographical errors distribution (figure 3.18, bottom) shows also two differentiated areas like the temperature error pattern: the Guadalquivir Valley, with the lowest errors (below 55 degrees benchmark value), and the mountain ranges, where the relatively larger errors are found. This may be caused by the interaction of the large-scale flow with the steep topography.

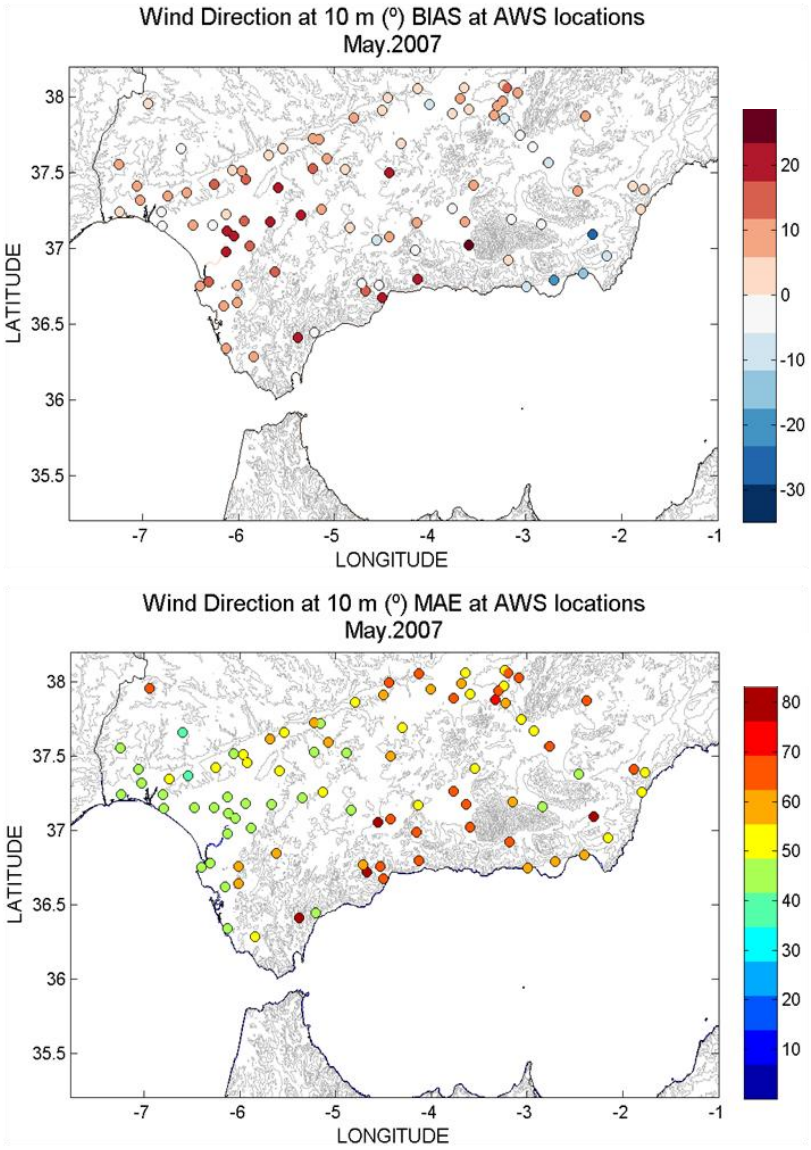

Figure 3.18.- Time-averaged bias (top) and MAE (bottom) distributions for wind direction over the month of May 2007.

4. Performance assessment of mesoscale phenomena: sea-land-breezes.

4.1. Sea-land breezes: qualitative comparison

Among all other mesoscale phenomena taken place in the area, sea-land breezes are probably the most studied, partially due to their strong relation to severe air pollution episodes, especially in summer months (Papanastasiou & Melas, 2009; Adame *et al.*, 2010; Adame *et al.*, 2012; Hernández-Ceballos *et al.*, 2013) and to their implication for coastal meteorology and climate processes (Case *et al.*, 2005; Lu *et al.*, 2009), such as ocean mixed-layer heat storage (Gille *et al.*, 2005).

Particularly, considering the context of this PhD thesis, it should also be pointed out the role of sea-land breezes in coastal areas on the "breeze-forced oscillations" (BFOs), in response to its periodic transfer of momentum and, furthermore, on promoting diapycnal mixing processes through breeze-forced diurnal-inertial currents (Aguiar-González *et al.*, 2011).

This is however a supplementary reason to analyze the performance of the mesoscale model by reproducing thermally-driven processes as land-sea breezes. In this sense, the model should be capable of simulating the two periods representative of different breeze patterns previously identified on the southwestern coastline of the Iberian Peninsula (Adame *et al.*, 2010): the non-pure and the pure sea-land breezes (table 3.4 summarizes the principal characteristics of both patterns). The influence of the background synoptic or mesoscale winds on the sea-land breeze patterns is also analyzed. An additional consideration may be addressed at this point, checking whether the breeze classification from Adame *et al.* (2010) could be generalized to the sea-land breeze patterns in the Mediterranean coast of the Strait of Gibraltar, including surface wind pattern and inland penetration of the sea-breeze front.

Table 3.4.- Summary of the principal characteristics of sea-land breezes patterns in the southwestern Iberian Peninsula.

Characteristics	Non-Pure breezes	Pure breezes
Prevailing weather condition	Synoptic northwesterly	Mesoscale easterly flow
Horizontal extension	200 km (under SW flows)	20-40 km
Vertical extension	1000 m	500 m
Distribution along the valley	Large homogeneity	Large variability
Sea (diurnal) breeze duration	< 8 hours	≈ 8 hours

Land (nocturnal) breeze duration	≈ 9 hours	≈ 5 hours
Transition (from sea to land) regimen duration	≈ 3 hours	≈ 6 hours
Air land temperatures	28°-30° daily maximum	37° daily maximum
Wind direction (with reference to the coastline)	Nonperpendicular	Perpendicular
Wind speed	Intense	Moderate
Occurrence of air pollution episodes	Unfavourable	Favourable
WRF-ARW model performance	Good	Observations are mainly overestimated

4.1.1. Pure sea-land breezes

The case of pure breeze was analyzed along two consecutive days on May 17 and 18, 2007, developed under anticyclonic conditions (with high pressure systems over the Azores and over the western Mediterranean) and a low isobaric gradient on the Iberian Peninsula. The weak synoptic wind allows the development of mesoscale circulation (figure 3.19).

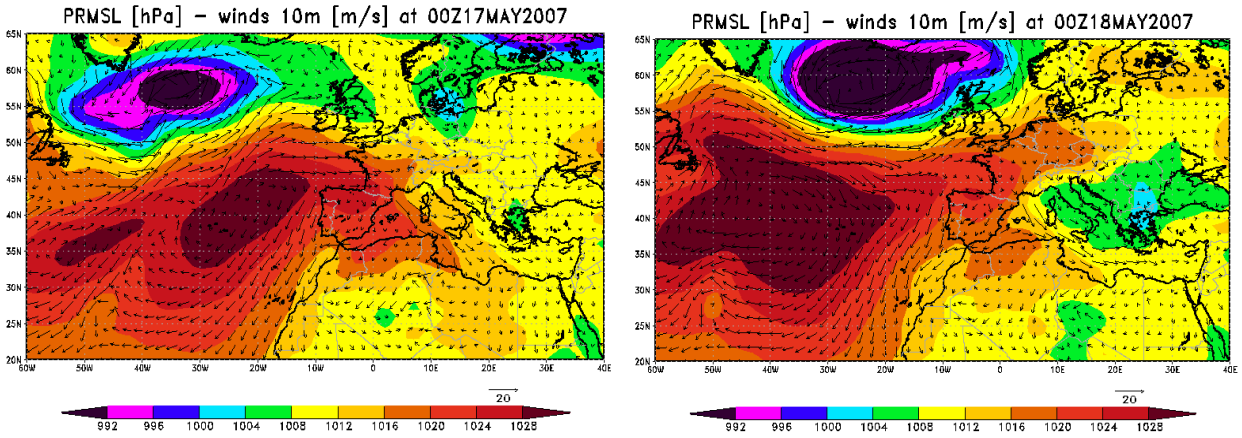

Figure 3.19.- Surface synoptic chart at 0000 UTC on May 17 (left) and on May 18 (right), 2007.

This situation is associated to low wind speeds in the lower troposphere (maximum regionwide average wind speed is 2.6 $m \cdot s^{-1}$, while the strongest observed wind was blowing up to 9.18 $m \cdot s^{-1}$), clear-sky periods and high maximum temperatures (figure 3.14, yellow shaded area correspond to the pure breeze period).

On 17 May, the regionwide averaged wind speed is slightly higher (2.6 $m \cdot s^{-1}$) than the consecutive day (2.4 $m \cdot s^{-1}$).

Since land-sea breeze wind forcing and solar heating are in phase (Gille *et al.*, 2005), the diurnal cycle of observed air temperature is analyzed to find the time of the maximum air-sea temperature differences, when the breeze is formed. On May 17, the

averaged air temperature (figure 3.14, top) measured throughout the 95 meteorological stations, ranges from 13.69 °C (at sunrise, 0500 UTC) to 29.05 °C (at 1500 UTC).

The daily averaged minimum air temperature on May 18 was of 13.83 °C (0500 UTC) and the maximum was of 31.65 °C (at 1500 UTC), presenting a wider temperature range.

Figure 3.20 and figure 3.21 show the observed (red arrows) and simulated (black arrows) wind field at 10 m, for two representative days of the pure breeze conditions, on May 17 and 18, 2007, respectively, at 0500 UTC and 1500 UTC.

On May 17, the observed wind circulation is dominated by mesoscale variability (land-sea and mountain-valley breeze circulation). Northeasterly surface winds along the Guadalquivir valley, intensified at the valley mouth, and transversal southeasterly flows crossing the Guadalhorce pass of the Baetic mountains were observed at 0500 UTC. Down-slope and down-valley winds in the Guadiana Menor and Guadalquivir valleys are observable at night (see red arrows in figure 3.20, top). Perpendicular land-breezes (offshore) were measured by the stations located along the Atlantic and the Mediterranean coast, being more intense the formers.

At 1500 UTC, northeasterly winds become more intense, particularly those channelled down the valley and specially at the mouth (see red arrows in figure 3.20, bottom). Valley breeze is also observed up the Guadiana Menor. Intense sea-breezes (onshore) blow perpendicular to the Mediterranean coast, while the prevailing off-shore surface wind from the land delays the onset and the horizontal extension of the sea breeze on the Atlantic side. The inland penetration of the formers was blocked by the local topography.

The simulated wind field (black arrows of figure 3.20), due the topography smoothing and land uses resolution, shows more homogeneity, with northeasterly winds channelled down the valley, while in the Strait of Gibraltar, the wind blows strongly from the east. Transversal weak flows are also appreciated but not during the daytime. Land-breezes on the Atlantic coast are simulated by the model but not on the Mediterranean side, where strong easterlies prevail. Sea-breezes are simulated along the Atlantic and the Mediterranean coastal areas. In general, observed wind intensity is overestimated by the model, particularly at night.

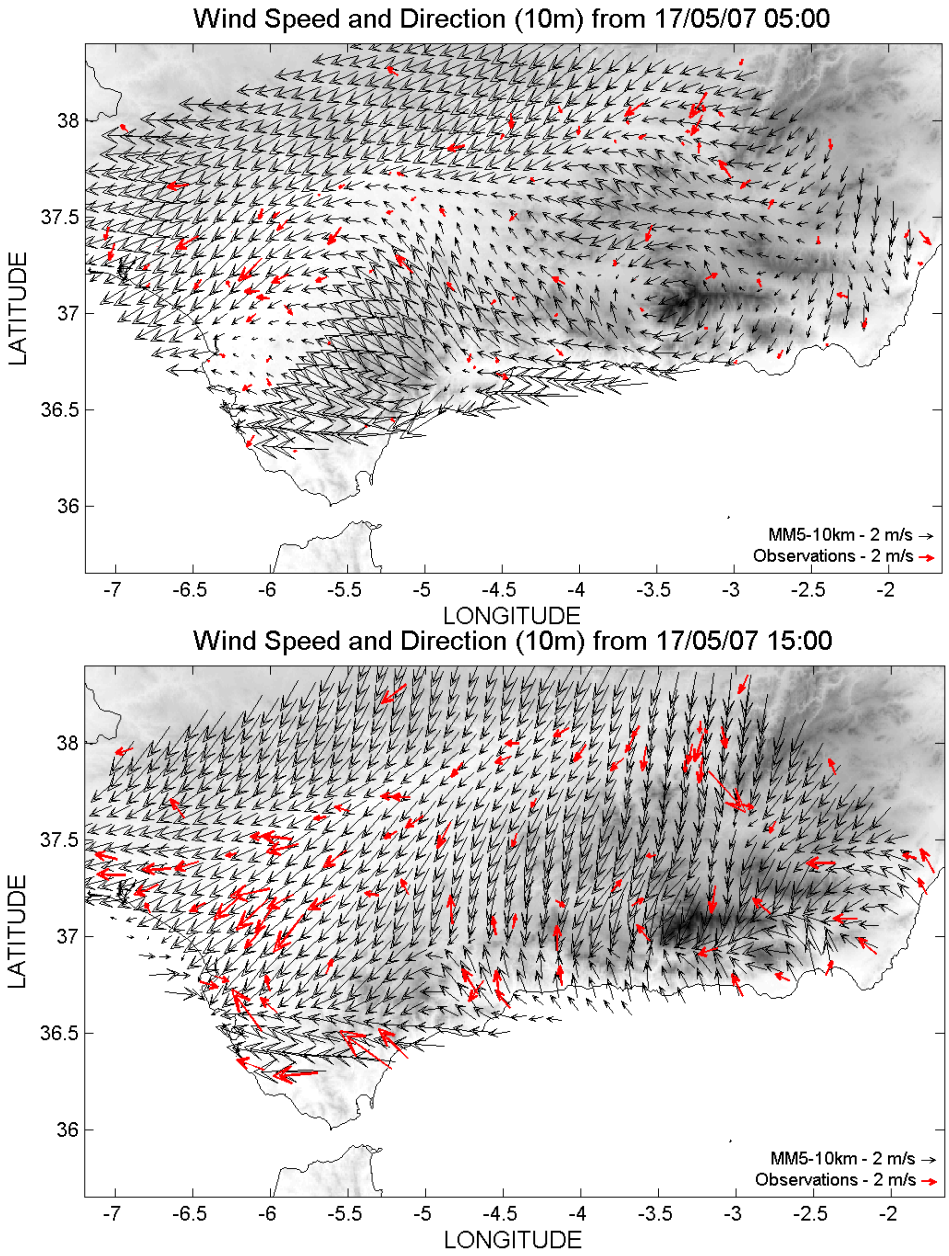

Figure 3.20.-Comparison of observed and simulated wind field at 10 m, on May 17, 2007 at 0500 UTC (top) and 1500 UTC (bottom) under the influence of easterly winds.

Daily maximum air temperature measured on May 18 was higher than the previous day, while the wind speed was lower (figure 3.14, top and middle for temperature and wind speed evolution, respectively). Therefore it is expected that the mesoscale circulation becomes reinforced, favouring the development and the intensity of the sea-breezes and the valley-breezes upslope the mountains during the daytime.

Observed wind field (see red arrows of figure 3.21) is highly variable on May 18 at 0500 UTC, with northeasterly winds at the mouth of the valley (below 100 m heights), downslope mountain breezes in the Guadiana Menor valley, weak

southeasterly transversal flows and perpendicular land-breezes along the Atlantic and Mediterranean coasts.

At 1500 UTC, the southeasterly flow becomes more intense and in the Guadiana Menor the wind starts shifting to valley breeze. Perpendicular sea-breezes take place along the entire coastline.

The model (black arrows of figure 3.21) does not resolve properly the variability of the nocturnal weak winds, neither the land-breezes on May 18. However, it is able to reproduce the intense sea-breezes perpendicular to the Atlantic and to the Mediterranean coasts and the southeasterly transversal flow.

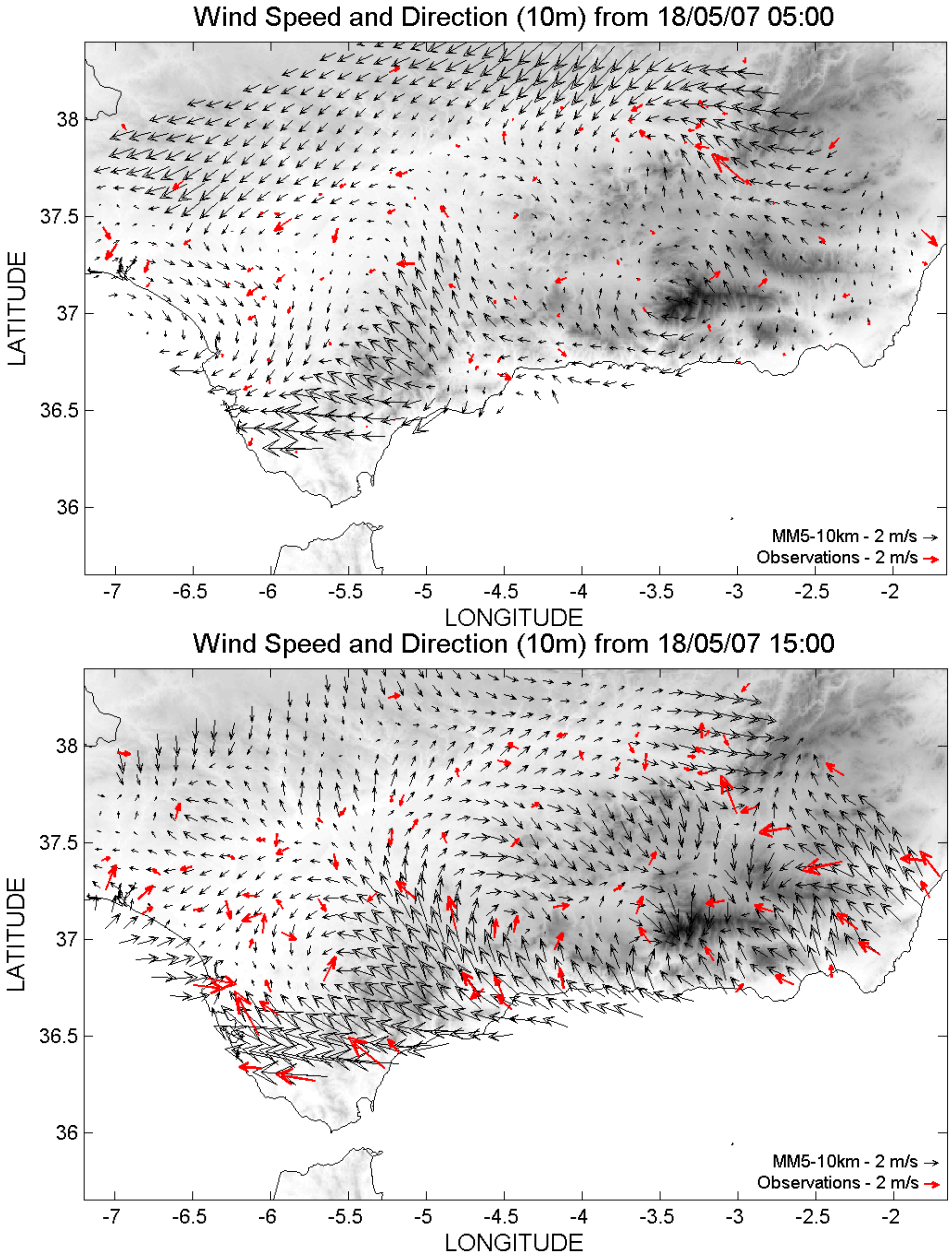

Figure 3.21.-Comparison of observed and simulated wind field at 10 m, on May 18, 2007 at 0500 UTC (top) and 1500 UTC (bottom) under the influence of easterly winds.

4.1.2. Non-pure sea-land breezes

For analyzing the breezes of the non-pure pattern, two consecutive days from the end of May 2007 were considered, both under the influence of synoptic northwesterlies caused by the location of the Azores anticyclone to the west of the Iberian Peninsula and a low pressure system over Central Europe (figure 3.22).

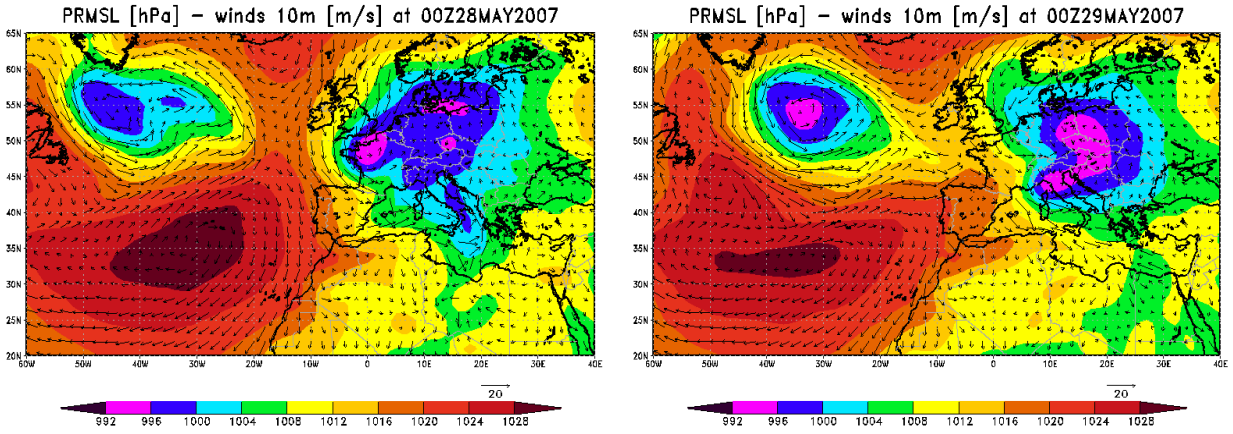

Figure 3.22.- Surface synoptic chart at 0000 UTC (left) on May 28 and (right) on May 29, 2007.

The minimum daily temperature (figure 3.14, green shaded area correspond to the non-pure breeze period) on May 28 was of 13.1 °C (at 0500 UTC) and the maximum 22.08 °C (at 1500 UTC). The next day, on May 29, minimum decreased down to 10.57 °C and the maximum increased up to 25.80 °C, widening more than 6 °C the temperature range from the previous day, but in any case, the temperature is much lower than those of the pure breeze days.

Winds under the non-pure breeze conditions are stronger than those under pure breezes, with a regionwide average wind of 3.2 $m \cdot s^{-1}$ and 2.8 $m \cdot s^{-1}$ on 28 and 29 May, respectively.

At 0500 UTC on May 28 (figure 3.23, top), observed (red arrows) and simulated (black arrows) synoptic northwesterly winds are modified by terrain effects along the Guadalquivir, Guadiana Menor and Guadalhorce valleys. Wind blows parallel to the Atlantic coast and perpendicularly off-shore on the Mediterranean coast, which masks land-breeze effects.

At 1500 UTC (figure 3.23, bottom), wind still blows from the northwest in most of the region. Nevertheless, strong sea-breeze is observed (see red arrows) on the Atlantic coast, not completely perpendicular, extending up the Guadalquivir valley. Horizontal inland penetration is not properly simulated (see black arrows). On the

Mediterranean coast, observed winds turns parallel to the coast, except close to the Málaga inlet, at the mouth of Guadalhorce river, where observed and simulated winds blow perpendicular offshore, funnelled downward the valley.

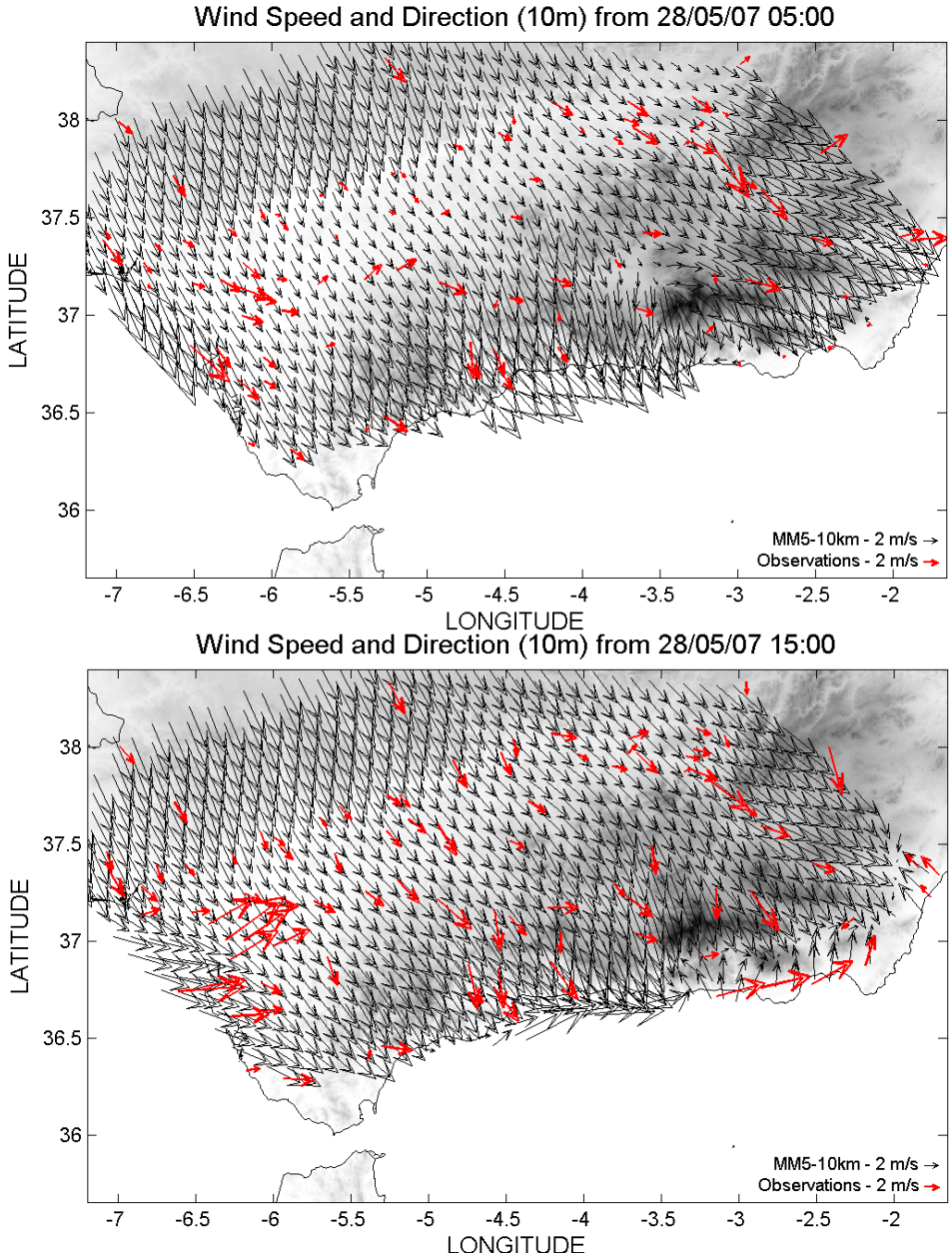

Figure 3.23.- Comparison of observed and model simulated wind field at 10 m, on May 28, 2007 at 0500 UTC (top) and 1500 UTC (bottom) under the influence of westerly winds.

Under moderate northwesterly winds, the next day (figure 3.24, top) at 0500 UTC, mountain breeze and downslope winds are observed in the Guadalquivir valley (see red arrows), especially on the lee-side of the mountains. Land-breezes are absent.

Well developed sea-breezes along the entire Andalusian coast are observed and simulated by the model at 1500 UTC on May 29 (see red arrows on figure 3.24,

bottom), under moderate northwesterly wind. Horizontal extension of the sea-breezes up to the valley is larger than the previous day. Although the model properly represents the breeze pattern of this particular day, it does not correctly simulate the inland penetration that the breeze reaches.

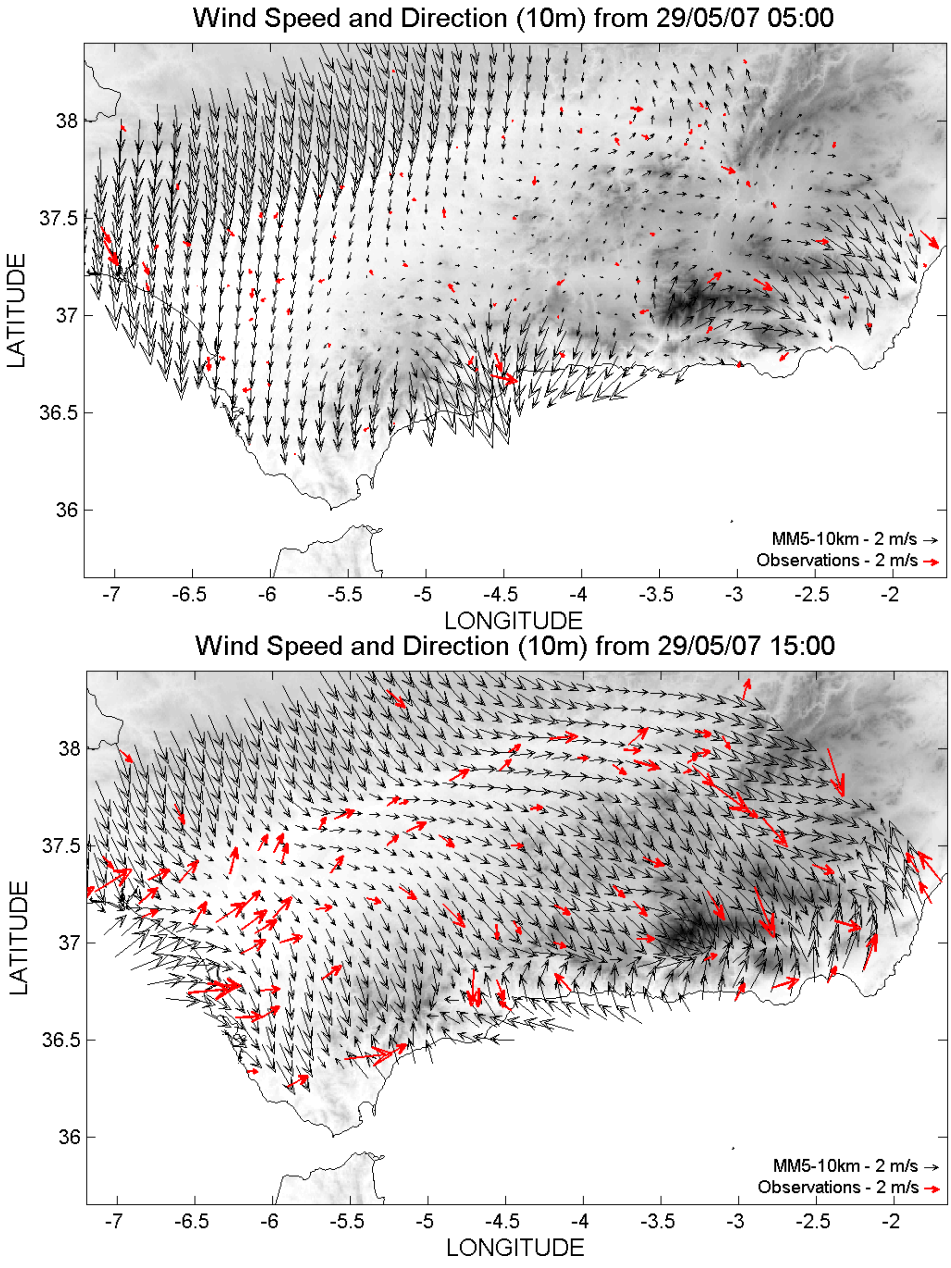

Figure 3.24.- Comparison of observed and model simulated wind field at 10 m, on May 29, 2007 at 0500 UTC (top) and 1500 UTC (bottom) under the influence of westerly winds.

On the basis of the above achievements, and in relation to the first of the issues raised in this section, the model was able to distinguish breeze patterns and the wind shift from offshore during the night to onshore during the daytime.

Pure sea-land breezes are developed under prevailing mesoscale circulation, as expected, along the entire Andalusian coast, associate to weak winds, clear-sky days, and high maximum temperatures. Although observed sea breezes (onshore) were captured by the model, land-breezes (offshore) were properly simulated only on the Atlantic side but not in the Mediterranean. This may be related to the warm bias at night due to stronger downward radiation from Dudhia scheme, which produces weaker offshore land breeze. Mountain and downslope (katabatic) winds develop inland at night time, while valley and upslope (anabatic) winds occur during daytime, being also reproduced by the model.

Synoptic forcing, prevailing under non-pure breeze event, related to lower temperatures and stronger winds, prevents the onset of land breeze at night on the Atlantic coast and masks the land breeze effect on the Mediterranean side, while the sea breeze is fully developed during daytime, particularly on the Atlantic coast.

Pure sea-breeze circulation is defined by a higher horizontal extension on the Mediterranean side because the prevailing synoptic northwesterly winds partially block the non-pure sea breezes. However, non-pure sea breezes penetrate further inland on the Atlantic coast, acting the Guadalquivir valley as a natural channel where the winds at all stations along the axis of the river basin are from southwest. Under this episode, the sea-breeze front onset, its gradual intensification and the large inland penetration up to the valley, particularly on May 29, was delayed up to 4 hours.

It should be noted that the diurnal cycle of sea surface temperature (SST) affects the evolution of mesoscale systems as sea-land breezes, particularly near coastal areas where land-sea temperature contrast is important (Sweeney *et al.*, 2014) and where sea surface temperature gradients exists, as it occurs in the Gulf of Cádiz (Folkard *et al.*, 1997). However, the daily mean SST value is held constant in time throughout the model run.

Regarding the second issue addressed on this section, concerning whether the sea-land breeze patterns is influenced by the background synoptic or mesoscale winds, it is worth noting that the main features remain, regardless of the wind intensity (strongest average wind is found under non-pure events) and surface temperature (pure breeze days are warmer). Although, the model performs better by reproducing non-pure sea-breeze events, particularly on the Atlantic coast, but it fails by simulating the inland penetration of the sea-breeze front. However, the model presents difficulties to capture the variability of the pure land-breezes, particularly on the Mediterranean coast.

Furthermore, the classification of sea-land breezes in the southwestern Iberian Peninsula (Adame *et al.*, 2010) should be valid to the Mediterranean coast of the Strait of Gibraltar, considering some modifications. These differences are related essentially to the sea-breeze inland penetration, larger during pure sea-breezes, in contrast with the higher horizontal extension of the sea-breeze front of the Atlantic coast during non-pure events. Nevertheless, an exhaustive study with a larger number of data will be required to conclude it.

4.2. Sea-land breezes: quantitative comparison

4.2.1. Daily variability of errors

The output from MM5 has also been statistically compared against meteorological observations to evaluate model skill for winds and air temperature over the region. Table 3.5 summarizes the statistical model evaluation performed for the representative days of each breeze type.

Table 3.5.-Statistical model evaluation for the representative days of pure and non-pure breezes at 0500 UTC and at 1500 UTC. Values within the shaded cells indicate exceedances of the (simple or complex) benchmarks. Boldface numbers denote the best score for each experiment and statistical measure. WS=10 m-Wind Speed; WD=10 m-Wind Direction; T2=2 m-Air Temperature.

	Scores	**BIAS**						**RMSE**		**MAE**			
	Variables	*WS (ms^{-1})*		*WD (º)*		*T2 (℃)*		*WS (ms^{-1})*		*WD*		*T2 (º)*	
	UTC / Dates	*0500*	*1500*	*0500*	*1500*	*0500*	*1500*	*0500*	*1500*	*0500*	*1500*	*0500*	*1500*
Pure	17.May	2.26	**1.33**	23.23	**-10.98**	**-0.32**	-2.99	2.29	**1.56**	53.13	**44.01**	**2.07**	3.01
	18.May	0.86	**0.36**	**-2.79**	17.89	**1.24**	-4.24	1.16	**1.11**	76.50	**62.28**	**2.41**	4.24
Non-pure	28.May	1.85	**1.58**	20.96	**11.59**	-1.68	**-0.92**	**2.05**	2.20	38.21	**30.37**	1.94	**1.50**
	29.May	1.45	**0.45**	**-3.33**	27.51	**0.02**	-1.95	1.61	**1.35**	75.51	**43.87**	**1.50**	2.59

Over the analyzed periods, the model temperature is colder than observed during the day, even more under pure breeze due to extremely clear-sky hot days (Crawford *et al.*, 2001) and warmer during the night, except on May 17 and 28, when winds were more intense.

MM5 better predicts the surface temperature daily evolution during the non-pure event (28-29 May), associated with a synoptic forcing, which modulates the turbulence processes, with a minor daily temperature variation and more vertical mixing.

As it has previously been found in the study of temporal variation of errors, wind direction and wind speed errors are smallest (boldfaced numbers) during the daytime, when the vertical mixing is greatest.

Wind direction errors decrease as the wind is more intense (on May 17 and 28), especially under non-pure breeze events (on May 28). Direction of weak nocturnal winds (on May 18 and 29) is not properly captured by the model as shown by the errors, which fall outside the benchmark values (grey shaded cells).

Meanwhile, the model performs slightly better by reproducing daytime wind speed under pure events, particularly under moderate wind intensity (on May 18). Wind speed and direction biases are, on average, positive, indicating that simulated winds are too geostrophic (with higher wind speed and rotated anticyclonically) during these hours.

4.2.2. Spatial distribution of errors

The influence of the background mesoscale and synoptic winds on the geographical distribution of time-averaged errors is also analyzed considering the representative periods of pure and non-pure breezes, respectively.

Under non-pure breeze event (on May 28 and 29), the signature of the Atlantic sea-breeze regime, enforced by the channelling, affects local circulation extending up to the head of the valley, in agreement with the findings of Melas *et al.* (1998) over Athens basin. So thus, the temperature bias (figure 3.25) shows two opposite patterns with warm bias over plains and the main valley and cold bias at the hills and mountains under non-pure days. MM5 surface temperature is too cool during the extremely hot days of pure breeze event.

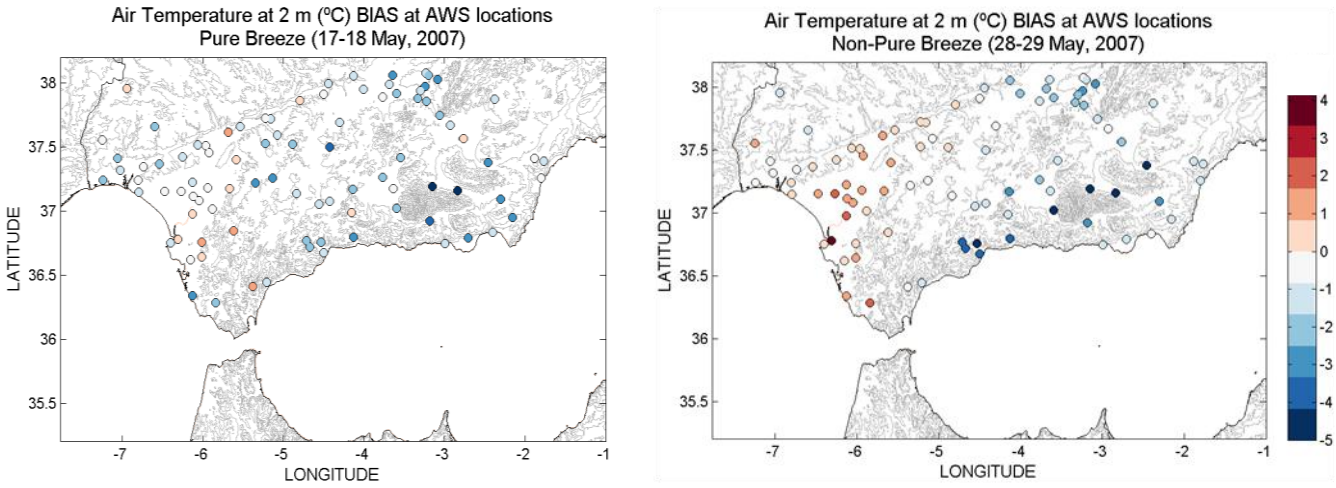

Figure 3.25.- Time-averaged BIAS for air temperature at 2 m under pure-breezes (left) and non-pure-breezes episodes (right).

The MAE spatial variation pattern (figure 3.26) is similar to that of the biases, with the largest errors over the mountains and the lower along the Guadalquivir valley,

indicating a systematic nature of errors. The model performs better by simulating land temperature under non-pure breeze conditions.

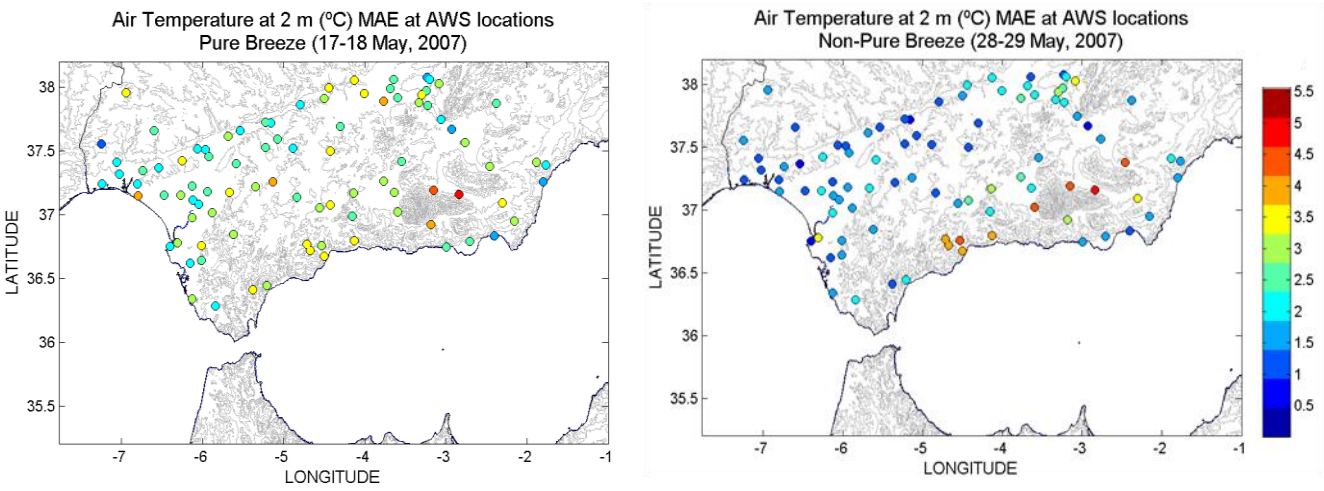

Figure 3.26.- Time-averaged MAE for air temperature at 2 m under pure-breezes (left) and non-pure-breezes episodes (right).

While the observed wind is channelled along the Guadalquivir valley (southwesterly) in non-pure breeze days, simulated winds blow from the northwest, showing a positive bias of wind direction (figure 3.27). Over the mountain ranges wind direction bias is almost inexistent under synoptic conditions.

As mesoscale circulation prevails (pure breeze episode), wind direction bias is reduced along the Guadalquivir Valley, while the bias is positive (anticyclonic rotation) at stations in the nearby of high terrain.

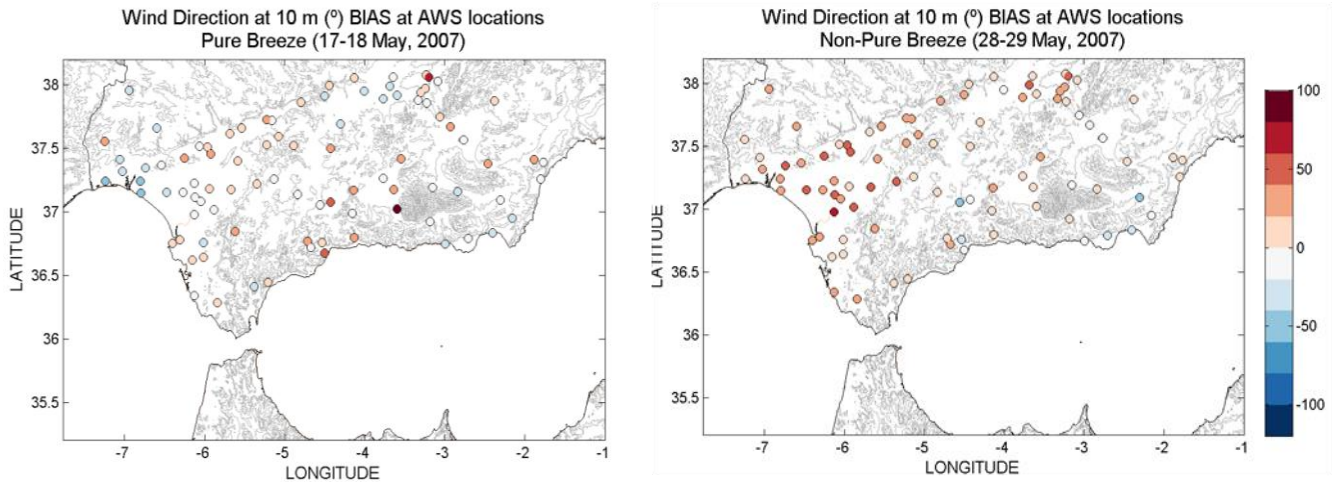

Figure 3.27.- Time-averaged BIAS for wind direction at 10 m under pure-breezes (left) and non-pure-breezes episodes (right).

Wind direction MAE values (figure 3.28) are larger during the days in which the weak wind conditions prevail, particularly under pure breeze and along the

Guadalquivir Valley (parallel to the prevailing northeasterly wind direction). Largest errors are found on the lee side of the mountain ranges.

The model wind direction improves under strong wind conditions, especially under non-pure breeze days and along the orographic depressions and valleys parallel to the northwesterly wind direction (Tinto and Odiel rivers channel, Guadiana Menor valley).

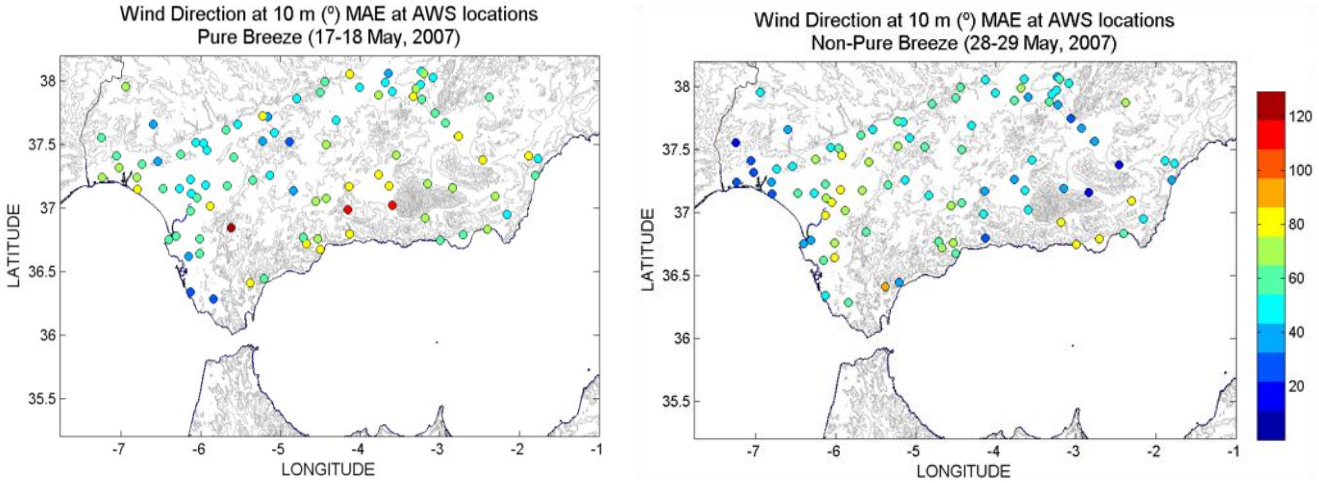

Figure 3.28.- Time-averaged MAE for wind direction at 10 m under pure-breezes (left) and non-pure-breezes episodes (right).

The wind speed is slightly overestimated (figure 3.29) throughout the domain under both synoptic conditions and mesoscale circulation, particularly at stations closer to the Strait of Gibraltar, where strong easterlies blow under the pure breeze event (on May 17 and 18) and along topographic channels parallel to northwesterly winds under non-pure breeze days.

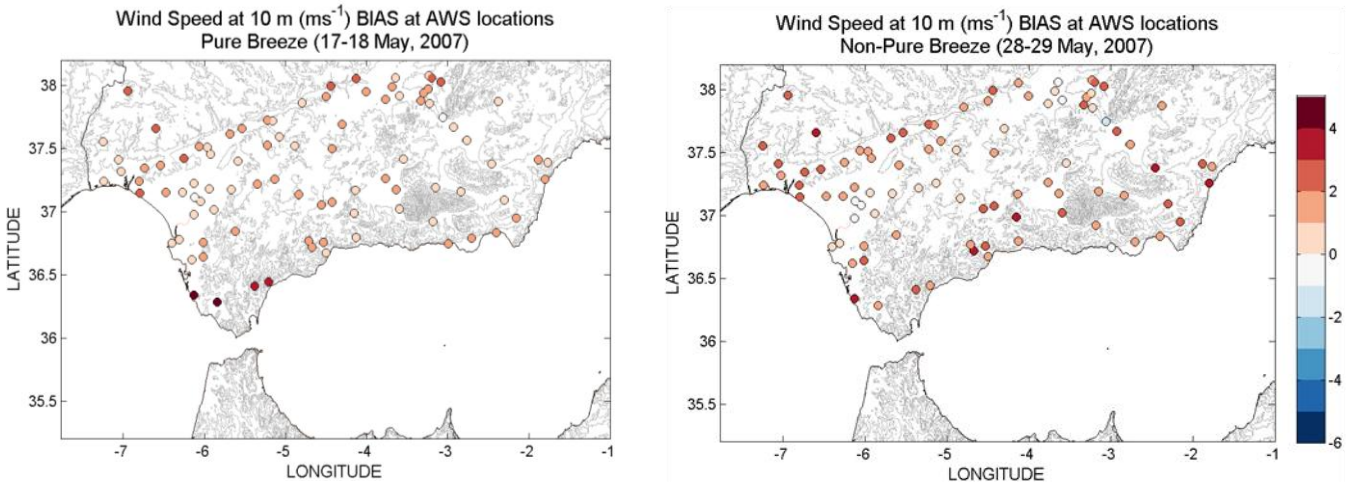

Figure 3.29.- Time-averaged BIAS for wind speed at 10 m under pure-breezes (left) and non-pure-breezes episodes (right).

RMSE values of wind speed (figure 3.30) are lower under mesoscale circulation (pure breeze days), being larger at stations closer to the Strait.

Errors growth on the lee side of the mountain range under synoptic northwesterlies (non-pure breeze days).

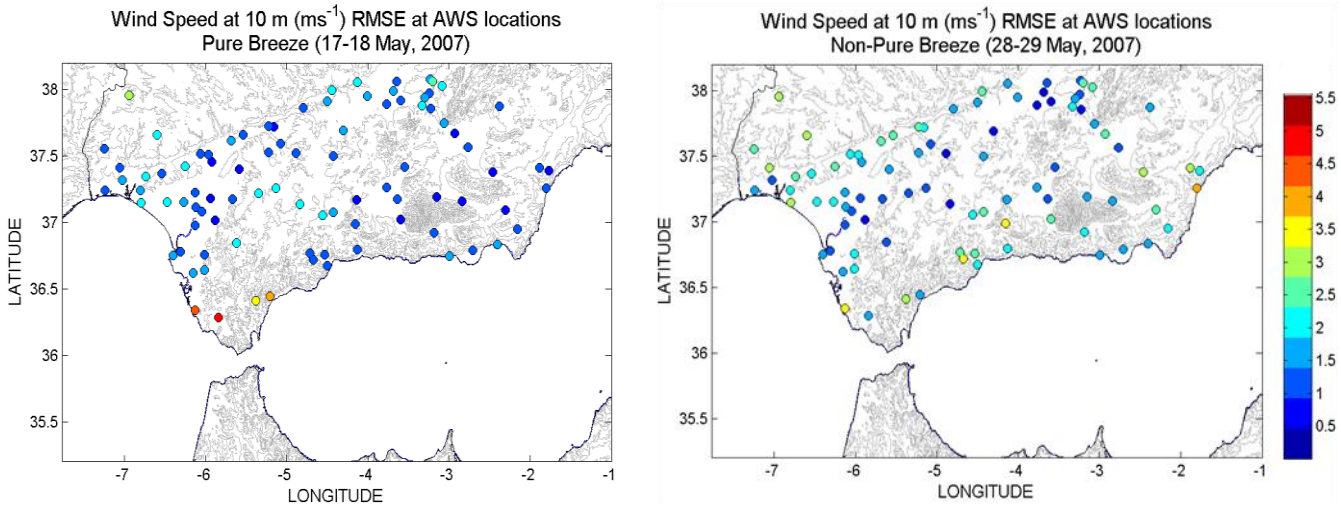

Figure 3.30.- Time-averaged RMSE for wind speed at 10 m under pure-breezes (left) and non-pure-breezes episodes (right).

5. Summary and conclusions

Being the atmospheric model MM5 a very useful free-available tool for modeling the wind-induced ocean circulation, it is fundamental an exhaustive model performance assessment (extensive verification of different combinations of parameterizations, improvement of model options and more detailed physiographic properties -landuse, topography and vegetation-). However, an optimal implementation of the model is beyond the scope of this work.

The goal of the model evaluation carried out, which determines how well specific events are forecast by assessing the realism of the simulation, is to build confidence in the use of the model wind field for an accurate initialization of the ocean model and to identify potential problems in the MM5 meteorological fields for further improvement work.

In this regard, a statistical evaluation of the model performance has been undertaken by means of pairwise comparison of different MM5 runs over the Strait of Gibraltar and observations from more than 100 surface stations on land and 2 deep ocean buoys for different periods related to:

- a sudden transition from westerlies to easterlies, a very common situation within the Strait of Gibraltar (20-23 August, 2004)

- sea-land breezes occurrence with a frequency greater than 30% throughout the month of May 2007.
- strong atmospheric perturbations due to the passage of consecutive cyclones during the period between September the 15th and October the 12th of 2008. Furthermore, this period coincides with the "*Gibraltar'08*" extensive oceanographic survey cruise.

Results of the performance assessment of high-resolution MM5 model in the Strait of Gibraltar are focused into: (i) the impact of horizontal resolution of the model, by examining the relationship between model resolution and predictive skill; (ii) the improvement on the previous model existent in the area, which has been addressed by comparing MM5 outputs with the hydrostatic grid-point HIRLAM; (iii) the impact of different initial conditions, by means of short-term operational forecast and hindcast errors study; (iv) the temporal evolution of the errors and (v) their spatial distribution; (vi) the model ability to correctly simulate mesoscale winds associated with sea-land breezes on the coastal area or mountain-valley breezes hinterland as well as (vii) the spatio-temporal variability of errors under both sea-land breeze events.

In general, the MM5 meteorological model has been shown to qualitative and quantitative reproduce large-scale weather patterns, mesoscale flows in complex terrain, mesoscale phenomena such as land-sea and mountain-valley sea breezes as well as events driven by strong forcing such as cyclones. However, there are some differences between modeled and observed data that can be attributed to model configuration, domain horizontal resolution, deficiencies in the initial and boundary conditions and model physics.

i. Examination of the relationship between model resolution and predictive skills allows to conclude that the MM5-10 km has slightly better wind field skill, particularly by simulating wind speed, than the MM5-30 km domain, but there is no improvement from 10 to 3.3-km. This is likely due to the fact that MM5 produces more stochastic variations at finer resolution, requiring the use of more detailed physiographic properties and an optimal combination of physical parameterizations, which is beyond the scope of this work. For this reason and in order to reduce interpolation errors, which worsen as the grid coarsens, between the atmospheric and ocean model grids, the MM5-10 km has been used to provide the meteorological forcing to the ocean model (~ 1 km nominal).

ii. MM5-10 km improves on the previous model existent in the area, the hydrostatic grid-point HIRLAM.

iii. Evaluation of short-term operational forecast and hindcast error indicates, unexpectedly, that short-term forecast better fits the analyzed meteorological fields inland than hindcast, while over the sea, it occurs the opposite, except for the surface temperature. Nevertheless, variations in model initial and boundary conditions did not significantly affect the model performance, suggesting a major influence of terrain and land-use heterogeneities on wind field.

iv. The MM5 model reproduces the temporal variability of surface temperature and wind field adequately along the month of May 2007. However, it may be concluded that the model underestimates the diurnal temperature range, presenting also difficulties in simulating weak nocturnal winds, shifting wind direction to larger angles.

v. Geographical distribution of errors was studied with the aim to highlighting MM5 shortcomings related to complex topography. Results suggest an error dependency to the terrain elevation and topographical effects, with a better model skill over the Guadalquivir valley and plains than at the hills and Baetic mountain range. Winds are generally overestimated over land, to a lesser extent over plains and valleys and with the highest wind speed and wind direction errors found over the high terrain and near sea-level stations. So thus, simulated winds are anticyclonically rotated from observed and more intense, associated to the unresolved roughness or friction of subgrid terrain, which in turns may indicate deficiencies in the model's representation of the topographic forcing. Surface temperature is clearly overestimated over plains while the hills are characterized by a cold bias.

vi. Pure sea-land breezes were developed under prevailing mesoscale conditions along the entire Andalusian coast whereas only non-pure sea-breezes were onset under synoptic ones and mainly on the Atlantic coast. The MM5 model is able to capture the diurnal wind oscillation associated with both sea-land breeze circulation patterns. However, the model performs better by reproducing non-pure sea-breeze events, particularly on the Atlantic coast, but it delays the sea-breeze front onset, its gradually intensification and the large inland penetration up to the Guadalquivir valley, which may be related to the use of constant SST in coastal areas where large temperature gradients between land and water exist.

At the same time, the model presents difficulties to capture the variability of the pure land-breezes, particularly on the Mediterranean coast.

vii. MM5 performs better by simulating land temperature under non-pure breeze conditions, particularly over the main valley and plains. The model wind direction improves under strong synoptic wind conditions of these days (28-29 May), particularly along the orographic depressions and valleys parallel to the northwesterly wind direction. Weak mesoscale winds and too warm surface temperature during the pure-breeze event trigger larger errors in wind direction and temperature, while the model better simulates daytime wind speed with the larger errors found at coastal stations closer to the Strait.

Capítulo 4

A high-resolution model for the wind-forced circulation in the Strait of Gibraltar

Capítulo 4

A HIGH-RESOLUTION MODEL FOR THE WIND-FORCED CIRCULATION IN THE STRAIT OF GIBRALTAR

The Strait of Gibraltar connects the Atlantic Ocean with the Mediterranean Sea. The mean circulation through the strait is composed of two counter flowing currents. In the upper layer Atlantic water flows eastward, toward the Mediterranean, and in the lower layer Mediterranean water flows westward, toward the Atlantic (Stommel & Farmer, 1953; Lacombe & Richez, 1982; Farmer & Armi, 1986; Bryden & Kinder, 1991; Bryden *et al.*, 1994).

Tidal currents (Lacombe & Richez, 1982; Candela *et al.*, 1990) and atmospheric pressure variations (Crepon, 1965; Candela *et al.*, 1989; García-Lafuente *et al.*, 2002a; Vázquez *et al.*, 2008) modulate the resulting mean exchange flow, as it does the direct action of the winds along the Strait (García-Lafuente *et al.*, 2002c; Macías *et al.*, 2008; Peliz *et al.*, 2009).

While tidal currents and the role of the atmospheric forcing, as the main driving force acting at subinertial frequencies in the Strait of Gibraltar, have been analyzed in depth in previous research, results have, however, not been conclusive so far, as subinertial flow fluctuations cannot be explained by atmospheric pressure variability

alone (García-Lafuente *et al.*, 2002a). The joint effect of wind stress was necessary to explain the fluctuations in some particular events.

In this chapter, we first evaluate the implementation of wind-stress forcing to the hydrodynamic model at high-resolution by comparing its output with observations. Then, we assess how the wind-forced ocean model simulates the response of the circulation to wind stress in relation to the ocean-alone model with tidal forcing. Finally, the fluctuations of the flow exchange and changes in the hydraulic control due to wind stress forcing in the Strait of Gibraltar are analyzed.

1. Validation of the wind-forced ocean model

Previous research (Sein *et al.*, 1998; Izquierdo *et al.*, 2001; Brandt *et al.*, 2004; Sannino, 2007) proved the UCA2.5D hydrodynamic model to be reliable for simulating tidal dynamics, the generation of interfacial disturbances (at Camarinal sill), the baroclinic exchange and internal bore propagation eastwards. It also predicts the occurrence of four averaged (over a tropical month) controls located to the west of the Espartel Sill, at the Espartel and Camarinal Sills and an apparent control in the Tarifa Narrows (Izquierdo *et al.*, 2001).

Once the wind-stress forcing was included in the hydrodynamic model, a validation of the simulation results have been carried out, comparing them with available observations.

Results obtained from the TIDE-WIND (the simulation includes tidal forcing and realistic wind field from the MM5-10 km) experiment (see figure 2.13 for further information related to the set of experiments performed) are compared with one-month current velocity data from a single-point current-meter deployed at the north of Camarinal Sill during the intensive oceanographic survey "*Gibraltar'08*". One-full-year period (1995) was also selected to allow validation against ADCP data measured over Camarinal Sill during the experiment "*Strait 94-96"*. Output was also compared with sea level data from three tide gauge stations, the interface depth obtained in the sigmoidal fit to salinity profiles from CTD casts, as well as with the lagrangian trajectories reported by surface drifters released in the area.

1.1. Model versus CTD casts

Simulated interface depth was compared with the interface depth range obtained in the sigmoidal fit to salinity profiles from CTD casts (figure 4.1), collected at five

different locations, during "*Gibraltar-08*" survey, under different tidal cycle conditions, referenced to the tidal level in Tarifa (005° 36.00' W - 36° 00.00' N). The effect of water column mixing and, therefore, the differences of the halocline thickness on the model reproduction of the interface depth, are also analyzed at each one of selected CTD stations.

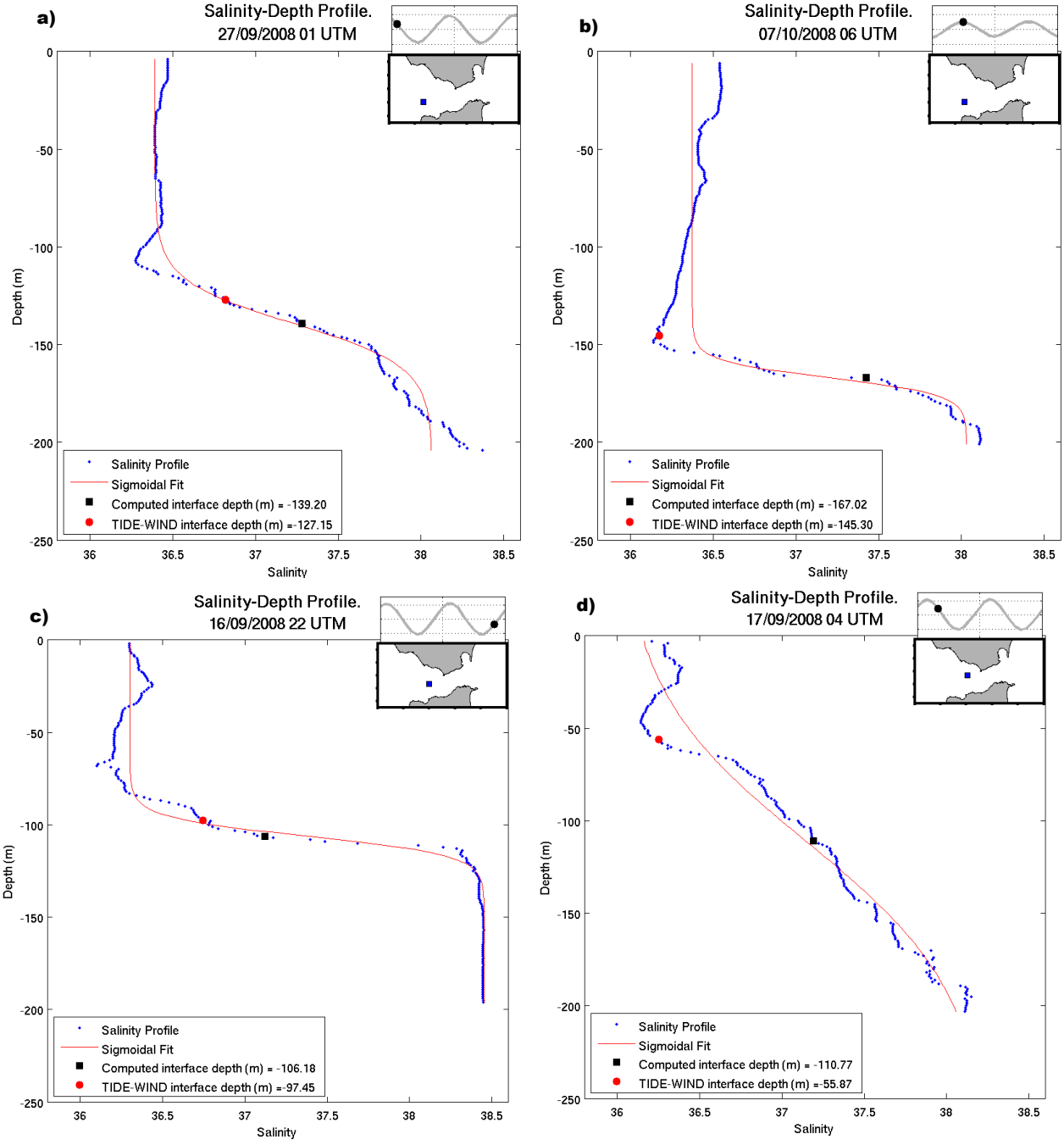

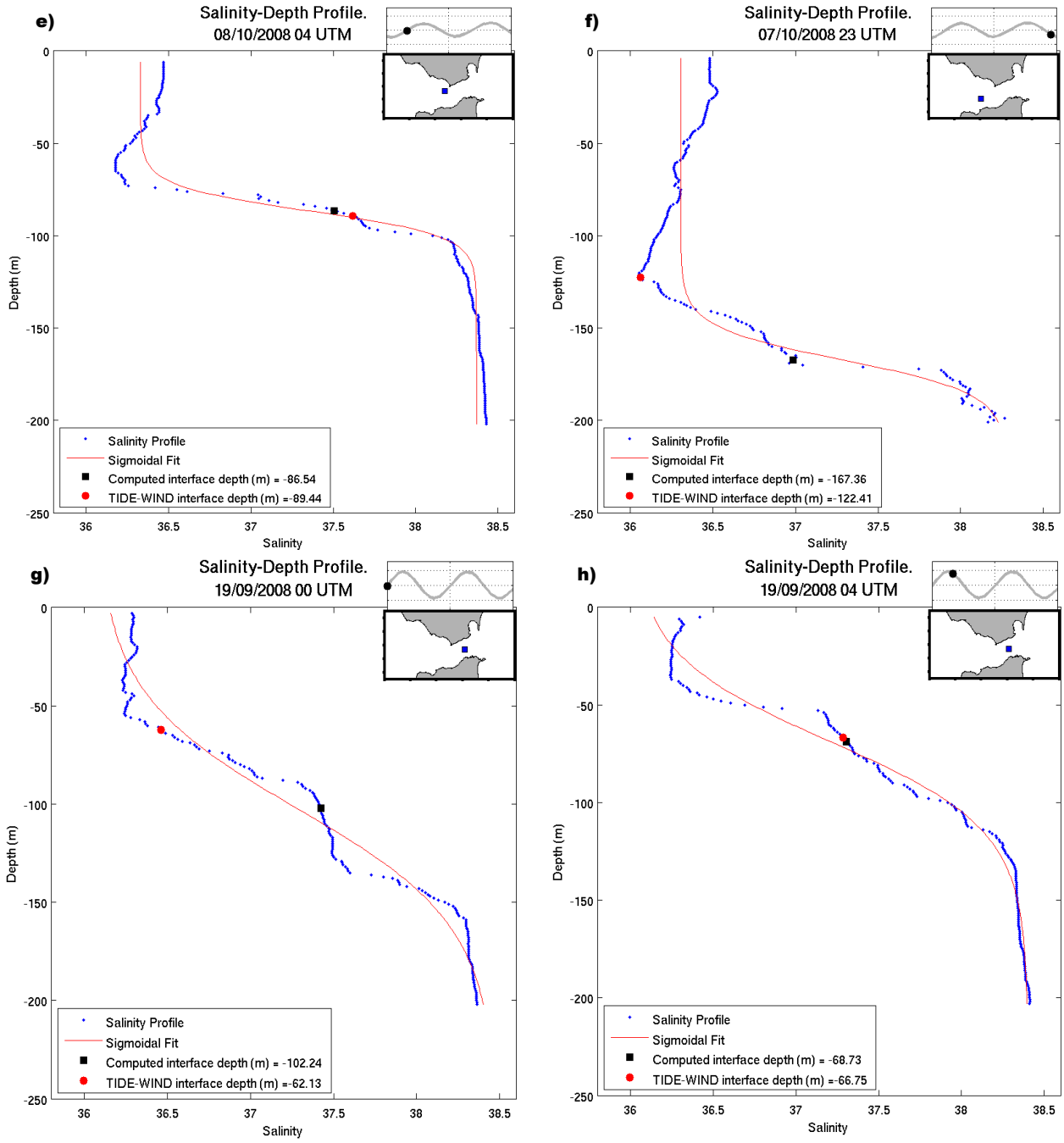
e)
Salinity-Depth Profile.
08/10/2008 04 UTM
Salinity Profile
Sigmoidal Fit
Computed interface depth (m) = -86.54
TIDE-WIND interface depth (m) =-89.44
f)
Salinity-Depth Profile.
07/10/2008 23 UTM
Salinity Profile
Sigmoidal Fit
Computed interface depth (m) = -167.36
TIDE-WIND interface depth (m) =-122.41
g)
Salinity-Depth Profile.
19/09/2008 00 UTM
Salinity Profile
Sigmoidal Fit
Computed interface depth (m) = -102.24
TIDE-WIND interface depth (m) =-62.13
h)
Salinity-Depth Profile.
19/09/2008 04 UTM
Salinity Profile
Sigmoidal Fit
Computed interface depth (m) = -68.73
TIDE-WIND interface depth (m) =-66.75
Depth (m)
Salinity

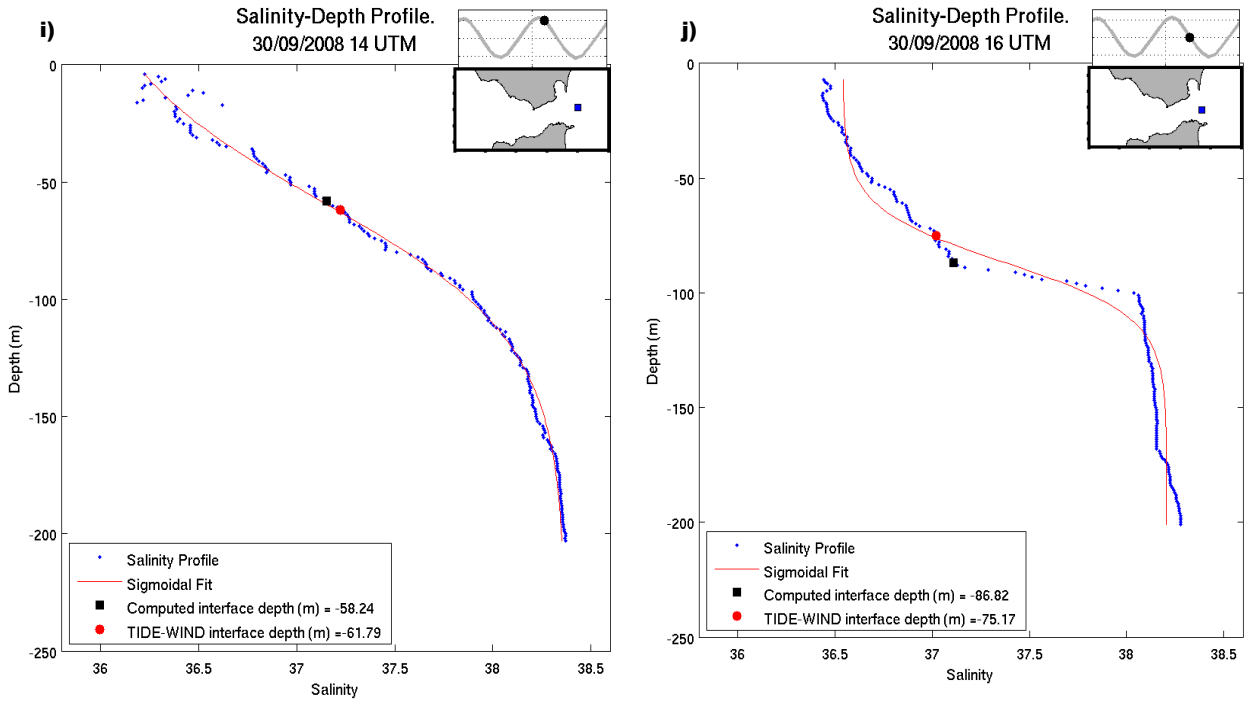

Figure 4.1.- Salinity profiles (blue points) along with sigmoidal fits (red lines) for different CTD stations (blue squares in the inset). The estimated interface depth (black square) and simulated (red point) by the TIDE-WIND experiment are also shown. Sea-level prediction at Tarifa is presented (black circle marks the moment when the CTD profile was made).

The simulated interface depth is always within the range of depths of the halocline and it matches the interface depth value of the sigmoidal fit at almost all stations. The assessment of the model becomes better under weak mixing conditions, when a well-developed piece-wise salinity profile is observed (a, b, c, e, h, i, j from figure 4.1). In this case, the two-layer hydrodynamic model is a good approximation to the true system dynamics. When the water column is continuously stratified, the halocline stretches in the vertical and the two-layer approximation is no longer valid (d and g from figure 4.1).

Note also that the simulated interface is, in some cases, significantly shallower than the one obtained from the sigmoidal fitness. This could be related to the fact that the mixing processes are neglected in the hydrodynamic model (Izquierdo *et al.*, 2001; Brandt *et al.*, 2004) and also due to the uncertainties introduced by the definition of the interface. In this sense, it must also be pointed out that the definitions of the interface as the depth of maximum vertical shear of the horizontal current velocity $\left(\frac{\partial U}{\partial z}\right)$ and as the maximum vertical salinity gradient $\left(\frac{\partial S}{\partial z}\right)$ coincide in the hydrodynamic model, although it is known that shear and halocline do not necessarily correspond (Pettigrew & Hyde, 1990) in the instantaneous flow.

Nevertheless, it must also be borne in mind that the fitting procedure approximates the real profiles with varying success (Bray *et al.*, 1995) and it could introduce some bias into the interface structure (see profile d from figure 4.1).

1.2. Model versus current meters

Validation of the along-strait current, simulated by the TIDE-WIND experiment, has also been performed against measurements of a current meter deployed at the northern part of Camarinal Sill (005° 44.31' W - 35° 58.85' N), placed at 120 m depth.

Despite the CTD salinity profile shows (figure 4.2) that the current meter lies in the lower limit of the upper layer, it is important to bear in mind that it is moored at the depth range over which the interface fluctuates along the tidal cycle (see red crosses in figure 4.2) and this fact is clearly reflected in the value of the mean along-strait velocity (0.022 $m \cdot s^{-1}$), close to zero[1].

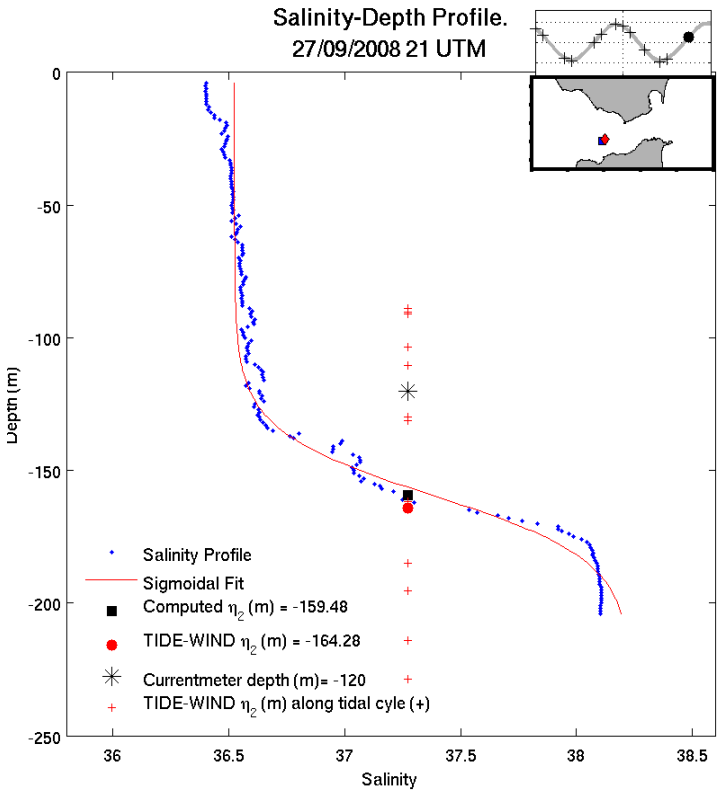

Figure 4.2. - Salinity profile (blue points) along with sigmoidal fit (red line) measured by CTD cast on the mooring place (red diamond). The estimated interface depth, η_2, (black square) and simulated (red point) by the TIDE-WIND experiment are also displayed. Sea-level prediction at Tarifa is presented (black circle marks the moment when CTD profile was made). Locations of the simulated interface (red crosses) within a tidal cycle (black crosses) are shown.

[1] The easier and more obvious definition of the interface is the surface of zero along strait velocity (Bray *et al.*, 1995). Other definitions are the surface of a certain salinity or the surface of maximum vertical shear of horizontal velocity.

Nevertheless, the measured current anomaly exhibits subinertial variations, which are assumed to be related to the atmospheric forcing and to the fortnightly tidal signal. So thus, the anomaly of the simulated subinertial upper layer along-strait current has been calculated, as the deviation from its mean value over the analyzed period, and it has been compared with the anomaly of the observations (figure 4.3). Additionally, the wind speed and direction at Camarinal Sill, and the atmospheric sea level pressure difference between the Alboran sea (3° 2' 22" W, 35° 58' 37" N) and the Camarinal Sill (6° 0' 1.4" W, 35° 59' 12"), simulated by the atmospheric model, are included in the figure 4.3, top.

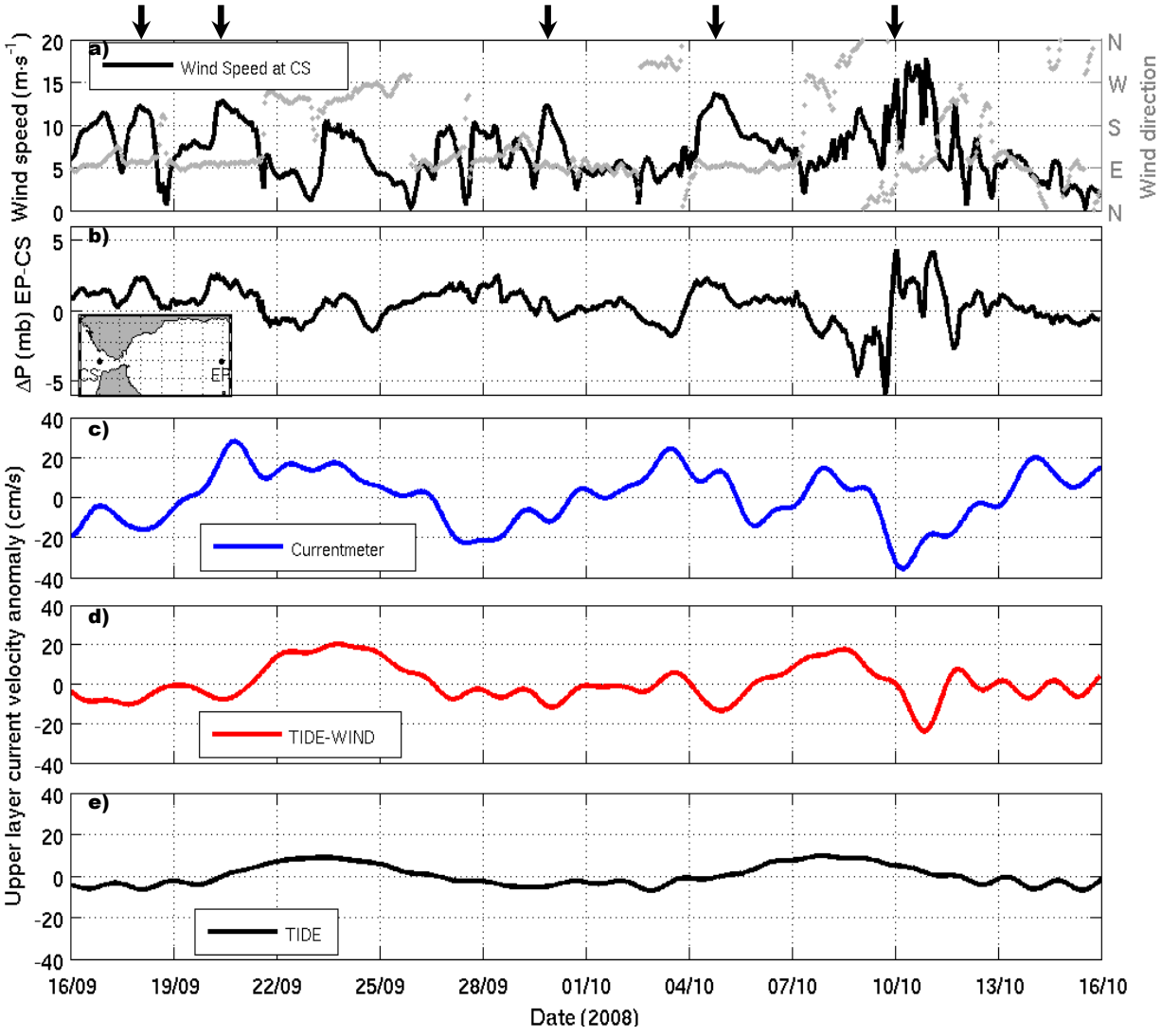

Figure 4.3. - Simulated wind speed (black line) and direction (grey dots) over Camarinal Sill (a) and along-strait sea level pressure difference between an eastern point (EP) and CS (b). Subinertial upper layer current velocity anomaly measured by the current meter (c), simulated by the TIDE-WIND (d) and by TIDE (e) experiments. Black arrows indicate the strong easterly wind events mentioned in the text.

It is worth noting that the correlation between the wind speed and the atmospheric sea level pressure difference along the Strait is very high, especially during strong easterly events, due to the ageostrophic nature of the winds in the area.

The comparison shows that, in general, the wind-forced model reproduces the subinertial variability of the along-strait current. Both, observed and modeled currents reverse (negative values toward the Atlantic) in response to easterly wind episodes (18/09, 20/09, 30/09, 05/10, 10/10 marked with black arrows in the figure 4.3), which are link to the atmospheric pressure increase at the eastern part of the Strait.

Particular attention should be given to the upper layer current decrease in response to easterly wind episode on October 10, 2008, related to a cyclone crossing the Strait westward, which triggered a 6 mb sea level pressure difference down the strait and low-level flow acceleration (see section 2.1 of Chapter 3 for further information).

The results noticeably improve for currents simulated by the wind-forced ocean model, as compared to the simulated current with tidal forcing alone.

One year of ADCP measurements over Camarinal Sill, from the experiment "*Strait 94-96"*, were also used to assess the model performance (figure 4.4).

The depth of maximum vertical shear of the subinertial along-strait velocity, used as interface definition (Pettigrew & Hyde, 1990; Tsimplis & Bryden, 2000), when salinity observations were not available, was computed from current profiles registered by the ADCP moored over Camarinal Sill. This definition of the interface allows us to make a two-layer decomposition of current profiles, comparing the subinertial along-strait current for the upper and lower layer, against the simulated ones (figure 4.6) and the depth of maximum vertical shear against the simulated interface depth (figure 4.7).

The semi-diurnal tide dominates high-frequency record in the Hovmöller diagram (figure 4.4, middle) revealing the reversion of the current, even near the bottom at each tidal cycle, which is even more evident during spring tides.

A low-pass filter (33-hour cut-off period) was applied to the hourly time series to remove tidal and inertial currents, thus obtaining subinertial series (figure 4.4, bottom). At the subinertial period the diagram shows the two layer structure of the flow over Camarinal Sill, with the depth of maximum vertical shear separating the eastward flow at the surface and the westward flow at depth. The maximum shear defined interface oscillates in a range of 60 m at the fortnightly frequency. In some episodes the interface reaches the near surface, disappearing the upper layer. The mean depth of the shear interface of 155 m, 8 m deeper than the value reported by (Tsimplis & Bryden, 2000).

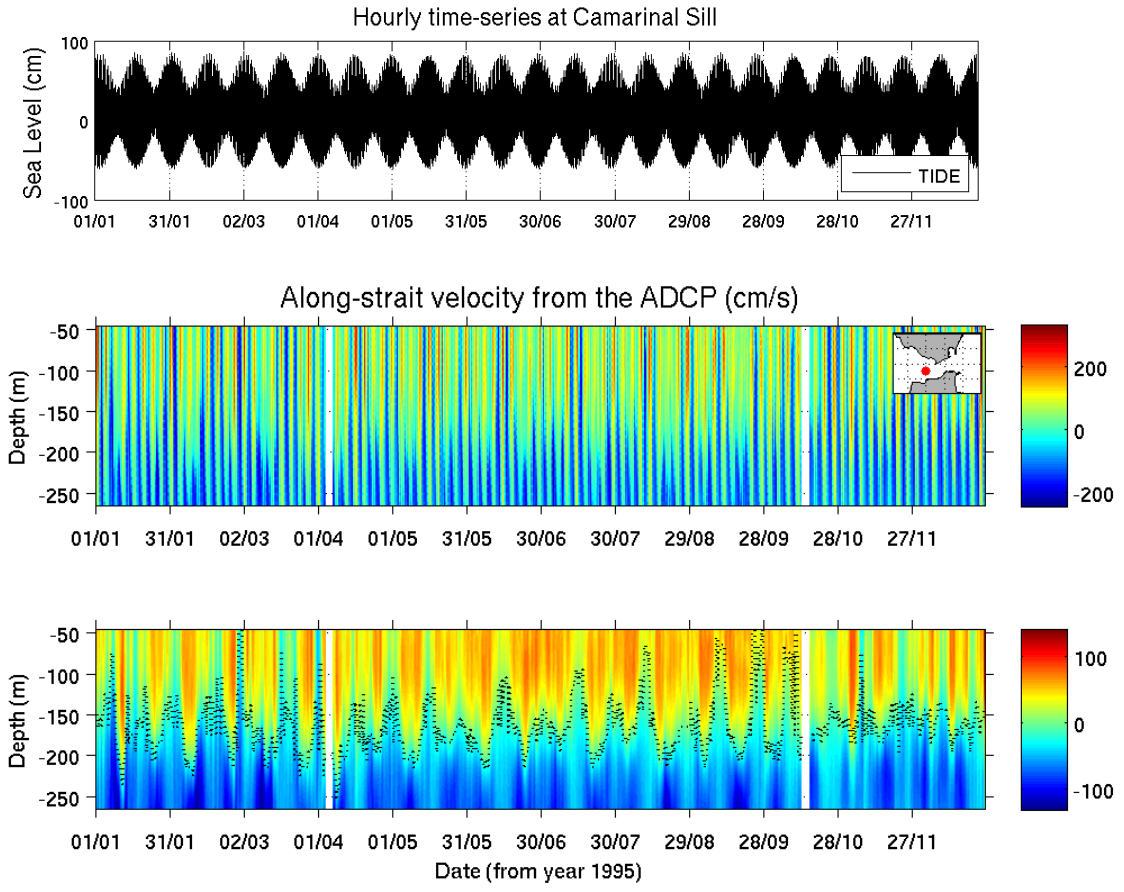

Figure 4.4.- Sea level at Camarinal Sill (top) from the TIDE run and Hovmöller diagrams of the along-strait current component from the ADCP (flowing eastward -positive values-): hourly records (middle) and low-pass filtered records with a cut-off period at 33 hours (bottom). The depth of maximum vertical shear is also plotted (dashed black line).

The vertical structure of the speed and direction of the mean current (figure 4.5) also reveals the two-layer character of the flow. The upper layer flows toward the Mediterranean Sea with a mean velocity of 0.42 $m \cdot s^{-1}$ (figure 4.5, center). Below 155 m, the water flows toward the Atlantic with gradually increasing velocity reaching a maximum mean value of 0.92 $m \cdot s^{-1}$.

The gradual change of the speed of the mean flow between 145 and 205 m indicates the depth range over which the interface fluctuates as a result of tidal oscillations. In order to carry out a two-layer decomposition of the ADCP velocities with the aim to be compared with the two-layer model predictions, we have ignored all bins located in this range of depths, diminishing the error of considering the interface layer as part of the upper or of the lower layer.

Maximum along-strait current is 0.42 $m \cdot s^{-1}$ toward the Atlantic layer, while in the lower layer the intensity increases up to 0.75 $m \cdot s^{-1}$ (figure 4.5, left).

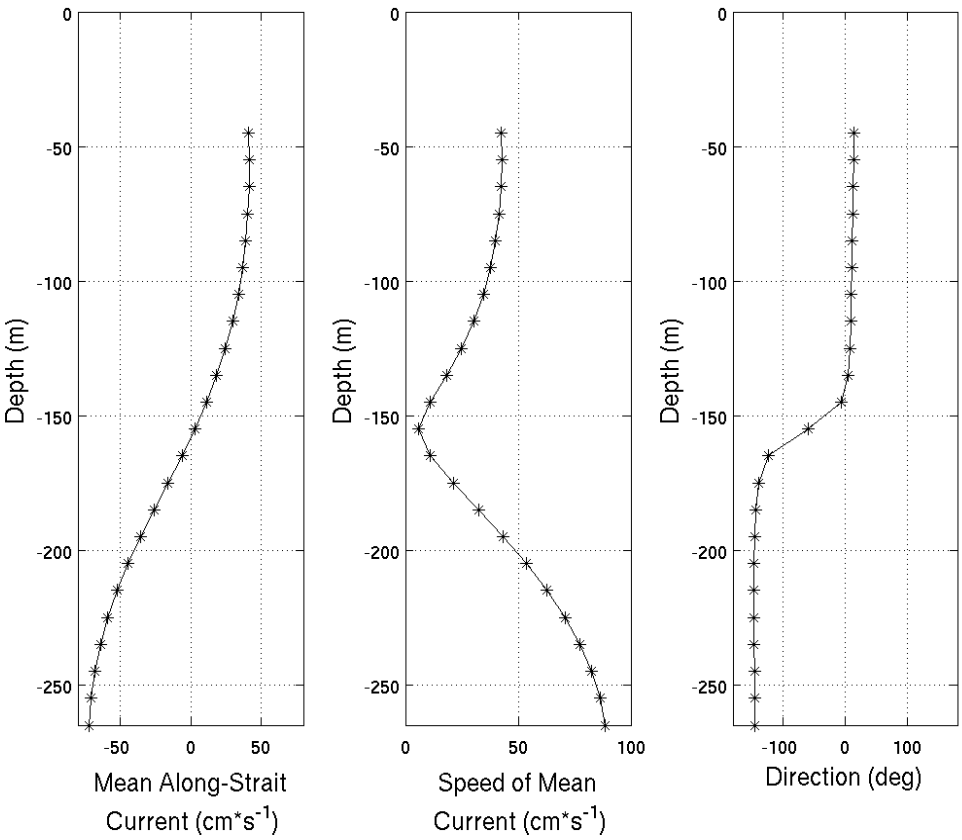

Figure 4.5.- Vertical distribution of the mean along-strait current (left), horizontal current velocity module (center) and direction (right) measured by the ADCP at Camarinal Sill.

The variability of the observed subinertial series responds, besides the fortnightly tidal signal and the atmospheric pressure variability, to the wind forcing. Subinertial upper layer current is able to reverse in very exceptional situations, mostly

related to extreme meteorological forcing. Most of these episodes occur during intense easterly winds over 15 $m \cdot s^{-1}$, as indicated by the black arrows in the figure 4.6.

Figure 4.6 also reveals a significant fortnightly signal of the lower layer current, either computed with observation or simulated by models, with a maximum velocity toward the Atlantic during neap tides. Simulated amplitudes are larger than the observed ones.

Mean values, over the analyzed period, for the ADCP upper and lower layer along-strait currents are 0.33 $m \cdot s^{-1}$ and 0.62 $m \cdot s^{-1}$, respectively. For the TIDE run, current mean values are 0.23 $m \cdot s^{-1}$ and 0.72 $m \cdot s^{-1}$, for the upper and lower layers, respectively, whereas for the TIDE-WIND experiments values are 0.24 $m \cdot s^{-1}$ and 0.78 $m \cdot s^{-1}$.

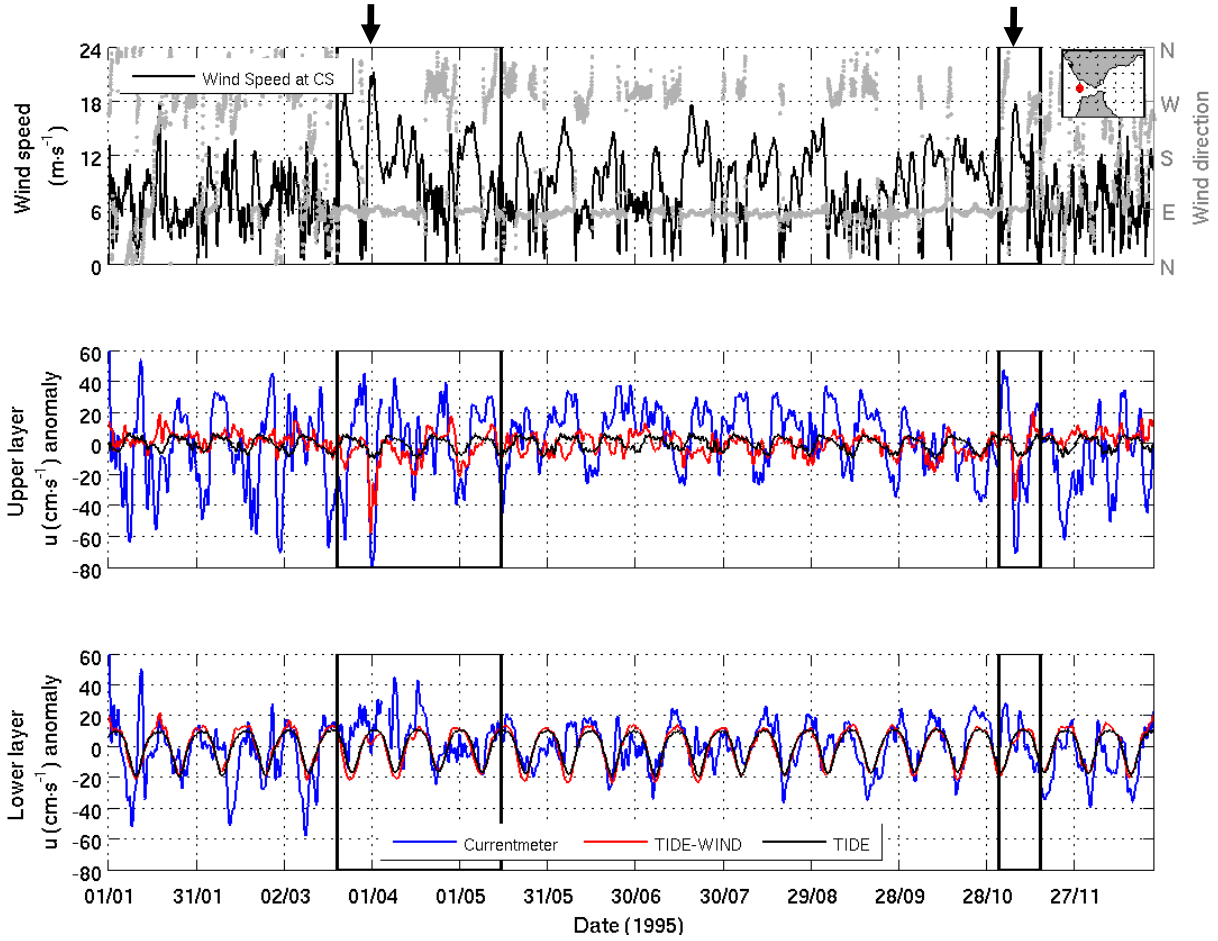

Figure 4.6. - Wind speed and direction (grey points) at Camarinal Sill (top). Upper (middle) and lower (bottom) layer along-strait current anomaly from the ADCP (blue line), from the TIDE (black line) and TIDE-WIND (red line) experiments. Black arrows indicate the strong easterly wind events mentioned in the text. Black boxes contain the periods shown in figure 4.8.

The fortnightly variability is also observed in the interface depth at Camarinal Sill (figure 4.7) with a deeper interface at neap tides and a shallower one at spring tides.

The simulated exchange interface is shallower (with a mean depth of 115.7 m for the TIDE-WIND and 109.3 m for the TIDE experiments, respectively) than the surface of maximum vertical shear of the horizontal velocity (with a mean value of 155 m depth) computed from the data of ADCP, due to the absence of model mixing. Nevertheless, the mean value of the wind-forced ocean model is closer to the mean interface depth observed than the one of the TIDE experiment.

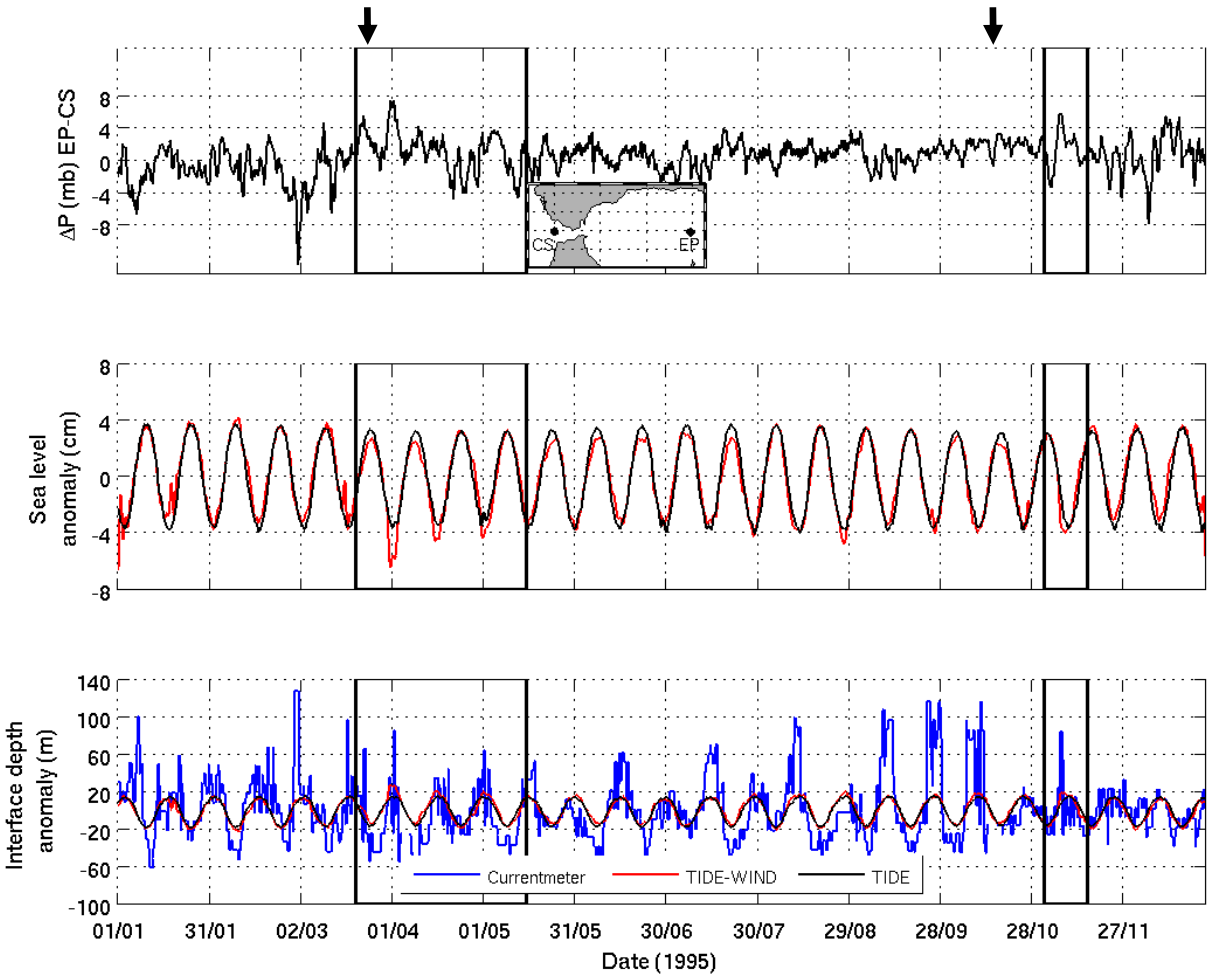

Figure 4.7. - Atmospheric sea level pressure difference along the Strait between points EP and CS (top). Sea level (middle) and interface depth (bottom) anomalies from the ADCP (blue line), the TIDE (black line) and the TIDE-WIND (red line) experiments. Black arrows indicate the strong easterly wind events mentioned in the text. Black boxes contain the periods shown in figure 4.8.

Note the extreme reversion episodes marked within the black boxes on the first day of April 1995 and on the 7th of November 1995 (see black arrows in figure 4.6 and figure 4.7), during spring tides, with easterly winds blowing up to 20 m·s^{-1} and 18 m·s^{-1}, respectively. On April 1, (figure 4.8, left), observations and TIDE-WIND simulated upper layer along-strait current anomalies reach -0.78 m·s^{-1} and -0.56 m·s^{-1} (toward the Atlantic), respectively. Even in the lower layer, the velocity increases toward the

Atlantic. On another hand, TIDE-WIND simulated interface rises almost 25 m and the sea level drops 6.3 cm above and below the mean values, respectively. Observed interface also rises 35.53 m above its mean value. On November 7, (figure 4.8, right), both observations and TIDE-WIND upper layer current anomalies flow westward reaching -0.70 and -0.36 $m \cdot s^{-1}$. Mediterranean outflow velocity is also slightly increased, while the interface shallows 19 m and 84 m from TIDE-WIND and observations, respectively. The sea level drops 4 cm in the TIDE-WIND experiment.

Similar behaviour has been found for all easterly wind episodes analyzed (see yellow shaded areas in figure 4.8) and results vary according to the wind speed.

In the case of westerlies (grey shaded areas in figure 4.8), the opposite ocean's response has been identified over the main Sill. Both, upper and lower layer velocities increase eastwards, the sea level rises and the interface becomes deeper, particularly with wind speed greater than 8 $m \cdot s^{-1}$.

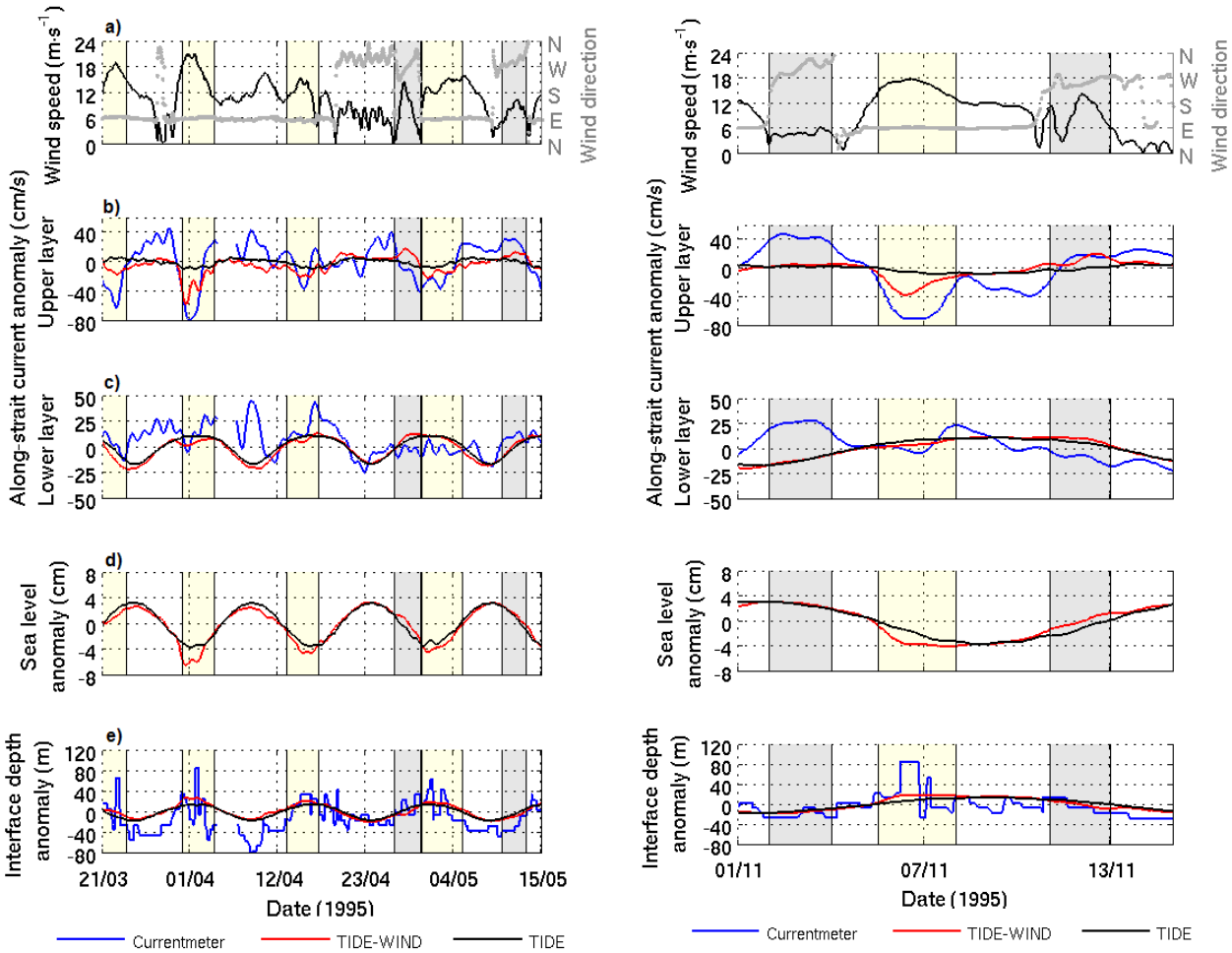

Figure 4.8. - Wind speed and direction (grey points) at Camarinal Sill (a). Upper (b) and lower (c) layer along-strait current anomaly. Sea level (d) and interface (e) anomaly from the ADCP (blue line), from the TIDE (black line) and TIDE-WIND (red line) experiments. Yellow and grey shaded areas indicate easterly and westerly winds events, respectively.

Wind-forced ocean model (TIDE-WIND experiment) drastically improve the subinertial fluctuations in the observations, due to the intense winds, regarding to the hydrodynamic model (TIDE experiment), showing the importance of the wind to reproduce the subinercial variability of the currents.

1.3. Model versus surface drifters

In October 2011, four surface drifters were released in the vicinity of Punta Carnero (Algeciras Bay), at the eastern entrance of the Strait. At the release time and during the following days, easterly wind prevailed in the area (figure 4.9).

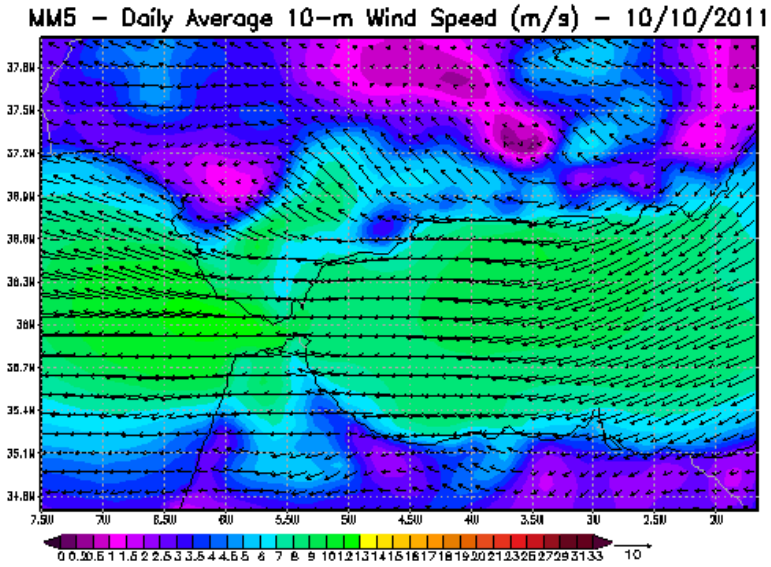

Figure 4.9. - MM5-10 km daily-averaged wind field on October 10, 2011.

Figure 4.10 presents the comparison of the four observed drifters and numerical particles trajectories for October 2011, simulated by the TIDE and TIDE-WIND experiments.

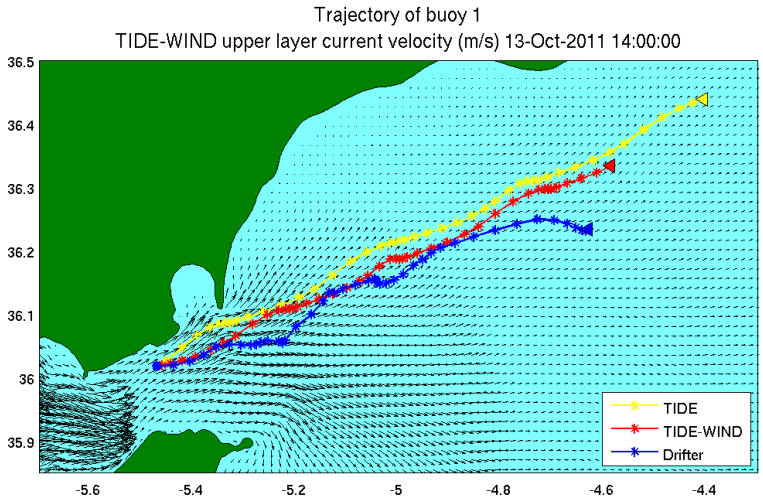

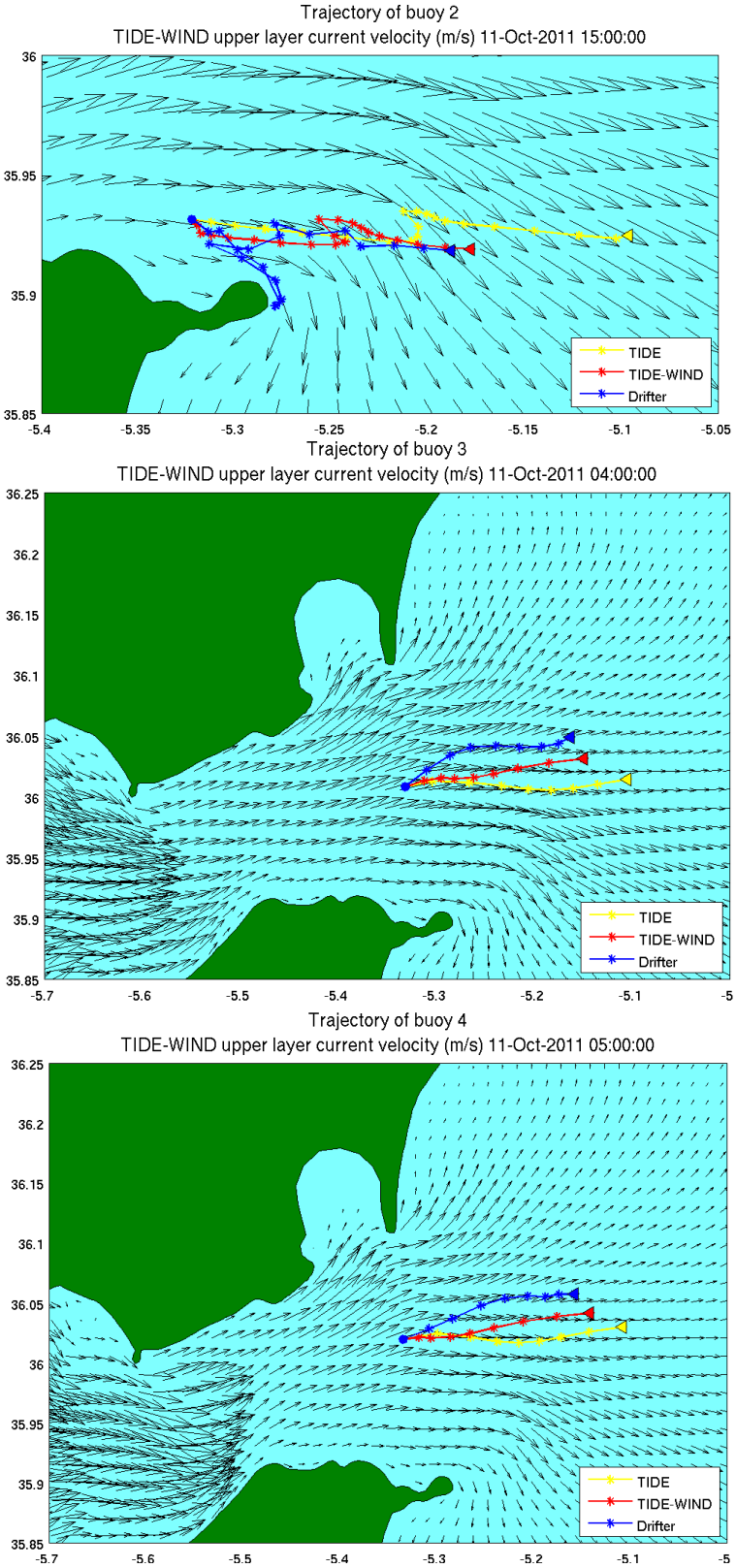

Figure 4.10. - Tracks of surface drifters (blue lines) and virtual drifters released into the TIDE (yellow lines) and TIDE-WIND (red lines) experiments. Points and triangles denote the start and the end of the tracks, respectively. TIDE-WIND upper layer current field map (arrows) corresponds to the last tracked hour.

In each case, the numerical drifter trajectories simulated using the wind-forced ocean model provide better agreement with the observed drifters. Particularly, in the case of the drifter number 1 during the first hours of deployment the distance between observed and modeled pathways is minimal while they are trapped in the Atlantic Jet. However, the numerical drifter pathways diverge from the observed once the latter enters in western boundary of the Western Alboran Gyre (WAG), which can not be properly reproduced by a two-layer model (Wang, 1987; Speich *et al.*, 1996).

The gyre seems to be in development during these days as suggested by the satellite-derived spatial distributions of Chl-a concentration from October 13, 2011. Satellite image (figure 4.11) shows a high productivity linked to the frontal zone associated to the northern edge of the WAG, justifying the surface drifter track.

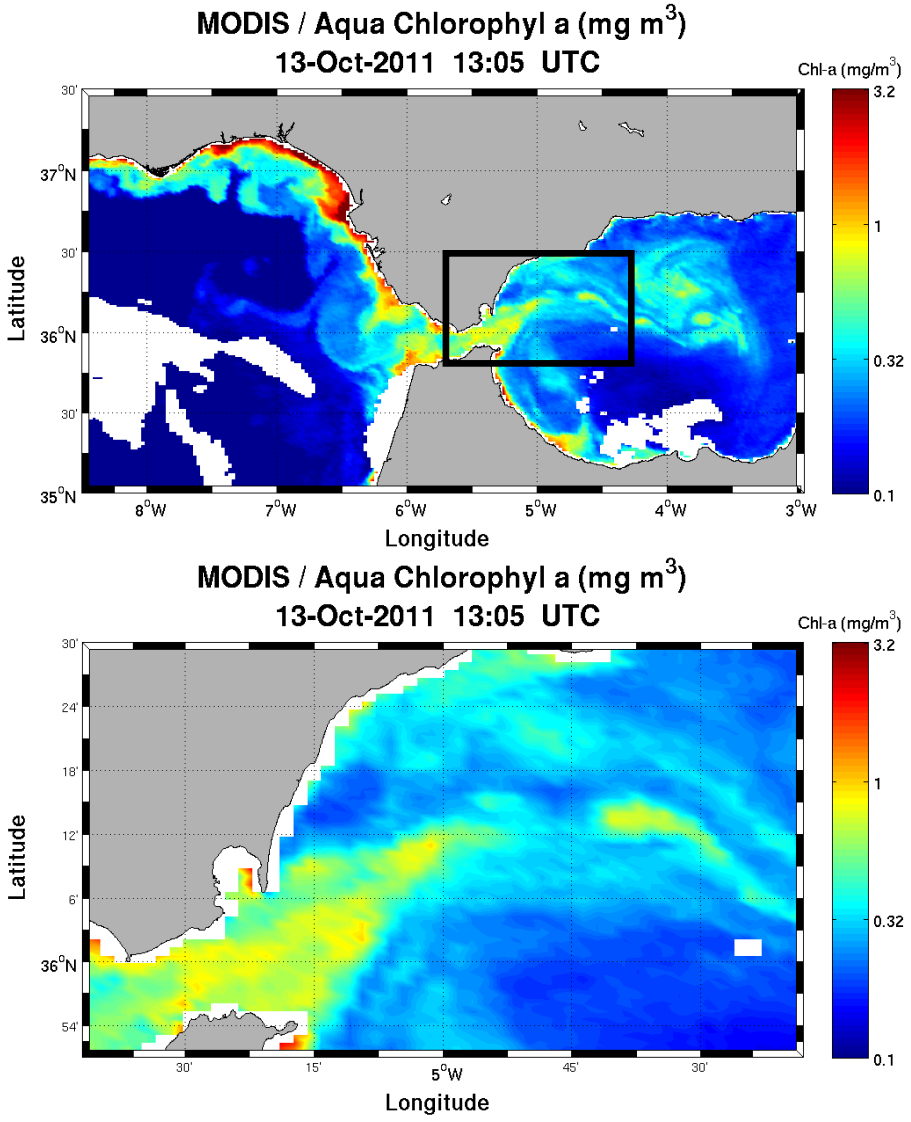

Figure 4.11.- MODIS / Aqua chlorophyll-a concentration satellite image over the study area (top) and a zoom (bottom) over the area covered by the first drifter track, marked with a black box.

The first track of the drifter number 1 reveals the existence of a semi-permanent westward countercurrent along the northern coast of the Strait. A countercurrent of such intensity and extension has not been reported before in this area. TIDE and TIDE-WIND experiments are also able to reproduce the coastal-counter-current (CCC), although on a more intermittent basis (in space and time). While TIDE experiment simulates an episodic and discontinuously distributed countercurrent along a narrow coastal strip, TIDE-WIND experiment reproduces a fully developed CCC along a continuous and wider band from Punta Europa to Tarifa.

Taking advantage of the high-resolution curvilinear grid of the model, figure 4.12 shows the upper layer current vectors and the drifter track for both experiments.

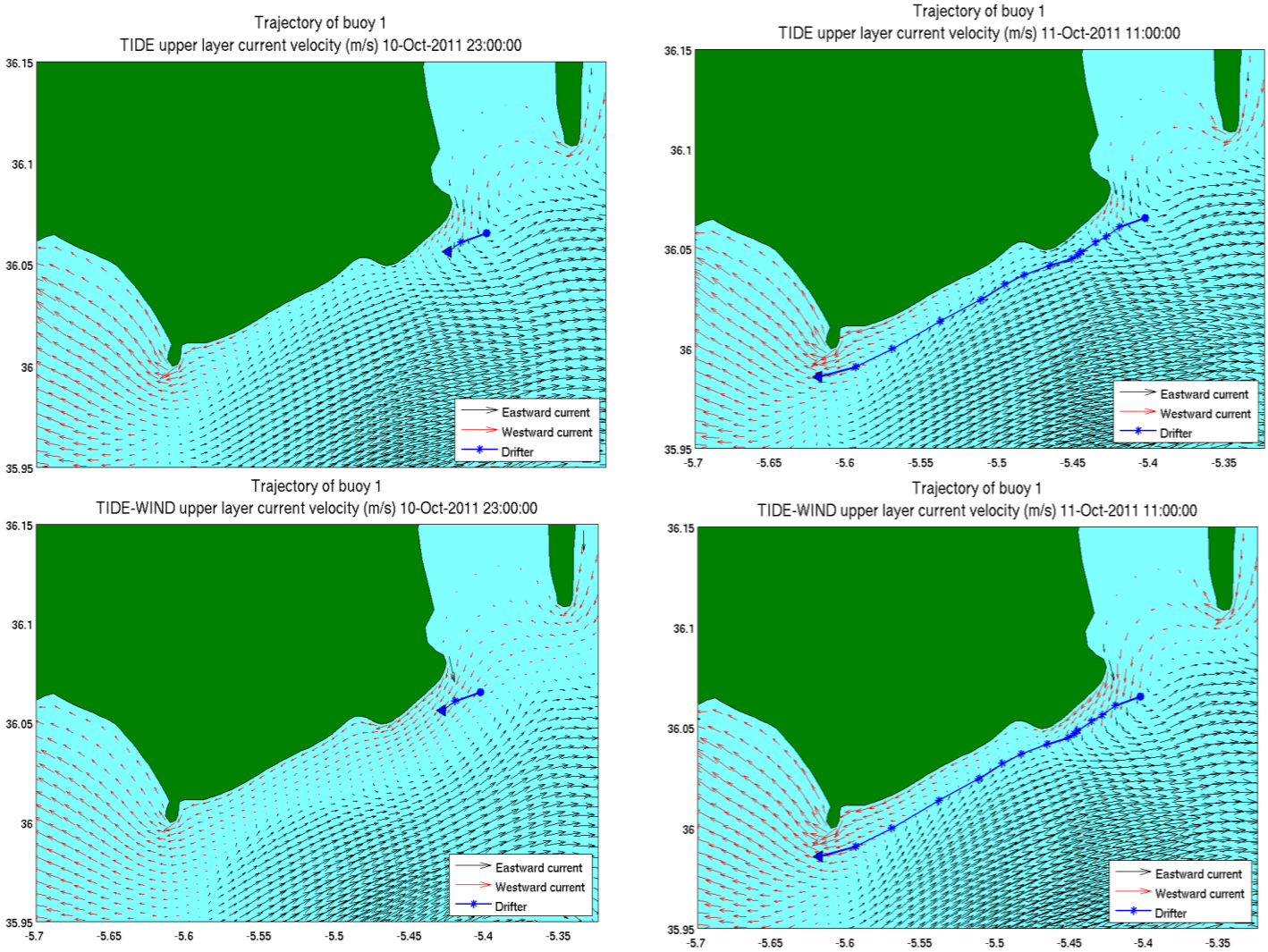

Figure 4.12.-Upper layer current map showing the CCC (red arrows) for the TIDE (top) and TIDE-WIND (bottom) experiments at the beginning (left) and at the final stages (right) of the drifter track (blue line). The dot and the triangle denote the start and the end of the track, respectively.

In the absence of easterlies, the countercurrent develops in each semidiurnal tidal cycle along the northern coast shelf while the remaining upper layer current is flowing toward the Atlantic (6 hours).

Under strong easterly winds (e.g. easterlies higher than 15 $m \cdot s^{-1}$ on September 10, 2008), a wider CCC is fully developed along a continuous band during more than 6 hours. In this case, only the TIDE-WIND experiment is able to properly simulate it (figure 4.13). It means that, even if the presence of easterly winds is not necessary for the CCC occurrence, they have a direct influence on its development by direct wind stress and due to the piling up of water on the northern coast of the Strait, as it has been reported for the Gulf of Cádiz counterflow (Barton & Relvas, 2005; Teles-Machado *et al.*, 2007).

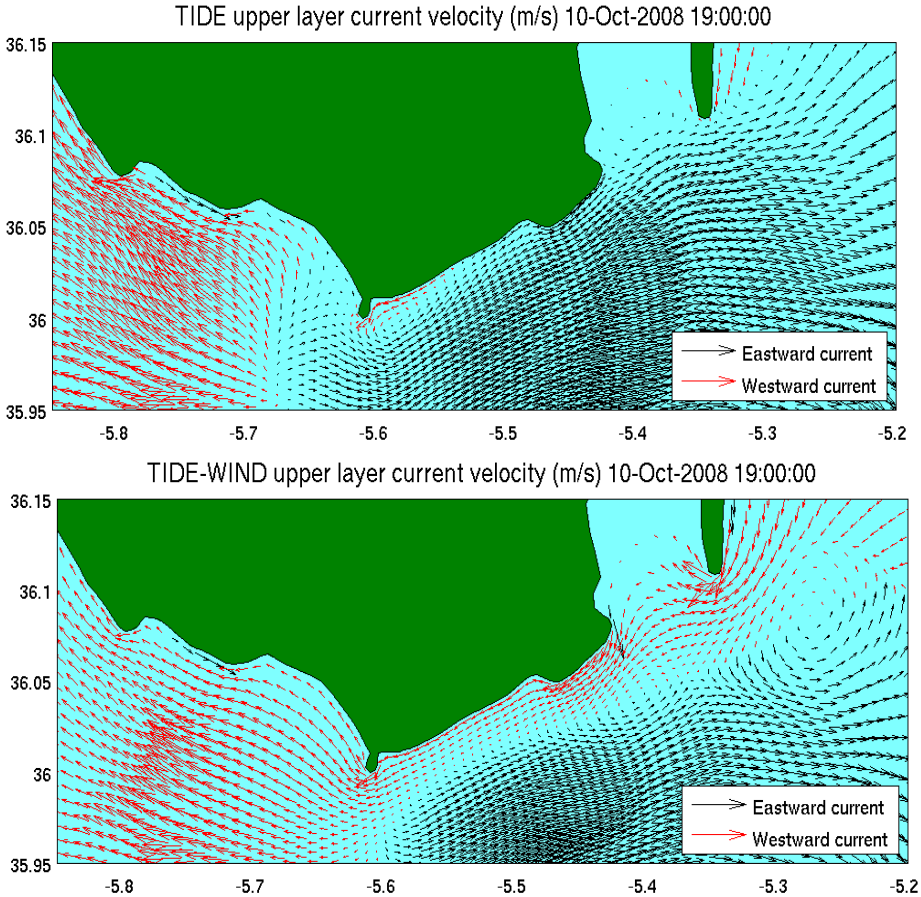

Figure 4.13.- Upper layer current map showing the CCC (red arrows) for the TIDE (top) and TIDE-WIND (bottom) experiments under strong easterly wind conditions on October 10, 2008.

To investigate further the importance of easterlies in the development of the counterflow, surface current fields from TIDE-E and TIDE-W experiments are compared in figure 4.14. As it can be seen, westerlies cancel out the appearance of the

CCC, whereas it is active with spatially uniform easterlies (10 $m \cdot s^{-1}$ wind speed), although weaker and narrower than in TIDE-WIND experiment.

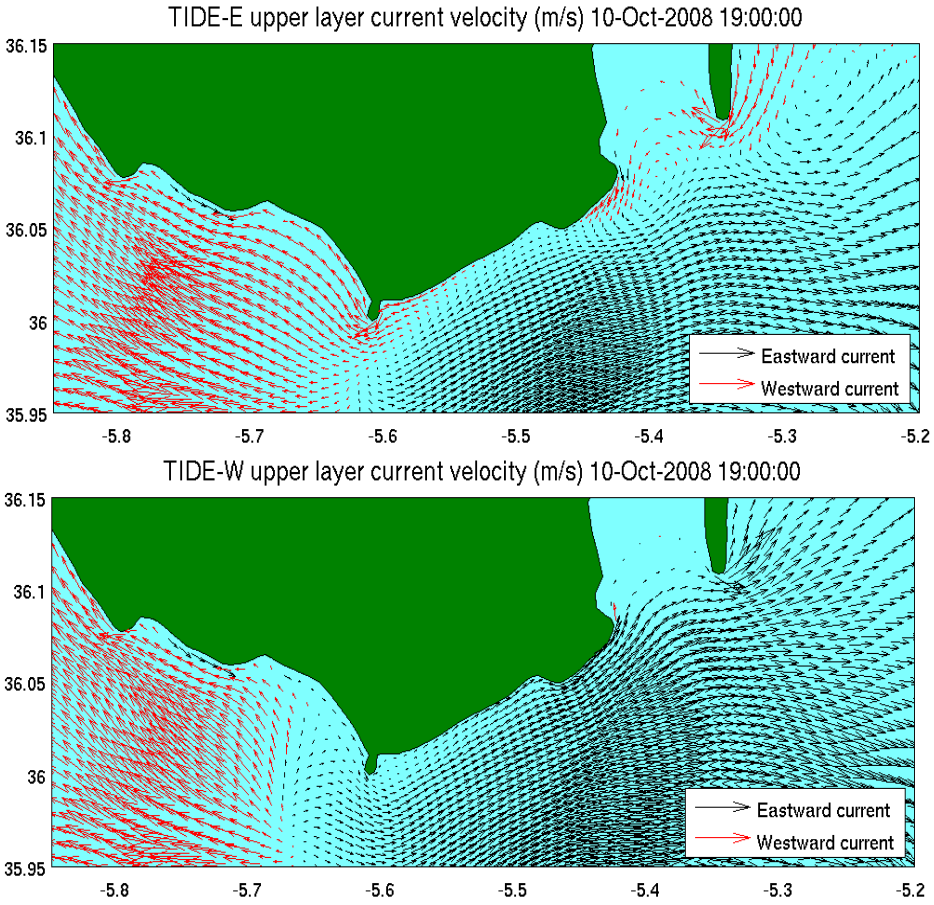

Figure 4.14.- Upper layer current map showing the CCC (red arrows) for the TIDE-E (top) and TIDE-W (bottom) experiments on October 10, 2008.

Nevertheless, the wind stress is only a modifying factor, but not the main driving force. The onset of the CCC is mainly due to lateral friction effect (Gan & Allen, 2002). Although at the closed boundaries of the model a free slip condition for the velocity is applied, in which the tangential shear at the boundary vanishes, lateral friction increases due to the shallower bottom, inducing lower intensity of tidal current at the coastal margin.

Friction effects, also favoured by changes in coastline orientation, induce a localized cyclonic gyre between Punta Tarifa and Punta Paloma (figure 4.15) during the eastward phase of the tidal current, which seems to be one of the mechanisms explaining the chlorophyll maxima on the coastal margin, being easily identified with a pool of cold water in high resolution SST images (Bruno *et al.*, 2013).

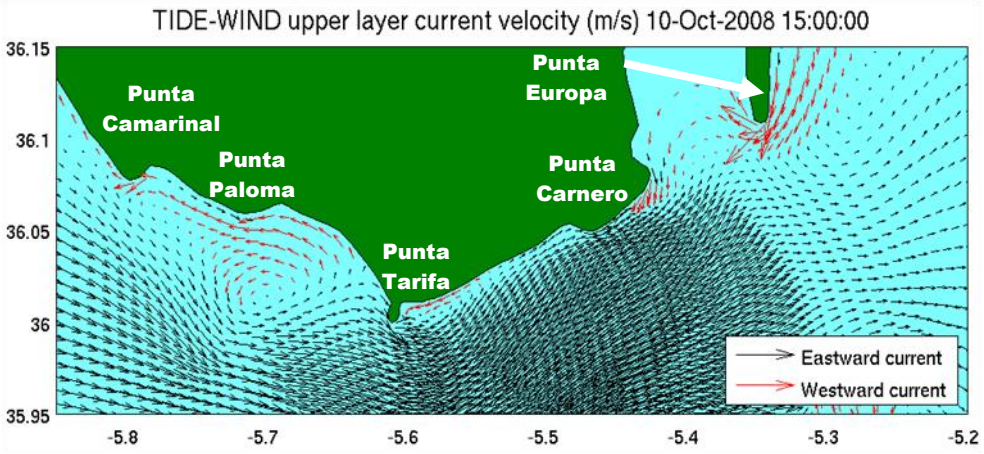

Figure 4.15. - Upper layer current map showing the cyclonic eddy in the leeward side of Punta Tarifa for the TIDE-WIND experiment.

1.4. Model versus tide gauge data

The Atlantic jet is well correlated with the cross-strait sea level difference. Stanichny *et al.* (2005) and Menemenlis *et al.* (2007) report a clear relationship between the zonal wind component and the Tarifa to Ceuta cross-strait sea level difference. They estimate that a westward 10 $m \cdot s^{-1}$ zonal wind will cause a sea level rise of 8.5 cm at the Spanish coast.

We used sea level data from coastal stations on both shores of the Strait (Tarifa and Algeciras on the northern coast and Ceuta on the southern one) to study the correlation between easterly wind episodes and the cross-strait sea level drop (figure 4.16).

Since astronomical tides are the largest components of the daily sea level fluctuations, the determination of the local, instantaneous sea level changes attributable to high winds, among other less predictable oscillations (Flick, 1998), from the recorded sea level height consists in the elimination of the tidal effect, obtaining the subinertial series. Furthermore, even the measurements from the three tide-gauge stations have been referred to a common datum, forming the RLR[2] datasets, the sea level anomaly has been finally used in order to be able to compare the time series.

Sea level difference anomaly (SLDA) across the Strait is examined between Ceuta-Algeciras and Ceuta-Tarifa (figure 4.16).

[2] The RLR datum at each station is defined to be approximately 7 m below the mean sea level, in order to avoid negative monthly and annual mean values.

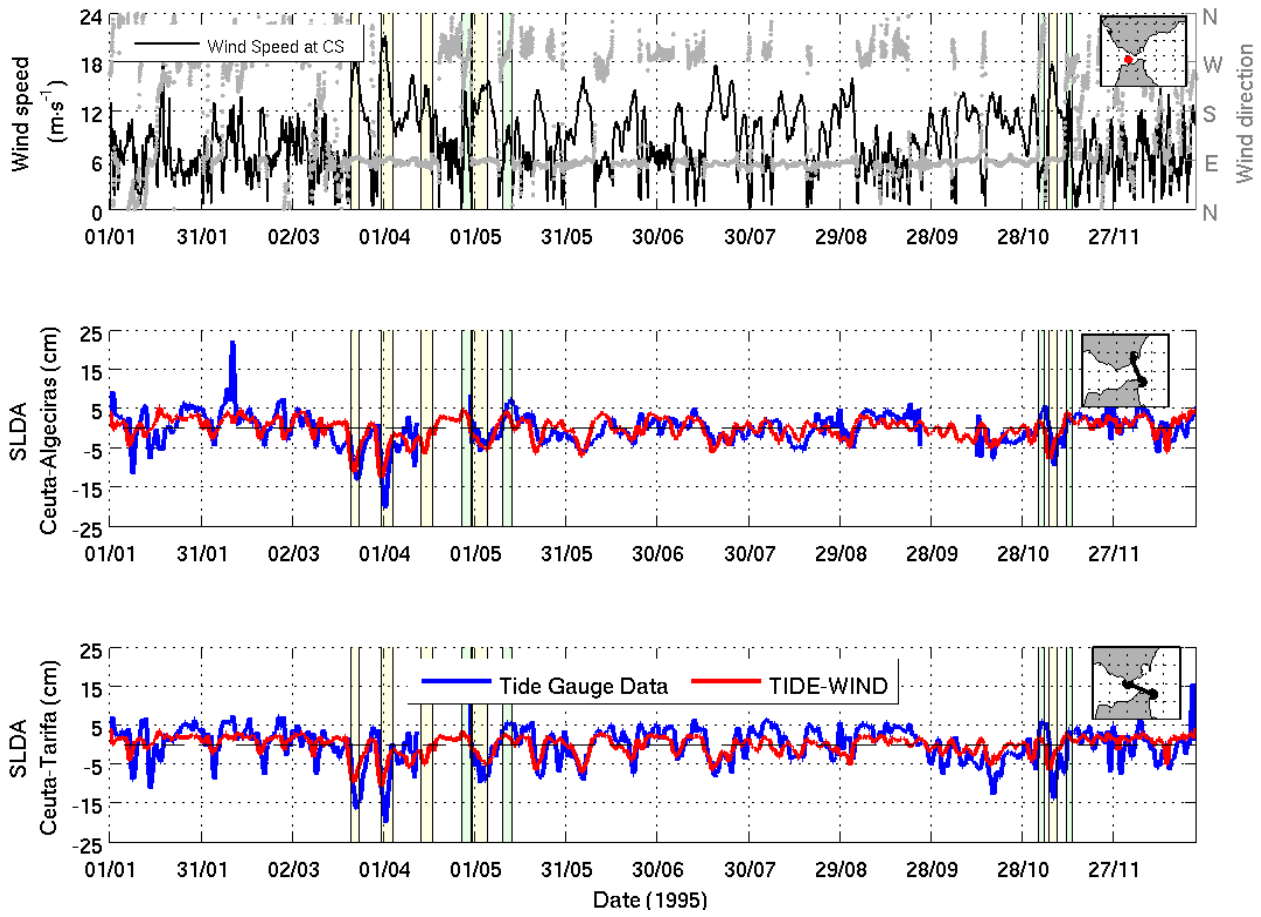

Figure 4.16.-Wind speed (black line) and direction (grey points) at Camarinal Sill (top). Comparison of observed (blue line) and TIDE-WIND simulated (red line) low-pass SLDA between Ceuta-Algeciras (middle) and Ceuta-Tarifa (bottom). Yellow and green shaded areas indicate easterly and westerly winds events, respectively.

Results of figure 4.16 show a high correspondence between the occurrence of intense easterly winds and a cross-strait sea level drop as previously reported by Stanichny *et al.* (2005), which becomes negative during these episodes (i. e. sea level in Ceuta lower than in Algeciras and even lower than in Tarifa, where wind speed is locally intensified). The change of sign in sea level difference during the event confirms the inflow reversal.

During the end of March and beginning of April (first two yellow shaded areas of figure 4.16), two episodes of strong easterly wind up to 18 $m \cdot s^{-1}$ and 20 $m \cdot s^{-1}$ caused a Ceuta-Algeciras cross-strait sea level drop (figure 4.16, middle) of 13 and 20 cm (below its mean value of 3.67 cm), respectively, being the drop in the Ceuta-Tarifa section (figure 4.16, bottom) of 16 and 19.6 cm (with mean value corresponding to 0.4 cm), as observed from tide gauge data. Simulated values in the Ceuta-Algeciras cross-strait section correspond to 11 cm and 12.6 cm (below the mean value, being 7.8 cm),

respectively, and in Ceuta-Tarifa the sea level dropped 9.5 and 10.5 cm (with mean value of 6.9 cm), respectively. Simulated values for Ceuta-Tarifa cross-section are slightly lower than observed ones, while they are closer at Ceuta-Algeciras section.

The first of April, the along-strait geostrophic current ($u_{geo} = -g\Delta\xi/fL$; being g the gravity acceleration, f the Coriolis parameter for 36ºN) originated by 20 m·s^{-1} wind, which induces an observed cross-strait sea level difference ($\Delta\xi$) between Ceuta and Tarifa (19.2 cm), separated by a distance of L =27.8 km, is of 0.79 m·s^{-1}. At the same time, between Ceuta and Algeciras (L =26.3 km) is of 16.3 cm and the westward geostrophic current is 0.7 m·s^{-1}.

It is noteworthy that easterly winds of 20 m·s^{-1} induce westward geostrophic currents of higher magnitude than those driven by atmospheric pressure fluctuations over the Mediterranean, estimated as 0.4 m·s^{-1} (Candela *et al.*, 1989). This result lead us to consider the remarkable impact of local wind stress, which is even able to compete with remote atmospheric forcing.

At this point, we underline the two-fold effect of easterly wind: from the one hand, it accelerates westward the surface water layer by the direct action of tangential stress. On the other hand, it piles up water in the northern coast of the Strait, which will induce a geostrophic current westward. For very intense easterly winds, the sea-level slope can be inverted, as well as the surface inflow, as being previously reported by Stanichny *et al.* (2005).

On the other hand, westerlies enhance the cross-strait sea level difference, with some remarkable episodes during the beginning of April, May and November (see green shaded areas in figure 4.16). At those moments, wind intensities up to 10 m·s^{-1} induced SLDA of more than 5 cm for observations (slightly less than 5 for TIDE-WIND simulations) between Ceuta and Algeciras, increasing the Atlantic Jet current velocity.

It is worth to mention the good correspondence between the observations and the simulations results obtained by the wind-forced ocean model (TIDE-WIND experiments).

The ocean response follows forcing with a time lag. The period of time taken by an easterly wind (W_s=20 m·s^{-1}) to develop a downwelling (upwelling) at the northern (southern) coast, for a two-layer ocean, can be calculated by means of the wind impulse (Cushman-Roisin & Beckers, 2008; Kämpf, 2010).

The *wind impulse* I is the integration of wind stress term over time, and it is defined by:

$$I = \frac{\langle \tau \rangle}{\rho_1 h_1} t^*, \tag{4.1}$$

Let us consider the final state of the ocean after the wind event, in which the interface has risen to the surface and a front has been formed, giving place to a full upwelling (Csanady, 1977) at the southern shore.

The alongshore velocity v at the front is:

$$v = (g' h_1)^{1/2} = 1.3784 \text{ m} \cdot \text{s}^{-1}; \tag{4.2}$$

being $g' = \text{g}(\Delta\rho/\rho_2)$ the reduced gravity and h_1 the upper layer thickness (~100 m).

On another hand, the offshore distance a of the front developed is defined in terms of the wind impulse as:

$$a = \frac{I}{f} - R \tag{4.3}$$

Since the displacement must be positive, it must be satisfied the following:

$$\frac{I}{f} \geq R; \;\; I \geq fR; \tag{4.4}$$

being R the internal Rossby radius of deformation, given by:

$$R = \frac{v}{|f|} = \frac{(g' h_1)^{1/2}}{|f|} = 16.14 \text{ km}; \tag{4.5}$$

For a full upwelling to develop, the wind forcing must be strong enough or wind must be blowing for a sufficiently long time so that the wind impulse is greater than the alongshore velocity at the front, given by (4.2).

Equating equations (4.1) and (4.4), we can estimate that the time t^* required to establish a full upwelling is equal or greater than 40.34 hours, in agreement with the experimental results of (Delgado, 2005), being in between 12 and 48 hours:

$$t^* \geq \rho_1 h_1 \frac{\sqrt{g' h_1}}{\langle \tau \rangle} \tag{4.6}$$

with $\langle \tau \rangle = \rho_{air} \cdot C_D \cdot W_s |W_s|$, being the time-averaged alongshore wind-stress, with ρ_{air} =1.22 kg·m^{-3}, C_D =0.002 and W_s=20 m·s^{-1}.

Nevertheless, this time required to establish an equilibrium state is reached before for the simulation results due to the fact of having wind acting in the two shores, which intensifies the sea surface slope (Defant, 1961).

2. Dynamic ocean response to wind

In order to study the individual and the joint effect of wind and tidal forcing on the circulation of the Strait of Gibraltar, different sets of simulations have been run. NON-TIDE experiments use the steady state solution reached at a lock-exchange experiment as initial condition and then, the model is driven by constant and homogeneous easterly (NON-TIDE-E) and westerly (NON-TIDE-W) winds of 10 $m \cdot s^{-1}$. Once the individual effect of wind on the oceans dynamic is understood after the analysis of the NON-TIDE runs, the joint effect of wind and tidal forcing is addressed by means of the TIDE experiments.

Results of the simulations with different types of forcing show the response of the sea level, interface depth and upper and lower layer currents to wind-stress specifications (easterly and westerly) for the *NON-TIDE* (figure 4.17 and figure 4.18) and *TIDE* experiments (figure 4.19 and figure 4.20).

2.1. NON-TIDE experiments

2.1.1. Sea level and interface depth

Steady sea surface and interface depth resulting from the NON-TIDE control solution are shown in figure 4.17 (top).

Along the strait, the mean sea surface elevation decreases toward the east, with more than twofold reduction of the sea level between the western (10 cm) and the eastern (3 cm) entrance of the Strait.

Across the strait, because of geostrophy, the sea level on the south side of the Strait is higher than on the north side. So, the steady state sea surface increases toward south with a cross-strait difference of 5 and 9 cm at the western and eastern entrances of the Strait, respectively.

The steady-state interface depth becomes deeper toward the south and toward the west, plunging down over the western face of Camarinal Sill.

For both variables, the stronger gradients are located between the Camarinal Sill and the Ceuta-Gibraltar section.

As compared to the NON-TIDE control solution, a constant easterly wind of 10 $m \cdot s^{-1}$ (NON-TIDE-E) originates a sea level rise between 2 and 5 cm from Tarifa to Gibraltar (figure 4.17, middle-left).

The simple model of Sandstrom (1980) estimates that the resulting sea level change at the coast is of approximately 3 cm for a 10 $m \cdot s^{-1}$ wind, being in agreement with our model results.

$$\eta_1 \cong \left(\frac{f\mathrm{L}}{g}\right) \cdot 0.03 \cdot \mathrm{W}; \quad \textbf{(4.7)}$$

where f is the Coriolis parameter ($\approx 8.5 \cdot 10^{-5}$ s^{-1}), W is the along-shore wind at 10 m (10 $m \cdot s^{-1}$) and L the cross-strait shelf width within the Strait of Gibraltar (~10 km).

Due to *baroclinic compensation* (Kämpf, 2009), flow convergence in the surface leads to the elevation of sea level, which is compensated by flow divergence in deeper layers of the ocean, leading to a downward displacement of density interfaces. So then, the Atlantic-Mediterranean interface deepens 25 m in the northeastern part of the Strait (figure 4.17, middle-right), increasing the Atlantic layer thickness for the case of the NON-TIDE-E experiment regarding the NON-TIDE one.

Using the relation between sea-level elevations and interface displacements in a two-layer ocean,

$$\eta_1 = -\frac{(\rho_2 - \rho_1)}{\rho_1}\eta_2; \quad \textbf{(4.8)}$$

where ρ_1 and ρ_2 are densities of the upper and lower layers, we estimate an interface displacement (η_2) of 25.675 m per 5 cm of sea-level elevation (η_1), in agreement with the model results.

On the opposite, westerlies enhance the upwelling at the Spanish coast, rising the interface (~12 m) and sinking the sea level (4 cm) in the northeastern part, with respect to the NON-TIDE experiment, reducing the upper layer thickness.

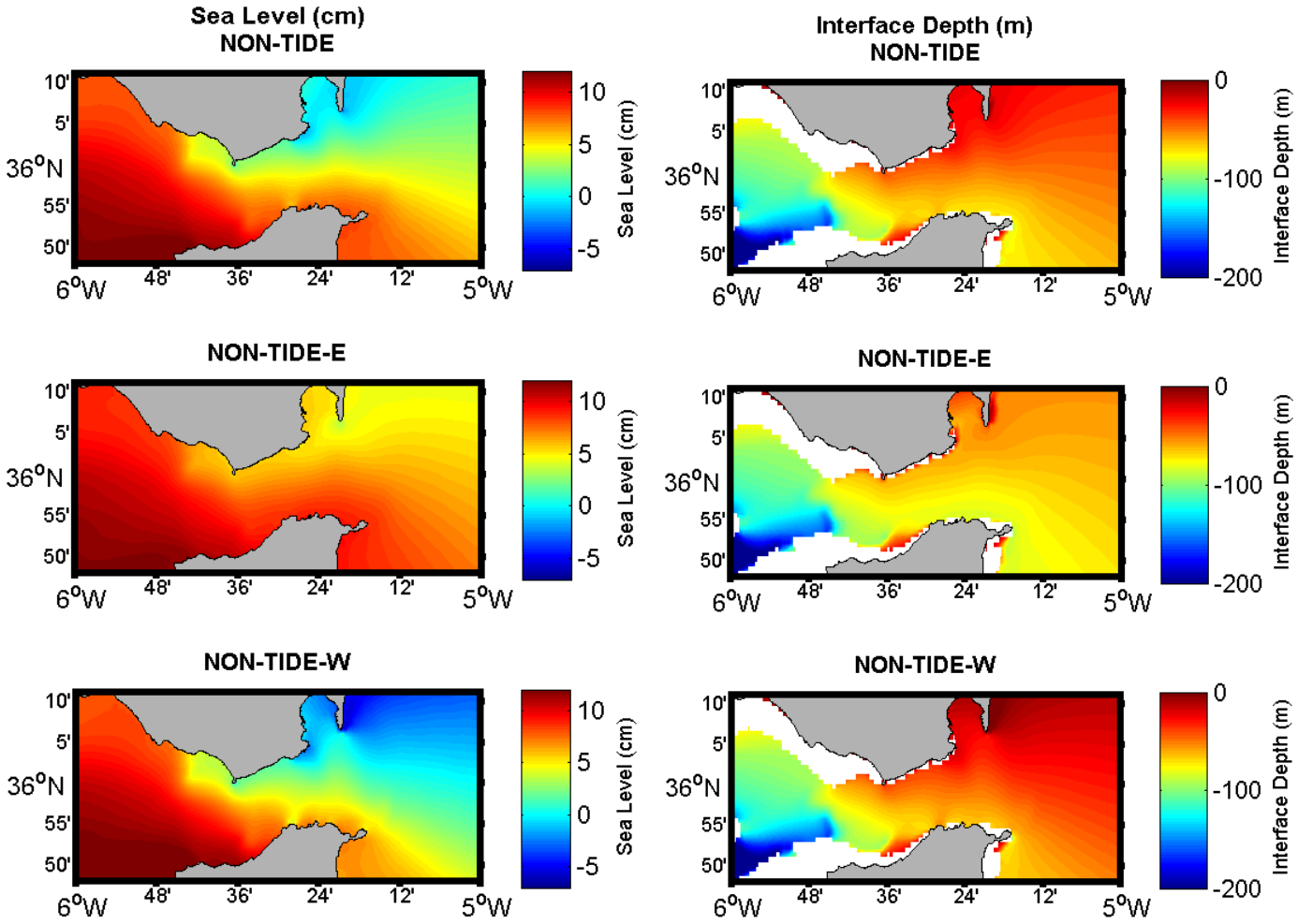

Figure 4.17.- Sea level (left) and interface depth (right) for the NON-TIDE (top), NON-TIDE-E (middle) and NON-TIDE-W (bottom) experiments. The white areas mark the regions where no lower layer is present.

2.1.2. Upper and lower layer current velocities

The steady-state solutions of upper and lower layer current velocities for all three NON-TIDE experiment are displayed in figure 4.18. Current flows toward the Mediterranean in the upper layer and toward the Atlantic in the lower layer. In the upper layer the highest intensities are reached between Camarinal Sill and Gibraltar, while bathymetric features (Camarinal and Espartel Sills) accelerate the flow through canyons leading to maximum bottom velocities with values up to 1.3 $m \cdot s^{-1}$ in the NON-TIDE experiment.

The direct response of eastward surface current to wind stress is to diminish (increase) the intensity, under the influence of the easterlies (westerlies), as it can be observed in figure 4.18 (left).

The accumulation of water in the northeastern part under steady easterlies (NON-TIDE-E) reduces the sea level slope from south-to-north and, by geostrophic balance, weakens the upper layer current velocity.

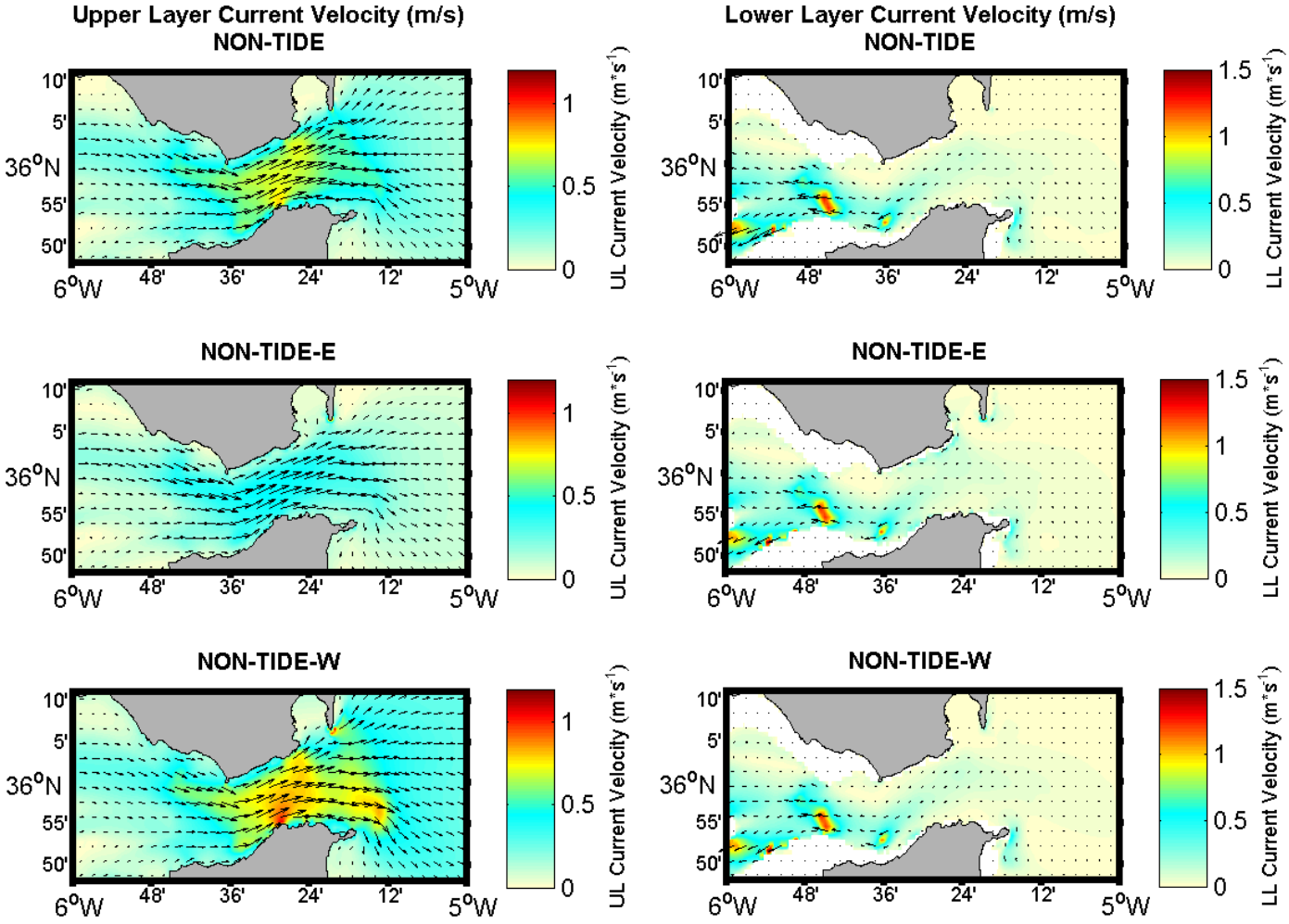

Figure 4.18.- Upper (left) and lower (right) layer current velocity for the *NON-TIDE* (top), NON-TIDE-E (middle) and NON-TIDE-W (bottom) experiments. The white areas mark the regions where no lower layer is present.

Indeed, results provide clear evidence that the surface current intensity decreases for the *NON-TIDE-E* and increases for the *NON-TIDE-W* experiment. By comparison, the upper layer current intensity for the *NON-TIDE-W* experiment is almost twice as intense as that of the *NON-TIDE-E* experiment (figure 4.18, left).

No big differences are found among the three experiments in the lower layer, although intensities are slightly higher, in the case of *NON-TIDE-E* experiment, between Punta Carnero and Tarifa. The fact that the lower layer velocity remains essentially unchanged is due to baroclinic compensation, which reduces and even cancels the surface pressure gradients in deeper water by adjusting changes in the sea surface and the interface steepness (Mellor & Wang, 1996).

That means that along-strait wind, together with the Earth's rotation, has a twofold effect. On the one hand, tangential wind stress causes a the direct effect upon the sea surface and, on the other, winds cause Ekman transport of surface water, which produces horizontal pressure gradients, due to water piling-up, inducing geostrophic currents. For the case of easterlies (westerlies), the Ekman transport moves water to the right of the wind direction, piling up water along the northern (southern) coast of the Strait. This induces a sea level rise, downwelling water in the northern (southern) coast and upwelling it along the southern (northern) one, to satisfy the mass conservation requirement, leading to the establishment of an additional cross-strait sea level gradient, which is followed by a gradual geostrophic adjustment of the flow (Rossby, 1938).

2.2. TIDE experiments

2.2.1. Sea level and interface depth

Once we include tidal forcing, prescribing surface elevation amplitudes and phases of the principal semidiurnal and diurnal constituents at the open boundaries, the time-averaged (over a tropical month) sea surface and interface depth (figure 4.19), upper and lower layer currents (figure 4.20) were calculated.

While the mean along and cross-strait sea level and interface gradients are similar between the steady state solution (NON-TIDE) and the control experiment with tidal forcing (TIDE), main differences are found over the Camarinal Sill cross-section, where the sea level drops and the interface becomes deeper toward west.

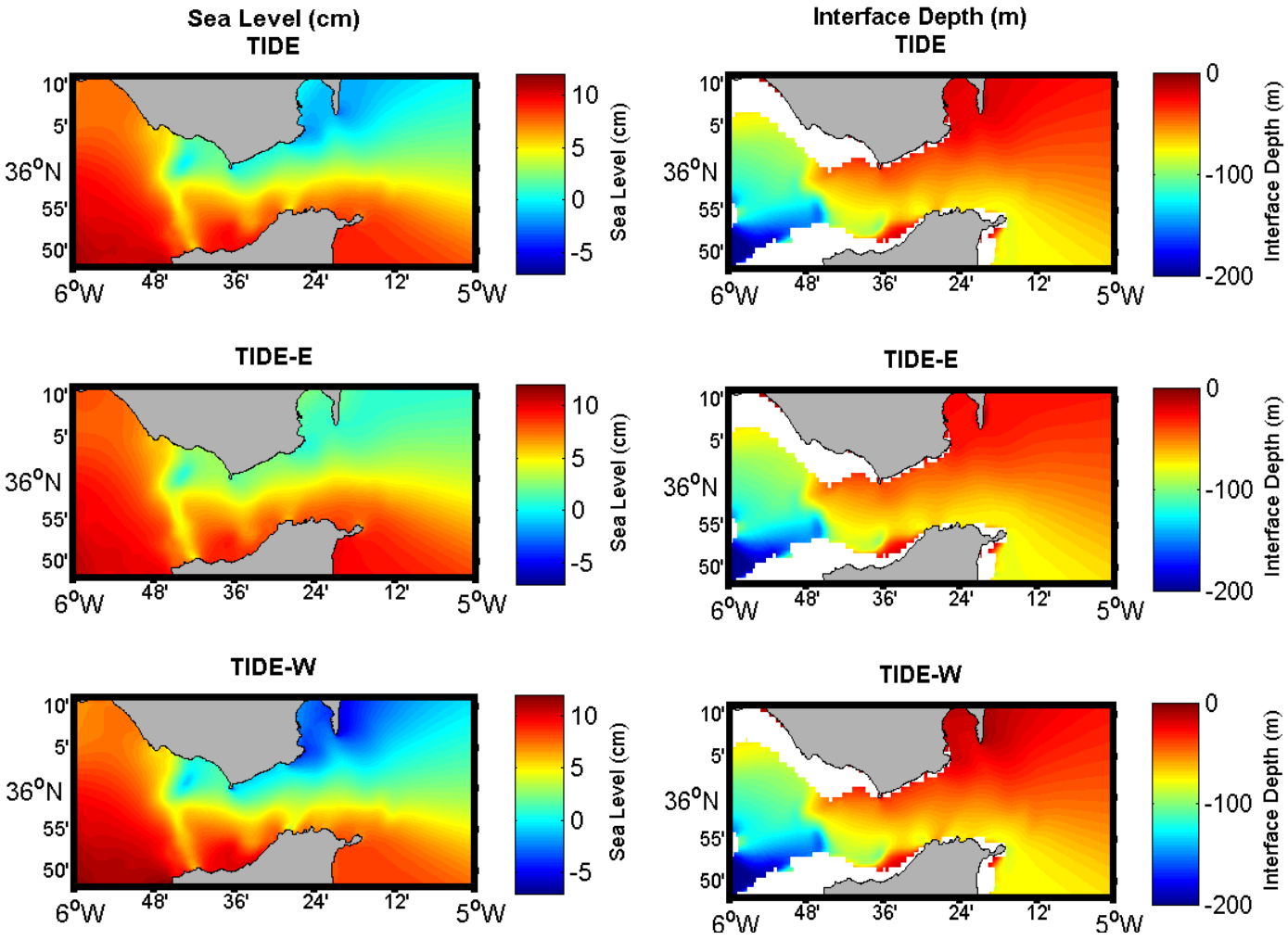

Figure 4.19.- Time-averaged sea surface (left) and interface depth (right) for the *TIDE* (top), TIDE-E (middle) and TIDE-W (bottom) experiments. The white areas mark the regions where no lower layer is present.

At the same time, a cross-strait sea-level difference of less than 7 cm and more than 12 cm for easterlies (TIDE-E) and westerlies (TIDE-W), respectively, at the eastern entrance of the Strait accounts for the noticeable importance of the Coriolis force in the presence of a variable upper-layer thickness. For all experiments, change in the across-strait sea level drop is larger at the northern shore than at the southern one, even more in the case of TIDE-W experiment.

Furthermore, the strong cross-strait gradient of the interface depth at the eastern entrance weakens under easterlies (TIDE-E), while it is reinforced under westerlies (TIDE-W). This leads to a stretching (decrease) of the upper layer thickness at the northeastern area under easterlies (westerlies).

2.2.2. Upper and lower layer current velocities

The time-averaged (over a tropical month) upper and lower-layer current velocities for the different wind forcing experiments are shown in figure 4.20.

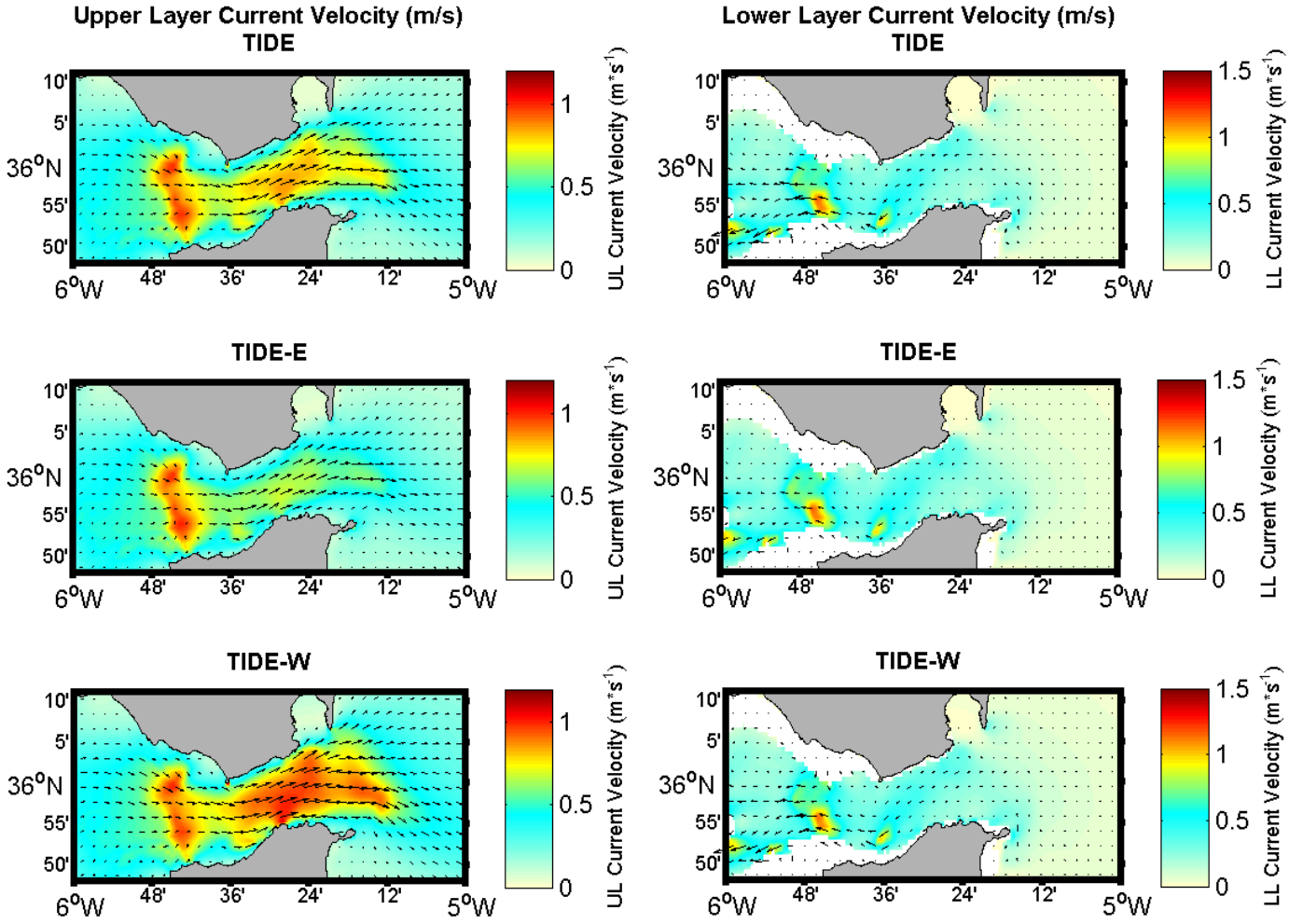

Figure 4.20.- Time-averaged upper (left) and lower (right) layer current velocities for the TIDE (top), TIDE-E (middle) and TIDE-W (bottom) experiments. The white areas mark the regions where no lower layer is present.

In the upper layer, the maximum amplitude is located over Camarinal Sill (up to 1.2 $m \cdot s^{-1}$) since it is the shallowest section and a stronger spatial acceleration of the flow occurs. Larger velocities are also found at the minimum width section, close to Tarifa Narrows, (up to 0.8 $m \cdot s^{-1}$). Velocities are even larger at the eastern section due to the mass conservation, when forcing with westerlies, and lower in the case of easterlies. It is mainly due to a change of the upper layer thickness, induced by wind forcing, which decreases under westerlies and increases under easterlies, as it has been previously mentioned.

In the same way as in the stationary solution results (NON-TIDE experiments), although with a higher amplitude, current in the lower layer is accelerated due to

bathymetric irregularities with values up to 1.3 $m \cdot s^{-1}$ over Camarinal and Espartel Sills. Differences between experiments are minimal, except in the case of TIDE-E experiment, in which the current intensity diminishes because the lower layer thickness increases westward Camarinal Sill.

It is important to highlight that these regions, Tarifa Narrows and Camarinal Sill corresponds to locations of hydraulic controls of the inflow, while at Espartel Sill the outflow is hydraulically controlled (Izquierdo *et al.*, 2001; Brandt *et al.*, 2004).

2.3. Internal waves

Three different days under spring tides, mid-tides and neap tides, on the 16th, 19th and 22nd of October, 2008, respectively (figure 4.21), have been chosen to study the along-strait variability of the interface anomaly associated with the fortnightly tidal cycle.

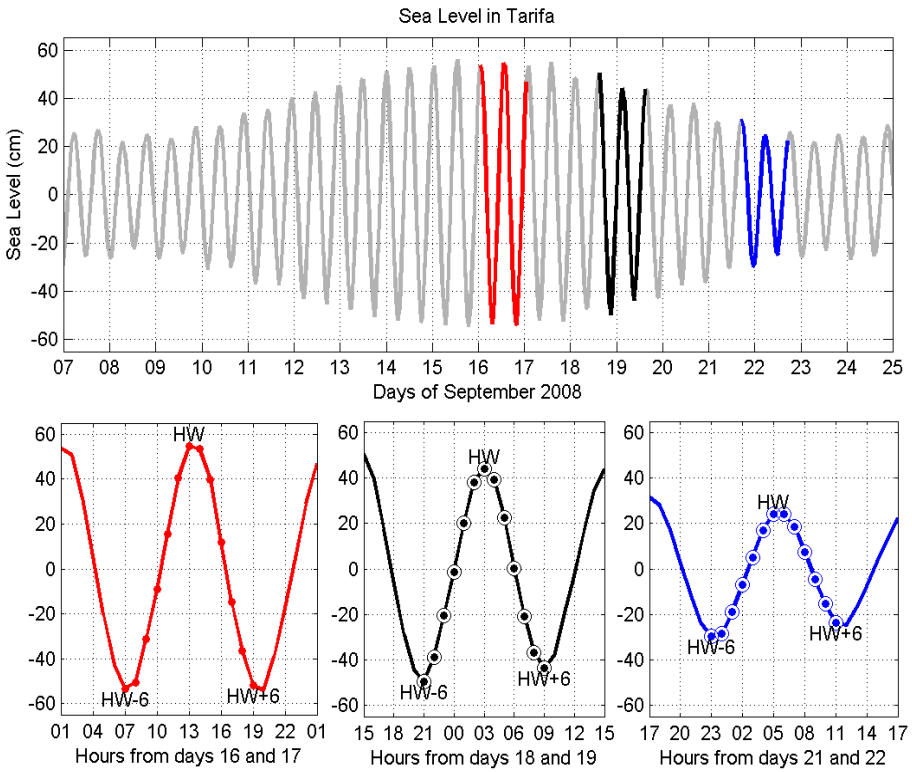

Figure 4.21.-Tidal height at Tarifa showing the analyzed periods at spring tides (red line), mid-tides (black line) and neap tides (blue line). Points correspond to the semi-diurnal tidal cycle analyzed in figure 4.22. White circles correspond to CTD casts at the eastern entrance of the Strait shown in figure 4.23.

Analysis has been carried out for the three *TIDE* experiments (*TIDE*, *TIDE-E* and *TIDE-W*) (figure 4.22), allowing us to evaluate the internal wave events under different tidal conditions and the effect of the wind in the generation, release and propagation of the internal bore.

In all cases, the internal bore is generated and propagated eastward (figure 4.22). Time has been expressed in terms of tidal cycle hours using as reference the predicted high-water (HW) at Tarifa. Nevertheless, simulated along-strait tidal current prediction over Camarinal Sill[3] (arrows indicating magnitude and direction), of the TIDE experiment has also been included.

Simulated along-strait velocity in the upper layer (figure 4.22, left, see black arrows) ranges from -2.1 $m \cdot s^{-1}$ to 2.2 $m \cdot s^{-1}$ during spring tide (on September 16) and from -0.4 $m \cdot s^{-1}$ to 1.3 $m \cdot s^{-1}$ (figure 4.22, right, see black arrows) during neap tide (on September 22) at Camarinal Sill. In the lower layer, along-strait velocity ranges from -1.7 $m \cdot s^{-1}$ to 1.2 $m \cdot s^{-1}$ during spring tide (figure 4.22, left, see grey arrows) and from -1.5 $m \cdot s^{-1}$ to 0.4 $m \cdot s^{-1}$ during neap tide (figure 4.22, right, see grey arrows). This means that, at spring tide, the upper layer along-strait velocity is higher than in the lower layer during the flood (the surface layer moves eastward toward the Mediterranean) and during certain moments of the ebb tide (the water moves westward toward the Atlantic Ocean). On the other hand, at neap tides, the upper layer moves faster during the flood (eastward moving) and the lower layer during the ebb tide (westward moving). Currents, over Camarinal Sill, reverses at both layers throughout 5 hours during spring tides (on September 16) and during 4 hours in neap tide (on September 22) in agreement with Vázquez *et al.* (2008).

The initial stage of the hydraulic jump generation over Camarinal Sill occurs during the westward tidal flow and the interface suddenly rise over the sill, while sinking abruptly on the lee side of the sill. During the analyzed spring and neap tides periods of the control experiment (TIDE), shown with black line in the figure 4.22, the generation started at HW-4, two hours before the maximum outflow over Camarinal Sill, in agreement with Vázquez López-Escobar (2006).

Then, the wave remains arrested at the lee side of the main sill, while it is growing in amplitude when critical or supercritical conditions are established. This happens during 5 hours after the start of the generation at both spring and neap tides.

[3] Outflow (OF) over Camarinal Sill takes place 3 hours before high water in Tarifa, due to the near-standing wave character of the barotropic tide in the Strait of Gibraltar.

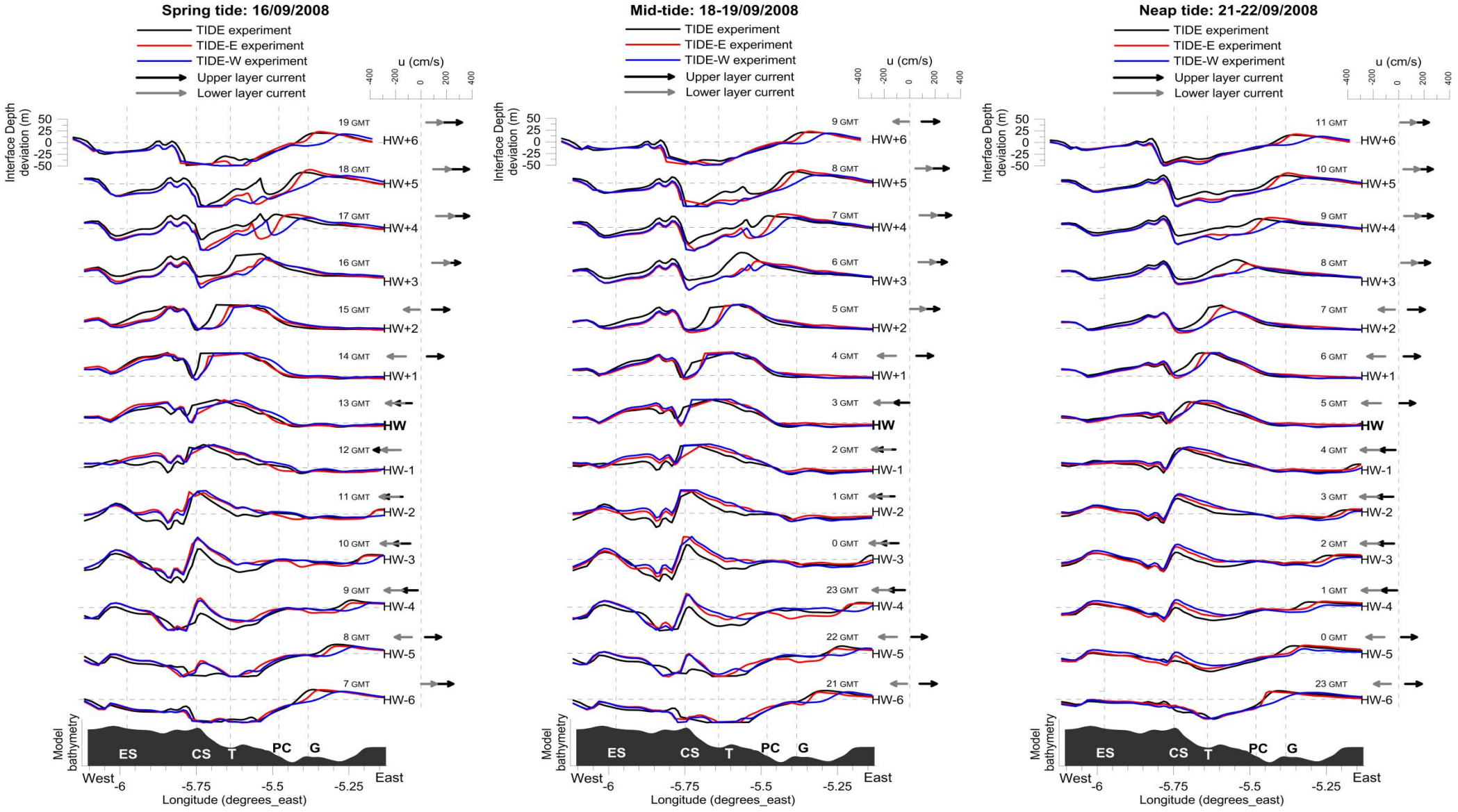

Figure 4.22.-Along-strait interface depth anomaly over a semidiurnal tidal cycle for spring tide (left), mid-tide (center) and neap tide (right). Black, red and blue lines correspond to the TIDE, TIDE-E and TIDE-W experiments, respectively. The arrows show the relative intensity and direction of the eastward tidal current component over Camarinal Sill for the upper (black arrows) and lower (grey arrows) layers. Cross-strait sections are also identified (ES=Espartel Sill; CS=Camarinal Sill; T=Tarifa; PC= Punta Cires; G= Gibraltar). Tidal cycle is referred to the high-water (HW) in Tarifa.

The release starts when the flow weakens, at the beginning of the inflow phase of the barotropic tidal currents (inflow toward the Mediterranean), in both cases (HW+1), in close agreement with the release times given by Vázquez *et al.* (2008).

After that, the internal bore starts to move eastward disintegrating into large-amplitude internal solitary waves. When passing, internal waves lower the interface, stretching the Atlantic layer and diminishing the Mediterranean layer thickness.

During the maximum inflow the internal wave reaches Tarifa (T) at HW+3, 2 hours after the release, in accordance with Armi & Farmer (1988), Farmer & Armi (1988) and Richez (1994). The arrival at Punta Cires (PC) delays 2 hours in both cases and another 2 hours till Gibraltar (G).

Corresponding to the travel times listed above, the bore speed is about 1.7 $m \cdot s^{-1}$ between Camarinal Sill and Tarifa (12.3 km), 2.5 $m \cdot s^{-1}$ between Tarifa and Punta Cires (17.7 km) and 1.5 $m \cdot s^{-1}$ between Punta Cires and Gibraltar (10.7 km), which are fully in agreement with those values computed by Izquierdo *et al.* (2001) and Sannino *et al.* (2004) and slightly higher than those given by Vázquez López-Escobar (2006).

Waves arrive to Gibraltar 7 hours after HW in Tarifa, which completely agree arrival times given by Ziegenbein (1970), also being within the range between 4 and 9 hours given by Watson & Robinson (1990) and those given by Vázquez López-Escobar (2006), being 6 hours on average.

One hour after the arrival of the internal wave at Gibraltar (11 hours after the generation of the internal bore over Camarinal Sill), a second internal bore is being generated over Camarinal Sill at spring tide. At neap tide, the second hydraulic jump takes place one hour later.

Easterlies and westerlies bring forward 1 hour the generation (HW-5) of the hydraulic jump and the release time (HW) of the internal wave at spring and neap tides, remaining invariable the arresting time (5 hours).

The rising of the interface over Camarinal Sill due to easterly winds and thus, the reduction of the upper layer thickness, together with the strong westward subinertial flow in the surface, which increases the tidal current during its outflow phase, favour the hydraulic jump generation on the lee side of the Sill. The physical mechanism is similar to the previously reported by Vázquez *et al.* (2008), considering the activation of large-amplitude internal wave generation under neap tide conditions, with strong subinertial flow directed toward the Atlantic in response to an increase of atmospheric pressure over the western Mediterranean.

In response to westerlies, the subinertial flow is intensified toward the Mediterranean, favouring the inflow and reducing the intensity of tidal current during the outflow phase.

While the time that the wave takes to reach Tarifa (2 hours) does not change due to winds, easterlies reduce the wave propagation speed from T to PC, delaying 3 hours because of the reduction in velocity east of Camarinal Sill. The travel times of the bore from PC to G remain unchanged for all experiments and both tidal conditions. Therefore, during westerly events the waves arrive 1 hour before to Gibraltar (HW+6), as compared to the TIDE and TIDE-E experiments. Travel times and bore speeds for the different experiments and for both tidal conditions are summarized in table 4.1.

Table 4.1.- Travel times and speed of the bore for the different experiments at spring (the 16th of September) and neap (the 22nd of September) tides between the cross-sections (figure 2.9).

INTERNAL WAVE		Spring tide 16/09/2008			Neap tide 22/09/2008		
		TIDE	TIDE-E	TIDE-W	TIDE	TIDE-E	TIDE-W
Bore Generation		HW-4	HW-5	HW-5	HW-4	HW-5	HW-5
Arrested time		5 h	5 h	5 h	5 h	5 h	5 h
Release		HW+1	HW	HW	HW+1	HW	HW
Eastward propagation	T	HW+3	HW+2	HW+2	HW+3	HW+2	HW+2
	PC	HW+5	HW+5	HW+4	HW+5	HW+5	HW+4
	G	HW+7	HW+7	HW+6	HW+7	HW+7	HW+6
Arrival time at G after bore generation		~11 h	~11 h	~10 h	~11 h	~11 h	~10 h
Bore speed (m·s-1)	CS-T	1.71	1.71	1.71	1.71	1.71	1.71
	T-PC	2.46	1.64	2.46	2.46	1.64	2.46
	PC-G	1.49	1.49	1.49	1.49	1.49	1.49

Generation and release times of the internal wave for all three experiments at mid-tide (on September 19) are very similar to those at spring-neap tides. Along-strait interface depth anomaly was analyzed this day to compare the arrival times of the internal waves to Punta Cires (PC) with those obtained with observations (which, on another hand, were not available at spring-tide).

During the "*Gibraltar'08*" oceanographic cruise, the vessel remained at the eastern entrance of the strait (5.485 ºW, 35.964 ºN), at the midpoint of Punta Cires (PC)

cross-section, on the lookout for the arrival of the internal waves. At that location, CTD casts were done at almost hourly intervals and current velocity profiles were measured by the vessel-mounted ADCP at mid-tide (on October 19, 2008) and during neap tide (on October 22, 2008), shown in figure 4.23.

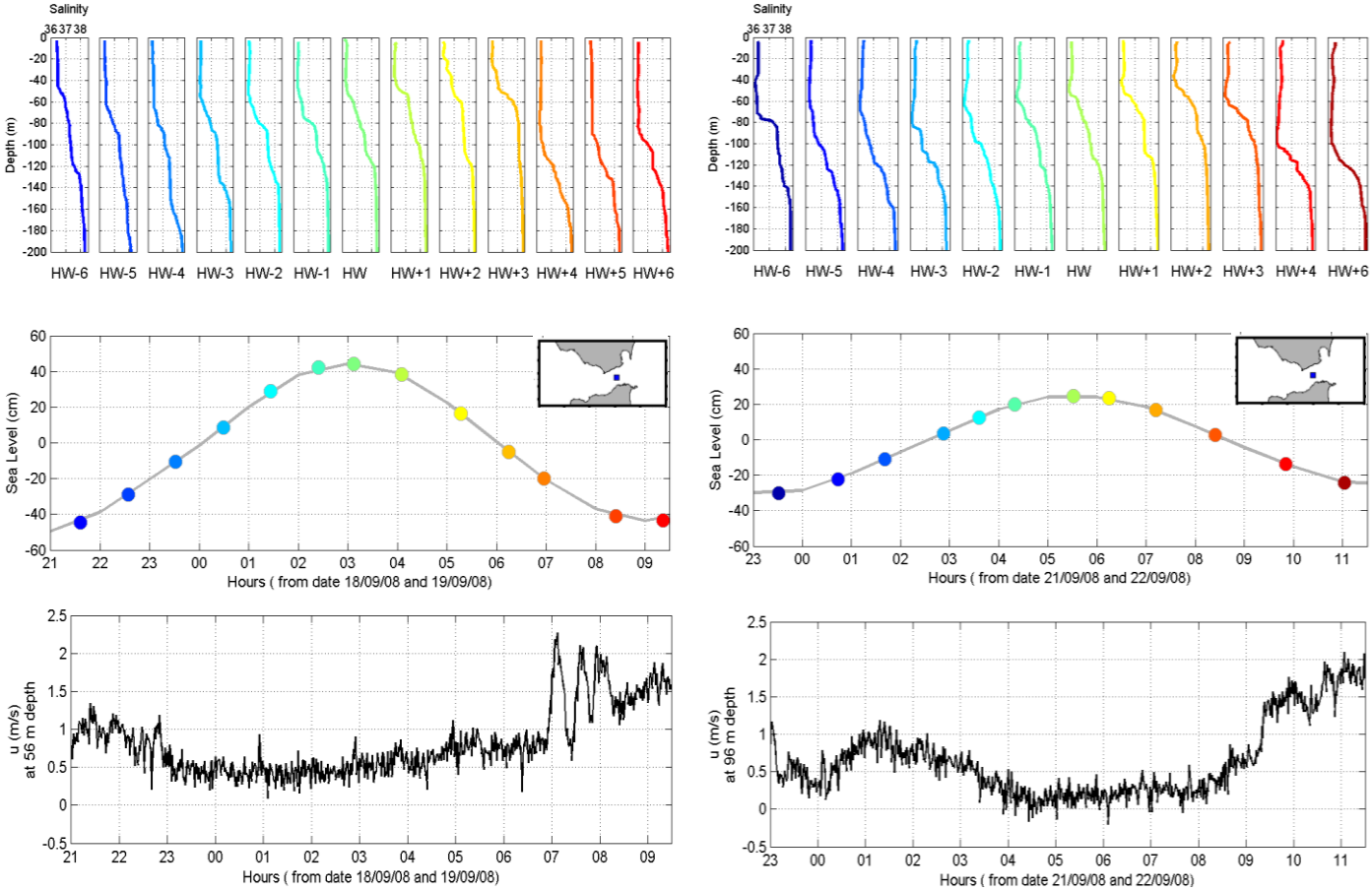

Figure 4.23.- Salinity profiles (top) at mid-tides on October 19 (left) and during neap tides on October 22 (right). Tidal sea level in Tarifa (middle) with the points indicating the CTD casts (map shows the location of the CTD cast with a blue square). Time series of ADCP-eastward current component at 56 m (mid-tides) and 96 m (neap-tides) are also displayed (bottom).

Until the arrival of the internal waves, the interface lies very shallow (54 m and 78 m at HW+3, for mid-tides and neap-tides, respectively). Interface layer is deepened (137 m and 121 m at HW+4, for mid-tides and neap-tides, respectively) behind the passing bore, being easily identified in the salinity profiles of figure 4.23 (top). The interface sinks more than 83 m from HW+3 until HW+4, which corresponds to the internal wave amplitude (on October 19). At neap tide, on October 22, the interface displacement is 43 m, from HW+3 until HW+4, half of that for mid-tide.

Additionally, a sharp increase of the eastward current velocities (figure 4.23, bottom) confirms the arrival of the internal wave to the CTD sampling station at HW+4

during mid (at 7 GMT) and neap (at 9 GMT) tides, as it has also been simulated by the model in figure 4.22.

Even more, during mid-tides it could also be observed the arrival of an internal solitary wave train with rank-ordered amplitudes (the largest at the front), which, on another hand, could not be simulated by the model because of the hydrostatic approximation used (Wang, 1989; Sannino *et al.*, 2004)

3. Hydraulic control variability

According to previous results, it is reasonable to assume that if wind forcing is able to modify the flow that may lead to changes in the internal bore generation west of Camarinal Sill, its release and eastward propagation, it can be related to its influence in the establishment of the hydraulic conditions within the Strait.

To better understand the role of the wind in the flow regime, it is necessary to know if the total barotropic flow is higher than the linear phase speed of the first baroclinic mode for the different experiments.

The relation between the flow velocity with the wave celerity for a two-layer flow is given by the *composite Froude number* $G^2 = F_1^2 + F_2^2$, where the *internal Froude number* F_i^2 is defined by (Armi, 1986) as follows,

$$F_i^2 = \langle \frac{u_i^2}{g' \cdot h_i} \rangle \qquad \textbf{(4.9)}$$

, being i the subscript for each layer ($i = 1$ for upper layer and $i = 2$ for lower layer), u_i the current velocity, h_i the layer thickness and $g' = g \cdot \Delta\rho/\rho_2$ the reduced gravity based on the density difference between the layers ($\Delta\rho$). Angle brackets denote time average over a tropical month.

Hydraulic control occurs when the flow velocity is equal or higher than the propagation speed of gravitational waves ($G^2 \geq 1$) and waves can no longer propagate against the flow so, any disturbance will remain stationary. Internal waves remain arrested on the lee side of the sill due to the establishment of critical or supercritical conditions, during the outflow phase of the barotropic tidal currents (Bruno *et al.*, 2002). In supercritical flow ($G^2 > 1$), the waves remain arrested and are amplified over Camarinal Sill. Subcritical flow over the Sill ($G^2 < 1$) allows the release of the internal waves toward the Mediterranean.

In order to analyze the hydraulic control response to the wind forcing, the internal Froude number (F_i^2) for the upper and lower layers as well as the composite Froude number (G^2) have been computed over a tropical month of the simulation of 2008 for the TIDE, TIDE-E and TIDE-W experiments (figure 4.24).

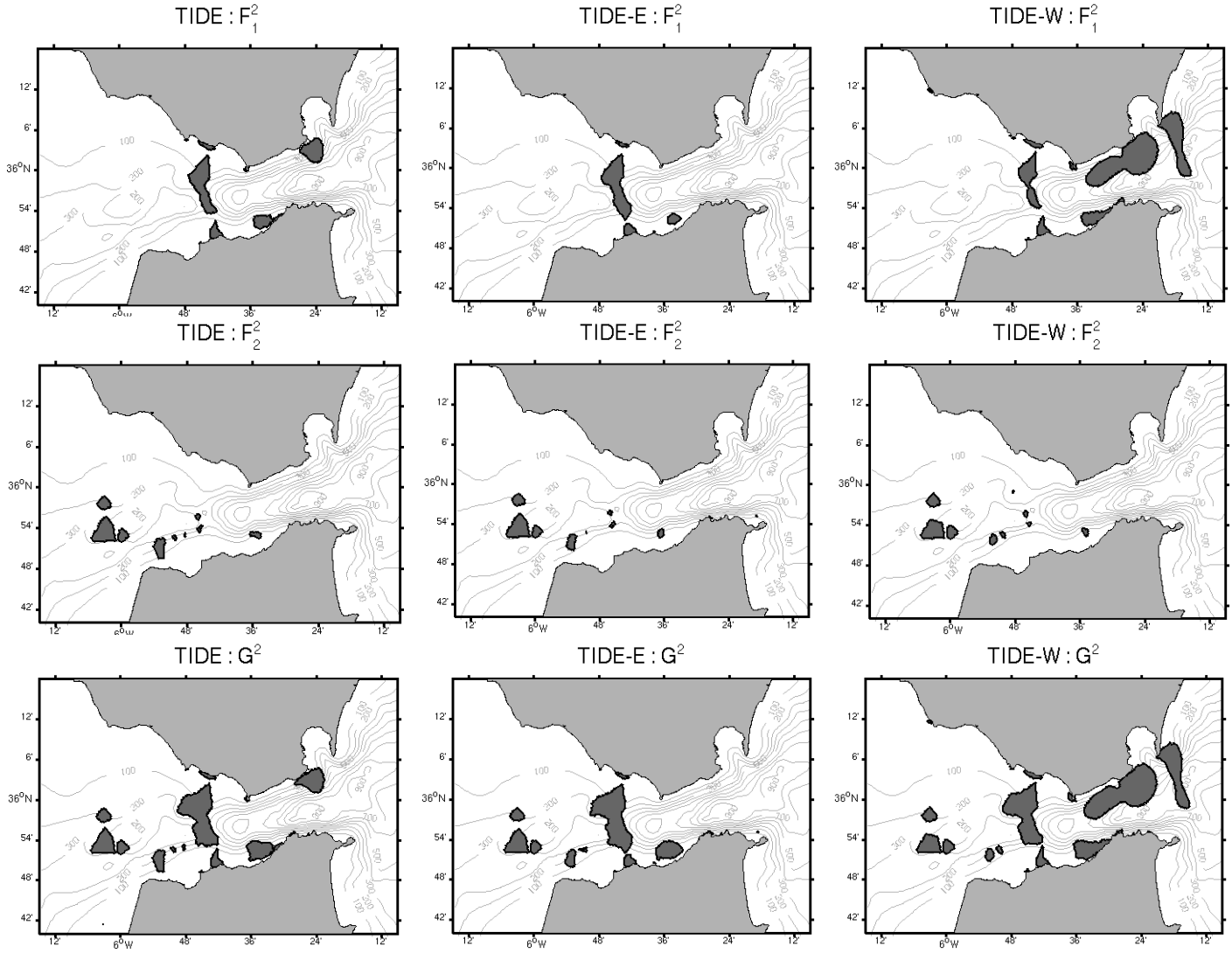

Figure 4.24.- Upper layer ($F_1^2 \geq 1$), lower layer ($F_2^2 \geq 1$), and composite ($G^2 \geq 1$) Froude numbers for the different experiments: TIDE (left), TIDE-E (middle) and TIDE-W (right). Grey contour lines represent the model bathymetry. Value over 1 are shaded.

Model results of the TIDE experiment show a hydraulic control of the inflow in the section of minimum depth (Camarinal Sill), historically being regarded as the main control section (Bryden & Stommel, 1984; Bormans & Garrett, 1989a; Izquierdo *et al.*, 2001; Brandt *et al.*, 2004). At Tarifa Narrows (section of minimum width) exists an apparent control (Izquierdo *et al.*, 2001) of the inflow, with some scattered regions limited to the north and south shore.

Froude number for the lower layer proves the existence of a supercritical region at the west of Espartel and just over the Sill as well as at the southern part of Tangier Basin (it separated Espartel Sill from Camarinal Sill), also in agreement with Izquierdo *et al.* (2001).

Both layers contribute to the supercritical regime over Camarinal Sill, particularly the upper layer. At the narrows, the interface is so shallow that it is the upper layer flow which essentially achieves the critical Froude number.

Some relevant differences are found in the hydraulic controls locations with wind forcing results in relation to the tidal forcing, mostly at the narrows and at the eastern entrance of the Strait.

In the case of the TIDE-E experiment, the control of the inflow increases over Camarinal Sill, mainly due to the raising of the interface (reducing the upper layer thickness) (figure 4.25, top-left). Further, as the results show, the supercritical scattered regions of the northern and northeastern of Tarifa Narrows, disappear as a consequence of the two-fold effect of easterlies in this area: On the one hand, the interface drops (increasing the upper layer thickness) and, on the other, the upper layer velocity slows down (figure 4.25, bottom-left). The controls over Espartel and at the west of the sill remain invariable, although the Froude number of the lower layer weakens at the southern part of Tangier basin.

With westerlies (TIDE-W), it is evident the weakening of the hydraulic control over Camarinal Sill because of an increased of the Atlantic layer thickness (deeper interface) (figure 4.25, top-right). The strengthening of the control at the northern and southern coast at the narrows and the existence of an additional supercritical region in the cross-section between Gibraltar and Ceuta could also be observed. The main reasons of these results are related to the response of the ocean to westerlies at the northeastern entrance of the Strait (figure 4.25, right): the interface rises (reducing the upper layer thickness) and the surface current increases. In the lower layer, the supercritical region at the western part of Espartel Sill slackens as well as the scattered regions at the south of Tangier basin.

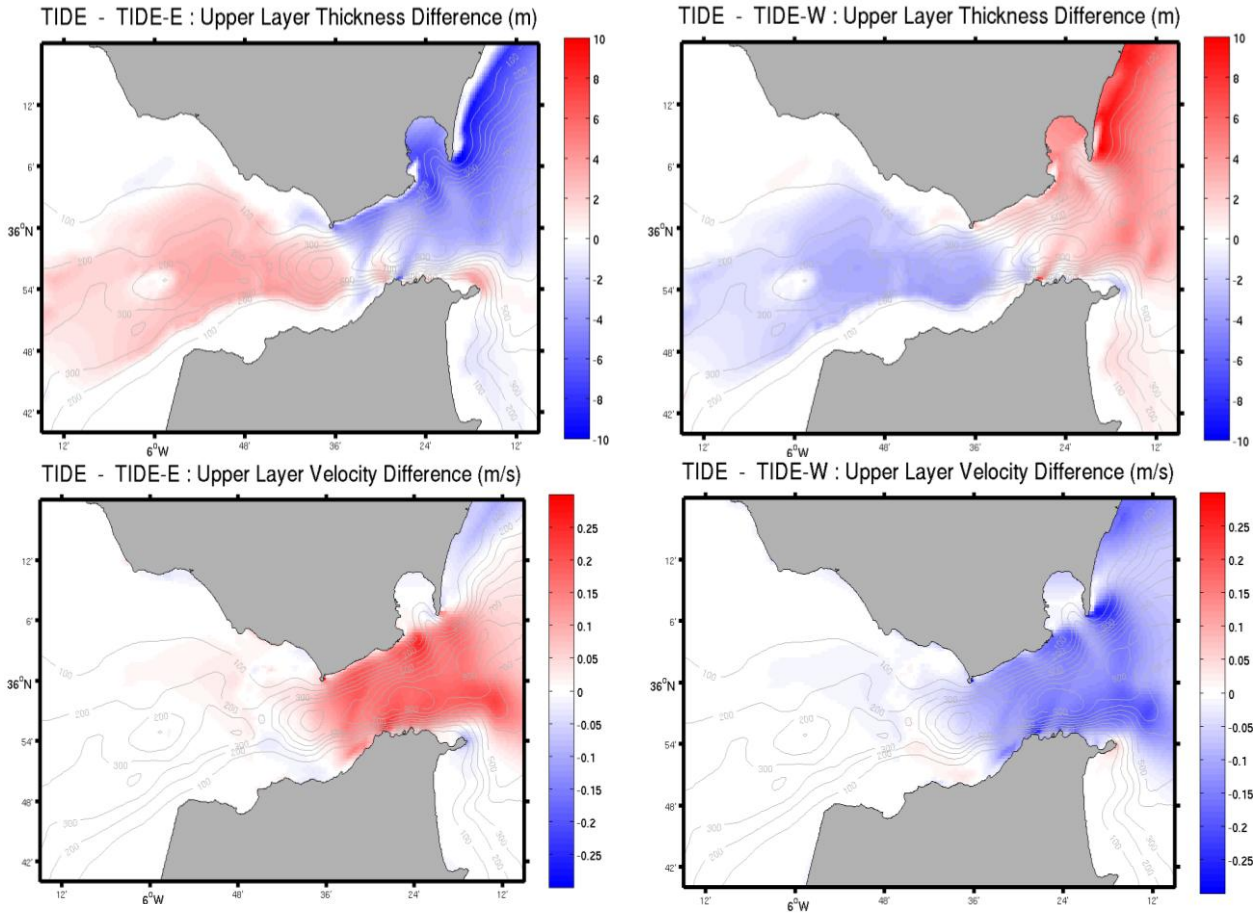

Figure 4.25.- Upper layer thickness (top) and velocity differences (bottom) of the control experiment *versus* TIDE-E (left) and *versus* TIDE-W(right). Grey contour lines represent the model bathymetry. Red (blue) colour implies a shallower (deeper) interface and a decrease (increase) on the velocity, due to wind forcing.

The existence of a single control over Camarinal Sill, for the TIDE and TIDE-E experiments, corresponds to a submaximal exchange throughout the Strait in the framework of the two-layer hydraulic control theory (Armi & Farmer, 1988; Farmer & Armi, 1988) and will generally produce smaller exchange rates, slower subcritial flow at the eastern end of the strait with a rather deep interface and so thus, a thicker upper layer (Bormans *et al.*, 1986; Bormans & Garrett, 1989a). Nevertheless, the simultaneous presence of an additional hydraulic control over the cross-strait section Gibraltar-Ceuta makes the exchange maximal throughout the Strait for TIDE-W experiment, corresponding to a fast supercritical flow at the eastern end of the strait with a shallow interface and a thin upper layer (Bormans *et al.*, 1986; Bormans & Garrett, 1989a).

4. Flow exchange

There are different ways of estimating the mean transport along-strait (Bryden *et al.*, 1994; Tsimplis & Bryden, 2000; García-Lafuente *et al.*, 2002a; Vargas *et al.*, 2006). Taking advantage of the formulation of the model in transport form, we define the instantaneous along-strait flow through the Camarinal Sill cross-section as follows:

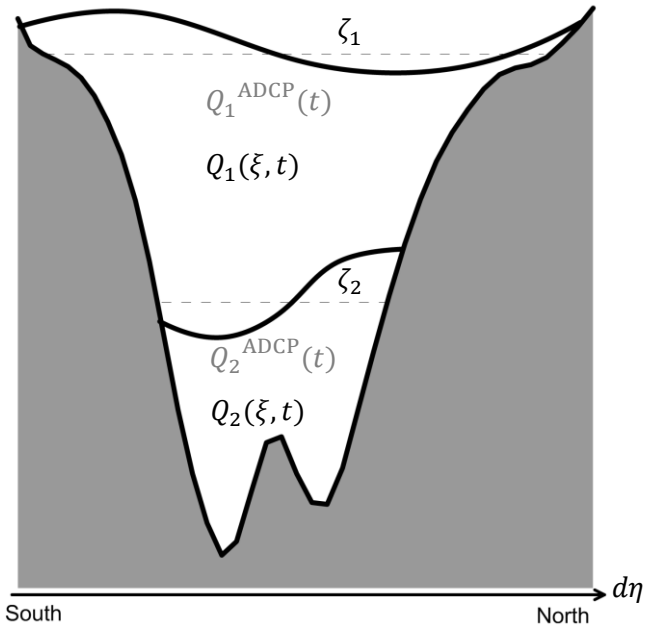

Figure 4.26.- Scheme representing the Camarinal Sill cross-section used for the inflow and outflow estimation. For ADCP transport estimates the interface depth in the mooring position at time t is taken as constant (dashed line) for the entire cross-section.

The instantaneous inflow Q_1, the outflow Q_2 and the net flow Q_0 are computed according to:

$$\boldsymbol{Q_1}(\xi,t) = \int_{\boldsymbol{\eta}} \boldsymbol{u_1}\,(\xi,\eta,t)d\eta \qquad \textbf{(4.10)}$$

$$\boldsymbol{Q_2}(\xi,t) = \int_{\boldsymbol{\eta}} \boldsymbol{u_2}\,(\xi,\eta,t)d\eta \qquad \textbf{(4.11)}$$

$$\boldsymbol{Q_0}(\xi,t) = \boldsymbol{Q_1}(\xi,t) + \boldsymbol{Q_2}(\xi,t); \qquad \textbf{(4.12)}$$

where $u_i(\xi,\eta,t)$ is the along-strait vertically integrated flow ($m^2 \cdot s^{-1}$) for the upper ($i = 1$) and lower ($i = 2$) layers.

Following equations (4.10) and (4.11), Atlantic inflow and Mediterranean outflow have been obtained, respectively, for the TIDE and TIDE-WIND experiments

throughout the year 1995. Then the mean inflow and outflow transports have been estimated by time-averaging these instantaneous transports.

On another hand, transports have been estimated with the along-strait currents measured by the ADCP over Camarinal Sill and the derived shear interface delimiting the layer thicknesses. Thus, transports were computed integrating the along-strait velocity $u(z,t)$ vertically from the bottom up to the depth of the (shear) interface, h(t), for the outflow, and from this depth up to the surface, for the inflow, and then meridionally, across the Camarinal Sill section, as follows:

$$\boldsymbol{Q_1}^{\mathbf{ADCP}}(\boldsymbol{t}) = \int_{\mathbf{y}} \int_{\mathbf{h(t)}}^{\mathbf{0}} \boldsymbol{u_1}\,(\boldsymbol{z},t)dzdy \tag{4.13}$$

$$\boldsymbol{Q_2}^{\mathbf{ADCP}}(\boldsymbol{t}) = \int_{\mathbf{y}} \int_{\boldsymbol{bottom}}^{\mathbf{h(t)}} \boldsymbol{u_2}\,(\boldsymbol{z},t)dzdy\,; \tag{4.14}$$

In this case, we assume that along-strait current values and interface depth over the Sill are representative and constant for the whole cross-section (as schematized in figure 4.26), ignoring the cross-channel structure of the flow. On another hand, due to the lack of ADCP current measurements for the upper 45 m, the velocity of the last bin (upward-looking ADCP) has been kept constant up to the surface.

Subinertial transport were obtained for all time series (ADCP, TIDE-WIND and TIDE) by applying a low-pass filter (33-hour cut-off period). Comparison of the subinertial transport anomalies together with the wind speed and direction, simulated with MM5-10 km, as well as sea level prediction (TIDE experiment) over CS are shown in figure 4.27.

A clear visual correlation between the transport anomalies and the winds is observed, being more noticeable in the upper layer and, particularly, under strong easterly and westerly episodes (see black and grey arrows of figure 4.27).

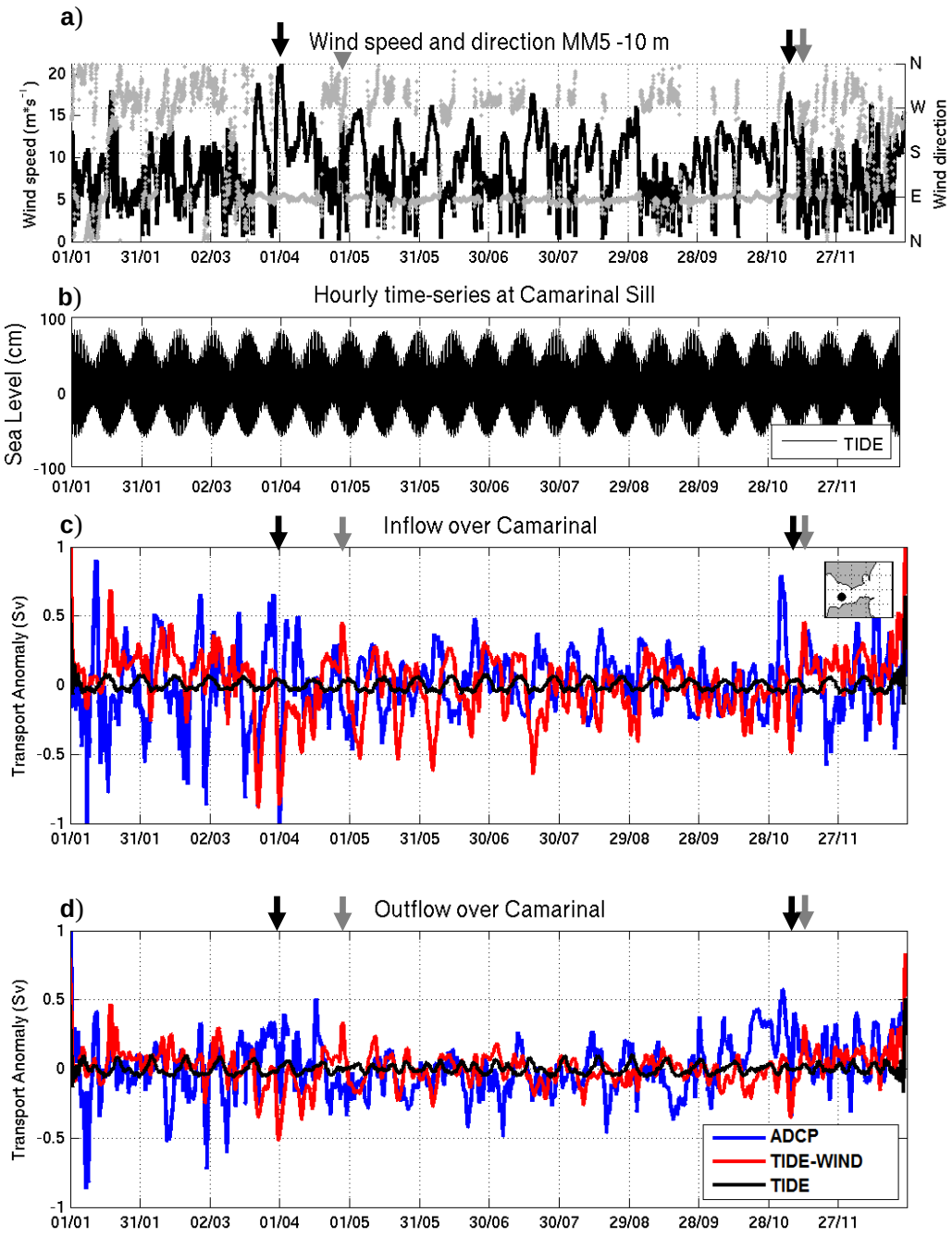

Figure 4.27.- Wind speed (black line) and direction (grey points) simulated at Camarinal Sill (a). Sea level at Camarinal Sill from the TIDE run (b). Subinertial upper (c) and lower layer (d) transport anomalies at Camarinal Sill estimated from the ADCP data set (blue line), resulting from the TIDE (black line) and TIDE-WIND (red line) experiments. Black (grey) arrows indicate the strong easterly (westerly) events mentioned in the text.

Minimum inflow and maximum outflow (minimum negative) values are associated with intense easterly wind episodes (shown with black arrows in figure 4.27), which diminish the exchange rates due to the interface rise over the main sill. On the contrary, maximum inflow and minimum outflow take place when the interface is

deeper at Camarinal Sill, coinciding with westerlies (shown with grey arrows in figure 4.27). Results noticeably improve for transports simulated by the wind-forced ocean model.

The subinertial time series of the Mediterranean outflow transport anomaly, computed from ADCP observations (figure 4.27, bottom), shows fortnightly variability, related to the spring-neap tidal cycle fluctuations of the interface depth at CS, which is shallower at spring tide (maximum outflow) and deeper at neap tide (maximum inflow).

As foreseen, as the ADCP and TIDE-WIND upper layer currents are clearly related, Atlantic inflow estimated from the ADCP measurements and from the TIDE-WIND experiment might also show high correlation.

Even thought yearly averaged inflow time series estimated for the TIDE-WIND and for the ADCP show poor correlation of around r=0.11, related to the fact that relevant processes that influence the exchange (e.g., the steric sea level variability, the density contrast, the remote forcing due to atmospheric pressure fluctuations over the Mediterranean) are neglected in the model and also due to assumptions made in the ADCP transport estimations, time series are strongly correlated for particular episodic wind events of one day, under predominance of easterlies and westerlies (table 4.2), highlighting the role of the local wind-stress in the subinertial variability of the exchange. In this sense, while annual transport estimated from the TIDE-WIND experiment is well correlated (r=-0.72) to wind-stress, as expected, this correlation decreases to -0.20 when the relationship between the ADCP estimated transport and wind-stress is considered, since wind is not the only factor influencing the flow exchange on an annual time scale.

Table 4.2.- Correlation coefficients between the low-pass TIDE-WIND and ADCP estimated inflow transports (Q_1) and between inflow time series and wind-stress (τ_{wind}), for easterly and westerly events.

Time series 1	Time series 2	Correlation coefficients (r)			
		Easterly		Westerly	
		01/04/1995	06/11/1995	28/04/1995	12/11/1995
$Q_1^{TIDE-WIND}$	Q_1^{ADCP}	0.84	0.87	0.92	0.71
$Q_1^{TIDE-WIND}$	τ_{wind}	-0.97	-0.99	0.91	0.77
Q_1^{ADCP}	τ_{wind}	-0.79	-0.87	0.93	0.95

As the upper layer current is correlated to the Atlantic inflow, it is apparent that westerlies tend to increase the eastward flow and conversely easterlies tend to decrease

it. In this regard, as shown in table 4.2, the estimated inflow for the TIDE-WIND and for ADCP is negatively correlated to wind-stress, under strong easterly wind conditions, and positively correlated under westerly wind events. The Atlantic flow, estimated for the TIDE-WIND experiment, agrees best with the wind stress under easterlies, while the correlation of the ADCP computed inflow is highest with westerlies. Slightly lower correlation values obtained in the case of easterlies might be due to the overestimation of the ADCP inflow associated with extrapolation near the surface (Tsimplis & Bryden, 2000).

With the aim to analyze the along-strait subinertial variability of the exchanged flows and the influence of wind forcing, inflow and outflow are shown over a year at four different cross-sections (figure 4.28 and figure 4.29 for TIDE and TIDE-WIND experiments, respectively).

At a first glance, it can be seen that Atlantic inflow is eastward and the Mediterranean outflow is westward everywhere and the exchange flows are along-strait dependent for both experiments. Atlantic inflow and Mediterranean outflow increases eastward until the narrowest section (TN), where the largest amplitude of the inflow and outflow occur, and then decreases on the eastern entrance of the Strait (PH).

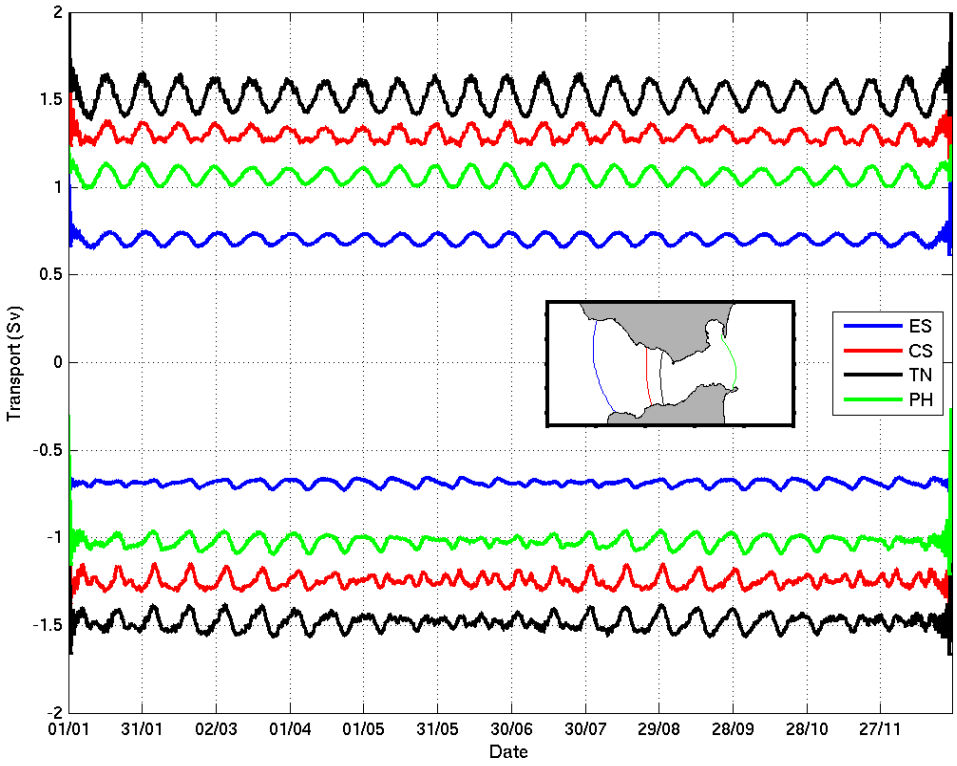

Figure 4.28.- Subinertial inflow (positive values) and outflow (negative values) transports, for the TIDE experiment, over the different cross-sections showed on the map.

In the case of the TIDE experiment (figure 4.28), the fortnightly variability prevails over the entire signal of both, the inflow and the outflow, which is related to the spring-neap cycle in semidiurnal tidal forcing and it is explained in terms of the nonlinear interactions among the main semidiurnal tidal constituents imposed by the volume conservation principle (Bruno *et al.*, 2010). Furthermore, the lower layer flow exhibits a clear annual modulation with a minimum outflow around early summer (June) and a maximum in late winter (February). This annual fluctuation seems to be in phase in the main sill, the narrows and the eastern entrance cross-sections, while in Espartel Sill the minimum and maximum are delayed until July and April (García-Lafuente *et al.*, 2007), respectively.

The above mentioned fortnightly variability is masked by meteorological subinertial fluctuations induced by wind-stress, which amplify the response of the transports, particularly of the inflow and especially during some intense easterly and westerly wind events (see black and grey arrows of figure 4.29).

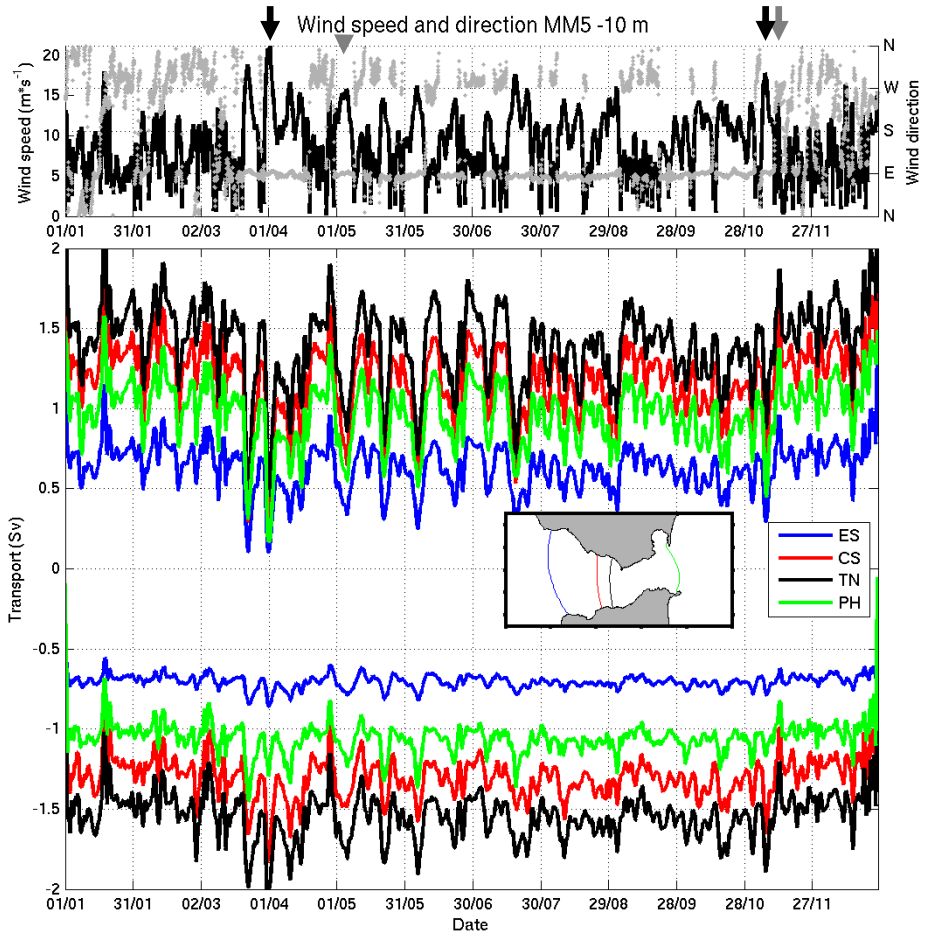

Figure 4.29.- Subinertial inflow (positive values) and outflow (negative values) transports for the TIDE-WIND experiment over the different cross-sections showed on the map. Black (grey) arrows indicate the strong easterly (westerly) events mentioned in the text.

Table 4.3 shows the estimated transports for the TIDE and the TIDE-WIND experiments for different cross-sections along the Strait. In the case of the TIDE-WIND experiment, transports have been obtained averaging over two days, one with predominantly easterly winds (01/04/1995) and the other with predominantly westerly winds (12/11/1995).

Table 4.3.- Time-averaged transport values obtained from TIDE and TIDE-WIND experiments over different cross-sections under .

Transports ($Sv \equiv 10^6\ m^3 \cdot s^{-1}$)	**TIDE 1995 (yearly averaged)**				**TIDE-WIND 01/04/1995 (easterly episode)**				**TIDE-WIND 12/11/1995 (westerly episode)**			
	ES	CS	TN	PH	ES	CS	TN	PH	ES	CS	TN	PH
Inflow ($\overline{Q_1}$)	0.69	1.29	1.52	1.06	0.19	0.47	0.64	0.22	0.91	1.57	1.81	1.30
Outflow ($\overline{Q_2}$)	-0.65	-1.25	-1.48	-1.02	-0.83	-1.68	-1.93	-1.16	-0.64	-1.03	-1.25	-0.86
Netflow ($\overline{Q_0}$)	0.04	0.04	0.04	0.04	-0.64	-1.21	-1.29	-0.94	0.27	0.54	0.56	0.45

The TIDE experiment is characterized by an increase of the Atlantic inflow and Mediterranean outflow eastward until TN, where the largest amplitude of transports occurs, in agreement with Sannino *et al.* (2004). Since interface strongly slopes up from west to east along the strait, reducing the upper layer thickness and so then the inflow section, the increase of the transports is mainly due to the effect of a stronger mean current.

The mean upper layer transport ranges from 0.70 Sv (Sverdrup, 1 Sv=10^6 $m^3 \cdot s^{-1}$) (ES) to 1.52 Sv (TN), while mean value of the Mediterranean outflow ranges between -0.69 Sv (ES) to -1.48 Sv (TN). At the main Sill (CS), the yearly averaged Atlantic inflow is 1.29 Sv and the outflow is -1.25 Sv. These values leads to an averaged net flow of 0.04 Sv (inflow being 5% greater than the outflow), as required to compensate for evaporative losses in the Mediterranean Sea, being in agreement with previous values for the exchange given by (Lacombe & Richez, 1982).

Comparison of transports computed for the TIDE-WIND experiment, regarding the TIDE experiment (table 4.3), shows that easterlies strongly diminish the inflow in all cross-sections, related to a reduction of the upper layer current and, on another hand, the outflow increases. Conversely, westerlies increase the inflow, as it speeds it up at the eastern end of the strait and reduce the outflow in all cross-sections. It is remarkable the fact that the variation of transports is by far higher under easterlies than under westerlies, and even more in the upper layer.

Inflow and outflow values leads to an averaged net flow over CS of one order of magnitude greater as the one required by the mass budget for the Mediterranean Sea, under westerlies. Lacombe & Richez (1982) also reported a strong incoming flux in the western end of the strait due to a south-southwesterly intense (18-20 knots) wind episode.

Under the easterly wind episode, the net flow reached a peak of -1.21 Sv (at the main sill) toward the Atlantic Ocean. This negative net flow fluctuation agrees with the values obtained by García-Lafuente *et al.* (2002b) related to the conjunction of rapid and large atmospheric pressure changes and strong and persistent easterlies within the Strait of Gibraltar, in February 1998, propitiating inflow interruption.

5. Summary and conclusions

In this study the role of the wind-stress and the associated dynamic ocean response has been analyzed by means of a wind-forced ocean model within the Strait of Gibraltar.

Results achieved cover a broad range of issues including: (i) the assessment of the wind-forced ocean model in relation to the ocean-alone model with tidal forcing by comparing their outputs with oceanographic observations; (ii) revealing of the existence of a semi-permanent westward countercurrent along the northern coast of the Strait; (iii) the clear relationship between the zonal wind component and the cross-strait sea level difference; (iv) the analysis of the wind induced geostrophic currents; (v) the individual and the joint effect of wind and tidal forcing on the circulation of the Strait of Gibraltar; (vi) the analysis of internal wave events under different tidal conditions and the effect of the wind in the process of the internal bore generation, release and propagation; (vii) the time-space variability of the hydraulic controls and (viii) the subinertial fluctuations of the exchange through the Strait of Gibraltar induced by wind patterns.

i. Comparison of model results with different available data shows that the wind-forced ocean model simulates interface within the range of depths of the halocline, it reproduces properly the subinertial variability of the along-strait current and the sudden response to cyclone crossing the Strait westward as well as the surface circulation, providing by far a better agreement with the observations than the ocean model with only tidal forcing.

ii. For the first time, a semi-permanent westward counter-current along the northern coast of the Strait (between Punta Carnero and Punta Europa) has been

observed, with the drifter track, and properly simulated with the wind-forced ocean model. Even the presence of easterly winds is not necessary for the CCC occurrence, they have a direct influence on its development by direct wind stress and due to the piling up of water on the northern coast.

iii. Comparison of model results against cross-strait sea level differences shows a high correspondence between the occurrence of intense easterly (westerly) winds and cross-strait sea level drop (rise). For very intense easterly winds the sea-level slope can be inverted, as well as the inflow.

iv. Local wind stress impact on the Strait circulation can be comparable to that of the remote atmospheric forcing since easterly winds over 20 $m \cdot s^{-1}$ induce westward geostrophic subinertial currents of similar and even higher magnitude than the barotropic subinertial currents driven by atmospheric pressure fluctuations over the Mediterranean.

v. The hydrodynamic patterns, induced by wind stress, are successfully simulated showing the two fold effect of the winds: from the one hand, the direct easterly (westerly) wind drag reduces (increases) the intensity of the eastward upper layer current. On the other hand, easterly (westerly) winds originate downwelling (upwelling) phenomena in the northeastern coast of the Strait of Gibraltar, which subsequently will induce an increase (reduction) of the upper layer thickness, deepening (rising up) the interface and rising (dropping) the sea level. Furthermore, the accumulation of water in the northern (southern) part reduces (reinforces) the downwards south-to-north sea surface slope, which induces a geostrophic current westward (eastward). Over Camarinal Sill, easterlies (westerlies) drop (rise) the sea level and the interface becomes shallower (deeper).

vi. Changes in the intensity of the inflow and fluctuations of the interface depth, due to wind forcing, bring forward 1 hour the generation of the hydraulic jump at the lee side of Camarinal Sill and the release time of the internal bore. Furthermore, easterlies reduce the wave propagation speed from Tarifa to Punta Cires, when compared with the tidal forcing solution.

vii. The fluctuations at the interface, due to wind forcing, impacts on the location of the hydraulic controls, being able to activate extra supercritical regions, in the cross-section between Gibraltar and Ceuta, (under westerly episodes) or to

inhibit the ones already existing, as the apparent control in the narrows (under easterly episodes).

viii. Estimations of Atlantic inflow and Mediterranean outflow noticeably improved when including wind-stress in the hydrodynamic model, particularly during the intense easterly wind events. Minimum inflow and maximum outflow values are associated with intense easterly wind episodes, which diminish the exchange rates due to the interface rise over the main sill and, which are even able to reverse the flow in the upper layer. Maximum inflow takes place when the interface is deeper at the Sill, coinciding with westerlies.

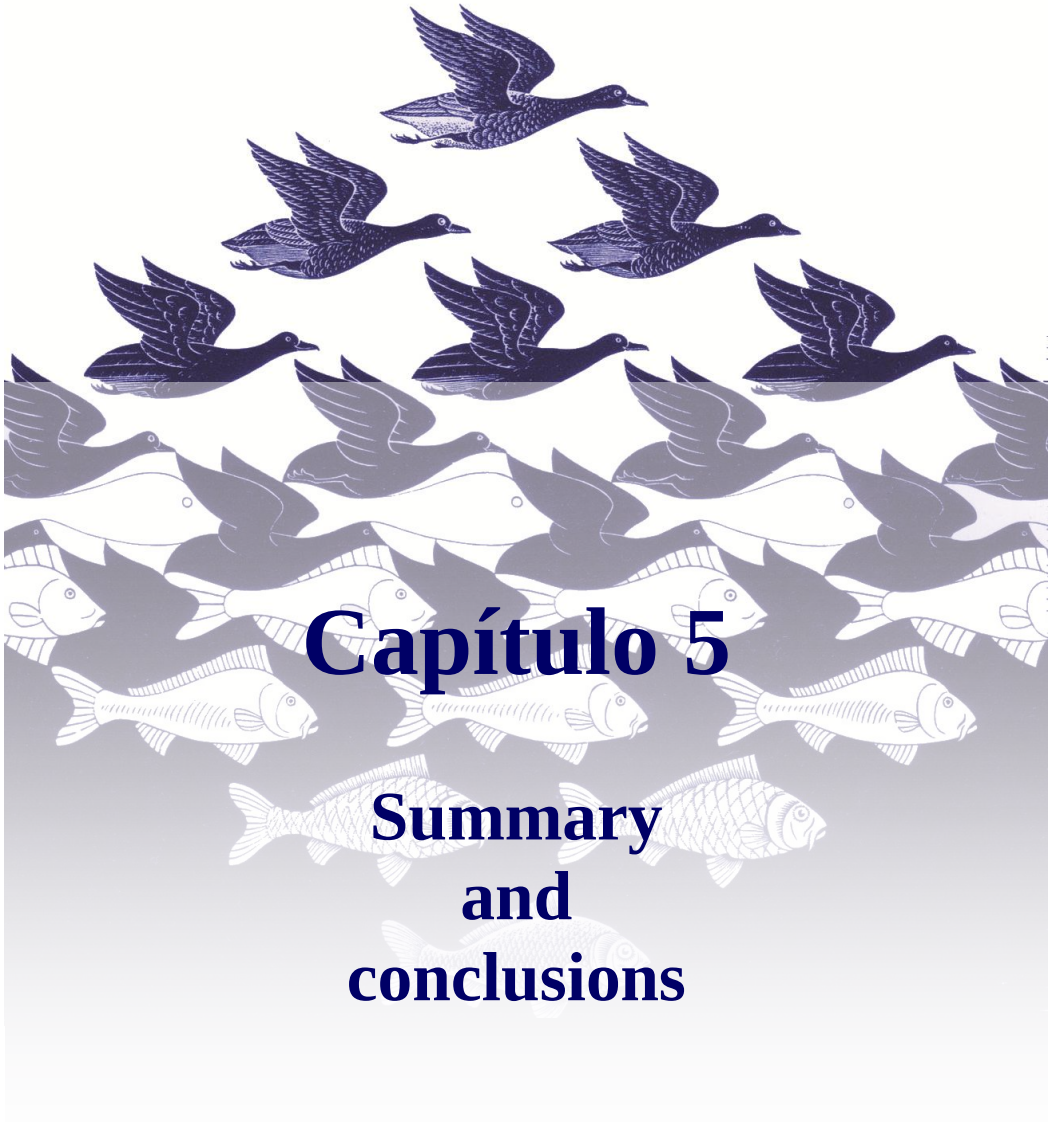

Capítulo 5

Summary and conclusions

Capítulo 5

SUMMARY AND CONCLUSIONS

1. Introduction

1.1. Background and previous work

The Strait of Gibraltar connects the Atlantic Ocean with the Mediterranean Sea along 60 km (figure 1.1 and figure 1.3 of Chapter 1 show the bathymetric map and the axial bathymetric profile along the Strait, respectively. The most notable geographical and undersea features are also indicated). The mean circulation through the Strait is composed of two counter flowing currents. In the upper layer fresher Atlantic water flows east toward the Mediterranean and, in the lower layer, saltier and denser Mediterranean water flows westward to the Atlantic (Stommel & Farmer, 1953; Lacombe & Richez, 1982; Farmer & Armi, 1986). The two-layer exchange is hydraulically controlled in the narrowest section of 14 km wide (Tarifa Narrows), at the main sill of 284 m deep (Camarinal Sill) as well as at Espartel Sill (Armi & Farmer, 1985; Farmer & Denton, 1985; Farmer & Armi, 1986; Armi & Farmer, 1987).

Tidal currents (Lacombe & Richez, 1982; Candela *et al.*, 1990), the interaction of the barotropic flow with Camarinal Sill (Armi & Farmer, 1988; Farmer & Armi, 1988), atmospheric pressure fluctuations within the Mediterranean (Crepon, 1965; Candela *et al.*, 1989; Garrett *et al.*, 1989) and the direct action of the winds (García-

Lafuente *et al.*, 2002a), together with the seasonal and interannual low-frequency fluctuations (García-Lafuente *et al.*, 2002c), modulate the resulting mean exchange flows.

Tides in the Strait of Gibraltar are by far the most energetic process, being of great significance to determine the circulation patterns and their time-space variability. Within the Strait the tide is principally semidiurnal (Candela *et al.*, 1990) and it could be strong enough to reverse inflow or outflow during certain phases of the tidal cycle in the Camarinal Sill section (Bruno *et al.*, 2000; García-Lafuente *et al.*, 2000; Bruno *et al.*, 2002), where it exhibits a noticeable barotropic structure.

Variable atmospheric pressure over the Mediterranean basin has always been considered to be the main driving force acting at subinertial frequencies in the Strait of Gibraltar (Crepon, 1965; Candela *et al.*, 1989; García-Lafuente *et al.*, 2002a). An increase (decrease) in the atmospheric pressure over the Mediterranean is followed by a subsequent decrease (increase) in the intensity of the Atlantic inflow, which consequently modulates the dynamic of the Western Alboran Gyre (Macías *et al.*, 2008), inducing changes in the distribution of biogeochemical variables. Atmospheric pressure fluctuations can also reinforce or inhibit the generation of internal waves (Vázquez *et al.*, 2008).

1.2. Statement of the problem

Despite the extensive efforts being made to study the meteorologically-driven circulation within the Strait of Gibraltar, results have, however, not been conclusive so far as: (i) subinertial flow fluctuations cannot be explained by atmospheric pressure variability by itself, being necessary the consideration of wind stress in some particular events of episodic reversions or strong reductions of the inflow (García-Lafuente *et al.*, 2002b); (ii) the baroclinic response of the exchanged flows to meteorologically induced barotropic fluctuations was analyzed by means of a barotropic model (García-Lafuente *et al.*, 2002a); (iii) the atmospheric forcing conditions were produced with a low spatial resolution meteorological hydrostatic model (García-Lafuente *et al.*, 2002a); (iv) when realistic atmospheric fields were considered based on high-resolution, non-hydrostatic model simulations, the joint effect of tidal and atmospheric forcing was not addressed (Peliz *et al.*, 2009). Even though the work of (Sánchez-Garrido *et al.*, 2014) uses a state-of-the-art regional circulation model of the Strait of Gibraltar to study the effect of

meteorologically forced flows, the analysis and validation of the model has been carried out inside the Bay of Algeciras, the target area of SAMPA[1] project.

2. General and specific objectives

In this work, a high-resolution wind-forced ocean model has been implemented, validated and analyzed to investigate the spatio-temporal variability of the ocean dynamics due to wind forcing within the Strait of Gibraltar and to study the wind-induced fluctuations of the flow exchange and the time-space variability of the hydraulic controls.

In order to address the problem posed in this study, the following tasks were undertaken:

- To study the spatio-temporal variability of the atmospheric phenomena within the Strait of Gibraltar, by means of the implementation, validation and output analysis of a high-resolution non-hydrostatic mesoscale meteorological model.
- To study the spatio-temporal variability of the wind-induced circulation patterns within the Strait of Gibraltar, on the basis of the results of a high-resolution ocean model forced by tides and winds.
- To assess the influence of wind on the subinertial scale studying the individual and joint impact of wind and tidal forcing on the circulation of the Strait of Gibraltar.

3. Hypothesis

The key questions related to the individual and joint role of wind and tidal forcing on the spatio-temporal variability of the hydrodynamic pattern in the Strait of Gibraltar have been raised and addressed. These questions constitute the working hypothesis of this research:

- Different wind fields would induce changes in the surface circulation patterns, particularly on the coastal areas.
- Bearing in mind the influence of the bottom and interfacial friction on the flow and how the inclusion of the former significantly affect the interface depth, we wonder which interface fluctuations would be induced by wind stress.

[1] SAMPA project (Sistema Autónomo de Medición, Predicción y Alerta – Autonomous System for Monitoring, Forecasting and Alert)

- As a direct consequence of the previous hypothesis, the question that arises is if those interface fluctuations, induced by wind, could modify the location of the hydraulic controls and even if the controlled regions may be inhibited or activated depending on the wind forcing.
- Intensity changes of the inflow and fluctuations of the interface depth, due to wind forcing, could induce modifications of the large-amplitude internal waves properties (amplitude, propagation speed). The bore generation, trapping and release times could also be modified under different wind patterns.
- Fluctuations in the interface depth, due to wind forcing, could also induce changes of the outflow, due to the modifications of upper and layer thicknesses.

4. Data sets and models

4.1. Data sets

Meteorological measurements comprise hourly wind speed and direction, air temperature and sea level pressure from:

- more than 100 Automatic Weather Stations over land: 95 belonging to the Andalusian Institute of Agricultural and Fisheries Research and Training (IFAPA) (Gavilán *et al.*, 2006; Estévez *et al.*, 2011), widely spaced over the Andalusian region and 12 from the State Meteorological Agency (AEMET), with seven of them measuring at daily interval. Name and location of the AWS from AEMET are summarized in table 2.1.
- 2 ocean buoys from the Deepwater Buoy Network owned by Puertos del Estado (State Ports Authority, Spain), which measure at 3 m above water surface level (see table 2.2 for more information).

Figure 2.1 shows the location of the AWS and buoys over a topographic map.

Oceanographic observations consists of:

- continuous measurements of ADCP current profile at Camarinal Sill location from the experiment "*Strait 94-96*" (table 2.3 summarizes the location of the mooring and the current measurements details).
- single-point currentmeter records deployed in the north part of Camarinal Sill during *"Gibraltar-08"* oceanographic survey (more information in table 2.4).
- salinity profiles from CTD casts, performed under different tidal conditions on an extensive grid (shown in figure 2.2) during *"Gibraltar-08"* oceanographic survey.

- historical sea-level data from 1995 of three different tide gauge stations (Ceuta, Algeciras and Tarifa) from the IEO network (table 2.5 shows their locations).
- surface trajectories from four drifter buoys deployed in the middle of the channel at the eastern entrance of the Strait during October 2011 (drifter's deployment time and location is summarized in table 2.6).

Figure 2.4 compiles all oceanographic measurements location over a bathymetric chart.

4.2. Models

4.2.1. Mesoscale meteorological model (MM5)

The Fifth-Generation NCAR / Penn State University Mesoscale Model (MM5) (Dudhia, 1993), has been used (version 3.7) as forecast model for simulating mesoscale atmospheric circulation.

MM5 is a limited-area, non-hydrostatic, primitive equation model with a terrain-following sigma-coordinate model. A triple one-way nested (Lozej & Bornstein, 1999) configuration was chosen with the outermost domain of 30-km spatial resolution, centred at the Iberian Peninsula, down to 10-km, covering the Andalusian region, and to 3.3-km, focused on the Strait of Gibraltar (see figure 2.7). Information flows in one direction, from the previously integrated forecast over the larger domain to the inner domain model.

All domains have 35 sigma levels. The upper boundary was fixed at 100 hPa. Time steps used for the simulations are 90, 30 and 10 seconds, for the domains 1, 2 and 3, respectively. The 25-categories U.S. Geological Survey (USGS) global land-use distribution in MM5 were used with 2 min (~4 km) latitude and longitude resolution in the coarse domain, and 30 s (0.9 km) in the inner ones (table 2.7).

The most suitable advanced physical parameterizations have been chosen for cumulus (Kain & Fritsch, 1993), the Medium Range Forecast model (MRF) scheme (Hong & Pan, 1998) for the planetary boundary layer (PBL), the cloud-radiation scheme (Dudhia, 1989), the five-layer soil temperature (Dudhia, 1996) as surface scheme and Reisner 2 scheme for microphysics (table 2.8).

The model is initialized and forced at the boundaries with operational forecasts of MM5-30 km performed at MeteoGalicia, using the run at 0000 UTC with a forecast horizon of 96 h (hereinafter referred to as MM5F). At the same time, the MM5-30 km

routinely obtained the initial and boundary conditions each 3 hours from NCEP GFS at 1º of horizontal resolution.

In the hindcast run (named hereinafter as MM5H simulation), the 1º × 1º GFS analysis from NCEP has been used as initial and boundary conditions, updated every six hours. Figure 2.8 shows a scheme of the MM5F and MM5H runs.

It is worth mentioning at this point that since 2007, the Research Group of Physical Oceanography from the University of Cádiz, in collaboration with MeteoGalicia, has been running MM5 in real time daily, with forecast horizon of 72 hours.

Model validation has been performed by qualitative and quantitative comparison of different MM5 runs over the Strait of Gibraltar and observations from more than 100 surface stations on land and 2 deep ocean buoys. The grid-to-point approach has been used because the observations are of significantly lower resolution than the model output.

Forecast errors and, therefore, the model performance, are described in terms of dimension[2] negatively-oriented[3] error statistics: the mean absolute error (MAE), the root mean square error (RMSE) and the bias error (BIAS). Slightly variations of these scores are used for wind direction (Jiménez & Dudhia, 2013), which is an angular variable and it could present problems associated with overlap from 0° and 360°.

The index of agreement (IOA) (Willmott, 1981) and the coefficients of determination (r-squared) and correlation (r) are also estimated. All mentioned scores were calculated for temperature at 2 m above the ground, sea level pressure and horizontal winds at 10 m above the ground.

Additionally, each statistical metric was compared to performance benchmarks (table 2.9), for simple (Emery *et al.*, 2001) and complex conditions (Kemball-Cook *et al.*, 2005), to determine the meteorological representativeness for the specific modeling period.

4.2.2. Hydrodynamic model (UCA2.5D)

Following the two-layer approximation, the dynamics of the Strait of Gibraltar was modeled using the UCA2.5D (Izquierdo *et al.*, 2001) hydrodynamic model. It is a two-dimensional, nonlinear, based on the shallow water equations of momentum and

[2] It expresses average error in the units of the variable of interest.
[3] The lower the values the better model assessment.

continuity, which are discretized on a Arakawa C grid and solved by employing a semi-implicit Crank-Nicolson scheme in a boundary-fitted curvilinear coordinates grid (figure 2.9 shows the UCA2.5D model grid and bathymetry). A complete model description, including governing equations is available in (Izquierdo *et al.*, 2001).

A steady-state solution (figure 2.10) for the mean interface depth and surface elevation is obtained from lock-exchange experiment and used as initial condition to simulate the tidal forcing by prescribing the surface elevation amplitudes and phases of the principal semidiurnal (M_2, S_2) and diurnal (K_1, O_1) tide constituents at the open boundaries, provided by the global tidal solution model FES95.2 (Le Provost *et al.*, 1998) and from coastal tide gauges.

The model is capable of accurately reproducing: (i) the semidiurnal tidal pattern, with diurnal inequality and the fortnightly variability within the Strait of Gibraltar; (ii) the existence of hydraulic controls located to the west of the Espartel Sill, at the Espartel and Camarinal Sills and the apparent control in the Tarifa Narrows as well as their time-space variability; (iii) the generation of internal bores, due to the interaction of the barotropic tidal flow with Camarinal Sill; (iv) the propagation of the large-amplitude baroclinic bore toward the Mediterranean and a small-amplitude, bore-like interfacial disturbance in the lee of the Espartel Sill. Furthermore, the substantially lower computational cost when compared with three-dimensional primitive-equation model justify the use of the UCA2.5D model.

4.2.3. Wind-forced ocean model (MM5UCA2.5D)

On the basis of the UCA2.5D ocean model, hourly values of wind stress, computed from the wind field provided by the mesoscale meteorological MM5-10 km model domain, drive the circulation at the sea surface.

Wind shear stress was computed, using a quadratic drag law (equation 2.19), from wind field at 10 m, and then linearly interpolated in time and bilinearly in space, appearing as an extra term in the momentum equation for the upper layer, given in cartesian coordinates, expressed in transport form, by equation (2.20).

Several sensitive experiments (parameters and values summarized in table 2.10) have been carried out in order to fix the parameters to guarantee the stability of the wind-forced ocean model simulations. Results show that the best suitable set of parameters are: 3 seconds for time-step, $2.0 \cdot 10^{-3}$, $1 \cdot 10^{-3}$ and $1 \cdot 10^{-2}$ $cm^2 s^{-1}$, for the wind, interfacial and bottom drag coefficients, respectively.

In order to study the individual and collective role of wind and tidal forcing on the circulation of the Strait of Gibraltar, different sets of simulations have been run:

- NON-TIDE experiments use the steady state solution reached at a lock-exchange experiment as initial condition. At the sea surface, the model is driven by constant and homogeneous easterly (NON-TIDE-E) and westerly (NON-TIDE-W) winds of 10 $m \cdot s^{-1}$ (figure 2.11 shows a schematic diagram of the NON-TIDE simulation).
- TIDE simulations include tidal forcing, as it has been previously described. Then, the model is being forced by constant and homogeneous E and W winds and by a realistic wind field simulated by the MM5-10 km (TIDE-WIND) (figure 2.12 presents the scheme of the TIDE experiments runs).

Results obtained from the TIDE-WIND experiment are compared with a one-month current velocity data series from a single-point current-meter deployed at the north of Camarinal Sill during the intensive oceanographic survey "*Gibraltar'08"*. One-full-year period (1995) was also selected to allow validation against ADCP data measured over Camarinal Sill during the experiment "*Strait 94-96*". Outputs were also compared with sea level data from three tide gauge stations, with the interface depth range obtained from the salinity profiles provided by the CTDs, as well as with the trajectories reported by surface drifters released in the area.

5. Conclusions

This section brings together the conclusions from this research.

The main findings of the implementation and performance assessment of the high-resolution non-hydrostatic MM5 model in the Strait of Gibraltar are outlined below:

i. Examination of the relationship between model resolution and predictive skills allows to conclude that the MM5-10 km has slightly better wind field skill, particularly by simulating wind speed, than the MM5-30 km domain, but there is no improvement from 10 to 3.3-km. This is likely due to the fact that MM5 produces more stochastic variations at finer resolution, requiring the use of more detailed physiographic properties and an optimal combination of physical parameterizations, which is beyond the scope of this work. For this reason and in order to reduce interpolation errors, which worsen as the grid coarsens,

between the atmospheric and ocean model grids, the MM5-10 km has been used to provide the meteorological forcing to the ocean model (~ 1 km nominal).

ii. MM5-10 km improves on the previous model existent in the area, the hydrostatic grid-point HIRLAM.

iii. Evaluation of short-term operational forecast and hindcast error indicates, unexpectedly, that short-term forecast better fits the analyzed meteorological fields inland than hindcast, while over the sea, it occurs the opposite, except for the surface temperature. Nevertheless, variations in model initial and boundary conditions did not significantly affect the model performance, suggesting a major influence of terrain and land-use heterogeneities on wind field.

iv. The MM5 model reproduces the temporal variability of surface temperature and wind field adequately along the month of May 2007. However, it may be concluded that the model underestimates the diurnal temperature range, presenting also difficulties in simulating weak nocturnal winds, shifting wind direction to larger angles.

v. Geographical distribution of errors was studied with the aim to highlighting MM5 shortcomings related to complex topography. Results suggest an error dependency to the terrain elevation and topographical effects, with a better model skill over the Guadalquivir valley and plains than at the hills and Baetic mountain range. Winds are generally overestimated over land, to a lesser extent over plains and valleys and with the highest wind speed and wind direction errors found over the high terrain and near sea-level stations. So thus, simulated winds are anticyclonically rotated from observed and more intense, associated to the unresolved roughness or friction of subgrid terrain, which in turns may indicate deficiencies in the model's representation of the topographic forcing. Surface temperature is clearly overestimated over plains while the hills are characterized by a cold bias.

vi. Pure sea-land breezes were developed under prevailing mesoscale conditions along the entire Andalusian coast whereas only non-pure sea-breezes were onset under synoptic ones and mainly on the Atlantic coast. The MM5 model is able to capture the diurnal wind oscillation associated with both sea-land breeze circulation patterns. However, the model performs better by reproducing non-pure sea-breeze events, particularly on the Atlantic coast, but it delays the sea-breeze front onset, its gradually intensification and the large inland penetration

up to the Guadalquivir valley, which may be related to the use of constant SST in coastal areas where large temperature gradients between land and water exist. At the same time, the model presents difficulties to capture the variability of the pure land-breezes, particularly on the Mediterranean coast.

vii. MM5 performs better by simulating land temperature under non-pure breeze conditions, particularly over the main valley and plains. The model wind direction improves under strong synoptic wind conditions of these days (28-29 May), particularly along the orographic depressions and valleys parallel to the northwesterly wind direction. Weak mesoscale winds and too warm surface temperature during the pure-breeze event trigger larger errors in wind direction and temperature, while the model better simulates daytime wind speed with the larger errors found at coastal stations closer to the Strait.

The major conclusions drawn from the study of the role of the wind-stress and the associated dynamic ocean response within the Strait of Gibraltar are the following:

viii. Comparison of model results with different available data shows that the wind-forced ocean model simulates interface within the range of depths of the halocline, it reproduces properly the subinertial variability of the along-strait current and the sudden response to cyclone crossing the Strait westward as well as the surface circulation, providing by far a better agreement with the observations than the ocean model with only tidal forcing.

ix. For the first time, a semi-permanent westward counter-current along the northern coast of the Strait (between Punta Carnero and Punta Europa) has been observed, with the drifter track, and properly simulated with the wind-forced ocean model. Even the presence of easterly winds is not necessary for the CCC occurrence, they have a direct influence on its development by direct wind stress and due to the piling up of water on the northern coast.

x. Comparison of model results against cross-strait sea level differences shows a high correspondence between the occurrence of intense easterly (westerly) winds and cross-strait sea level drop (rise). For very intense easterly winds the sea-level slope can be inverted, as well as the inflow.

xi. Local wind stress impact on the Strait circulation can be comparable to that of the remote atmospheric forcing since easterly winds over 20 $m \cdot s^{-1}$ induce westward geostrophic subinertial currents of similar and even higher magnitude

than the barotropic subinertial currents driven by atmospheric pressure fluctuations over the Mediterranean.

xii. The hydrodynamic patterns, induced by wind stress, are successfully simulated showing the two fold effect of the winds: from the one hand, the direct easterly (westerly) wind drag reduces (increases) the intensity of the eastward upper layer current. On the other hand, easterly (westerly) winds originate downwelling (upwelling) phenomena in the northeastern coast of the Strait of Gibraltar, which subsequently will induce an increase (reduction) of the upper layer thickness, deepening (rising up) the interface and rising (dropping) the sea level. Furthermore, the accumulation of water in the northern (southern) part reduces (reinforces) the downwards south-to-north sea surface slope, which induces a geostrophic current westward (eastward). Over Camarinal Sill, easterlies (westerlies) drop (rise) the sea level and the interface becomes shallower (deeper).

xiii. Changes in the intensity of the inflow and fluctuations of the interface depth, due to wind forcing, bring forward 1 hour the generation of the hydraulic jump at the lee side of Camarinal Sill and the release time of the internal bore. Furthermore, easterlies reduce the wave propagation speed from Tarifa to Punta Cires, when compared with the tidal forcing solution.

xiv. The fluctuations at the interface, due to wind forcing, impacts on the location of the hydraulic controls, being able to activate extra supercritical regions, in the cross-section between Gibraltar and Ceuta, (under westerly episodes) or to inhibit the ones already existing, as the apparent control in the narrows (under easterly episodes).

xv. Estimations of Atlantic inflow and Mediterranean outflow noticeably improved when including wind-stress in the hydrodynamic model, particularly during the intense easterly wind events. Minimum inflow and maximum outflow values are associated with intense easterly wind episodes, which diminish the exchange rates due to the interface rise over the main sill and, which are even able to reverse the flow in the upper layer. Maximum inflow takes place when the interface is deeper at the Sill, coinciding with westerlies.

REFERENCES

Adame, J.A., Serrano, E., Bolívar, J.P., De la Morena, B.A., (2010). On the tropospheric ozone variations in a coastal area of the sourthwestern Europe under mesoscale circulation. *Journal of Applied Meteorology and Climatology*, 49, 748-759.

Adame, J.A., Hernández-Ceballos, M.A., Bolívar, J.P., De la Morena, B., (2012). Assessment of an air pollution event in the southwestern Iberian Peninsula. *Atmospheric Environment*, 55 (0), 245-256.

AEMET, (2007). Informe mensual climatológico. Mayo de 2007. Instituto Nacional de Meteorología. Ministerio de Medio Ambiente, p. 6

Aguiar-González, B., Rodríguez-Santana, Á., Cisneros-Aguirre, J., Martínez-Marrero, A., (2011). Diurnal-inertial motions and diapycnal mixing on the Portuguese shelf. *Continental Shelf Research*, 31 (11), 1193-1201.

Álvarez, O., Izquierdo, A., Tejedor, B., Mañanes, R., Tejedor, L., Kagan, B.A., (1999). The influence of sediment load on tidal dynamics, a case study: Cádiz Bay. *Estuarine, Coastal and Shelf Science*, 48 (4), 439-450.

American Meteorological Society., (2013). : "mesoscale". Glossary of Meteorology. [Available online at http://glossary.ametsoc.org/wiki/Mesoscale]

Arakawa, A., Lamb, V.R., (1977). Computational design of the basic dynamical process of the UCLA general circulation model. *Methods in Computational Physics*, 17, 173-265.

Armi, L., Farmer, D.M., (1985). The internal hydraulics of the Strait of Gibraltar and associated sill and narrows. *Oceanologica Acta*, 8, 37-46.

Armi, L., (1986). Hydraulics of two flowing layers with different densities. *Journal of Fluid Mechanics*, 163, 27-58.

Armi, L., Farmer, D.M., (1986). Maximal two-layer exchange through a contraction with barotropic net flow. *Journal of Fluid Mechanics*, 164, 27-51.

Armi, L., Farmer, D., (1987). A generalization of the concept of maximal exchange in a Strait. *J. Geophys. Res.*, 92 (C13), 14679-14680.

Armi, L., Farmer, D.M., (1988). The flow of Mediterranean water through the Strait of Gibraltar. *Progress in Oceanography*, 21, 1-105.

Armstrong, M.A., (2000). Comparison of MM5 forecast shortwave radiation with data obtained from the atmospheric radiation measurement program.

Assaf, G., Hecht, A., (1974). Sea straits: a dynamical model. *Deep-Sea Research and Oceanographic Abstracts*, 21 (11), 947-958.

Ayala, F.J., Ferrer, M., González de Vallejo, L., Beltrán de Herdia, F. (Eds.), (1988). Catálogo Nacional de Riesgos Geológicos. Ingeniería GeoAmbiental, Madrid.

Backhaus, J.O., (1983). A semi-implicit scheme for the shallow water equations for application to shelf sea modelling. *Continental Shelf Research*, 2, 243-254.

Backhaus, J.O., Hainbucher, D., (1987). A finite difference general circulation model for shelf sea and its applications to low frequency variability on the North European Shelf. In: Jamart, J.C.N.a.B.M. (Ed.), Three dimensional model of marine and estuarine dynamics. Elservier, Amsterdam, pp. 221-244.

Ballentine, R.J., Stamm, A.J., Chermack, E.E., Byrd, G.P., Schleede, D., (1998). Mesoscale model simulation of the 4-5 January 1995 lake-effect snowstorm. *Weather Forecasting*, 13, 893-919.

Barton, E.D., Relvas, P., (2005). A separated jet and coastal counterflow during upwelling relaxation off Cape São Vicente (Iberian Peninsula). *Continental Shelf Research*, 25, 29-49.

Bascheck, B., Send, U., García-Lafuente, J., Candela, J., (2001). Transport estimates in the Strait of Gibraltar with a tidal inverse model. *Journal of Geophysical Research.*, 106 (C12), 31033-31044.

Bendall, A.A., (1982). Low-level flow through the Strait of Gibraltar. *The Meteorological Magazine*, 111, 149-153.

Blumberg, A.F., Mellor, G.L. (Eds.), (1987). A description of a three-dimensional coastal ocean circulation model. Ed. American Geophysical Union.

Bormans, M., Garrett, C., Thompson, K., (1986). Seasonal variability of the surface inflow through the Strait of Gibraltar. *Oceanologica Acta*, 9 (4), 403-414.

Bormans, M., Garrett, C., (1989a). The effects of nonrectangular cross section, friction, and barotropic fluctuations on the exchange through the Strait of Gibraltar. *Journal of Physical Oceanography*, 19 (10), 1543-1557.

Bormans, M., Garrett, C., (1989b). The effect of rotation on the surface inflow through the Strait of Gibraltar. *Journal of Physical Oceanography*, 19, 1535-1542.

Brandt, P., Alpers, W., Backhaus, J.O., (1996). Study of the generation and propagation of internal waves in the Strait of Gibraltar using a numerical model and synthetic aperture radar images of the European ERS 1 satellite. *Journal of Geophysical Research*, 101 (C6), 14237-14252.

Brandt, P., Rubino, A., Sein, D.V., Baschek, B., Izquierdo, A., Backhaus, J.O., (2004). Sea level variations in the western Mediterranean studied by a numerical tidal model of the Strait of Gibraltar. *Journal of Physical Oceanography*, 34 (2), 433-443.

Braun, S.A., Tao, W.-K., (2000). Sensitivity of high-resolution simulations of hurricane Bob (1991) to planetary boundary layer parameterizations. *Monthly Weather Review*, 128 (12), 3941-3961.

Bray, N.A., Ochoa, J., Kinder, T.H., (1995). The role of the interface in exchange through the Strait of Gibraltar. *Journal of Geophysical Research*, 100 (C6), 10755-10776.

Bruno, M., Mañanes, R., Alonso, J.J., Izquierdo, A., Tejedor, L., Kagan, B.A., (2000). Vertical structure of the semidiurnal tidal currents at Camarinal Sill, the strait of Gibraltar. *Oceanologica Acta*, 23 (1), 15-24.

Bruno, M., Juan Alonso, J., Cózar, A., Vidal, J., Ruiz-Cañavate, A., Echevarría, F., Ruiz, J., (2002). The boiling-water phenomena at Camarinal Sill, the strait of Gibraltar. *Deep Sea Research Part II: Topical Studies in Oceanography*, 49 (19), 4097-4113.

Bruno, M., Macías, J., González-Vida, J.M., Vázquez, A., (2010). Analyzing the tidal-related origin of subinertial flows through the Strait of Gibraltar. *Journal of Geophysical Research: Oceans*, 115 (C12), C12075.

Bruno, M., Chioua, J., Romero, J., Vázquez, A., Macías, D., Dastis, C., Ramírez-Romero, E., Echevarria, F., Reyes, J., García, C.M., (2013). The importance of sub-mesoscale processes for the exchange of properties through the Strait of Gibraltar. *Progress in Oceanography*, 116 (0), 66-79.

Bryden, H.L., Stommel, H., (1984). Limiting processes that determine basic features of the circulation in the Mediterranean Sea. *Oceanologica Acta*, 7, 289-296.

Bryden, H.L., Kinder, T.H., (1991). Steady two-layer exchange through the Strait of Gibraltar. *Deep Sea Research, Part A*, 38, 445-463.

Bryden, H.L., Candela, J., Kinder, T.H., (1994). Exchange through the Strait of Gibraltar. *Progress in Oceanography*, 33 (3), 201-248.

Candela, J., Winant, C.D., Bryden, H.L., (1989). Meteorologically forced subinertial flows through the Strait of Gibraltar. *Journal of Geophysical Research*, 94 (C9), 12667-12679.

Candela, J., Winant, C., Ruiz, A., (1990). Tides in the Strait of Gibraltar. *J. Geophys. Res.*, 95 (C5), 7313-7335.

Candela, J., Winant, C.D., Bryden, H.L., (1991). The Gibraltar Strait and its role in the dynamics of the Mediterranean Sea. *Dynamics of Atmospheres and Oceans*, 15, 267-299.

Candela, J., Lozano, C.J., (1994). Barotropic response of the western Mediterranean to observed atmospheric pressure forcing. *Seasonal and Interannual Variability of the Western Mediterranean Sea. Coastal and Estuarine Studies*, 46, 325-359.

Candela, J., (2001). Mediterranean Water and Global Circulation.

Carpenter, W.B., Jeffreys, G., J., (1870). Report on Deep-Sea Researches carried on during the months of July, August, and September 1870, in H.M. Surveying-Ship "Porcupine". *Proceedings of the Royal Society of London (1854-1905)*, 19, 145-221.

Case, J.L., Wheeler, M.M., Manobianco, J., Weems, J.W., Roeder, W.P., (2005). A 7-Yr climatological study of land breezes over the Florida Spaceport. *Journal of Applied Meteorology*, 44, 340-356.

Colle, B.A., Mass, C.F., (1998). Windstorms along the Western Side of the Washington Cascade Mountains. Part I: A High-Resolution Observational and Modeling Study of the 12 February 1995 Event. *Monthly Weather Review*, 126 (1), 28-52.

Colle, B.A., Mass, C.F., (2000a). The 5-9 February 1996 Flooding Event over the Pacific Northwest: Sensitivity Studies and Evaluation of the MM5 Precipitation Forecasts. *Monthly Weather Review*, 128 (3), 593-617.

Colle, B.A., Mass, C.F., (2000b). High-resolution observations and numerical simulations of easterly gap flow through the Strait of Juan de Fuca on 9-10 December 1995. *Monthly Weather Review*, 128 (7), 2398-2422.

Colle, B.A., Olson, J.B., Tongue, J.S., (2003). Multiseason Verification of the MM5. Part I: Comparison with the Eta Model over the Central and Eastern United States and Impact of MM5 Resolution. *Weather and Forecasting*, 18 (3), 431-457.

Crawford, T.M., Stensrud, D., Mora, F., Merchant, J., Wetzel, P., (2001). Value of incorporating satellite-derived land cover data in MM5/PLACE for simulating surface temperatures. *Journal of Hydrometeorology*, 2, 453-468.

Crepon, M., (1965). Influence de la presion armospherique sur le niveau moyén de la Mediterranée Occidentale el sur le flux á travers le Detroit de Gibraltar. *Cah. Oceanography*, 1, 15-23.

Cressman, G., (1959). An operational objective analysis system. *Mon. Weather Rev.*, 87, 367-374.

Csanady, G.T., (1977). Intermittent 'full' upwelling in Lake Ontario. *Journal of Geophysical Research*, 82 (3), 397-419.

Cushman-Roisin, B., Beckers, J.-M., (2008). *Introduction to Geophysical Fluid Dynamics. Physical and numerical aspects*. Vol. 101, Academic Press, 773 pp.

Charney, J.G., (1948). On the scale of atmospheric motions. *Geophys. Publ. Oslo*, 17 (2), 1-17.

Chen, F., Dudhia, J., (2001). Coupling an Advanced Land Surface–Hydrology Model with the Penn State–NCAR MM5 Modeling System. Part I: Model Implementation and Sensitivity. *Monthly Weather Review*, 129, 17 p.

Davis, C.A., Warner, T.T., Astling, E., Bowers, J., (1999). Development and application of an operational, relocatable, mesogamma-scale weather analysis and forecasting system. *Tellus Series A-dynamic Meteorology and Oceanography*, 51 (5), 710-727.

Defant, A., (1961). *Physical oceanography*. Vol. 1, Pergamon Press.

Delgado, J., (2005). Oscilaciones de corto período en el Estrecho de Gibraltar, Tesis Doctoral, Universidad de Granada. Facultad de Ciencias, España, Granada.

Dorman, C.E., Beardsley, R.C., Limeburner, R., (1995). Winds in the Strait of Gibraltar. *Quarterly Journal - Royal Meteorological Society*, 121 (528), 1903-1921.

Doyle, J.D., (1997). The Influence of Mesoscale Orography on a Coastal Jet and Rainband. *Monthly Weather Review*, 125 (7), 1465-1488.

Dudhia, J., (1989). Numerical study of convection observed during winter monsoon experiment using a mesoscale two-dimensional model. *Journal of Atmospheric Science*, 46, 3077-3107.

Dudhia, J., (1993). A non-hydrostatic version of the Penn State-NCAR Mesoscale Model: Validation tests and simulation of an Atlantic cyclone and cold front. *Monthly weather review.*, 121, 1493-1513.

Dudhia, J., (1996). A multi-layer soil temperature model for MM5. 6th PSU/NCAR Mesoscale Model User's Workshop, National Center for Atmospheric Research, p. 14 pp.

Dudhia, J., Gill, D., Manning, K., Wang, W., Bruyere, C., (1999). PSU/NCAR Mesoscale modeling system. Tutorial Class Notes and User's Guide: MM5 Modeling System Version 3. Mesoscale and Microscale Meteorology Division. National Center for Atmospheric Research.

Emery, C., Tai, E., Yarwood, G., (2001). Enhanced Meteorological Modeling and Performance Evaluation for Two Texas Ozone Episodes. Final report submitted to Texas Natural Resources Conservation Commission. ENVIRON International Corporation, Novato, CA, p. 235.

Esteras, M.M., (1984). Geología del Estrecho de Gibraltar. *Revista de Obras Públicas*, Julio-Agosto, 505-526.

Estévez, J., Gavilán, P., Giráldez, J.V., (2011). Guidelines on validation procedures for meteorological data from automatic weather stations. *Journal of Hydrology*, 402 (1-2), 144-154.

Faccenna, C., Piromallo, C., Crespo-Blanc, A., Jolivet, L., Rossetti, F., (2004). Lateral slab deformation and the origin of the western Mediterranean arcs. *Tectonics*, 23 (1), TC1012.

Farmer, D.M., Denton, R.A., (1985). Hydraulic control of flow over the sill in Observatory Inlet. *Journal of Geophysical Research*, 90 (C5), 9051-9068.

Farmer, D.M., Armi, L., (1986). Maximal two-layer exchange over a sill and through the combination of a sill and contraction with barotropic flow. *Journal of Fluid Mechanics*, 164, 53-76.

Farmer, D.M., Armi, L., (1988). The flow of Atlantic water through the Strait of Gibraltar. *Progress in Oceanography*, 21 (1), 1-103.

Flick, R.E., (1998). Comparison of California tides, storm surges, and mean sea level during the El Niño winters of 1982–1983 and 1997–1998. *Shore and Beach*, 66 (3), 7-11.

Folkard, A.M., Davies, P.A., Fiúza, A.F.G., Ambar, I., (1997). Remotely sensed sea surface thermal patterns in the Gulf of Cadiz and the Strait of Gibraltar: Variability, correlations, and relationships with the surface wind field. *Journal of Geophysical Research: Oceans*, 102 (C3), 5669-5683.

Fukumori, I., Menemenlis, D., and Lee, T., (2007). A near-uniform basin-wide sea level fluctuation of the Mediterranean Sea. *Journal of Physical Oceanography*, 37, 338-358.

Gan, J., Allen, J.S., (2002). A modeling study of shelf circulation off northern California in the region of the Coastal Ocean Dynamics Experiment: Response to relaxation of upwelling winds. *Journal of Geophysical Research: Oceans*, 107 (C9), 3123.

García-Lafuente, J., Vargas, J.M., Plaza, F., Sarhan, T., Candela, J., Bascheck, B., (2000). Tide at the eastern section of the Strait of Gibraltar. *Journal of Geophysical Research*, 105 (C6), 14197-14213.

García-Lafuente, J., Álvarez Fanjul, E., Vargas, J.M., Ratsimandresy, A.W., (2002a). Subinertial variability in the flow through the Strait of Gibraltar. *Journal of Geophysical Research*, 107 (C10), 3168.

García-Lafuente, J., Delgado, J., Criado, F., (2002b). Inflow interruption by meteorological forcing in the Strait of Gibraltar. *Geophysical Research Letters*, 29 (19).

García-Lafuente, J., Delgado, J., Vargas, J.M., Vargas, M., Plaza, F., Sarhan, T., (2002c). Low-frequency variability of the exchanged flows through the Strait of Gibraltar during CANIGO. *Deep Sea Research Part II: Topical Studies in Oceanography*, 49 (19), 4051-4067.

García-Lafuente, J., Sánchez-Román, A., Díaz del Río, G., Sannino, G., Sánchez Garrido, J.C., (2007). Recent observations of seasonal variability of the Mediterranean outflow in the Strait of Gibraltar. *J. Geophys. Res.*, 112 (C10), C10005.

Garrett, C., Akerley, J., Thompson, K., (1989). Low-frequency fluctuations in the Strait of Gibraltar from MEDALPFX sea level data. *Journal of Physical Oceanography*, 19 (11), 1682-1696.

Garrett, C., Thompson, K., Blanchard, W., (1990a). Is the exchange through the Strait of Gibraltar maximal or submaximal? . In: Ed. L.J. Pratt, K. (Ed.), Proceedings of NATO/ONR Workshop on the Physical Oceanography of Sea Straits., pp. 271-294.

Garrett, C., Thompson, K., Blanchard, W., (1990b). Sea-level flips. *Nature*, 348 (6299), 292.

Garrett, C.J.R., (1983). Variable sea level and strait flows in the Mediterranean: a theoretical study of the response to meteorological forcing. *Oceanologica Acta*, 6 (1), 79-87.

Gavilán, P., Lorite, I.J., Tornero, S., Berengena, J., (2006). Regional calibration of Hargreaves equation for estimating reference ET in a semiarid environment. *Agricultural Water Management*, 81 (3), 257-281.

Gille, S.T., Llewellyn Smith, S.G., Statom, N.M., (2005). Global observations of the land breeze. *Geophysical Research Letters*, 32.

Grell, G.A., Dudhia, J., Stauffer, D.R., (1994). A description of the fifth-generation Penn State/NCAR mesoscale model (MM5). NCAR Technical Note, NCAR/TN-398+STR, 117 pp.

Guichard, F., Parsons, D.B., Dudhia, J., Bresch, J., (2003). Evaluating Mesoscale Model Predictions of Clouds and Radiation with SGP ARM Data over a Seasonal Timescale. *Monthly Weather Review*, 131 (5), 926-944.

Hamilton, K., (1981). Latent Heat Release as a Possible Forcing Mechanism for Atmospheric Tides. *Monthly Weather Review*, 109 (1), 3-17.

Hernández-Ceballos, M.A., Adame, J.A., Bolívar, J.P., De la Morena, B.A., (2013). A mesoscale simulation of coastal circulation in the Guadalquivir valley (southwestern Iberian Peninsula) using the WRF-ARW model. *Atmospheric Research*, 124 (0), 1-20.

Hervella, B., Pérez-Muñuzuri, V., Balseiro, C.F., Montero, P., (2002). Application of the non-hydrostatic ARPS model to the 21st-23rd Decembre 2000 extreme weather event., 4th EGS Plinius Conference. Universitat de les Illes Balears (Spain), Mallorca, Spain.

Hong, S.-Y., Pan, H.-L., (1998). Convective trigger function for a mass-flux cumulus parameterization scheme. *Monthly Weather Review*, 126 (10), 2599-2620.

Hu, X.-M., Nielsen-Gammon, J.W., Zhang, F., (2010). Evaluation of Three Planetary Boundary Layer Schemes in the WRF Model. *Journal of Applied Meteorology and Climatology*, 49 (9), 1831-1844.

Izquierdo, A., Tejedor, L., Sein, D.V., Backhaus, J.O., Brandt, P., Rubino, A., Kagan, B.A., (2001). Control variability and internal bore evolution in the Strait of Gibraltar: A 2-D two-layer model study. *Estuarine Coastal and Shelf Science*, 53, 637-651.

Jiménez, P.A., Dudhia, J., (2012). Improving the Representation of Resolved and Unresolved Topographic Effects on Surface Wind in the WRF Model. *Journal of Applied Meteorology and Climatology*, 51 (2), 300-316.

Jiménez, P.A., Dudhia, J., (2013). On the Ability of the WRF Model to Reproduce the Surface Wind Direction over Complex Terrain. *Journal of Applied Meteorology and Climatology*, 52 (7), 1610-1617.

Kain, J.S., Fritsch, J.M., (1993). Convective parameterization for mesoscale models: The Kain-Fritsch scheme. Representation of Cumulus Convection in Numerical Models. American Meteorological Society, Boston, MA, pp. 165-170.

Kalnay, E., Kanamitsu, M., Kistler, R., Collins, W., Deaven, D., Gandin, L., Iredell, M., Saha, S., White, G., Woollen, J., Zhu, Y., Leetmaa, A., Reynolds, R., Chelliah, M., Ebisuzaki, W., Higgins, W., Janowiak, J., Mo, K.C., Ropelewski, C., Wang, J., Jenne, R., Joseph, D., (1996). The NCEP/NCAR 40-Year Reanalysis Project. *Bulletin of the American Meteorological Society*, 77 (3), 437-471.

Källén, E., (1996). HIRLAM Documentation Manual, system 2.5. *Technical report, SMHI, S-601 76 Norrköping, Sweden.*

Kämpf, J., (2009). *Ocean Modelling for beginners.Using Open-Source Software.* Springer-Verlag Berlin.

Kämpf, J., (2010). *Advanced ocean modelling using open-source software.* Springer-Verlag Berlin.

Kelly, K.A., Dickinson, S., McPhaden, M.J., Johnson, G.C., (2001). Ocean currents evident in satellite wind data. *Geophysical Research Letters*, 28 (12), 2469-2472.

Kemball-Cook, S., Jia, T., Emery, C., Morris, R., (2005). Alaska MM5 Modeling for the 2002 Annual Period to Support Visibility Modeling.Prepared for the Western Regional Air Partnership, by ENVIRON International Corporation. Novato, CA.

Kinder, T.H., Bryden, H.L., (1987). The 1985-86 Gibraltar Experiment: data collection and preliminary results. *Eos, Eos, Transactions of the American Geophysical Union*, 68 (40), 786-794.

Knudsen, M., (1899). Dehydrografiskeforhold i de danske farvande inden for Skagen i 1894–1898 [The hydrographical condition in the Danish Coastal waters inside Skagen during 1894–1898] *Bereit. Komm. Vidensk. Unders. Dan. Farvande* 2(2), 19-79.

Lacombe, H., Richez, C., (1982). The regime of the Strait of Gibraltar. Elsevier Oceanography Series, pp. 13-73.

Le Provost, C., Lyard, F., Molines, J.M., Genco, M.L., Rabilloud, F., (1998). A hydrodynamic ocean tide model improved by assimilating a satellite altimeter-derived data set. *Journal of Geophysical Research*, 103 (C3), 5513-5529.

Lenderink, G., Meijgaard, E., Selten, F., (2009). Intense coastal rainfall in the Netherlands in response to high sea surface temperatures: analysis of the event of August 2006 from the perspective of a changing climate. *Climate Dynamics*, 32 (1), 19-33.

Leung, L.R., Qian, Y., (2003). The Sensitivity of Precipitation and Snowpack Simulations to Model Resolution via Nesting in Regions of Complex Terrain. *Journal of Hydrometeorology*, 4 (6), 1025-1043.

Lindzen, R.S., (1967). Thermally driven diurnal tide in the atmosphere. *Quarterly Journal of the Royal Meteorological Society*, 93 (395), 18-42.

Lozej, C., Bornstein, R.D., (1999). Comparison of nesting techniques within a meteorological model. In: Brebbia, C.A., Jacobson, M. and Power, H. (Ed.), Air pollution VII. Computacional Mechanics Publications, Billerica, p. 13 p.

Lu, X., Chown, K.-C., Yao, T., Fung, J.C.H., Lau, A.K.H., (2009). Seasonal variation of the land–sea breeze circulation in the Pearl River Delta region. *Journal of Geophysical Research.*, 114.

Macías, D., Bruno, M., Echevarría, F., Vázquez, A., García, C.M., (2008). Meteorologically-induced mesoscale variability of the North-western Alboran Sea (southern Spain) and related biological patterns. *Estuarine Coastal and Shelf Science*, 78, 250-266.

Manning, K.W., Davis, C.A., (1997). Verification and Sensitivity Experiments for the WISP94 MM5 Forecasts. *Weather and Forecasting*, 12 (4), 719-735.

Mañanes, R., Bruno, M., Alonso, J., Fraguela, B., Tejedor, L., (1998). Non-linear interaction between tidal and subinertial barotropic flows in the Strait of Gibraltar. *Oceanologica Acta*, 21 (1), 33-46.

Marshall, J., Adcroft, A., Hill, C., Perelman, L., Heisey, C., (1997a). A finite-volume, incompressible Navier-Stokes model for studies of the ocean on parallel computers. *Journal of Geophysical Research*, 102, 5733-5752.

Marshall, J., Hill, C., Perelman, L., Adcroft, A., (1997b). Hydrostatic, quasi-hydrostatic, and nonhydrostatic ocean modeling. *Journal of Geophysical Research*, 102 (C3), 5733-5752.

Marsigli, L.F., (1681). Osservazioni intorno al Bosforo Tracio overo Canale di Constantinopoli rappresentate in lettera all sacra real maesta di Cristina Regina di Svezia, Roma.

Marsland, S.J., Haak, H., Jungclaus, J.H., Latif, M., Röske, F., (2003). The Max-Planck-Institute global ocean/sea ice model with orthogonal curvilinear coordinates. *Ocean Modelling*, 5 (2), 91-127.

Martin, G., (1998). An outstanding performance by the Eta-10 for the southern California storm of 23 February 1998. *Western Regional Attachment*, 98 (36), 4.

Mass, C.F., Ovens, D., (2011). Fixing WRF's high speed wind bias: a new subgrid scale drag parameterization and the role of detailed verification. 24th Conference on Weather and Forecasting and 20th Conference on Numerical Weather Prediction, Preprints, 91st Americal Meteorological Society Annual Meeting, Seattle, WA.

McQueen, J.T., Draxler, R.R., Rolph, G.D., (1995). Influence of Grid Size and Terrain Resolution on Wind Field Predictions from an Operational Mesoscale Model. *Journal of Applied Meteorology*, 34 (10), 2166-2181.

Melas, D., Ziomas, I., Klemm, O., Zerefos, C.S., (1998). Anatomy of the sea-breeze circulation in Athens area under weak large-scale ambient winds. *Atmospheric Environment*, 32 (12), 2223-2237.

Mellor, G.L., Wang, X.H., (1996). Pressure Compensation and the Bottom Boundary Layer. *Journal of Physical Oceanography*, 26 (10), 2214-2222.

Menemenlis, D., Fukumori, I., Lee, T., (2007). Atlantic to Mediterranean sea level difference driven by winds near Gibraltar Strait. *Journal of Geophysical Oceanography*, 37, 359-376.

Mesinger, F., Arakawa, A. (Eds.), (1976). Numerical methods used in atmospheric models. GARP Publications.

Michelson, S.A., Bao, J.-W., (2006). Comparison of two meteorological community models for air-quality applications. 14-th Joint Conference on the Applications of Air Pollution Meteorology with the Air and Waste Management Association. American Meteorology Society, Atlanta, Georgia.

Oncley, S.P., Dudhia, J., (1995). Evaluation of surface fluxes from MM5 using observations. *Monthly Weather Review*, 125, 3344-3357.

Orlanski, I., (1975). A rational subdivision of scales for atmospheric processes. *Bulletin of the American Meteorological Society*, 56 (5), 527-530.

Paegle, J., Yang, Q., Wang, M., (1997). Predictability in limited area and global models. *Meteorology and Atmospheric Physics*, 63, 53-69.

Papanastasiou, D.K., Melas, D., (2009). Climatology and impact on air quality of sea breeze in an urban coastal environment. *International Journal of Climatology*, 29 (2), 305-315.

Peliz, A.l., Teles-Machado, A., Marchesiello, P., Dubert, J., Lafuente, J.G., (2009). Filament generation off the Strait of Gibraltar in response to Gap winds. *Dynamics of Atmospheres and Oceans*, 46, 36-45.

Penabad, E., Alvarez, I., Balseiro, C.F., deCastro, M., Gómez, B., Pérez-Muñuzuri, V., Gómez-Gesteira, M., (2008). Comparative analysis between operational weather prediction models and QuikSCAT wind data near the Galician coast. *Journal of Marine Systems*, 72 (1-4), 256-270.

Pérez de los Cobos, P., Carazo, J.I., Padilla, F., (2003). Agroclimatic Information System for Irrigation Areas. In: Madrid: Ministerio de Medio Ambiente (Ed.), 3ª Conferencia Internacional sobre Experiencias con Estaciones Meteorológicas Automáticas, Torremolinos (Málaga).

Pettigrew, N.R., Needell, G.L., (1989). Flow structure and variability in the Tarifa narrows section of the Strait of Gibraltar. Seminario sobre la oceanografia física del estrecho de Gibraltar. SECEG, Madrid, pp. 207-229.

Pettigrew, N.R., Hyde, R.A., (1990). The Structure of the Internal Bore in the Strait of Gibraltar and its Influence on the Atlantic Inflow. The Physical Oceanography of Sea Straits. Springer Netherlands, pp. 493-508.

Pielke, R.A. (Ed.), (1984). Mesoscale meteorological modeling. Acedemic Press, Orlando.

Rao, P.A., Fuelberg, H.E., Droegemeier, K.K., (1999). High-resolution modeling of the Cape Canaveral area land-water circulations and associated features. *Mon. Weather Rev.*, 127, 1808-1821.

Richez, C., (1994). Airborne synthetic aperture radar tracking of internal waves in the Strait of Gibraltar. *Progress in Oceanography*, 33 (2), 93-159.

Rossby, C.G., (1938). On the mutual adjustment of pressure and velocity distributions in certain simple current systems II. *Journal of Marine Research*, 1, 239-263.

Sánchez-Garrido, J.C., Sannino, G., Liberti, L., García, L., J., Pratt, L.J., (2011). Numerical modeling of three-dimensional stratified tidal flow over Camarinal Sill, Strait of Gibraltar. *Journal of Geophysical Research*, 116, 1-17.

Sánchez-Garrido, J.C., Lafuente, J.G., Sammartino, S., Naranjo, C., de los Santos, F.J., Ávarez Fanjul, E., (2014). Meteorologically-driven circulation and flushing times of the Bay of Algeciras, Strait of Gibraltar. *Marine Pollution Bulletin*, 80 (1-2), 97-106.

Sánchez-Román, A., Sannino, G., García-Lafuente, J., Carillo, A., Criado-Aldeanueva, F., (2009). Transport estimates at the western section of the Strait of Gibraltar: A combined experimental and numerical modeling study. *Journal of Geophysical Research*, 114 (C06002).

Sánchez Ayllo, J.L., Nuche Benito, F., Ruiz Cañavate, A., (1983). Oceanografía y Meteorología del Estrecho de Gibraltar. *Revista General de Marina*, 206, 789-791.

Sánchez, P., Pascual, J.R. (Eds.), (1988). Primeras experiencias en la modelación del Estrecho de Gibraltar., Escuela Superior Ing. Cammos, Canales y Puertos, Madrid.

Sandstrom, H., (1980). On the wind-induced sea level changes on the Scotian Shelf. *Journal of Geophysical Research*, 85, 461-468.

Sannino, G., Bargagli, A., Artale, V., (2002). Numerical study of the hydraulics of the mean flow through the Strait of Gibraltar. The Second Meeting on the Physical Oceanography of Sea Straits, Villefranche.

Sannino, G., Bargagli, A., Artale, V., (2004). Numerical modeling of the semidiurnal tidal exchange through the Strait of Gibraltar. *Journal of Geophysical Research*, 109 (C5), C05011.

Sannino, G., (2007). The role of the interfacial layer in exchange and hydraulics in the Strait of Gibraltar: a 3D numerical modeling study., PhD Thesis, Università degli Studi di Napoli Parthenope, Italy, Napoli.

Santhi, C., Arnold, J.G., Williams, J.R., Dugas, W.A., Srinivasan, R., Hauck, L.M., (2001). Validation of the SWAT model on a large river basin with point and nonpoint sources. *Journal of the American Water Resources Association*, 37 (5), 1169-1188.

Sanz, J.L., Acosta, J., Esteras, M., Herranz, P., Palomo, C., Sandoval, N.G., (1991). Prospección geofísica del Estrecho de Gibraltar: resultados del programa Hércules (1980-1983). *Instituto Español del Oceanografía. Publicación Especial.*, 7, 1:48.

Sein, D.V., Backhaus, J.O., Brandt, P., Izquierdo, A., Kagan, B.A., Rubino, A., Tejedor, L., (1998). Flow exchange and tidally induced dynamics in the Strait of Gibraltar derived from a two-layer, boundary-fitted coordinate model. In: 2000, U. (Ed.), Oceanic fronts and related phenomena. Konstantin Fedorov Internation Memorial Symposium. 1999, Pushkin, Saint Petersburg. Russian Federation.

Send, U., Baschek, B., (2001). Intensive shipboard observations of the flow through the Strait of Gibraltar. *Journal of Geophysical Research: Oceans*, 106 (C12), 31017-31032.

Shchepetkin, A.F., McWilliams, J.C., (2005). The regional oceanic modeling system (ROMS): a split-explicit, free-surface, topography-following-coordinate oceanic model. *Ocean Modelling*, 9 (4), 347-404.

Skamarock, W.C., Klemp, J.B., Dudhia, J., Gill, D.O., Barker, D.M., Wang, W., Powers, J.G., (2005). A description of the advanced research WRF version 2. *NCAR Technical Notes*, NCAR/TN-468+STR.

Soler, M.R., Hinojosa, J., Bravo, M., Pino, D., Vilà-Guerau de Arellano, J., (2003). Analyzing the basic features of different complex terrain flows by means of a Doppler Sodar and a numerical model: Some implications for air pollution problems. *Meteorology and Atmospheric Physics*, 14 p.

Soriano, C., Jorba, O., Baldasano, J.M. (Eds.), (2002). One-way nesting versus two-way nesting: Does it really make a difference?. Ed. Borrego and Schayes. Kluwer Academic/Plenum Publishers, New York.

Speich, S., Madec, G., Crepon, M., (1996). A Strait Outflow Circulation Process Study: The Case of the Alboran Sea. *Journal of Physical Oceanography*, 26 (3), 320-340.

Stanichny, S., Tigny, V., Stanichnaya, R., Djenidi, S., (2005). Wind driven upwelling along the African coast of the Strait of Gibraltar. *Geophysical Research Letters*, 32 (4), L04604.

Stauffer, D.R., Seaman, N.L., (1990). Use of four-dimensional data assimilation in a limited-area mesoscale model. Part I: Experiments with synoptic-scale data. *Monthly Weather Review*, 118, 1250-1277.

Steeneveld, G.J., Vilá -Guerau de Arellano, J., Holtslag, A.A.M., Mauritsen, T., Svensson, G., de Bruijn, E.I.F., (2008). Evaluation of Limited-Area Models for the Representation of the Diurnal Cycle and Contrasting Nights in CASES-99. *Journal of Applied Meteorology and Climatology*, 47 (3), 869-887.

Stenger, R.A., (2000). Sensitivity studies on a limited area mesoscale model: an examination of lateral boundary placement, grid resolution and nesting type Master's thesis, Air Force Institute of Technology, Wright-Patterson AFB, OH. School of Engineering.

Stommel, H., Farmer, H.G., (1953). Control of salinity in an estuary by a transition. *Journal of Marine Research*, 12 (1), 13-20.

Stull, R.B. (Ed.), (1988). An introduction to boundary layer meteorology. Kluwer Academic Publishing, Netherlands.

Sweeney, J.K., Chagnon, J.M., Gray, S.L., (2014). A case study of sea breeze blocking regulated by sea surface temperature along the English south coast. *Atmos. Chem. Phys.*, 14 (9), 4409-4418.

Tejedor, L., Izquierdo, A., Sein, D.V., Kagan, B.A., (1999). Tides and tidal energetics of the Strait of Gibraltar: a modelling approach. *Tectonophysics*, 294 (3-4), 333-347.

Teles-Machado, A., Peliz, Á., Dubert, J., Sánchez, R.F., (2007). On the onset of the Gulf of Cadiz Coastal Countercurrent. *Geophysical Research Letters*, 34 (12), L12601.

Tesche, T.W., McNally, D.E., Tremback, C., (2002). Operational evaluation of the MM5 meteorological model over the continental United States: Protocol for Annual and Episodic Evaluation.

Tsimplis, M.N., Bryden, H.L., (2000). Estimation of the transports through the Strait of Gibraltar. *Deep Sea Research Part I: Oceanographic Research Papers*, 47 (12), 2219-2242.

Undén, P., Rontu, L., Järvinen, H., Lynch, P., Calvo, J., Cats, G., Cuxart, J., Eerola, K., Fortelius, C., García-Moya, J.A., Jones, C., Lenderlink, G., McDonald, A., McGrath, R., Navascues, B., Nielsen, N.W., Ödegaard, V., Rodriguez, E., Rummukainen, M., Rööm, R., Sattler, K., Sass, B.H., Savijärvi, H., Schreur, B.W., Sigg, R., The, H., Tijm, A., (2002). HIRLAM-5 Scientific Documentation, HIRLAM-5 Project. Scientific Documentation Available at SMHI, S-60176, Norrköping, Sweden.

Van, L., M, W., Arnold, J, G., Garbrecht, J, D., (2003). *Hydrologic simulation on agricultural watersheds: Choosing between two models*. Vol. 46, American Society of Agricultural Engineers, 13 pp.

Vargas, J.M., García Lafuente, J., Candela, J., Sánchez Román, A., (2006). Fortnightly and monthly variability of the exchange through the Strait of Gibraltar. *Progress in Oceanography*, 70 (2-4), 466-485.

Vázquez, A., Stashchuk, N., Vlasenko, V., Bruno, M., Izquierdo, A., Gallacher, P.C., (2006). Evidence of multimodal structure of the baroclinic tide in the Strait of Gibraltar. *Geophysical Research Letters*, 33 (17), L17605.

Vázquez, A., Bruno, M., Izquierdo, A., Macías, D., Ruiz-Cañavate, A., (2008). Meteorologically forced subinertial flows and internal wave generation at the main sill of the Strait of Gibraltar. *Deep-Sea Research I*, (55), 1277– 1283.

Vázquez López-Escobar, Á., (2006). Ondas internas en el Estrecho de Gibraltar y procesos de mezcla inducidos, Tesis Doctoral, Universidad de Cádiz, España, Servicio de Publicaciones

Vilà-Guerau de Arellano, J., Vellinga, O.S., Holtslag, A.A.M., Bosveld, F.C., Klein Baltink, H., (2001). Observational evaluation of PBL parameterizations modelled by MM5. In: Proceedings MM5 Workshop on Impact of physical parameterizations on mesoscale numerical simulations, Boulder, USA, pp. 102-106.

Vlasenko, V.I., Sánchez Garrido, J.C., Stashchuk, N., García Lafuente, J., Losada, M., (2009). Three-dimensional evolution of large-amplitude internal waves in the Strait of Gibraltar. *Journal of Physical Oceanography*, 39, 2230-2246.

Wang, D.-P., (1987). The strait surface outflow. *Journal of Geophysical Research: Oceans*, 92 (C10), 10807-10825.

Wang, D.P., (1989). Model of mean and tidal flows in the Strait of Gibraltar. *Deep Sea Research Part A, Oceanographic Research Papers*, 36 (10), 1535-1548.

Watson, G., Robinson, I.S., (1990). A Study of Internal Wave Propagation in the Strait of Gibraltar Using Shore-Based Marine Radar Images. *Journal of Physical Oceanography*, 20 (3), 374-395.

White, B.G., Paegle, J., Steenburgh, W.J., Horel, J.D., Swanson, R.T., Cook, L.K., Onton, D.J., Miles, J.G., (1999). Short-Term Forecast Validation of Six Models. *Weather and Forecasting*, 14 (1), 84-108.

Wilks, D., (1995). *Statistical methods in the atmospheric sciences*. Vol. 59, *International Geophysics Series*, Academic Press, 464 pp pp.

Willmott, C.J., (1981). On the validation of models. *Physical Geography*, 2, 184-194.

Willmott, C.J., (1982). Some comments on the evaluation of model performance. *Bulletin of the American Meteorological Society*, 63, 1309-1313.

Willmott, C.J., (1984). On the evaluation of model performance in physical geography
In: Gaile, G.L.a.W., C. J., Reidel D., (Ed.), Spatial Statistics and Models, Hingham, Mass.

Willmott, C.J., Ackleson, S.G., Davis, R.E., Feddema, J.J., Klink, K.M., Legates, D.R., O'Donnell, J., Rowe, C.M., (1985). Statistics for the evaluation and comparison of models. *Journal of Geophysical Research: Oceans*, 90 (C5), 8995-9005.

Willmott, C.J., Matsuura, K., (2005). Advantages of the mean absolute error (MAE) over the root mean square error (RMSE) in assessing average model performance. *Climate Research*, 30 (1), 79-82.

Willmott, C.J., Robeson, S.M., Matsuura, K., (2012). A refined index of model performance. *International Journal of Climatology*, 32 (13), 2088-2094.

Wyszogrodzki, A., Liu, Y., Jacobs, N., Childs, P., Zhang, Y., Roux, G., Warner, T., (2013). Analysis of the surface temperature and wind forecast errors of the NCAR-AirDat operational CONUS 4-km WRF forecasting system. *Meteorology and Atmospheric Physics*, 122 (3-4), 125-143.

Zhang, D.-L., Zheng, W.-Z., (2004). Diurnal Cycles of Surface Winds and Temperatures as Simulated by Five Boundary Layer Parameterizations. *Journal of Applied Meteorology*, 43 (1), 157-169.

Zhong, S., Fast, J., (2003). An evaluation of the MM5, RAMS and Meso-Eta models at subkilometer resolution using VTMX field campaign data in the Salt Lake valley. *Monthly Weather Review*, 131, 1301-1322.

Zhong, S., In, H., Clements, C., (2007). Impact of turbulence, land surface, and radiation parameterizations on simulated boundary layer properties in a coastal environment. *Journal of Geophysical Research: Atmospheres*, 112 (D13), D13110.

Ziegenbein, J., (1970). Spatial observations of short internal waves in the Strait of Gibraltar. *Deep Sea Research and Oceanographic Abstracts*, 17 (5), 867-875.

El presente trabajo de investigación aborda el estudio de la influencia del viento en la variabilidad espacio-temporal de la circulación del Estrecho de Gibraltar (sur de la Península Ibérica) y de las respuestas inducidas que se producen en las fluctuaciones barotrópicas y del intercambio baroclino, mediante un modelo oceánico forzado por viento.

This research work makes an incremental step in understanding the role of the wind-stress and the associated dynamic ocean response of the barotropic and baroclinic exchange fluctuations by means of a wind-forced ocean model within the Strait of Gibraltar (south of Iberian Peninsula).

25 años
1989-2014
Facultad de Ciencias
del Mar y Ambientales

UCA
Universidad
de Cádiz